

Physical Processes in Protoplanetary Disks

Philip J. Armitage

Abstract This review, based on lectures given at the 45th Saas-Fee Advanced Course “From Protoplanetary Disks to Planet Formation”, introduces physical processes in protoplanetary disks relevant to accretion and the initial stages of planet formation. After a brief overview of the observational context, I introduce the elementary theory of disk structure and evolution, review the gas-phase physics of angular momentum transport through turbulence and disk winds, and discuss possible origins for the episodic accretion observed in Young Stellar Objects. Turning to solids, I review the evolution of single particles under aerodynamic forces, and describe the conditions necessary for the development of collective gas-particle instabilities. Observations show that disks can exhibit pronounced large-scale structure, and I discuss the types of structures that may form from gas and particle interactions at ice lines, vortices and zonal flows, prior to the formation of large planetary bodies. I conclude with disk dispersal.

Philip J. Armitage
JILA, University of Colorado & NIST, Boulder, Colorado, CO 80309-0440, USA, e-mail: pja@jilau1.colorado.edu

1 Preamble

The objective of this review is to introduce the physical processes in protoplanetary disks that are relevant to protostellar accretion and the initial stages of planet formation. Protoplanetary disks, as well as being interesting objects of study in their own right, are also simultaneously an outcome of star formation and initial conditions for planet formation. As such, we need to understand the evolution of both the dominant gaseous component and the trace of solid material that is critical for planet formation. Much interesting complexity occurs due to interactions between the two.

The review is organized around three motivating questions; how do protoplanetary gas disks evolve over time, how are solids transported and concentrated within the gas, and how do gas-phase and solid processes interact to form structure within disks? I begin in §2 with a brief summary of the observational context. The review proper starts in §3 by outlining the equilibrium structure of disks. Disk evolution is described in §4 and §5, first following the classical approach in which the origin of angular momentum transport is unspecified, and subsequently in a more modern presentation where angular momentum transport and loss processes are ascribed to specific fluid instabilities. §6 discusses candidate theoretical explanations, some of them directly related to angular momentum transport processes, for episodic accretion outbursts. In §7 the focus switches to solids, and I review how single solid particles settle, drift, diffuse and concentrate relative to the gas. §8 then describes how these processes can give rise to structure within the disk on various scales, either at transient “particle traps” or at persistent locations such as ice lines where the disk structure varies rapidly. Finally, §9 reviews what is known about the processes, including photoevaporation, that can disperse protoplanetary disks.

The lectures, even expanded as in this review, could not touch upon all of the physics that an aspiring researcher in the field might require. In an effort to cover as much as possible — and to accommodate the diverse backgrounds of participants (and readers) — the material is presented with varying degrees of detail and rigor. For most topics I begin with a self-contained discussion of essential material that would often be assumed as background in papers or talks. I then discuss the underlying physics of more recent results, and give entry points to the relevant literature.

One caution is in order. Quantities are generally defined and labeled following conventions in the literature, to make it easier for the reader who needs to fill in missing details or to explore further. Given the broad scope of the review there is considerable overloading of notation, with the same symbols being used to represent unrelated quantities in different sections. Take care!

2 Observational context

The challenges of observing protoplanetary disks are formidable. Around Solar mass stars the lifetime of primordial disks of gas and dust is a small fraction — $10^{-3} - 10^{-4}$ — of the main sequence lifetime. Disks around stars are hence rare, and even the nearest examples are relatively distant and hard to resolve. A small number of disks, including particularly well-studied examples such as TW Hya, are as close as $d \approx 50$ pc, but for larger samples we need to look out at least as far as low-mass star forming regions such as Taurus, at $d \approx 140$ pc [408]. Regions where massive stars are forming alongside low mass stars, such as Orion, are yet further away at $d \approx 400$ pc [223]. Spatially resolved imaging of disks with scales comparable to that of the Solar System, $\sim 10^2$ AU, requires sub-arcsecond resolution that has only become available in relatively recent times from the *Hubble Space Telescope* [307], from the *Atacama Large Millimeter / submillimeter Array (ALMA)* and earlier mm / sub-mm interferometers [8], and from high-contrast imaging instruments on large ground-based telescopes [152, 133, 296]. Today we have exquisite imaging and spatially resolved spectroscopy of a moderate number of protoplanetary disks, along with a larger amount of data that derives from a time when unresolved observations were the norm.

Williams & Cieza (2011) [435] review observations of protoplanetary disks up to a time just prior to the advent of *ALMA*. The focus of this review is on theory, but to set the stage and introduce some ubiquitous terminology we begin with a brief discussion of the observational context. What do we know about disks that might constrain theoretical models, and how do we know it?

2.1 The classification of Young Stellar Objects

Young Stellar Objects (YSOs) frequently show more emission in the infra-red than would be expected from a pre-main-sequence star's photosphere. The IR excess is attributed to the presence of dust in the vicinity of the star, and its strength forms the basis for an empirical classification scheme for YSOs that dates back to work by Lada & Wilking [235] in the early 1980s. We define the slope of the spectral energy distribution (SED) between near-IR and mid-IR wavelengths,

$$\alpha_{\text{IR}} \equiv \frac{d \log \nu F_{\nu}}{d \log \nu} \equiv \frac{d \log \lambda F_{\lambda}}{d \log \lambda}. \quad (1)$$

The anchor points in the near- and mid-IR for the determination of α_{IR} vary from study to study, but are typically something like $2 \mu\text{m}$ and $25 \mu\text{m}$. Based on α_{IR} four or five classes of YSO are recognized [435],

- **Class 0:** heavily obscured sources with no optical or near-IR emission (α_{IR} is therefore undefined).
- **Class I:** $\alpha_{\text{IR}} > 0.3$.

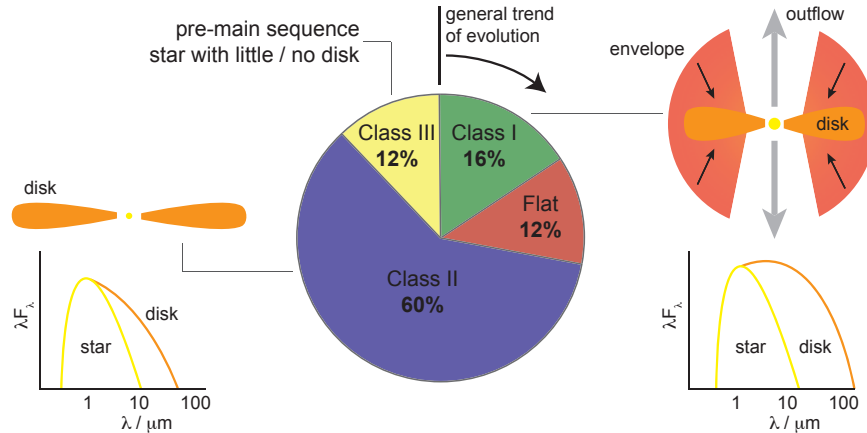


Fig. 1 The physical picture underlying the classification of Young Stellar Objects [235, 2] is shown together with statistics from the *Spitzer* c2d Legacy survey for the fraction of sources falling into each class [125]. The classification scheme is based upon the slope of the spectral energy distribution between the near- and mid-infra-red. This maps to a structural (and essentially evolutionary) sequence in which Class 0 and Class I YSOs are accreting from disks, which themselves are being fed by gas falling in from envelopes. Class II YSOs (also called Classical T Tauri stars) are pre-main-sequence stars with surrounding disks, while Class III YSOs (or Weak-lined T Tauri stars) are pre-main-sequence stars with little or no primordial gas remaining in orbit around them.

- **Flat spectrum sources:** $-0.3 < \alpha_{\text{IR}} < 0.3$.
- **Class II:** $-1.6 < \alpha_{\text{IR}} < -0.3$.
- **Class III:** $\alpha_{\text{IR}} < -1.6$. These sources have at most weak IR-excess emission, and have SEDs that resemble isolated pre-main-sequence stellar photospheres.

Figure 1 shows how these empirically derived classes match up against the expected evolution of circumstellar material over time [2]. Stars form from the collapse of molecular cloud cores which have vastly more angular momentum than can be accommodated in a star [157]. Some of that angular momentum can be lost via magnetic braking [250], or subsumed into the orbital angular momentum of binaries [351], but it is an observational fact that enough is commonly left over to form a rotationally supported disk. The free-fall time scale of molecular cloud cores is shorter than the lifetime of disks, so the youngest (Class 0 and Class I) YSOs are surrounded by disks which themselves are fed by infall from envelopes. Older YSOs (Class II) have lost their envelopes but retain relatively massive and often actively accreting gas disks. Finally the gas disk dissipates, leaving behind a Class III YSO.

For the subset of YSOs that are optically visible some of the terminology derives from an even older classification scheme that is based on the equivalent width of the $\text{H}\alpha$ line [208]. $\text{H}\alpha$ is a diagnostic of gas accreting on to the star, so Class II sources with disks are largely equivalent to “Classical T Tauri stars” with high $\text{H}\alpha$ equivalent widths. “Weak-lined T Tauri stars” are likewise essentially the same objects as Class III sources.

Determining the absolute ages of young stars is a difficult exercise that leads to uncertainty in estimates of the mean duration of the different phases. An easier task is to estimate the *relative* durations. Provided that we survey enough regions of recent and ongoing star formation, we may reasonably assume that the proportions of YSOs in the different classes reflect the amount of time that a typical YSO spends in each class. Figure 1 shows the distribution of YSOs among the classes, as determined by the “Cores to Disks” legacy project that used the *Spitzer* space telescope [125]. One sees that Class I sources with envelopes are much less numerous than Flat Spectrum and Class II sources that have disks but little or no envelope. Most of the circumstellar disk lifetime therefore consists of relatively isolated star-disk systems that have completed the primary phase of accretion from the envelope¹.

There is no uniform definition of the term “protoplanetary disk”. In this review, our main focus is on isolated disks where envelope accretion has largely ceased. Observationally this would correspond to Flat Spectrum and Class II YSOs. Most of the action in planet formation, reviewed in Willy Kley’s contribution to this volume, is also commonly assumed to occur in an isolated disk environment. One should be aware, however, that scant empirical evidence underlies this assumption, and that the time scales of planet formation processes through to (at least) planetesimal scales can be rapid. Important aspects of planet formation could be already well-advanced during the embedded Class 0 and Class I phases of YSO evolution.

2.2 Accretion rates and lifetimes

The accretion rate \dot{M} of gas through the disk is one of the most important quantities that we would like to determine. It can only be measured with any confidence at small radii, where the gas from the disk is flowing on to the star. As we will discuss in §4.2.2, for typical Classical T Tauri stars there is abundant evidence that the stellar magnetic field disrupts the inner disk at a magnetospheric radius R_m . Gas interior to R_m follows trajectories that are tied to magnetic field lines, before crashing on to the stellar surface at close to the free fall speed [73]. For a star of mass M_* and radius R_* the accretion luminosity will be,

$$\begin{aligned} L_{\text{acc}} &\simeq GM_*\dot{M} \left(\frac{1}{R_*} - \frac{1}{R_m} \right) \\ &\sim 0.2 \left(\frac{M_*}{M_\odot} \right) \left(\frac{R_*}{1.5 R_\odot} \right)^{-1} \left(\frac{\dot{M}}{10^{-8} M_\odot \text{ yr}^{-1}} \right) L_\odot, \end{aligned} \quad (2)$$

where for the numerical estimate we have taken $R_m \gg R_*$ and adopted typical numbers for T Tauri stars. The accretion luminosity will be radiated from shocks or hotspots on the stellar surface. We will be able to estimate \dot{M} provided that we know

¹ Accretion from lower density gas within the star forming region could persist to later times [405].

the basic stellar parameters and can distinguish the emission arising from accretion from the stellar photospheric emission.

In practice the determination of \dot{M} from a stellar spectrum can be attempted in several ways, which differ in observational expense and fidelity. The most direct measurements require access to the entire ultraviolet (UV) spectrum, including short wavelengths that are not accessible from the ground. An example of early work of this type, using data from the *International Ultraviolet Explorer*, are the accretion rate measurements by Gullbring et al. [166]. Next best is observations from the ground, which can cover enough of the UV spectrum (down to about 300 nm) to allow a direct determination of L_{acc} [167, 180]. Recent studies, such as that by Manara et al. [275] take advantage of instruments with a wide spectral coverage to simultaneously determine the accretion rate and the stellar parameters. Finally, the luminosity in a number of different spectral lines has been shown to correlate well with the total accretion luminosity [359], and measurements of line luminosities can be converted to accretion rates at the cost of some additional uncertainty.

The inferred accretion rates in Class II YSOs are found to vary strongly with the stellar mass M_* [300]. In the Chamaeleon I star forming region, for example, Manara et al. determine a stellar mass / accretion rate relation of the form [275],

$$\log\left(\frac{\dot{M}}{M_{\odot} \text{ yr}^{-1}}\right) = (1.83 \pm 0.35) \log\left(\frac{M_*}{M_{\odot}}\right) - (8.13 \pm 0.16). \quad (3)$$

This is a fairly representative result. Mean accretion rates through protoplanetary disks around Solar mass stars are of the order of $10^{-8} M_{\odot} \text{ yr}^{-1}$, with a stellar mass scaling that is significantly steeper than linear.

By estimating ages from the position of pre-main-sequence stars in the H-R diagram Hartmann et al. [171] showed that the median accretion rate for T Tauri stars in Taurus and Chamaeleon I declined with time. Consistent with this result, and with common sense expectations, the *fraction* of stars that host primordial disks declines with stellar age. This is commonly expressed not on a star-by-star basis, but rather by measuring the fraction of stars in a cluster with near-IR excess, and assigning a representative age to that cluster [170]. Using this method Hernández et al. [181] find that the disk fraction drops to 50% at about 3 Myr. Caution is needed, however, because the ages of young clusters remain hard to determine, with some assessments suggesting that uncertainties may be as large as a factor of two [385].

The astronomically inferred disk lifetime is compatible with the chronology derived independently from the radioactive dating of primitive Solar System materials. The oldest Solar System samples are calcium-aluminum-rich inclusions (CAIs) found within chondritic meteorites. CAIs are dated to 4567.30 ± 0.16 million years ago. Chondritic meteorites also contain (and are named after) *chondrules* — 0.1-1 mm spheres of rock that were heated to approximately their melting temperature in short-lived events in the early Solar System (see e.g. the short review by Connolly & Jones [101]). How chondrules formed remains unclear, but it is known that their production (and possibly repeated subsequent heating events) began at the same time as the CAIs and continued for about 4 Myr [71]. If chondrule heating occurred

predominantly in a primordial gas disk environment, one would conclude from this that the lifetime of the Solar System's gas disk was fairly typical. At the least, there is no evidence for any inconsistency between astronomical and meteoritic dating results.

2.3 Inferences from the dust continuum

At disk temperatures $T < 1500$ K the opacity in protoplanetary disks is dominated by the contribution from rocky or icy grains (generically “dust”). Observations of continuum radiation from thermal dust emission provide information about the radial temperature distribution in the disk, the disk mass, and the size of dust particles. To illustrate how this works, consider a toy model of a thin disk in which dust emits thermal radiation with a single temperature at each radius (we defer discussion of realistic complications associated with the vertical structure to §3.2). We assume that the gas surface density Σ and dust temperature T_d are power laws in radius,

$$\begin{aligned}\Sigma &\propto r^{-p}, \\ T_d &\propto r^{-q},\end{aligned}\tag{4}$$

and adopt a frequency dependent opacity (defined per unit mass of gas),

$$\kappa_\nu = \kappa_0 \nu^\beta.\tag{5}$$

The vertical optical depth through the disk is then $\tau_\nu = \Sigma \kappa_\nu$. For a face-on disk the formal solution of the radiative transfer equation (e.g. [366]) gives the flux density F_ν as,

$$F_\nu = \frac{1}{D^2} \int_{r_{\text{in}}}^{r_{\text{out}}} B_\nu(T_d) (1 - e^{-\tau_\nu}) 2\pi r dr,\tag{6}$$

where D is the distance to the source, r_{in} and r_{out} are the inner and outer radii of the disk, and B_ν is the Planck function,

$$B_\nu = \frac{2h\nu^3}{c^2} \frac{1}{\exp[h\nu/k_B T_d] - 1}.\tag{7}$$

Let us consider what we can learn from F_ν in the limit where the disk is either optically thick ($\tau_\nu > 1$) or optically thin.

Taking the $\tau_\nu \gg 1$ limit first, let us assume that we observe the disk at wavelengths where the entire disk is optically thick. This will be true in the near- and mid-IR. Setting $e^{-\tau_\nu} = 0$ in equation (6) we obtain²,

$$\nu F_\nu \propto \nu^{4-2/q}.\tag{8}$$

² To see this, substitute $x \equiv h\nu/k_B T$ and approximate the limits as $r_{\text{in}} = 0$ and $r_{\text{out}} = \infty$.

The slope of the infra-red spectral energy distribution thus provides a constraint on the **radial variation of the dust temperature** within the disk.

In the mm / sub-mm region of the spectrum (i.e. $\lambda \sim 1$ mm) the bulk of the emission comes instead from optically thin regions of the disk. Taking the limit where the entire disk is optically thin at the frequencies of interest, we have that $(1 - e^{-\tau_\nu}) \approx \tau_\nu = \Sigma \kappa_\nu$. Equation (6) then takes the form,

$$F_\nu = \frac{B_\nu(\bar{T}_d) \kappa_\nu}{D^2} \int_{r_{\text{in}}}^{r_{\text{out}}} 2\pi r \Sigma dr, \quad (9)$$

where \bar{T} is an weighted average of the temperature of the emitting material that we can determine from the infra-red part of the SED. From this we can infer two disk properties. First, we note that the integral in the above expression is just the disk mass, M_{disk} . If we know the distance to the source, the opacity, and the disk temperature, a measurement of the flux density at optically thin wavelengths **determines the disk mass**. Second, at sufficiently long wavelengths we will be on the Rayleigh-Jeans tail of the Planck function. In this limit $B_\nu \propto \nu^2$ and we find,

$$\nu F_\nu \propto \nu^{\beta+3}. \quad (10)$$

A measurement of the spectral slope at optically thin wavelengths in the mm / sub-mm thus determines the **frequency dependence of the opacity**. The opacity, in turn, is determined by the size distribution, structure, and composition of the solid particles within the disk [114]. For many disks, the integrated emission implies a value for $\beta \approx 1 \pm 0.5$ that is significantly smaller than the value ($\beta \approx 2$) found for dust in either the interstellar medium or in molecular clouds [56]. This result provides evidence for the growth of solid particles up to sizes of at least mm within protoplanetary disks [361, 352].

It is noteworthy that we can extract constraints on the mass, temperature distribution, and particle properties from the SED of even an unresolved disk. Continuum observations become even more powerful if the disk can be spatially resolved at multiple wavelengths. Tazzari et al. [401], for example, perform a multi-wavelength analysis of three disks (DR Tau, AS 209 and FT Tau) using mm and radio data covering the range between 0.88 mm and 1 cm. They find evidence for a radial dependence of the maximum particle size, that is both broadly consistent with and a critical test of theoretical models for particle evolution in disks [65].

With great power comes great responsibility, and several caveats should be borne in mind when interpreting dust continuum observations. There are well-known sources of uncertainty in disk mass estimates derived from mm / sub-mm data:

- The most directly inferred quantity is the mass of *optically thin dust* with particle sizes roughly the same as the observing wavelengths. Additional mass could be hidden, even in similar sized particles, at radii where the emission is optically thick. Moreover, the conversion between the observed flux and the mass depends on the opacity, which (in detail) is a function of the unknown structural and compositional properties of the particles. (Going beyond the simplest con-

tinuum observations, some mineralogical information is available by modeling the broad silicate feature seen in disk spectra near $10\ \mu\text{m}$ [313].)

- The total mass of *solid material* could be much larger than the mass inferred from the optically thin emission if (a) particles have grown to radii $s \gg \lambda_{\text{max}}$ (where λ_{max} , the longest wavelength for which thermal emission is securely measurable, is usually a few cm) and, (b) the size distribution places most of the mass in the largest particles. Objects of meter size and above are essentially “dark matter” and unobservable in protoplanetary disks.
- Conversion to a *gas mass* involves educated guesswork, because several physical processes affect the solid and gas components in different ways. For example, radial drift (see §7.1) is expected to change the gas to dust ratio as a function of both radius and time [438], while photoevaporation (see §9.1) preferentially removes gas from the disk leaving all but the smallest solid particles behind.

Notwithstanding all these uncertainties, the results of sub-mm disk surveys provide highly suggestive hints of the typical environment for planet formation. In Taurus-Auriga, Andrews & Williams [9] deduce a lognormal distribution of disk masses, with a mean $M_{\text{disk}} \approx 5 \times 10^{-3} M_{\odot}$ and a median mass ratio between disk and star of 5×10^{-3} . Larger masses (for the disk *plus* envelope) are inferred from modeling of Class I sources in the same region [121]. In Ophiuchus, resolved observations of a sample of relatively more massive disks suggest a disk surface density profile $\Sigma \propto r^{-1}$ [11].

2.4 Molecular line observations

In addition to the continuum emission in the IR and mm / sub-mm, a number of molecules and molecular ions have been detected in line radiation. In the mm / sub-mm the workhorse molecule is CO (and its isotopologues such as ^{13}CO and C^{18}O), but several other fairly simple and abundant species including CS, HCN, N_2H^+ and DCO^+ are observable [118]. Some of the same molecules (albeit at different disk radii) are also observable in the near-IR, including CO. The far-IR provides access to additional molecules, including water [186, 335] and ammonia [367].

Given the difficulty in reliably determining disk masses from dust continuum data, one might hope to do better using molecular emission. This is also hard. H_2 is a homonuclear diatomic molecule with no electric dipole moment, and as a result cannot produce a rotational or vibrational spectrum in the dipole approximation [366]. The bulk of the mass in cold H_2 within protoplanetary disks is thus observationally inaccessible. There are some loopholes. Hot H_2 in the atmosphere of the disk (with $T > 2000\ \text{K}$) can be excited by stellar $\text{Ly}\alpha$ radiation, and detected via electronic transitions that lie in the far-UV [138]. These observations, however, do not furnish any simple path toward measuring disk masses. More promisingly, emission from HD (specifically the $J = 1 \rightarrow 0$ rotational transition at $\lambda \approx 112\ \mu\text{m}$) was detected using *Herschel* data for the TW Hya system [62]. The original analysis of this data yielded a disk mass estimate, $M_{\text{disk}} \geq 0.05 M_{\odot}$, that was surprisingly

large given the 3-10 Myr age typically assumed for the star. More recent analyses, using different disk models, confirm that the disk mass is high but give somewhat lower numbers (Kama et al. find $2.3 \times 10^{-2} M_{\odot}$ [209]; Trapman et al. find $7.7 \times 10^{-3} M_{\odot} \leq M_{\text{disk}} \leq 2.3 \times 10^{-2} M_{\odot}$ [410]). Two other disks, GM Aur and DM Tau, have HD disk mass estimates [288]. The *Herschel* observatory stopped taking data in 2013, leaving us with no ongoing capability for further measurements. Determining disk masses using HD is, however, a strong science driver for proposed missions sensitive to these far-IR wavelengths.

Other molecules can be used to estimate gas masses. CO itself is not useful as the emission is optically thick, but a combination of CO isotopologues can be used instead [434]. Gas phase CO in disks can be photo-dissociated, freeze-out in cold dense regions, and be processed into other species. A subset of these processes can be observationally constrained. Qi et al. [344], for example, used imaging in N_2H^+ to infer that the CO snow line in TW Hya lies at a radius of about 30 AU. In general, however, a chemical model is needed to estimate the fraction of carbon (typically of the order of 10%) that resides in observable gas-phase CO [295], followed by a final step of converting the CO mass to a total gas mass.

Molecular line observations also provide a wealth of kinematic information. The instrumental resolution of spectra in the mm / sub-mm is typically better than the expected thermal width of molecular lines, so for bright disks that are well-resolved spatially an observation yields a “data cube” expressing the line emission as a function of sky position (x, y) and line of sight velocity v_{los} . At the lowest order, such data can be used to measure the rotation profile of the disk gas and hence the mass of the central star. Beyond that we may try to measure the contribution that thermal and turbulent broadening make to the line profile. The strength of disk turbulence, in particular, is a key quantity for both disk evolution (see §5) and planet formation (see Willy Kley’s contribution in this volume), that desperately needs empirical constraint. If the turbulence can be represented as a small-scale fluid process³ the summed contribution to the line width is,

$$\Delta v = \frac{v}{c} \sqrt{\frac{2k_B T}{\mu m_H} + v_{\text{turb}}^2}, \quad (11)$$

where μ is the molecular weight of the observed species in units of the mass of a hydrogen atom m_H , T is the temperature, and v_{turb} is a root-mean-square estimator of the turbulence. We generally expect turbulence in disks to be subsonic, but by observing relatively heavy molecules such as CO or CS it is possible to attain sensitivity to v_{turb} values that are significantly below the sound speed. Using molecules with differing optical depths (e.g. isotopologues of CO) opens up the possibility of mapping v_{turb} as a function of height above the disk mid-plane.

³ Representing fluid motions as microturbulence is a standard approximation for stellar atmospheres, but whether it is generally valid for disk turbulence is not obvious. Simon et al. [382] showed that it works reasonably well in the case where turbulence is driven by the magnetohydrodynamic instabilities discussed in §5.4.4.

Recent attempts to measure the turbulent velocity have focused on large disks with simple kinematics that can be modeled precisely. Flaherty et al. [130, 129] have analyzed *ALMA* data for the disk around the nearby A star HD 163296. Using a combination of molecular species and transitions (CO, ^{13}CO , C^{18}O and DCO^+), the observed data cubes were found to be consistent with models that included only orbital motion and thermal broadening. No evidence was found for a turbulent contribution. The derived upper limits are below a tenth of the sound speed throughout the vertical extent of the disk. For TW Hya, Teague et al. [402] analyzed *ALMA* data that included transitions of CO, CN and CS. Turbulent velocities in the range of 0.2-0.4 c_s were inferred for this disk on scales of around 50-100 AU. These measurements, while important and (for HD 163296) provocative to theorists, remain in their infancy. It will be valuable to obtain a larger sample of disks, to acquire data in additional molecular lines, and to compare different analysis techniques.

2.5 Large-scale-structure in disks

The reliable determination of quantities such as disk lifetimes, masses, and accretion rates has been the focus of observational effort for several decades. Although there remain uncertainties the strengths and weaknesses of the different methods have been exhaustively litigated, and we think we have a decent physical picture for what is going on. The same cannot be said of more recent observations that show a variety of large-scale-structure in disks. Very basic questions — including whether the observed structure is an intrinsic property of the fluid dynamics of disks or rather a sign of planet-disk interactions — remain open. In advance of the theoretical discussion in §8, we summarize here the main families of observed structures.

2.5.1 Transition disks

The term transition disk [124] is an umbrella for a subset of disks that do not fit neatly into the SED-based classification scheme described in §2.1. Strom et al. [392] identified a number of YSOs that had little-to-no near IR excess (resembling Class III sources) but robust mid- and far-IR emission (resembling Class II sources). Observations with the *Spitzer* space telescope showed that this type of SED is by no means uncommon. The exact numbers depend upon the adopted definitions but in Taurus, for example, one study found that the fraction of disks classified as “transitional” or “evolved” (meaning that they are becoming optically thin at both near- and mid-IR wavelengths) is about 15% [266]. The transitional disk class includes several well-known systems, including TW Hya, GM Aur, IRS 48 and LkCa15, for which a wealth of observational data is available.

The geometric interpretation of transition disk SEDs is straightforward. Near-IR excesses originate in the inner disk, which in a normal Class II source is expected to be the region with the highest optical depth. Seeing little or no near-IR emission,

while mid-IR emission persists, implies a disk with a hole or cavity in the dust distribution. This inference is supported by imaging in the sub-mm, which directly reveals the presence of dust cavities within transition disks. Andrews et al. [10] used the Submillimeter Array (SMA) to image a sample of 12 transition disks in nearby star-forming regions at $880 \mu\text{m}$. The found cavities with radii between 15 AU and 73 AU, and estimated that 20-25% of the brightest disks (in mm emission) exhibited such inner clearings.

The cavities in transition disks are for the most part not empty. Most transitional sources are accreting, at rates which can be as high as normal Classical T Tauri stars [276] (though the median accretion rate is probably significantly reduced — Kim et al. [215] find a suppression of approximately an order of magnitude for Class II YSOs in Orion A). Moreover, although the defining feature of transitional disks is a cavity in the dust distribution, some transition disks' spectra indicate the presence of very low levels of dust close to the star (for example GM Aur [78]). The overall picture is thus one in which a relatively unexceptional outer disk is truncated at some cavity radius r_{cavity} . Inside the cavity the column density of (observable) dust is severely depleted, but gas persists and continues to accrete on to the star.

2.5.2 Rings

Long baseline observations with *ALMA* have enabled imaging of a number of protoplanetary disks with an angular resolution as good as 0.025 arcseconds. A major surprise has been the discovery of multiple rings of emission in several sources. In HL Tau, continuum imaging at wavelengths between 0.87 mm and 2.9 mm detects seven pairs of bright / dark ring-like structures at orbital radii between 20 AU and 100 AU [8]. Qualitatively similar rings, though with lesser contrast, are seen between 2.4 AU and 40 AU in TW Hya [13]. TW Hya's rings are also visible at near-IR wavelengths that probe sub-micron-sized dust particles near the disk surface [421]. Other examples of systems with rings of dust emission imaged by *ALMA* are HD 163296 [194], HD 169142 [127] and AA Tau [259].

2.5.3 Azimuthal asymmetries

Non-axisymmetric structure is also evident in high resolution disk images. One class of non-axisymmetric structure is horseshoe-shaped emission in the mm / sub-mm. A prototypical example is the transition disk system IRS 48. Van der Marel et al. [422] found that the mm-sized particles surrounding the cavity at $r \approx 60$ AU, traced by 0.44 mm continuum emission, were strongly concentrated in a crescent-shaped feature on one side of the star. No such asymmetry was evident in either the gas or in micron-sized dust traced by mid-IR imaging. A broadly similar morphology is observed in HD 142527 [83], in LkH α 330 [195], and in a number of other transition disk sources.

Spiral structure represents a separate class of non-axisymmetric features. Spirals are seen in the very young protostellar source L1448 IRS3B [406], in the disk around the young star Elias 2-27 [328], and in the transitional disk source MWC 758 (in high resolution near-IR imaging [161]).

2.5.4 Interpretation

The physical origin of the large-scale-structure seen in protoplanetary disks remains unclear. Planets orbiting within the gas disk can produce cavities and spirals, and can form local pressure maxima and vortices that would trap dust in ring-like or horseshoe-shaped configurations. There is no doubt that planets can form or migrate to the large radii where most disk structure is seen — the HR 8799 system has four super-Jovian mass planets with projected orbital separations between 15 AU and 70 AU [280, 281]. Some observable disk structure is thus surely of planetary origin. Whether all or even most of the currently observed structure is caused by planets is less clear. Theoretically, as we will discuss in §8, there are a number of processes that may be able to form structures in disks without fully-formed planets. Observationally, direct imaging surveys suggest that wide separation planetary systems with planets of roughly Jupiter mass and above are not common [146, 87, 420]. Empirical constraints on the abundance of lower mass planets, however, remain weak.

- The lifetime of disks around Young Stellar Objects is a few Myr. The bulk of this time is spent in the relatively isolated Class II (or Classical T Tauri star) phase, though critical events for subsequent disk evolution (such as magnetic field loss) and planet formation (such as planetesimal formation) may start earlier while the disk itself is still accreting from an envelope.
- Key observational diagnostics include the optical / UV spectrum (used to measure the accretion rate on to the star), thermal emission from dust in the IR out to mm wavelengths (used to measure disk masses and particle properties, albeit with significant uncertainties), and molecular line emission (used to measure kinematics, constrain chemical models, and infer the strength of disk turbulence).
- High resolution imaging of protoplanetary disks in both thermal emission and scattered light shows that disks can sustain a variety of large-scale-structure, which may be related to intrinsic disk processes or to the interaction of planets with the gas and dust within the disk.

3 Disk structure

The few Myr lifetime of protoplanetary disks equates to millions of dynamical times in the inner disk and thousands of dynamical times in the outer disk at 100 AU. To a first approximation we can treat the disk as evolving slowly through a sequence of axisymmetric static structures as mass accretes on to the star and is lost through disk winds, and our first task is to discuss the physics that determines those structures. Quantities that we are interested in include the density $\rho(r, z)$, the gas and dust temperatures $T(r, z)$ and $T_d(r, z)$, the chemical composition, and the ionization fraction. The density of solid particles (“dust”) ρ_d is also important, but we will defer saying much about that until we have discussed turbulence, radial drift, and the aerodynamic coupling of solids and gas.

3.1 Vertical and radial structure

3.1.1 Vertical structure

The vertical profile of gas density in protoplanetary disks is determined by the condition of hydrostatic equilibrium. The simplest case to consider is an optically thick disk that is heated by stellar irradiation, has negligible mass compared to the mass of the star, and is supported by gas pressure. We can then approximate the optically thick interior of the disk as isothermal, with constant sound speed c_s and pressure $P = \rho c_s^2$. The sound speed is related to the temperature via $c_s^2 = k_B T / \mu m_H$, where k_B is Boltzmann’s constant, m_H is the mass of a hydrogen atom, and where under normal disk conditions the mean molecular weight $\mu \simeq 2.3$. In cylindrical co-ordinates, the condition for vertical hydrostatic equilibrium (Figure 2) is,

$$\frac{dP}{dz} = -\rho g_z = -\frac{GM_*}{r^2 + z^2} \sin \theta \rho, \quad (12)$$

where M_* is the stellar mass. For $z \ll r$,

$$g_z = \frac{GM_*}{(r^2 + z^2)^{3/2}} z \simeq \Omega_K^2 z, \quad (13)$$

where $\Omega_K \equiv \sqrt{GM_*/r^3}$ is the Keplerian orbital velocity (here defined at the mid-plane, later in §3.1.2 we will need to distinguish between the mid-plane and other locations). Equation (12) then becomes,

$$c_s^2 \frac{d\rho}{dz} = -\Omega_K^2 \rho z, \quad (14)$$

which integrates to give,

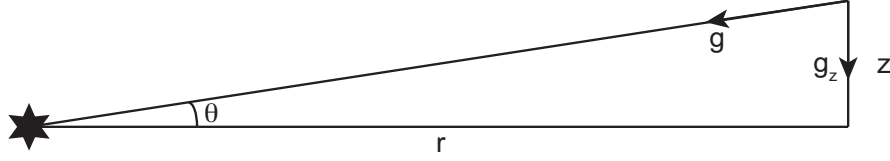


Fig. 2 The geometry for calculating the vertical hydrostatic equilibrium of a non-self-gravitating protoplanetary disk. The balancing forces are the vertical component of stellar gravity and the vertical pressure gradient.

$$\rho(z) = \rho_0 \exp[-z^2/2h^2], \quad (15)$$

where ρ_0 is the mid-plane density and we have defined the *vertical scale height* $h \equiv c_s/\Omega_K$. Because the effective gravity increases with height (and vanishes at the mid-plane) this standard disk profile is gaussian, rather than exponential as in a thin isothermal planetary atmosphere. A consequence is that the scale over which the density drops by a factor of e gets smaller with z ; loosely speaking disks become more “two dimensional” away from the mid-plane. Defining the surface density $\Sigma = \int \rho dz$, the central density is,

$$\rho_0 = \frac{1}{\sqrt{2\pi}} \frac{\Sigma}{h}. \quad (16)$$

Up to straightforward variations due to differing conventions (e.g. some authors define $h = \sqrt{2}c_s/\Omega_K$) these formulae define the vertical structure of the most basic disk model (isothermal, with a gaussian density profile). For many purposes it is an adequate description, especially if one is mostly worried about conditions within a few h of the mid-plane, .

The most obvious cause of gross departures from a gaussian density profile is a non-isothermal temperature profile. If the disk is accreting, gravitational potential energy that is thermalized in the optically thick interior will need a vertical temperature gradient $dT/dz < 0$ in order to be transported to the disk photosphere and radiated. We will return to this effect in §3.2 and §4, after assessing the other assumptions inherent in equation (15). We first note that the simplification to $z \ll r$ is convenient but not necessary, and that we can integrate equation (12) without this assumption to give,

$$\rho = \rho_0 \exp \left[\frac{r^2}{h^2} \left((1 + z^2/r^2)^{-1/2} - 1 \right) \right]. \quad (17)$$

Protoplanetary disks *are* geometrically thin, however, with $h/r \approx 0.05$ being fairly typical. In this regime, as is shown in Figure 3, departures from a gaussian are negligibly small. We only really need to worry about the full expression for vertical gravity when considering disk winds, which flow beyond $z \sim r$.

What about the contribution of the disk itself to the vertical component of gravity? Approximating the disk as an infinite sheet with (constant) surface density Σ ,

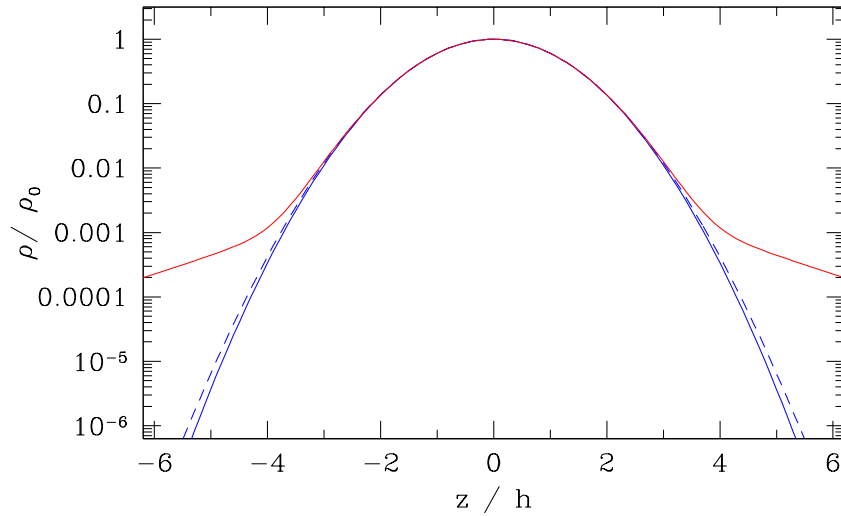


Fig. 3 Simple models for the vertical density profile of an isothermal disk, in units of the disk scale height h . The solid blue line shows the gaussian density profile valid for $z \ll r$, the dashed blue line shows the exact solution relaxing this assumption (the two are essentially identical for this disk, with $h/r = 0.05$). The red dashed curve shows a fit to numerical simulations that include a magnetic pressure component [185].

Gauss' theorem tells us that the gravitational acceleration above the sheet is independent of height,

$$g_z = 2\pi G\Sigma. \quad (18)$$

Comparing this acceleration with the vertical component of the star's gravity at $z = h$, we find that the disk dominates if,

$$\Sigma > \frac{M}{2\pi} \frac{h}{r^3}. \quad (19)$$

Very roughly we can write the disk mass $M_{\text{disk}} \sim \pi r^2 \Sigma$, which allows us to write the condition for the disk's own gravity to matter as,

$$\frac{M_{\text{disk}}}{M_*} > \frac{1}{2} \left(\frac{h}{r} \right). \quad (20)$$

For $h/r = 0.05$, a disk mass of a few percent of the stellar mass makes a non-negligible change to the vertical structure, and such masses are not unreasonably large. As we will see in §5, however, when disk masses $M_{\text{disk}}/M_* \sim h/r$ are encountered we tend to have bigger fish to fry, as this is also the approximate condition for the onset of disk self-gravity, the formation of spiral arms, and substantial departures from axisymmetry.

Magnetic pressure $P_B = B^2/8\pi$ is likely to impact the vertical density profile, at least for $z \gg h$ (here and subsequently, we use units such that B is measured in Gauss). No simple principle for predicting the strength or vertical variation of the magnetic field is known, so we turn to numerical simulations for guidance. Hirose & Turner [185] completed radiation magnetohydrodynamic (MHD) simulations of the protoplanetary disk at 1 AU, adopting fairly typical numbers for the key disk and stellar parameters (a disk surface density $\Sigma = 10^3 \text{ g cm}^{-2}$, stellar mass $M_* = 0.5 M_\odot$, stellar effective temperature $T_{\text{eff}} = 4000 \text{ K}$, and stellar radius $R_* = 2 R_\odot$). Their simulations included Ohmic diffusion but ignored both ambipolar diffusion and the Hall effect (see §5 for further discussion of these processes). They found that the model disk was gas pressure dominated near the mid-plane, but that the atmosphere (or corona) was magnetically dominated. An empirical fit to their density profile is [413],

$$\rho = \frac{\rho_0}{1 + \varepsilon} \left[\exp(-z^2/2h^2) + \varepsilon \exp(-|z|/kh) \right], \quad (21)$$

with $\varepsilon \simeq 1.25 \times 10^{-2}$ and $k \simeq 1.5$. This fit is shown in Figure 3. Magnetic pressure beats out gas pressure for $|z| > 4h$, leading to a low density exponential atmosphere that is much more extended than a standard isothermal disk. Even if the atmosphere itself gives way to a disk wind at still higher altitudes (as suggested by other simulations), these results suggest that observational probes of conditions near the disk surface may be sampling regions where the magnetic field dominates. Moreover, simulations of the inner disk ($r \sim 1 \text{ AU}$) that include the Hall effect [241] show that it may be possible to generate strong azimuthal magnetic fields whose magnetic pressure may exceed that of the gas within one scale height, or even at the mid-plane. Such fields would lead to larger departures from the standard purely thermal definition of the scale height.

3.1.2 Radial structure

The radial run of the surface density cannot be predicted from considerations of static disk structure, because two dimensional equilibrium density distributions $\rho(r, z)$ can be constructed for a broad class of surface density profiles. Not all such distributions would be stable against rapid hydrodynamic instabilities, but even if we enforce stability as an additional requirement we have no way to discriminate between commonly adopted surface density profiles (e.g. $\Sigma \propto r^{-1}$ versus $\Sigma \propto r^{-3/2}$). Instead, the surface density profile must either be measured observationally [11] or studied using time-dependent models (§4)⁴. Given an assumed surface density profile, however, we can derive useful results for the azimuthal velocity v_ϕ . If the disk is static (and even if it is slowly evolving) the azimuthal component of the momentum

⁴ The *minimum mass Solar Nebula* (MMSN) [431, 175], an approximate lower bound for the amount of disk gas needed to form the planets in the Solar System, can be useful as a reference model despite its tenuous connection to actual conditions in the disk at the time of planet formation. The MMSN has a gas surface density profile $\Sigma(r) = 1.7 \times 10^3 (r/\text{AU})^{-3/2} \text{ g cm}^{-2}$.

equation,

$$\frac{\partial \mathbf{v}}{\partial t} + (\mathbf{v} \cdot \nabla) \mathbf{v} = -\frac{1}{\rho} \nabla P - \nabla \Phi \quad (22)$$

can be written in the mid-plane as,

$$\frac{v_\phi^2}{r} = \frac{GM_*}{r^2} + \frac{1}{\rho} \frac{dP}{dr}. \quad (23)$$

Here P is the pressure and all quantities are mid-plane values. Let's start with an explicit example of the consequences of this force balance in protoplanetary disks. Consider a disk with $\Sigma \propto r^{-1}$ and central temperature $T_c \propto r^{-1/2}$. We then have $c_s \propto r^{-1/4}$, $\rho \propto r^{-9/4}$ and $P \propto r^{-11/4}$. Substituting into equation (23) yields,

$$v_\phi = v_K \left[1 - \frac{11}{4} \left(\frac{h}{r} \right)^2 \right]^{1/2}. \quad (24)$$

From this we deduce,

- The deviation from strict Keplerian rotation, $v_K = \sqrt{GM_*/r}$, is of the order of $(h/r)^2$.
- Its magnitude is *small*. For a disk with $h/r = 0.03$ at 1 AU, the difference between the disk azimuthal velocity and the Keplerian value is about 0.25%, or, in absolute terms $|v_\phi - v_K| \simeq 70 \text{ m s}^{-1}$.

When we come to discuss the evolution of particles within disks (§7), it will turn out that this seemingly small effect is of paramount importance. Particles do not experience the radial pressure gradient that is the cause of the mismatch in speeds, and as a result develop a differential velocity with respect to the gas that leads to aerodynamic drag and (usually) inspiral. Because this process is so important it is worth studying not just the magnitude of the effect but also its vertical dependence. To do so, we follow Takeuchi & Lin [397] and consider an axisymmetric vertically isothermal disk supported against gravity by gas pressure. The vertical density profile is then gaussian (equation 15) and in equilibrium (equation 22) we have,

$$r\Omega_g^2 = \frac{GM_*}{(r^2 + z^2)^{3/2}} r + \frac{1}{\rho} \frac{\partial P}{\partial r}. \quad (25)$$

We distinguish between the gas angular velocity, $\Omega_g(r, z)$, the Keplerian angular velocity $\Omega_K(r, z) = GM_*/(r^2 + z^2)^{3/2}$, and its mid-plane value $\Omega_{K, \text{mid}}$. The disk is fully specified by the local power-law profiles of surface density and temperature,

$$\Sigma \propto r^{-\gamma} \quad (26)$$

$$T_c \propto r^{-\beta}, \quad (27)$$

with $\gamma = 1$ and $\beta = 1/2$ being typically assumed values. Evaluating $\partial P/\partial r$ using equation (15) with $h = h(r)$ allows us to determine the equilibrium gas angular

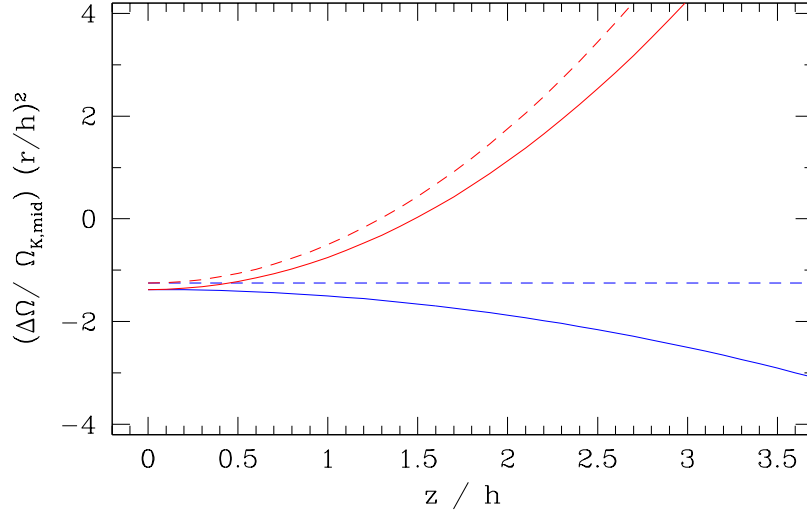


Fig. 4 The variation in angular velocity with height in the disk. In blue, the angular velocity of gas relative to the mid-plane Keplerian value, $(\Omega_g - \Omega_{K,\text{mid}})/\Omega_{K,\text{mid}} \times (r/h)^2$. In red, the difference between the Keplerian angular velocity and the *local* gas angular velocity, $(\Omega_g - \Omega_K)/\Omega_{K,\text{mid}} \times (r/h)^2$. The assumed disk has $\Sigma \propto r^{-1}$ and $T_c \propto r^{-1/2}$ (solid curves) or radially constant T_c (dashed curves).

velocity in terms of the mid-plane Keplerian value,

$$\Omega_g \simeq \Omega_{K,\text{mid}} \left[1 - \frac{1}{4} \left(\frac{h}{r} \right)^2 \left(\beta + 2\gamma + 3 + \beta \frac{z^2}{h^2} \right) \right]. \quad (28)$$

Provided that the temperature is a locally decreasing function of radius ($\beta > 0$), the sense of the vertical shear is that the gas rotates slower at higher z . Like the sub-Keplerian mid-plane velocities, the magnitude of the shear is only of the order of $(h/r)^2$, but this small effect may nevertheless be detectable with ALMA data [364].

For particle dynamics, what matters is the difference between the gas velocity and the local Keplerian speed. To order z^2/r^2 , the vertical dependence of the Keplerian velocity is,

$$\Omega_K \simeq \Omega_{K,\text{mid}} \left(1 - \frac{3}{4} \frac{z^2}{r^2} \right). \quad (29)$$

This function decreases faster with height than Ω_g , so the difference between them, plotted in Figure 4, switches sign for sufficiently large z ,

$$\Omega_g - \Omega_K \simeq -\frac{1}{4} \left(\frac{h}{r} \right)^2 \left[\beta + 2\gamma + 3 + (\beta - 3) \frac{z^2}{h^2} \right] \Omega_{K,\text{mid}}. \quad (30)$$

Particles that orbit the star at the local Keplerian speed move slower than the gas near the mid-plane (and thus experience a “headwind”), but faster at high altitude. For typical parameters, the changeover occurs at about $z \approx 1.5h$.

The orbital velocity will also deviate from the point mass Keplerian form if the disk mass is sufficiently high. The gravitational potential of a disk is *not* that of a point mass (and does not have a simple form for realistic disk surface density profiles), but for an approximation we assume that it is. Then the modified Keplerian velocity depends only upon the enclosed disk mass,

$$v'_K \simeq v_K \left(1 + \frac{M_{\text{disk}}}{M_*} \right)^{1/2}. \quad (31)$$

For disk masses $M_{\text{disk}} \sim 10^{-2} M_*$ the effect on the rotation curve is of comparable magnitude (but opposite sign) to the effect of the radial pressure gradient.

The deviations from Keplerian rotation due to pressure gradients in a planar axisymmetric disk are relatively subtle effects. Larger kinematic departures are possible if the disk is either eccentric or warped. Observationally, there are known examples of strongly warped disks (such as HD 142527 [82]) that can be traced using molecular line observations. Theoretically, we might expect disks formed from the collapse of turbulent molecular cloud cores to start out kinematically disturbed, and the rate of decay such disturbances remains a subject of active research [52]. It’s thus worth remembering, especially when interpreting precise kinematic observations, that un-modeled warps or eccentricities as small as $e \sim (h/r)^2$ could be significant.

3.2 Thermal physics

We seek to determine the temperature of gas and dust as $f(r, z)$. Our first task is to calculate the interior temperature of a disk heated solely by starlight. This is straightforward. At most radii of interest the dust opacity is high enough for the disk to be optically thick to both stellar radiation and to its own re-emitted radiation, which hence has a thermal spectrum. It is then a geometric problem to work out how much stellar radiation each annulus of the disk intercepts, and what equilibrium T results. We will then consider the temperatures of gas and dust in the surface layers of disks. These problems are trickier. The surface layers are both optically thin and of low density, so we have to account explicitly for the heating and cooling processes and allow for the possibility that the dust and gas are too weakly coupled to maintain the same temperature. We defer until §4 the question of how accretion heating modifies these solutions.

A disk whose temperature is set by stellar irradiation is described as “passive”. The model problem is a flat razor-thin disk that absorbs all incoming stellar radiation and re-emits it locally as a blackbody. We seek the temperature of the blackbody disk emission as $f(r)$. Modeling the star as a sphere of radius R_* , and constant brightness I_* , we define spherical polar coordinates such that the axis of the coordinate system

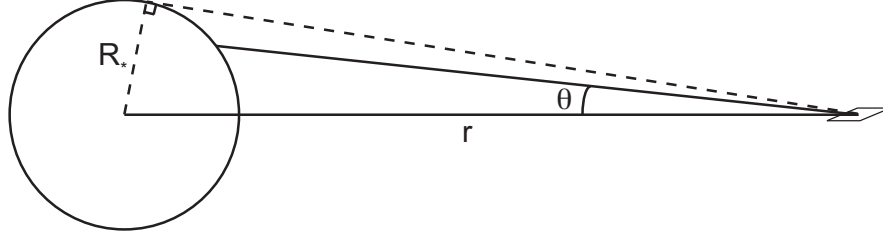


Fig. 5 The setup for calculating the radial temperature distribution of an optically thick, razor-thin disk. We consider a ray that makes an angle θ to the line joining the area element to the center of the star. Different rays with the same θ are labeled with the azimuthal angle ϕ ; $\phi = 0$ corresponds to the “twelve o’clock” position on the stellar surface.

points to the center of the star (figure 5). The stellar flux passing through a surface at distance r is,

$$F = \int I_* \sin \theta \cos \phi d\Omega, \quad (32)$$

where $d\Omega$ represents the element of solid angle. We count the flux coming from the top half of the star only (and later equate that to radiation from only the top surface of the disk), so the integral has limits,

$$\begin{aligned} -\pi/2 < \phi \leq \pi/2 \\ 0 < \theta < \sin^{-1} \left(\frac{R_*}{r} \right). \end{aligned} \quad (33)$$

Substituting $d\Omega = \sin \theta d\theta d\phi$, the integral evaluates to,

$$F = I_* \left[\sin^{-1} \left(\frac{R_*}{r} \right) - \left(\frac{R_*}{r} \right) \sqrt{1 - \left(\frac{R_*}{r} \right)^2} \right]. \quad (34)$$

A star with effective temperature T_* has brightness $I_* = (1/\pi)\sigma T_*^4$, with σ the Stefan-Boltzmann constant. Equating F to the one-sided disk emission σT_{disk}^4 the temperature profile is,

$$\left(\frac{T_{\text{disk}}}{T_*} \right)^4 = \frac{1}{\pi} \left[\sin^{-1} \left(\frac{R_*}{r} \right) - \left(\frac{R_*}{r} \right) \sqrt{1 - \left(\frac{R_*}{r} \right)^2} \right]. \quad (35)$$

The exact result is unnecessarily complicated. To simplify, we expand the right hand side in a Taylor series for $(R_*/r) \ll 1$ (i.e. far from the stellar surface) to obtain,

$$T_{\text{disk}} \propto r^{-3/4}, \quad (36)$$

as the power-law temperature profile of a thin, flat, passive disk. This implies a sound speed profile, $c_s \propto r^{-3/8}$, and a disk thickness $(h/r) \propto r^{1/8}$. We therefore

predict that the disk becomes geometrically thicker (“flares”) at larger radii. We can also integrate equation (35) exactly over r , with the result that the luminosity from both side of the disk sums to $L_{\text{disk}}/L_* = 1/4$.

A more detailed calculation of the dust emission from passive disks requires consideration of two additional physical effects [212]. First, as we just noted, the disk thickness as measured by the gas scale height flares to larger radii. If dust is well-mixed with the gas — which may or may not be a reasonable assumption — a flared disk intercepts more stellar radiation in its outer regions than a flat one, which will tend to make it flare even more strongly. We therefore need to solve for the self-consistent *shape* of the disk that simultaneously satisfies hydrostatic and thermal equilibrium at every radius. This is conceptually easy, and the slightly messy geometry required to generalize the flat disk calculation is clearly described by Kenyon & Hartmann [212]. Second, small dust grains that are directly exposed to stellar irradiation (i.e. those where the optical depth to stellar radiation along a line toward the star $\tau < 1$) emit as a dilute blackbody with a temperature higher than if they were true blackbody emitters [212]. The reason for this is that small dust grains, of radius s , have an emissivity $\varepsilon = 1$ only for wavelengths $\lambda \leq 2\pi s$. At longer wavelengths, their emissivity declines. The details depend upon the composition and structure of the dust grains, but roughly the emissivity (and opacity κ) scale inversely with the wavelength. In terms of temperature,

$$\varepsilon = \left(\frac{T}{T_*}\right)^\beta \quad (37)$$

with $\beta = 1$. A dust particle exposed to the stellar radiation field is then in radiative equilibrium at temperature T_s when absorption and emission are in balance,

$$\frac{L_*}{4\pi r^2} \pi s^2 = \sigma T_s^4 \varepsilon(T_s) 4\pi s^2. \quad (38)$$

The resulting temperature,

$$T_s = \frac{1}{\varepsilon^{1/4}} \left(\frac{R_*}{2r}\right)^{1/2} T_*, \quad (39)$$

exceeds the expected blackbody temperature by a substantial factor if $\varepsilon \ll 1$.

An illustrative analytic model that incorporates these effects was developed by Chiang & Goldreich [90]. They considered a disk with a surface density profile $\Sigma = 10^3 (r/1 \text{ AU})^{-3/2} \text{ g cm}^{-2}$ around a star with $M_* = 0.5 M_\odot$, $T_* = 4000 \text{ K}$ and $R_* = 2.5 R_\odot$. Within about 100 AU, their solution has half of the bolometric luminosity of the disk emitted as a blackbody at the interior temperature,

$$T_i \approx 150 \left(\frac{r}{1 \text{ AU}}\right)^{-3/7} \text{ K}, \quad (40)$$

with equal luminosity at each radius emerging from a hot surface dust layer at,

$$T_s \approx 550 \left(\frac{r}{1 \text{ AU}} \right)^{-2/5} \text{ K.} \quad (41)$$

The Chiang & Goldreich solution is a two-layer approximation to dust continuum radiative transfer for a passive, hydrostatic disk. Approximations in the same spirit have been developed that incorporate heating due to accretion [151], but the full problem requires numerical treatment. Several codes are available for the efficient solution of the full radiative transfer problem [67, 122, 360, 388].

Under most circumstances dust dominates both the absorption of starlight and the thermal emission of reprocessed stellar radiation and accretion heating. If the density is high enough, collisions between dust particles and gas molecules will establish a common temperature for both, and there is no need to explicitly consider the thermal physics of the gas. Kamp & Dullemond (2004), for example, find that T_g and T_d are within about 10% of each other for an optical extinction $A_V > 0.1$ [210]. This criterion will be met in the disk mid-plane within the normal planet forming region (i.e. excluding very large orbital distances where the disk is becoming optically thin). The gas temperature near the surface of the disk is, however, of critical importance for a number of applications,

- Interpretation of sub-mm data, where the observable emission is rotational transitions of molecules such as CO and HCO⁺. These observations frequently probe the outer regions of disks, at depths where the molecules are not photo-dissociated but where the gas is warm and not in equilibrium with the dust.
- Interpretation of near-IR and far-IR data, often from the inner disk, where we are seeing ro-vibrational transitions of molecules along with fine-structure cooling lines such as [CII] and [OI].
- Chemistry. It's cold at the disk mid-plane, and chemical reactions are sluggish. Although the densities are much lower in the disk atmosphere, the increased temperatures and exposure to higher energy stellar photons make the upper regions of the disk important for chemistry [177].

The properties of gas near the surface of disks are very closely tied to the incident flux of ultraviolet radiation from the star. Stellar UV radiation ionizes and dissociates atoms and molecules, and heats the gas by ejecting electrons from dust grains (grain photoelectric heating). Depending upon the temperature and density, the heating is balanced by cooling from rotational transitions of molecules (especially CO) and atomic fine structure lines. Also important is energy exchange due to inelastic collisions between gas molecules and dust particles (thermal accommodation) — if this process is too efficient the gas temperature will revert to match the dust which is absorbing and emitting the bulk of the star's bolometric luminosity.

Photoelectric heating [113] is typically the dominant process for dusty gas exposed to an ultraviolet radiation field. The work function of graphite grains (the minimum energy required to free an electron from them) is around 5 eV, so 10 eV FUV photons can eject electrons from uncharged grains with 5 eV of kinetic energy that ultimately heats the gas. Ejection occurs with a probability of the order of 0.1, so the overall efficiency (the fraction of the incident FUV energy that goes into heating the gas rather than the dust) can be rather high, around 5%.

A detailed evaluation of the photoelectric heating rate is involved, and resistant to a fully first-principles calculation. Weingartner & Draine [432] give a detailed description. Here, we sketch the main principles following Kamp & van Zadelhoff [211], who developed models for the gas temperature in A star disks. We consider a stellar radiation spectrum F_ν impinging on grains of graphite (work function $w = 4.4$ eV [432]) and silicate ($w = 8.0$ eV). For micron-sized grains the work function, which is a property of the bulk material, is equivalent to the ionization potential — the energy difference between infinity and the highest occupied energy level in the solid. Additionally, the probability for absorption when a photon strikes a grain is $Q_{\text{abs}} \approx 1$. Most absorbed photons, however, do *not* eject electrons, rather their energy goes entirely into heating the dust grain. The yield of emitted electrons is some function of photon energy $Y(h\nu)$, and they have some spectrum of kinetic energy E , roughly described by [113] $f(E, h\nu) \propto (h\nu - w)^{-1}$. If the grains are charged (e.g. by prior emission of photoelectrons) then the kinetic energy ($E - eU$) available to heat the gas is that left over once the electron has escaped the electrostatic potential eU of the grain. The heating rate is then [211],

$$\Gamma_{pe} = 4n_H\sigma \int_{E_{\text{min}}}^{E_{\text{max}}} \left(\int_{\nu_{\text{th}}}^{\nu_{\text{max}}} Q_{\text{abs}} Y(h\nu) f(E, h\nu) F_\nu d\nu \right) (E - eU) dE, \quad (42)$$

where n_H is the number density of hydrogen atoms, σ is the geometric cross-section per hydrogen nucleus, and the lower limits express the minimum frequency ν_{th} of a photon that can overcome the work function and the minimum energy of a photoelectron that can escape from a charged grain. An assessment of the photoelectric heating rate then requires knowledge of the functions Y and f , specification of the radiation field F_ν , and calculation of the typical charge on grains of different sizes [116, 432]. The physics is conceptually identical but quantitatively distinct when the grains in question are *extremely small* (e.g. Polycyclic Aromatic Hydrocarbons, PAHs) [42, 432].

The rate of energy exchange from inelastic gas-grain collisions can be calculated with a collision rate argument. Consider grains with geometric cross-section $\sigma_d = \pi \langle s^2 \rangle$ and number density n_d , colliding with hydrogen atoms with number density n_H . The thermal speed of the hydrogen atoms is $v_{\text{th}} = (8k_B T_g / \pi m_H)^{1/2}$ and the average kinetic energy of the molecules on striking the surface is $2k_B T_g$. The cooling rate per unit volume due to gas-grain collisions can then be written in the form [77],

$$\Lambda_{g-d} = n_d n_g \sigma_d \left(\frac{8k_B T_g}{\pi m_H} \right)^{1/2} \alpha_T (2k_B T_g - 2k_B T_d), \quad (43)$$

where T_g and T_d are the temperatures of the gas and dust respectively. The subtleties of the calculation are reflected in the “accommodation co-efficient” α_T , which is typically $\alpha_T \approx 0.3$ for silicate and carbon grains. For a specified volumetric heating rate (and assumptions as to the gas to dust ratio and properties of the grains), this expression can be used to estimate the density below which the thermal properties of gas and dust decouple.

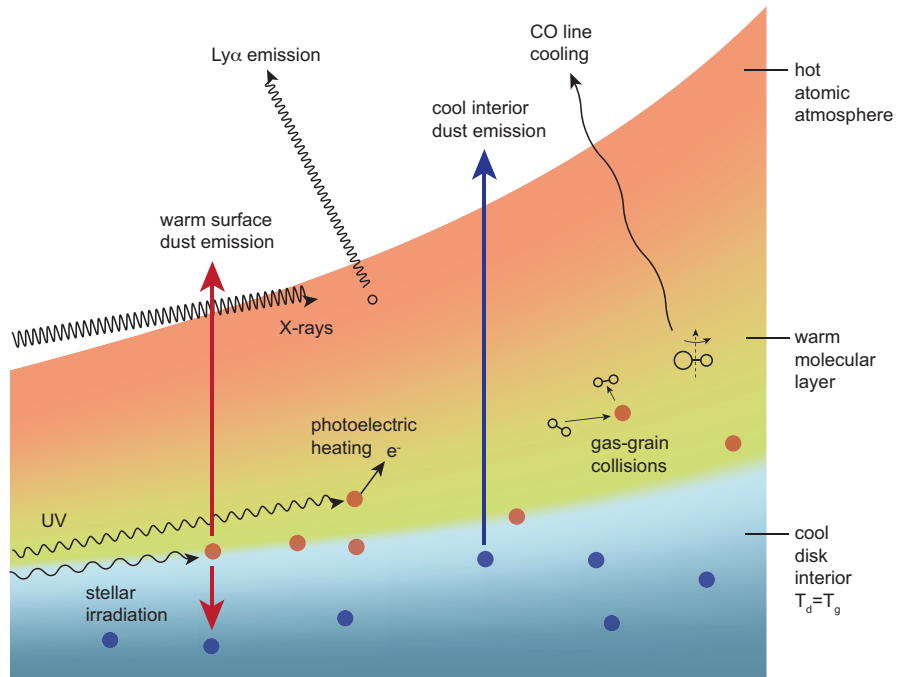


Fig. 6 Illustration of some of the physical processes determining the temperature and emission properties of irradiated protoplanetary disks.

In addition to cooling that occurs indirectly, as a consequence of gas-grain collisions, gas in the upper layers of disks also cools radiatively. In the molecular layer of the disk, the dominant coolant is typically CO, as this is the most abundant molecule that is not homonuclear (diatomic molecules, such as H_2 , have no permanent electric dipole moment and hence radiate inefficiently). At higher temperatures — only attained in the very rarefied uppermost regions of the disk atmosphere — cooling by $\text{Ly}\alpha$ emission becomes important. Qualitatively, there are then three distinct layers in the disk:

- A cool mid-plane region, where dust and gas have the same temperature and dust cooling is dominant.
- A warm surface layer in which both dust and gas have temperatures that exceed the mid-plane value. The gas in the warm layer can be substantially hotter than the dust ($T \sim 10^3$ K at 1 AU), and cools both by dust-gas collisions and by CO rotational-vibrational transitions.
- A hot, low-density atmosphere, where $\text{Ly}\alpha$ radiation and other atomic lines (e.g. O[II]) cool the gas.

The disk structure that results from these heating and cooling processes is illustrated in Figure 6.

3.3 Ionization structure

The degree of ionization of the gas in protoplanetary disks is important because it is key to understanding how gas couples to magnetic fields, and thence to understanding the role of magnetic fields in the formation of disks, in the sustenance of turbulence within them, and in the generation of jets and magnetohydrodynamic (MHD) winds. At the most basic level, we care about the ratio of the number density of free electrons n_e to the number density of neutrals,

$$x_e \equiv \frac{n_e}{n_n}, \quad (44)$$

though we should remember that dust grains can also bear charges and carry currents. We will consider separately the thermodynamic equilibrium process of *thermal* (or collisional) ionization, which typically dominates above $T \sim 10^3$ K, and *non-thermal* ionization due to photons or particles that have an energy well in excess of the typical thermal energy in the gas.

In anticipation of results that will be derived in §5, we note that very low and seemingly negligible levels of ionization — $x_e \ll 10^{-10}$ — often suffice to couple magnetic fields to the fluid. We need to worry about small effects when considering ionization.

3.3.1 Thermal ionization

Thermal ionization of the alkali metals is important in the innermost regions of the disk, usually well inside 1 AU. In thermal equilibrium the ionization state of a single species with ionization potential χ is obeys the Saha equation [366],

$$\frac{n^{\text{ion}} n_e}{n} = \frac{2U^{\text{ion}}}{U} \left(\frac{2\pi m_e k_B T}{h^2} \right)^{3/2} \exp[-\chi/k_B T]. \quad (45)$$

Here, n^{ion} and n are the number densities of the ionized and neutral species, and n_e ($= n^{\text{ion}}$) is the electron number density. The partition functions for the ions and neutrals are U^{ion} and U , and the electron mass is m_e . The temperature dependence is not quite just the normal exponential Boltzmann factor, because the ionized state is favored on entropy grounds over the neutral state.

In protoplanetary disks thermal ionization becomes significant when the temperature becomes high enough to start ionizing alkali metals. For potassium, the ionization potential $\chi = 4.34$ eV. We write the abundance of potassium relative to all other neutral species as $f = n_K/n_n$, and define the ionization fraction x ,

$$x \equiv \frac{n_e}{n_n}. \quad (46)$$

While potassium remains weakly ionized, the Saha equation gives,

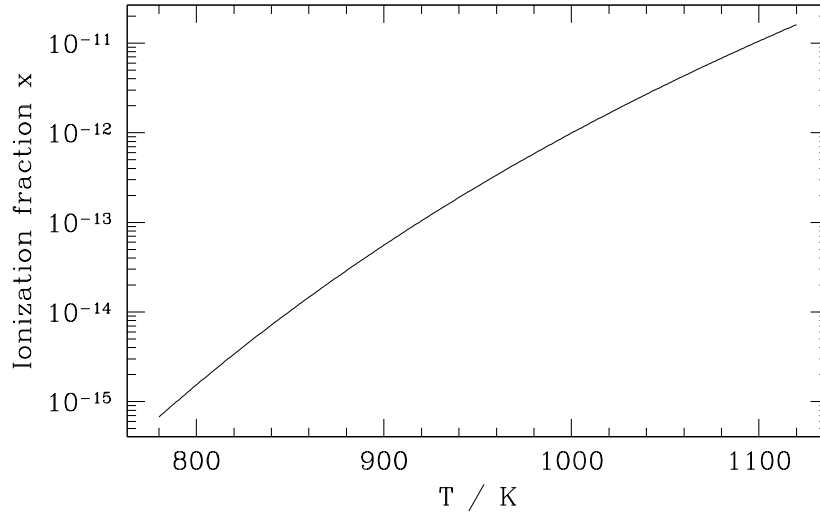


Fig. 7 The thermal ionization fraction as a function of temperature predicted by the Saha equation for the inner disk. Here we assume that potassium, with ionization potential $\chi = 4.34$ eV and fractional abundance $f = 10^{-7}$, is the only element of interest for the ionization. The number density of neutrals is taken to be $n_n = 10^{15} \text{ cm}^{-3}$.

$$x \simeq 10^{-12} \left(\frac{f}{10^{-7}} \right)^{1/2} \left(\frac{n_n}{10^{15} \text{ cm}^{-3}} \right)^{-1/2} \left(\frac{T}{10^3 \text{ K}} \right)^{3/4} \frac{\exp[-2.52 \times 10^4 / T]}{1.14 \times 10^{-11}} \quad (47)$$

where the final numerical factor in the denominator is the value of the exponent at 10^3 K. The ionization fraction at different temperatures is shown in Figure 7. Ionization fractions large enough to be interesting for studies of magnetic field coupling are reached at temperatures of $T \sim 10^3$ K although the numbers remain extremely small – of the order of $x \sim 10^{-12}$ for these parameters.

3.3.2 Non-thermal ionization

Outside the region close to the star where thermal ionization is possible, any remnant levels of ionization are controlled by non-thermal processes. Considerations of thermodynamic equilibrium are not relevant, and we need to explicitly balance the rate of ionization by high-energy particles or photons against the rate of recombination within the disk gas.

There are several potentially important sources of ionization. Ordering them roughly in order of their penetrating power, ideas that have been suggested include,

- Ultraviolet photons (from the star, or from other stars in a cluster)
- Stellar X-rays

- Cosmic rays
- Energetic protons from a stellar corona [414]
- Particles produced from radioactive decay of nuclides within the disk [389]
- Electric discharges. [299]

We will limit our discussion to the first three of these processes. Ionization due to radioactive decay, although undoubtedly present, leads to a very small electron fraction, while the level of ionization due to energetic protons and electric discharges is quite uncertain⁵.

The coronae of T Tauri stars are powerful sources of keV X-rays [337]. Typical luminosities are $L_X \simeq 10^{28} - 10^{31} \text{ erg s}^{-1}$, in X-rays with temperatures $k_B T_X$ of a few keV. The physics of the interaction of these X-rays with the disk gas involves Compton scattering and absorption by photo-ionization, which has a cross-section $\sigma \sim 10^{-22} \text{ cm}^2$ for keV energies, decreasing with photon energy roughly as E_{phot}^{-3} . Given an input stellar spectrum and assumptions as to where the X-rays originate, the scattering and absorption physics can be calculated using radiative transfer codes to deduce the ionization rate within the disk [123].

Depending upon the level of detail needed for a particular application, the results of numerical radiative transfer calculations can be approximated analytically. For a relatively hard stellar spectrum ($k_B T_X = 5 \text{ keV}$), the ionization rate fairly deep within the disk scales with radius r and vertical column from the disk surface Σ as $r^{-2} \exp[-\Sigma/8 \text{ g cm}^{-2}]$ [415]. A more detailed fit is given by Bai & Goodman (2009) [35]. For an X-ray luminosity scaled to $L_{X,29} = L_X/10^{29} \text{ erg s}^{-1}$ they represent the numerical results with two components,

$$\frac{\zeta_X}{L_{X,29}} \left(\frac{r}{1 \text{ AU}} \right)^{-2.2} = \zeta_1 \exp[-(\Sigma/\Sigma_1)^\alpha] + \zeta_2 \exp[-(\Sigma/\Sigma_2)^\beta] + \dots \quad (48)$$

where Σ is the vertical column density from the top of the disk and symmetric terms in the column density from the bottom of the disk are implied. For $k_B T_X = 3 \text{ keV}$ and Solar composition gas the fit parameters are $\zeta_1 = 6 \times 10^{-12} \text{ s}^{-1}$, $\zeta_2 = 10^{-15} \text{ s}^{-1}$, $\Sigma_1 = 3.4 \times 10^{-3} \text{ g cm}^{-2}$, $\Sigma_2 = 1.59 \text{ g cm}^{-2}$, $\alpha = 0.4$ and $\beta = 0.65$. For $k_B T_X = 5 \text{ keV}$ the fit parameters are $\zeta_1 = 4 \times 10^{-12} \text{ s}^{-1}$, $\zeta_2 = 2 \times 10^{-15} \text{ s}^{-1}$, $\Sigma_1 = 6.8 \times 10^{-3} \text{ g cm}^{-2}$, $\Sigma_2 = 2.27 \text{ g cm}^{-2}$, $\alpha = 0.5$ and $\beta = 0.7$.

Figure 8 shows the estimates for $\zeta(\Sigma)$ for a stellar X-ray luminosity of $L_X = 10^{30} \text{ erg s}^{-1}$ incident on the disk at 1 AU. If one is mainly interested in regions of the disk more than $\approx 10 \text{ g cm}^{-2}$ away from the surfaces the single exponential fit given by Turner & Sano (2008) [415] may suffice. The more complex fitting function given by equation (48) captures the much higher rates of ionization due to X-rays higher up in the disk atmosphere.

Cosmic rays are another potential source of disk ionization. A standard description of the interstellar cosmic ray flux gives them an unattenuated ionization rate of

⁵ Note that the amount of *power* involved in any of these non-thermal ionization processes is rather small when compared to that liberated by accretion [193]. Any additional processes that could convert even a small fraction of the accretion energy into non-thermal particles would likely matter for the ionization state.

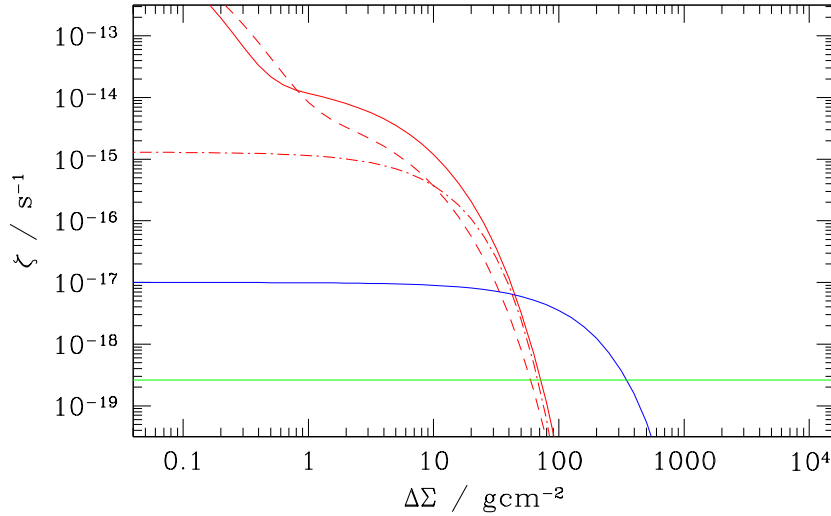


Fig. 8 Estimates of the non-thermal ionization rate due to X-rays (red curves), unshielded cosmic rays (blue) and radioactive decay of short-lived nuclides (green), plotted as a function of the vertical column density from the disk surface. The solid red curve shows the Bai & Goodman (2009) result for an X-ray temperature $k_B T_X = 5$ keV, the dashed curve their result for $k_B T_X = 3$ keV. The dot-dashed red curve shows a simpler formula proposed by Turner & Sano (2008). All of the X-ray results have been normalized to a flux of $L_X = 10^{30}$ erg s^{-1} and a radius of 1 AU.

$\zeta_{CR} \sim 10^{-17} - 10^{-16}$ s $^{-1}$ and an exponential stopping length of 96 g cm $^{-2}$ (substantially greater than even high energy stellar X-rays)⁶. With these parameters, X-rays would remain the primary source of ionization in the upper ≈ 50 g cm $^{-2}$ of the disk, but cosmic rays would dominate in the region between about 50 and 500 g cm $^{-2}$. It is unclear, however, whether the unattenuated interstellar medium flux of cosmic rays typically reaches the surfaces of protoplanetary disks. The magnetic fields embedded in the *Solar* wind form a partial barrier to incoming cosmic ray particles, whose effect is seen in a modulation of the observed flux with the Solar cycle. T Tauri stars could have much stronger stellar winds that exclude cosmic rays efficiently. Indeed, chemical modeling of molecular line data suggests that cosmic rays are substantially excluded (to a level $\zeta_{CR} \sim 10^{-19}$) from the disk around the nearby star TW Hya [98], though how pervasive this phenomenon is remains unknown. If cosmic rays are not present, the only guaranteed source of ionization at columns more than ≈ 100 g cm $^{-2}$ away from the disk surfaces is radioactive decay.

If our main interest is in conditions at $r \sim 1$ AU the surface density in gas is typically $\Sigma \sim 10^3$ g cm $^{-2}$ and X-rays, which are our main concern, will not reach the

⁶ Umabayashi & Nakano noted that if cosmic rays have an approximately isotropic angular distribution at the disk surface, geometric effects lead to a faster than exponential attenuation deep in the disk [417].

mid-plane. The situation is different further out. At 100 AU typical surface densities are much lower — 1 g cm^{-2} might be reasonable — and X-rays will sustain a non-zero rate of ionizations throughout that column. On these scales ultraviolet photons can also be important. Stellar FUV radiation will ionize carbon and sulphur atoms near the disk surface, yielding a relatively high electron fraction $x_e \sim 10^{-5}$. The ionized skin that results is shallow, penetrating to a vertical column of just $0.01 - 0.1 \text{ g cm}^{-2}$, but enough to be significant in the tenuous outer disk [329].

As with ionization, the rate of recombination within the disk can be calculated from complex numerical models that track reactions (often numbering in the thousands) between dozens of different species. The following discussion, which borrows heavily from the description given by Ilgner & Nelson (2006) [189] and Fromang (2013) [141], is intended only to outline some of the important principles. At the broadest level of discussion we need to consider gas-phase recombination reactions (involving molecular and gas-phase metal ions) along with recombination on the surface of dust grains.

The principles of gas-phase recombination can be illustrated by considering the possible reactions between electrons and generic molecules m and metal atoms M [314, 189]. The basic reactions are then,

- Ionization,



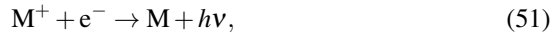
with rate ζ . A specific example is $\text{H}_2 \rightarrow \text{H}_2^+ + e^-$.

- Recombination with molecular ions,



with rate $\alpha = 3 \times 10^{-6} T^{-1/2} \text{ cm}^3 \text{ s}^{-1}$. An example is the dissociative recombination reaction $\text{HCO}^+ + e^- \rightarrow \text{CO} + \text{H}$.

- Recombination with gas-phase metal ions,



with rate $\gamma = 3 \times 10^{-11} T^{-1/2} \text{ cm}^3 \text{ s}^{-1}$. An example is $\text{Mg}^+ + e^- \rightarrow \text{Mg} + h\nu$.

- Charge exchange reactions,



with rate $\beta = 3 \times 10^{-9} \text{ cm}^3 \text{ s}^{-1}$. An example is $\text{HCO}^+ + \text{Mg} \rightarrow \text{Mg}^+ + \text{HCO}$.

From such a set of reactions we form differential equations describing the time evolution of the number density of species involved. For the molecular abundance n_m , for example, we have,

$$\frac{dn_m}{dt} = -\zeta n_m + \alpha n_e n_{m^+} + \beta n_M n_{m^+} = 0, \quad (53)$$

where the second equality follows from assuming that the system has reached equilibrium. The resulting system of algebraic equations has simple limiting solutions. For example, if there are no significant reactions involving metals then the above equation, together with the condition of charge neutrality ($n_{m^+} = n_e$), gives an electron fraction $x_e = n_e/n_m$,

$$x_e = \sqrt{\frac{\zeta}{\alpha n_m}}. \quad (54)$$

In the more general case, the network yields a cubic equation which can be solved for the electron fraction as a function of the gas-phase metal abundance [189]. Typically the presence of metal atoms and ions is important for the ionization level.

Recombination can also occur on the surfaces of dusty or icy grains. The simplest reactions we might consider are,



If the first of these reactions is rate-limiting, then we can write a modified version of the ordinary differential equation (equation 53) that includes grain processes. Ignoring metals for simplicity,

$$\frac{dn_m}{dt} = -\zeta n_m + \alpha n_e n_{m^+} + \sigma v_e n_{\text{gr}} n_{e^-}, \quad (56)$$

where σ is the cross-section of grains to adhesive collisions with free electrons and v_e is the electron thermal velocity. In the limit where *only* grains contribute to recombination we then find,

$$x_e = \frac{\zeta}{\sigma v_e n_{\text{gr}}}. \quad (57)$$

If the grains are mono-disperse with radius s , then $x_e \propto 1/\sigma n_{\text{gr}} \propto s$, and recombination on grain surfaces will be more important for small grain sizes. We also note that the dependence on the ionization rate ζ is linear, rather than the square root dependence found in the gas-phase case. As for metals, grain populations with commonly assumed size distributions are found to matter for the ionization level.

The above discussion of recombination leaves a great deal unsaid. For grains, an important additional consideration is related to the typical charge state, which needs to be calculated [116]. A good comparison of different networks for the calculation of the ionization state is given by Ilgner & Nelson (2006) [189], while Bai & Goodman (2009) [35] provide a clear discussion of the important processes. In wading into this literature the reader who encounters a problem involving the ionization level is advised to first evaluate whether a simple analytic approximation is adequate for their application, or whether solution of a full chemical network is required. The accuracy needed from calculations of ionization equilibrium is strongly problem-dependent, and in some cases, such as if we don't know if cosmic rays are present for a particular system, high accuracy may be illusory.

- The vertical density profile of disks is determined by hydrostatic equilibrium. The simplest (vertically isothermal) model yields a gaussian density profile. More complex models need to incorporate vertical thermal gradients and the possible contribution of magnetic pressure. Generally, the optically thin atmospheres of disks have higher temperatures than at the mid-plane, and distinct temperatures for the gas and dust components.
- The radial temperature profile is set by the balance between stellar irradiation and local cooling, supplemented by dissipation of accretion energy if \dot{M} is high enough. These processes yield a mid-plane temperature scaling roughly in the range between $r^{-3/4}$ and $r^{-1/2}$. The radial profile of the surface density cannot be determined by similarly simple physical considerations. However, on average we expect the mid-plane pressure to decline with radius, and this causes the gas to orbit at slightly less than the Keplerian speed.
- The disk close to the star is thermally ionized at levels sufficient to couple magnetic fields to the gas where the temperature exceeds about 10^3 K. At larger radii the ionization is non-thermal, due to stellar X-rays, FUV photons, radioactive decays, and cosmic rays if they are not screened from the disk. The ionization state varies radially and vertically depending on the balance of ionization and recombination reactions, which may occur in the gas phase or on dust grain surfaces.

4 Disk evolution

The population of protoplanetary disks is observed to evolve, but the dominant physical processes responsible for this evolution remain unclear. For a geometrically thin, low-mass disk, the deviation from a point-mass Keplerian rotation curve is small (c.f. equation 24) and the specific angular momentum,

$$l(r) = r^2 \Omega_K = \sqrt{GM_* r} \propto r^{1/2}, \quad (58)$$

is an increasing function of orbital radius. To accrete, gas in the disk must lose angular momentum, and the central theoretical problem in disk evolution is to understand this process.

Within any shearing fluid momentum is transported in the cross-stream direction because the random motion of molecules leads to collisions between particles that have different velocities. The classical approach to disk evolution [268, 340] treats the disk as a vertically thin axisymmetric sheet of viscous fluid, and leads to a fairly simple equation for the time evolution of the disk surface density $\Sigma(r, t)$. There appears to be a fatal flaw to this approach, because the molecular viscosity of the gas is much too small to lead to any significant rate of disk evolution. But it's not as bad as it seems. The classical disk evolution equation involves few assumptions beyond the immutable laws of mass and angular momentum conservation, and as we shall see is therefore approximately valid if the "viscosity" is re-interpreted as the outcome of a turbulent process. We will have (much) more to say about the possible origin of disk turbulence in §5.

Redistribution of angular momentum within the gas disk is not the only route to evolution. An almost equally long-studied suggestion [69] is that gas accretes because a magnetohydrodynamic (MHD) wind *removes* angular momentum entirely from the disk. Winds and viscosity have frequently been seen as orthogonal and competing hypotheses for disk evolution, but there is evidence suggesting that both processes are simultaneously important in regions of protoplanetary disks.

4.1 The classical equations

The evolution of a flat, circular and geometrically thin ($(h/r) \ll 1$) viscous disk follows from the equations of mass and angular momentum conservation [340]. Given a surface density $\Sigma(r, t)$, radial velocity $v_r(r, t)$ and angular velocity $\Omega(r)$, the continuity equation in cylindrical co-ordinates yields,

$$r \frac{\partial \Sigma}{\partial t} + \frac{\partial}{\partial r} (r \Sigma v_r) = 0. \quad (59)$$

Angular momentum conservation gives,

$$r \frac{\partial}{\partial t} (r^2 \Omega \Sigma) + \frac{\partial}{\partial r} (r^2 \Omega \cdot r \Sigma v_r) = \frac{1}{2\pi} \frac{\partial G}{\partial r}, \quad (60)$$

where $\Omega(r)$ is time-independent but need not be the point mass Keplerian angular velocity. The rate of change of disk angular momentum is given by the change in surface density due to radial flows and by the *difference* in the torque exerted on the annulus by stresses at the inner and outer edges. For a viscous fluid the torque G has the form,

$$G = 2\pi r \cdot \nu \Sigma r \frac{d\Omega}{dr} \cdot r, \quad (61)$$

where ν is the kinematic viscosity. The torque is the product of the circumference, the viscous force per unit length, and the lever arm r , and scales with the gradient of the angular velocity.

To obtain the surface density evolution equation in its usual form we first eliminate v_r by substituting for $\partial \Sigma / \partial t$ in equation (60) from equation (59). This gives an expression for $r \Sigma v_r$, which we substitute back into equation (59) to yield,

$$\frac{\partial \Sigma}{\partial t} = -\frac{1}{r} \frac{\partial}{\partial r} \left[\frac{1}{(r^2 \Omega)'} \frac{\partial}{\partial r} (\nu \Sigma r^3 \Omega') \right], \quad (62)$$

where the primes denote differentiation with respect to radius. Specializing to a point mass Keplerian potential ($\Omega \propto r^{-3/2}$) we then find that viscous redistribution of angular momentum within a thin disk obeys an equation,

$$\frac{\partial \Sigma}{\partial t} = \frac{3}{r} \frac{\partial}{\partial r} \left[r^{1/2} \frac{\partial}{\partial r} (\nu \Sigma r^{1/2}) \right]. \quad (63)$$

This equation is a diffusive partial differential equation for the evolution of the gas, which has a radial velocity,

$$v_r = -\frac{3}{\Sigma r^{1/2}} \frac{\partial}{\partial r} (\nu \Sigma r^{1/2}). \quad (64)$$

The equation is linear if the viscosity ν is independent of Σ .

Some useful rules of thumb for the rate of evolution implied by equation (63) can be deduced with a change of variables. Defining,

$$X \equiv 2r^{1/2}, \quad (65)$$

$$f \equiv \frac{3}{2} \Sigma X, \quad (66)$$

and taking the viscosity ν to be constant, we get a simpler looking diffusion equation,

$$\frac{\partial f}{\partial t} = D \frac{\partial^2 f}{\partial X^2}, \quad (67)$$

with a diffusion coefficient D ,

$$D = \frac{12\nu}{X^2}. \quad (68)$$

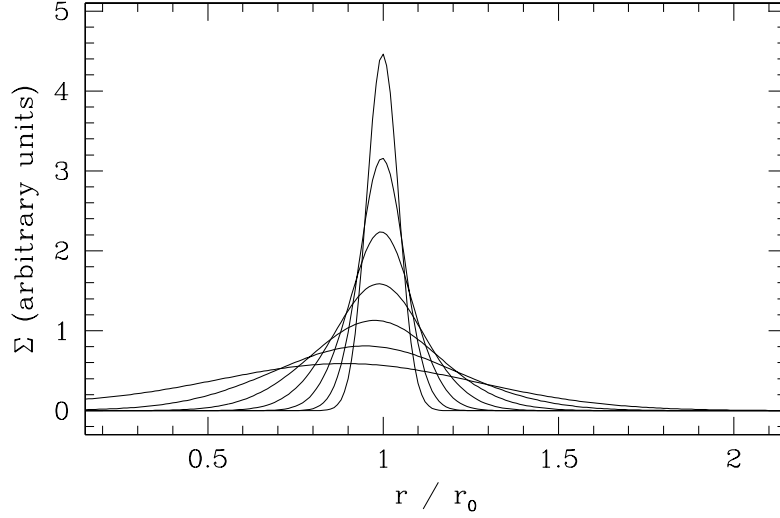


Fig. 9 The time-dependent solution to the disk evolution equation with $\nu = \text{constant}$, showing the spreading of a ring of gas initially orbiting at $r = r_0$. From top down the curves show the surface density as a function of the scaled time variable $\tau = 12\nu r_0^{-2}t$, for $\tau = 0.004$, $\tau = 0.008$, $\tau = 0.016$, $\tau = 0.032$, $\tau = 0.064$, $\tau = 0.128$, and $\tau = 0.256$.

The diffusion time scale across a scale ΔX for an equation of the form of equation (67) is just $(\Delta X)^2/D$. Converting back to the physical variables, the time scale on which viscosity will smooth surface density gradients on a scale Δr is $\tau_v \sim (\Delta r)^2/\nu$. For a disk with characteristic size r , the surface density at all radii will evolve on a time scale,

$$\tau_v \approx \frac{r^2}{\nu}. \quad (69)$$

This is the *viscous time scale* of the disk.

We can gain some intuition into how equation (63) works by inspecting time-dependent analytic solutions that can be derived for special forms of the viscosity $\nu(r)$. For $\nu = \text{constant}$ a Green's function solution is possible. Suppose that at $t = 0$ the gas lies in a thin ring of mass m at radius r_0 ,

$$\Sigma(r, t = 0) = \frac{m}{2\pi r_0} \delta(r - r_0), \quad (70)$$

where $\delta(r - r_0)$ is a Dirac delta function. With boundary conditions that impose zero-torque at $r = 0$ and allow for free expansion toward $r = \infty$ the solution is [268],

$$\Sigma(x, \tau) = \frac{m}{\pi r_0^2} \frac{1}{\tau} x^{-1/4} \exp\left[-\frac{(1+x^2)}{\tau}\right] I_{1/4}\left(\frac{2x}{\tau}\right), \quad (71)$$

in terms of dimensionless variables $x \equiv r/r_0$, $\tau \equiv 12\nu r_0^{-2}t$, and where $I_{1/4}$ is a modified Bessel function of the first kind. This solution is plotted in Figure 9 and illustrates generic features of viscous disk evolution. As t increases the ring spreads diffusively, with the mass flowing toward $r = 0$ while the angular momentum is carried by a negligible fraction of the mass toward $r = \infty$. This segregation of mass and angular momentum is generic to the evolution of a viscous disk, and must occur if accretion is to proceed without overall angular momentum loss (for example in a magnetized disk wind).

4.1.1 Limits of validity

Protoplanetary disks are not viscous fluids in the same way that honey is a viscous fluid (or, for that matter, in the same way as the mantle of the Earth is viscous). To order of magnitude precision, the viscosity of a gas $\nu \sim v_{\text{th}}\lambda$, where v_{th} is the thermal speed of the molecules and the mean-free path λ is,

$$\lambda \sim \frac{1}{n\sigma}. \quad (72)$$

Here n is the number density of molecules with collision cross-section σ . Taking σ to be roughly the physical size of a hydrogen molecule, $\sigma \sim \pi(10^{-8} \text{ cm})^2$, and conditions appropriate to 1 AU ($n \sim 10^{15} \text{ cm}^{-3}$, $v_{\text{th}} \sim 10^5 \text{ cm s}^{-1}$) we estimate,

$$\begin{aligned} \lambda &\sim 3 \text{ cm} \\ \nu &\sim 3 \times 10^5 \text{ cm}^2 \text{ s}^{-1}. \end{aligned} \quad (73)$$

This is not a large viscosity. The implied viscous time according to equation (69) is of the order of 10^{13} yr, far in excess of observationally inferred time scales of protoplanetary disk evolution. If we nevertheless press on and use equation (63) to model disk evolution, we are implicitly modeling a system that is not an ordinary viscous fluid with a viscous equation. We need to understand when this is a valid approximation.

The first possibility, introduced by Shakura & Sunyaev (1973) in their paper on black hole accretion disks [372], retains the idea that angular momentum is conserved within the disk system, but supposes that turbulence rather than molecular processes is the agent of angular momentum transport. Looking back at the derivation of the disk evolution equation (63), we note that the fluid properties of molecular viscosity only enter twice, (i) in the specific expression for G (for example in the fact that the torque is hardwired to be linear in the rate of shear) and (ii) in the more basic assumption that angular momentum transport is determined by the *local* fluid properties. The rest of the derivation involves only conservation laws that hold irrespective of the nature of transport. Plausibly then, a disk in which angular momentum is redistributed by the action of turbulence should still be describable by a diffusive equation, provided that the turbulence is a local process. Proceeding rigorously, Balbus & Papaloizou (1999) [47] showed that MHD turbulence is in principle

local in this sense, whereas angular momentum transport by self-gravity is in principle not. At the level of the basic axisymmetric evolution equation then — before we turn to questions of what determines v , or how boundary layers behave where the shear is reversed — we have not committed any cardinal sin in starting from the viscous disk equation.

Greater care is needed in situations where the disk flow is no longer axisymmetric. Fluids obey the Navier-Stokes equations, but there is no guarantee that a turbulent disk with a complex geometry will behave in the same way as a viscous Navier-Stokes flow with effective kinematic and bulk viscosities. In eccentric disks, for example, even the most basic properties (such as whether the eccentricity grows or decays) depend upon the nature of the angular momentum transport [309].

The disk evolution equation will also need modification if there are external sources or sinks of mass or angular momentum. If the disk gains or loses mass at a rate $\dot{\Sigma}(r,t)$, and *if that gas has the same specific angular momentum as the disk*, then the modification is trivial,

$$\frac{\partial \Sigma}{\partial t} = \frac{3}{r} \frac{\partial}{\partial r} \left[r^{1/2} \frac{\partial}{\partial r} \left(v \Sigma r^{1/2} \right) \right] + \dot{\Sigma}. \quad (74)$$

Disk evolution in the presence of thermally driven winds (such as photo-evaporative flows) can be described with this equation. Alternatively, we may consider a disk subject to an external torque that drives a radial flow with velocity $v_{r,ext}$. This adds an advective term,

$$\frac{\partial \Sigma}{\partial t} = \frac{3}{r} \frac{\partial}{\partial r} \left[r^{1/2} \frac{\partial}{\partial r} \left(v \Sigma r^{1/2} \right) \right] - \frac{1}{r} \frac{\partial}{\partial r} (r \Sigma v_{r,ext}). \quad (75)$$

The qualitative evolution of the disk — for example the tendency for the outer regions to expand to conserve angular momentum, or the steady-state surface density profile at small radii [396] — can be changed if there is even a modest external torque on the system.

From an observational point of view the relative simplicity of equation (63) means that it is often used to model the evolution of disk populations and to fit the surface density profile of individual disks. This provides a useful connection to disk theory, but it should be remembered that the general validity of the simple diffusion equation is itself an open question. In the outer regions, especially, it is possible that the initial surface density distribution is modified more by thermal or magnetic winds than by internal redistribution of angular momentum.

4.1.2 The α prescription

Molecular viscosity depends in a calculable way upon the density, temperature and composition of the fluid. Can anything similar be said about the “effective viscosity” present in disks? The standard approach is to write the viscosity as the product of characteristic velocity and spatial scales in the disk,

$$v = \alpha c_s h, \quad (76)$$

where α is a dimensionless parameter. This ansatz (introduced in a related form in [372]) is known as the Shakura-Sunyaev α prescription.

We can view the α prescription in two ways. The weak version is to regard it as a re-parameterization of the viscosity that describes the leading order scaling expected in disks (so that α is a more slowly varying function of temperature, radius etc than v). This is useful, and along with convention is the reason why numerical simulations of turbulent transport are invariably reported in terms of an effective α . One can also adopt a strong version of the prescription in which α is assumed to be a constant. This is powerful as it allows for the development of a predictive theory of disk structure that is based on only one free parameter (for a textbook discussion see Frank, King & Raine [139], or for an application to protoplanetary disks see, e.g. [58]). However, its use must be justified on a case by case basis, as there is no reason why α should be a constant. Constant α models probably work better in highly ionized disks around black holes and neutron stars, where angular momentum transport across a broad range of radii occurs via the simplest version of the magnetorotational instability [45], than in protoplanetary disks where the physical origin of angular momentum transport is more complex [19].

4.2 Boundary conditions

Solving equation (63) requires the imposition of boundary conditions. The most common, and simplest, is a zero-torque inner boundary condition, which exactly conserves the initial angular momentum content of the disk. If the star has a dynamically significant magnetic field, however, or if the disk is part of a binary system, other boundary conditions may be more appropriate.

4.2.1 Zero-torque boundary conditions

A steady-state solution to equation (63) with a zero-torque inner boundary condition is derived by starting from the angular momentum conservation equation (equation 60). Setting the time derivative to zero and integrating we have,

$$2\pi r \Sigma v_r \cdot r^2 \Omega = 2\pi r^3 v \Sigma \frac{d\Omega}{dr} + \text{constant}. \quad (77)$$

In terms of the mass accretion rate $\dot{M} = -2\pi r \Sigma v_r$, we can write this in the form,

$$-\dot{M} \cdot r^2 \Omega = 2\pi r^3 v \Sigma \frac{d\Omega}{dr} + \text{constant}, \quad (78)$$

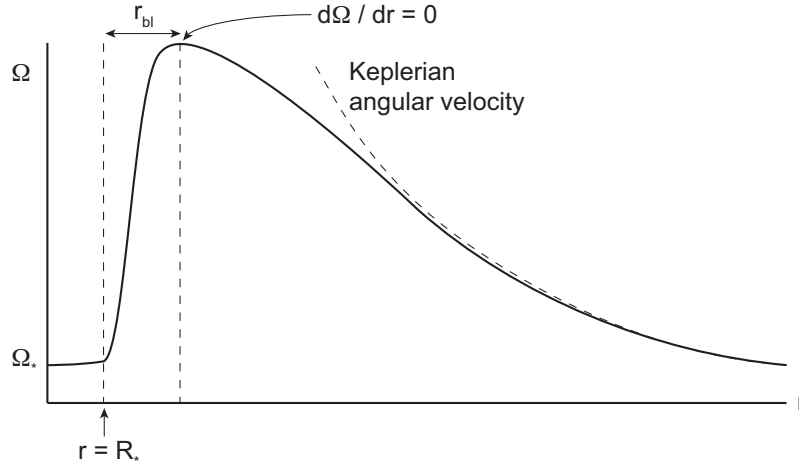


Fig. 10 A sketch of what the angular velocity profile $\Omega(r)$ must look like if the disk extends down to the surface of a slowly rotating star. By continuity there must be a point — usually close to the stellar surface — where $d\Omega/dr = 0$ and the viscous stress vanishes.

where the constant of integration, which is an angular momentum flux, is as yet undermined. To specify the constant we note that if there is a point where $d\Omega/dr = 0$ the viscous stress vanishes, and the constant is just the advective flux of angular momentum,

$$\text{constant} = -\dot{M} \cdot r^2 \Omega. \quad (79)$$

The physical situation where $d\Omega/dr = 0$ is where the protoplanetary disk extends all the way down to the surface of a slowly rotating star. The disk and the star form a single fluid system, and the angular velocity (shown in Figure 10) must be a continuous function that connects $\Omega \approx 0$ in the star to $\Omega \propto r^{-3/2}$ within the disk. The viscous stress must then vanish at some radius $R_* + r_{bl}$, where r_{bl} is the width of the *boundary layer* that separates the star from the Keplerian part of the disk. Within the boundary layer the angular velocity increases with radius, and gravity is balanced against a combination of rotation and radial pressure support. Elementary arguments [339] show that in many cases the boundary layer is narrow, so that $R_* + r_{bl} \simeq R_*$. We then find that,

$$\text{constant} \simeq -\dot{M} R_*^2 \sqrt{\frac{GM_*}{R_*^3}}, \quad (80)$$

and the steady-state solution for the disk simplifies to,

$$v\Sigma = \frac{\dot{M}}{3\pi} \left(1 - \sqrt{\frac{R_*}{r}} \right). \quad (81)$$

For a specified viscosity this equation gives the steady state surface density profile of a disk with a constant accretion rate \dot{M} . Away from the inner boundary $\Sigma(r) \propto v^{-1}$, and the radial velocity (equation 64) is $v_r = -3v/2r$.

In obtaining equation (81) we have derived an expression for a *Keplerian* disk via an argument that relies on the *non-Keplerian* form of $\Omega(r)$ in a boundary layer. The resulting expression for the surface density is valid in the disk at $r \gg R_*$, but would not work well close to the star *even if there is a boundary layer*. To model the boundary layer properly, we would need equations that self-consistently determine the angular velocity along with the surface density [336].

4.2.2 Magnetospheric accretion

For protoplanetary disks the stellar magnetic field can have a dominant influence on the disk close to the star [220]. The simplest magnetic geometry involves a dipolar stellar magnetic field that is aligned with the stellar rotation axis and perpendicular to the disk plane. The unperturbed field then has a vertical component at the disk surface,

$$B_z = B_* \left(\frac{r}{R_*} \right)^{-3}. \quad (82)$$

In the presence of a disk, the vertical field will thread the disk gas and be distorted by differential rotation between the Keplerian disk and the star. The differential rotation twists the field lines that couple the disk to the star, generating an azimuthal field component at the disk surface B_ϕ and a magnetic torque per unit area (counting both upper and lower disk surfaces),

$$T = \frac{B_z B_\phi}{2\pi} r. \quad (83)$$

Computing the perturbed field accurately is hard (for simulation results see, e.g. [362]), but it is easy to identify the qualitative effect that it has on the disk. For a star with rotation period P , we define the co-rotation radius r_{co} as the radius where the field lines have the same angular velocity as that of Keplerian gas in the disk,

$$r_{\text{co}} = \left(\frac{GM_* P^2}{4\pi^2} \right)^{1/3}. \quad (84)$$

There are then two regions of star-disk magnetic interaction:

- Interior to co-rotation ($r < r_{\text{co}}$) the disk gas has a greater angular velocity than the field lines. Field lines that link the disk and the star here are dragged forward by the disk, and exert a braking torque that removes angular momentum from the disk gas.
- Outside co-rotation ($r > r_{\text{co}}$) the disk gas has a smaller angular velocity than the field lines. The field lines are dragged backward by the disk, and there is a positive torque on the disk gas.

Young stars are typically rapid rotators [75], so the co-rotation radius lies in the inner disk. For $P = 7$ days, for example, the co-rotation radius around a Solar mass star is at $r_{\text{co}} \simeq 15 R_{\odot}$ or 0.07 AU.

The presence of a stellar magnetic torque violates the assumption of a zero-torque boundary condition, though the steady-state solution we derived previously (equation 81) will generally still apply at sufficiently large radius. The strong radial dependence of the stellar magnetic torque means that there is only a narrow window of parameters where the torque will be significant yet still allow the disk to extend to the stellar surface. More commonly, a dynamically significant stellar field will disrupt the inner disk entirely, yielding a magnetospheric regime of accretion in which the terminal phase of accretion is along stellar magnetic field lines. The disruption (or magnetospheric) radius r_m can be estimated in various ways [220], but all yield the same scaling as the spherical Alfvén radius that is obtained by equating the magnetic pressure of a dipolar field to the ram pressure of spherical infall,

$$r_m \simeq \left(\frac{k B_*^2 R_*^6}{\dot{M} \sqrt{GM_*}} \right)^{2/7}. \quad (85)$$

Here B_* is the stellar surface field (defined such that $B_* R_*^3$ is the dipole moment) and k a constant of the order of unity. Taking $k = 1$ for a Solar mass star,

$$r_m \simeq 14 \left(\frac{B_*}{\text{kG}} \right)^{4/7} \left(\frac{R_*}{2 R_{\odot}} \right)^{12/7} \left(\frac{\dot{M}}{10^{-8} M_{\odot} \text{ yr}^{-1}} \right)^{-2/7} R_{\odot}. \quad (86)$$

Often, the magnetospheric radius is comparable to the co-rotation radius. This is to some extent expected, since if r_m is substantially different from r_{co} the magnetic torque acting on the star will tend to modify P in the direction of reducing the difference.

4.2.3 Accretion on to and in binaries

Boundary conditions for disk evolution also need modification in binary systems. For a coplanar disk orbiting *interior* to a prograde stellar binary companion, tidal torques from the companion remove angular momentum from the outer disk and prevent it from expanding too far [324]. The tidal truncation radius roughly corresponds to the largest simple periodic orbit in the binary potential [322], which is at about 40% of the orbital separation for a binary with mass ratio $M_2/M_1 = 0.5^7$. The tidal torque is a function of radius, but to a first approximation one may assume that tides impose a rigid no-expansion condition at $r = r_{\text{out}}$. From equation (64),

$$\left. \frac{\partial}{\partial r} \left(v \Sigma r^{1/2} \right) \right|_{r=r_{\text{out}}} = 0. \quad (87)$$

⁷ The size of the disk (and even whether it is tidally truncated at all) will be different if the disk is substantially misaligned with respect to the orbital plane of the binary [262, 294].

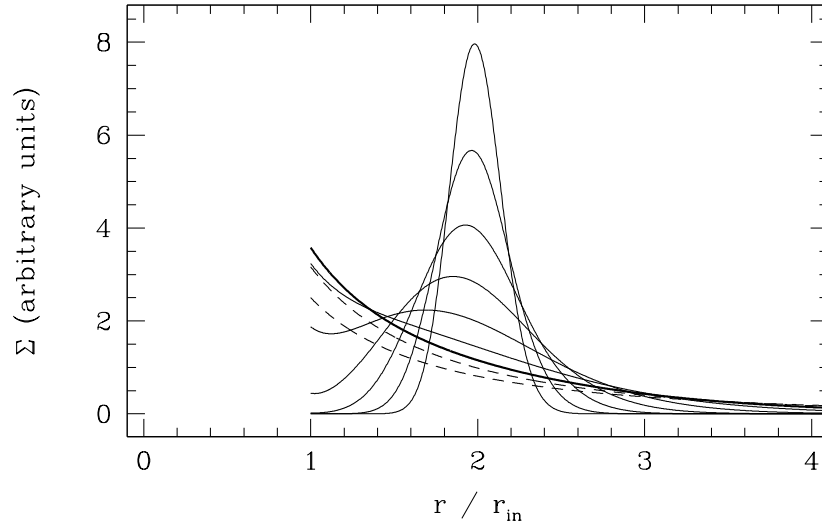


Fig. 11 The time-dependent analytic solution (equation 90) to the disk evolution equation with a $v_r = 0$ boundary condition at $r = 1$ for the case $v = r$. The solid curves show the evolution of a ring of gas initially at $r = 2$, at times $t = 0.002$, $t = 0.004$, $t = 0.008$ etc. The bold curve is at $t = 0.128$, and dashed curves show later times. Gas initially accretes, but eventually *decretes* due to the torque being applied at the boundary.

This type of boundary condition may also be an appropriate approximation for a circumplanetary disk truncated by stellar tides [284].

An exterior *circumbinary* disk will also experience stellar gravitational torques, which in this case add angular momentum to the disk and slow viscous inflow. How best to model these torques is an open question, particularly in the case of extreme mass ratio binaries composed of a star and a massive planet. Pringle [341] derived an illuminating analytic solution for circumbinary disk evolution under the assumption that tidal torques *completely prevent* inflow past some radius $r = r_{\text{in}}$. With this assumption the boundary condition at $r = r_{\text{in}}$ is $v_r = 0$, and the task is to find a solution to equation (63) with this finite radius boundary condition. A simple solution is possible for $v = kr$, with k a constant. Defining scaled variables,

$$\begin{aligned} x &= r^{1/2} \\ \sigma &= \Sigma r^{3/2}, \end{aligned} \quad (88)$$

the $t > 0$ solution for an initial mass distribution,

$$\sigma(x, t = 0) = \sigma_0 \delta(x - x_1), \quad (89)$$

is [341],

$$\sigma = \frac{\sigma_0 t^{-1/2}}{4(3\pi k)^{1/2}} \left\{ \exp\left[-(x-x_1)^2/3kt\right] + \exp\left[-(x+x_1-2x_{\text{in}})^2/3kt\right] \right\}. \quad (90)$$

The solution, plotted in Figure 11, can be compared to the zero-torque solution (Figure 9, though note this is for a constant viscosity). The initial evolution is similar, but at late times the torque that precludes inflow past r_{in} causes qualitatively different behavior. The disk switches from an accretion to a *decretion* disk, with an outward flow of mass driven by the binary torque.

The classical decretion disk solution was developed as a model for disk evolution around binaries. It is not clear, however, whether it is ever realized in the binary context. Numerical simulations of the interaction between a binary and a circumbinary disk show that angular momentum transfer to the disk co-exists with persistent inflow into a low density cavity containing the binary [25, 112]. How best to represent this complexity in a one-dimensional model is not entirely obvious. The decretion disk solution may be a better description of other astrophysical situations, such as disks around rapidly rotating and strongly magnetized stars.

4.3 Viscous heating

Although stellar irradiation is often the dominant source of heat for protoplanetary disks (§3.2), dissipation of gravitational potential energy associated with accretion is also important. Ignoring irradiation for the time being, we can derive the effective temperature profile of a steady-state viscous disk. In the regime where the classical equations are valid, the fluid dissipation per unit area is [340],

$$Q_+ = \frac{9}{4} \nu \Sigma \Omega^2. \quad (91)$$

Using the steady-state solution for $\nu \Sigma$ (equation 81) we equate Q_+ to the rate of local energy loss by radiation. If the disk is optically thick, the disk radiates (from both sides) at a rate $Q_- = 2\sigma T_{\text{disk}}^4$, with σ being the Stefan-Boltzmann constant. This yields an effective temperature profile,

$$T_{\text{disk}}^4 = \frac{3GM_*\dot{M}}{8\pi\sigma r^3} \left(1 - \sqrt{\frac{R_*}{r}} \right). \quad (92)$$

Away from the inner boundary, the steady-state temperature profile for a viscous disk ($T_{\text{disk}} \propto r^{-3/4}$) is steeper than for irradiation. For any accretion rate, we then expect viscous heating to be most important in the inner disk, whereas irradiation always wins out at sufficiently large radii.

The viscous disk temperature profile is **not** what we get from considering just the local dissipation of potential energy. The gradient of the potential energy per unit mass \mathcal{E} , is $d\mathcal{E}/dr = GM_*/r^2$. For an accretion rate \dot{M} , the luminosity available to be radiated from an annulus of width Δr due to local potential energy release would

be,

$$L = \frac{1}{2} \frac{GM_* \dot{M}}{r^2} \Delta r, \quad (93)$$

where the factor of a half accounts for the fact that half the energy goes into increased kinetic energy, with only the remainder available to be thermalized and radiated. Equating this luminosity to the black body emission from the annulus, $2\sigma T_{\text{disk}}^4 \cdot 2\pi r \Delta r$, would give a profile that is a factor three different from the asymptotic form of equation (92). The difference arises because the radial transport of angular momentum is accompanied by a radial transport of energy. The local luminosity from the disk surface at any radius then has a contribution from potential energy liberated closer in.

The optically thick regions of irradiated protoplanetary disks will be vertically isothermal. When viscous heating dominates, however, there must be a vertical temperature gradient to allow energy to be transported from the mid-plane toward the photosphere. What this gradient looks like, in detail, depends on the vertical distribution of the heating, which is not well known. However, an approximation to $T(z)$ can be derived assuming that the energy dissipation due to viscosity is strongly concentrated toward the mid-plane. We define the optical depth to the disk mid-plane,

$$\tau = \frac{1}{2} \kappa_R \Sigma, \quad (94)$$

where κ_R is the Rosseland mean opacity. The vertical density profile of the disk is $\rho(z)$. If the vertical energy transport occurs via radiative diffusion then for $\tau \gg 1$ the vertical energy flux $F(z)$ is given by the equation of radiative diffusion [366]

$$F_z(z) = -\frac{16\sigma T^3}{3\kappa_R \rho} \frac{dT}{dz}. \quad (95)$$

Now assume for simplicity that *all* of the dissipation occurs at $z = 0$. In that case $F_z(z) = \sigma T_{\text{disk}}^4$ is constant with height. We integrate from the mid-plane to the photosphere at z_{ph} assuming that the opacity is also constant,

$$-\frac{16\sigma}{3\kappa_R} \int_{T_c}^{T_{\text{disk}}} T^3 dT = \sigma T_{\text{disk}}^4 \int_0^{z_{\text{ph}}} \rho(z') dz' \quad (96)$$

$$-\frac{16}{3\kappa_R} \left[\frac{T^4}{4} \right]_{T_c}^{T_{\text{disk}}} = T_{\text{disk}}^4 \frac{\Sigma}{2}, \quad (97)$$

where the final equality relies on the fact that for $\tau \gg 1$ almost all of the disk gas lies below the photosphere. For large optical depth $T_c^4 \gg T_{\text{disk}}^4$ and the equation simplifies to,

$$\frac{T_c^4}{T_{\text{disk}}^4} \simeq \frac{3}{4} \tau. \quad (98)$$

Often *both* stellar irradiation and accretional heating contribute significantly to the thermal balance of the disk. If we define $T_{\text{disk,visc}}$ to be the effective temperature

that would result from viscous heating in the absence of irradiation (i.e. the quantity called T_{disk} , with no subscript, above) and T_{irr} to be the irradiation-only effective temperature, then,

$$T_c^4 \simeq \frac{3}{4} \tau T_{\text{disk,visc}}^4 + T_{\text{irr}}^4 \quad (99)$$

is an approximation for the central temperature, again valid for $\tau \gg 1$.

These formulae can be applied to estimate the location of the snow line. In the Solar System meteoritic evidence [297] places the transition between water vapor and water ice, which occurs at a mid-plane temperature of 150-180 K, at around 2.7 AU. This is substantially further from the Sun than would be expected if the only disk heating source was starlight. Including viscous heating, however, an accretion rate of $2 \times 10^{-8} M_{\odot} \text{ yr}^{-1}$ could sustain a mid-plane temperature of 170 K at 2.7 AU in a disk with $\Sigma = 400 \text{ g cm}^{-2}$ and $\kappa_R = 1 \text{ cm}^2 \text{ g}^{-1}$. This estimate (from equation 98) is consistent with more detailed models for protoplanetary disks [58], though considerable variation in the location of the snow line is introduced by uncertainties in the vertical structure [282].

4.4 Warped disks

The classical equation for surface density evolution needs to be rethought if the disk is non-planar. Disks may be warped for several reasons; the direction of the angular momentum vector of the gas that forms the disk may not be constant, the disk may be perturbed tidally by a companion [237, 306], or warped due to interaction with the stellar magnetosphere [236].

A warp affects disk evolution through physics that is independent of its origin (for a brief review, see [305]). In a warped disk, neighboring annuli have specific angular momenta that differ in direction as well as in magnitude. If we define a unit tilt vector $\mathbf{l}(r,t)$ that is locally normal to the disk plane, the shear then has a vertical as well as a radial component [310],

$$\mathbf{S} = r \frac{d\Omega}{dr} \mathbf{l} + r\Omega \frac{\partial \mathbf{l}}{\partial r}. \quad (100)$$

The most important consequence of the vertical shear is that it introduces a periodic vertical displacement of radially separated fluid elements. As illustrated in Figure 12 this displacement, in turn, results in a horizontal pressure gradient that changes sign across the mid-plane and is periodic on the orbital frequency. In a Keplerian disk this forcing frequency is resonant with the epicyclic frequency.

How the disk responds to the warp-generated horizontal forcing depends on the strength of dissipation [325]. If the disk is sufficiently viscous, specifically if,

$$\alpha > \frac{h}{r}, \quad (101)$$

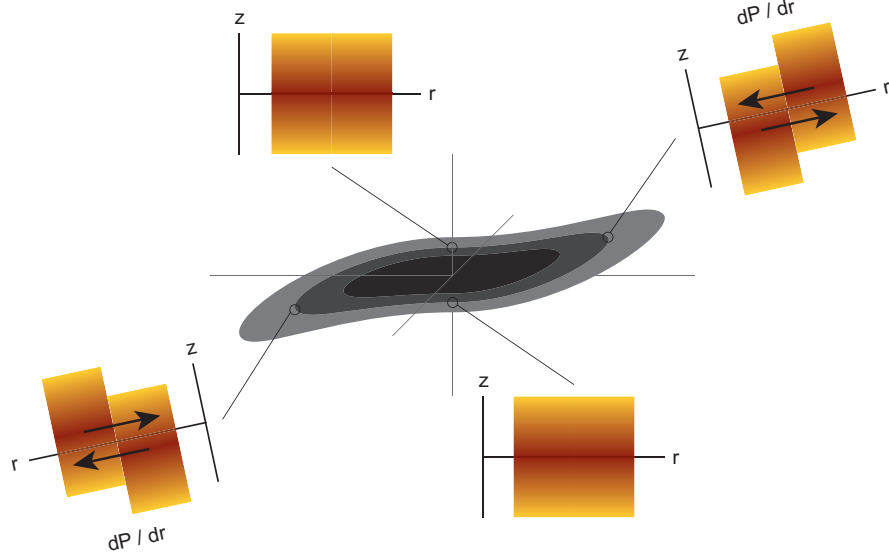


Fig. 12 Illustration (after [255, 305]) of how a warp introduces an oscillating *radial* pressure gradient within the disk. As fluid orbits in a warped disk, vertical shear displaces the mid-planes of neighboring annuli. This leads to a time-dependent radial pressure gradient $dP/dr(z)$. Much of the physics of warped disks is determined by how the disk responds to this warp-induced forcing.

the additional shear is damped locally. The equation for the surface density and tilt evolution (the key aspects of which are derived in [342], though see [308] for a complete treatment) then includes terms which diffusively damp the warp at a rate that is related to the radial redistribution of angular momentum. Normally, warp damping is substantially faster than the viscous evolution of a planar disk. Even for a Navier-Stokes viscosity — which is fundamentally isotropic — the *effective* viscosity which damps the warp is a factor $\approx 1/2\alpha^2$ larger than its equivalent in a flat disk. Rapid evolution also occurs in the opposite limit of an almost inviscid disk with,

$$\alpha < \frac{h}{r}, \quad (102)$$

but in this case the component of angular momentum associated with the warp is communicated radially in the form of a wave. For a strictly inviscid disk the linearized fluid equations for the evolution of the tilt vector take a simple form [263],

$$\frac{\partial^2 \mathbf{l}}{\partial t^2} = \frac{1}{\Sigma r^3 \Omega} \frac{\partial}{\partial r} \left(\Sigma r^3 \Omega \frac{c_s^2}{4} \frac{\partial \mathbf{l}}{\partial r} \right). \quad (103)$$

The speed of the warp wave is $v_w \approx c_s/2$.

In most cases we expect protoplanetary disks to have $\alpha < h/r$, and warps will evolve in the wave-like regime. We expect, however, that the details of warp evolution will depend upon the nature of angular momentum transport, and little is

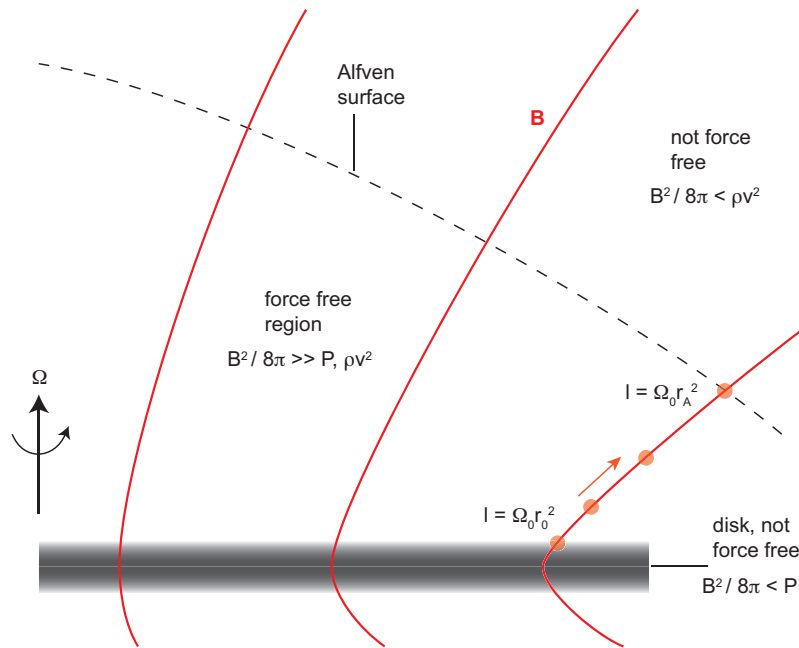


Fig. 13 Illustration, after Spruit [386], of the different regions of a disk wind solution.

known about how warps behave for the transport mechanisms (such as non-ideal MHD) most relevant to protoplanetary disks. The extent of the differences between warp evolution with realistic transport and that with a Navier-Stokes viscosity are undetermined.

4.5 Disk winds

Viscous evolution driven by redistribution of angular momentum is a consequence of turbulent (or possibly laminar) stresses that are internal to the fluid. Evolution can also be driven by external torques, the most important of which is the magnetic torque that an MHD wind exerts on the surface of the disk. An excellent pedagogical introduction to disk winds is the review by Spruit [386], while Königl & Salmeron [222] provide a more recent account that addresses the peculiarities specific to protoplanetary disks.

Winds that are driven solely by pressure gradients (“thermal winds”) are of interest as a mechanism for disk dispersal (§9) but do not change the qualitative character of disk evolution. Instead, we consider here MHD winds, with the simplest case being that of a well-ionized disk is threaded by a large-scale ordered poloidal magnetic field. In the ideal MHD limit the fluid is tied to magnetic field lines, which can facil-

itate acceleration of the wind while exerting a back reaction on the disk that removes angular momentum. This type of MHD wind is known as a Blandford-Payne wind [69]. Other varieties of MHD outflow could also occur. Winds could be launched by a gradient of *toroidal* magnetic field pressure [267], perhaps during or shortly after the collapse of the cloud that forms both the star and the disk. Jets can also originate from the interaction between the stellar magnetosphere and the disk [374].

Returning to the specific case of Blandford-Payne winds, their structure, illustrated in Figure 13, generically has three regions. Within the disk the energy density in the magnetic field, $B^2/8\pi$, is smaller than ρc_s^2 , the thermal energy⁸. Due to flux conservation, however, the energy in the vertical field component, $B_z^2/8\pi$, is roughly constant with height for $z < r$, while the gas pressure typically decreases at least exponentially with a scale height $h \ll r$. This leads to a region above the disk surface where magnetic forces dominate. The magnetic force per unit volume is,

$$\frac{\mathbf{J} \times \mathbf{B}}{c} = -\nabla \left(\frac{B^2}{8\pi} \right) + \frac{\mathbf{B} \cdot \nabla \mathbf{B}}{4\pi}, \quad (104)$$

where the current,

$$\mathbf{J} = \frac{c}{4\pi} \nabla \times \mathbf{B}. \quad (105)$$

The force, in general, can be written as shown above as the sum of a magnetic pressure gradient and a force due to magnetic tension. In the disk wind region where magnetic forces dominate, the requirement that they exert a finite acceleration on the low density gas implies that the force approximately vanishes, i.e. that,

$$\mathbf{J} \times \mathbf{B} \approx 0. \quad (106)$$

The structure of the magnetic field in the magnetically dominated region is then described as being “force-free”, and in the disk wind case (where B changes slowly with z) the field lines must be approximately straight to ensure that the magnetic tension term is also small. If the field lines support a wind, the force-free structure persists up to where the kinetic energy density in the wind, ρv^2 , first exceed the magnetic energy density. This is called the Alfvén surface. Beyond the Alfvén surface, the inertia of the gas in the wind is sufficient to bend the field lines, which tend to wrap up into a spiral structure as the disk below them rotates.

Magneto-centrifugal driving can launch a wind from the surface of a cold gas disk if the magnetic field lines are sufficiently inclined to the disk normal. The critical inclination angle in ideal MHD can be derived via an *exact* mechanical analogy. To proceed, we note that in the force-free region the magnetic field lines are (i) basically straight lines, and (ii) enforce rigid rotation out to the Alfvén surface at an angular velocity equal to that of the disk at the field line’s footpoint. The geometry is shown in Figure 14. We consider a field line that intersects the disk at radius r_0 , where the angular velocity is $\Omega_0 = \sqrt{GM_*/r_0^3}$, and that makes an angle θ to the disk normal.

⁸ We can also consider situations where the magnetic pressure in the disk is stronger than the gas pressure, though it must always be weaker than ρv_ϕ^2 .

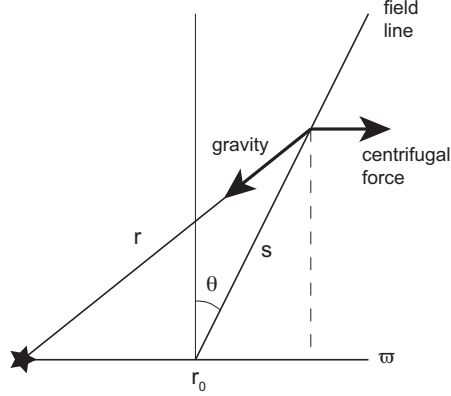


Fig. 14 Geometry for the calculation of the critical angle for magneto-centrifugal wind launching. A magnetic field line s , inclined at angle θ from the disk normal, enforces rigid rotation at the angular velocity of the foot point, at cylindrical radius $\varpi = r_0$ in the disk. Working in the rotating frame we consider the balance between centrifugal force and gravity.

We define the spherical polar radius r , the cylindrical polar radius ϖ , and measure the distance along the field line from its intersection with the disk at $z = 0$ as s . In the frame co-rotating with Ω_0 there are no magnetic forces along the field line to affect the acceleration of a wind; the sole role of the magnetic field is to constrain the gas to move along a straight line at constant angular velocity. Following this line of argument, the acceleration of a wind can be fully described in terms of an effective potential,

$$\Phi_{\text{eff}}(s) = -\frac{GM_*}{r(s)} - \frac{1}{2}\Omega_0^2\varpi^2(s). \quad (107)$$

The first term is the gravitational potential, while the second describes the centrifugal potential in the rotating frame.

Written out explicitly, the effective potential is,

$$\Phi_{\text{eff}}(s) = -\frac{GM_*}{(s^2 + 2sr_0 \sin \theta + r_0^2)^{1/2}} - \frac{1}{2}\Omega_0^2(r_0 + s \sin \theta)^2. \quad (108)$$

This function is plotted in Figure 15 for various values of the angle θ . If we consider first a vertical field line ($\theta = 0$) the effective potential is a monotonically increasing function of distance s . For modest values of θ there is a potential barrier defined by a maximum at some $s = s_{\text{max}}$, while for large enough θ the potential decreases from $s = 0$. In this last case purely magneto-centrifugal forces suffice to accelerate a wind off the disk surface, even in the absence of any thermal effects. The critical inclination angle of the field can be found by computing θ_{crit} , specified though the condition,

$$\left. \frac{\partial^2 \Phi_{\text{eff}}}{\partial s^2} \right|_{s=0} = 0. \quad (109)$$

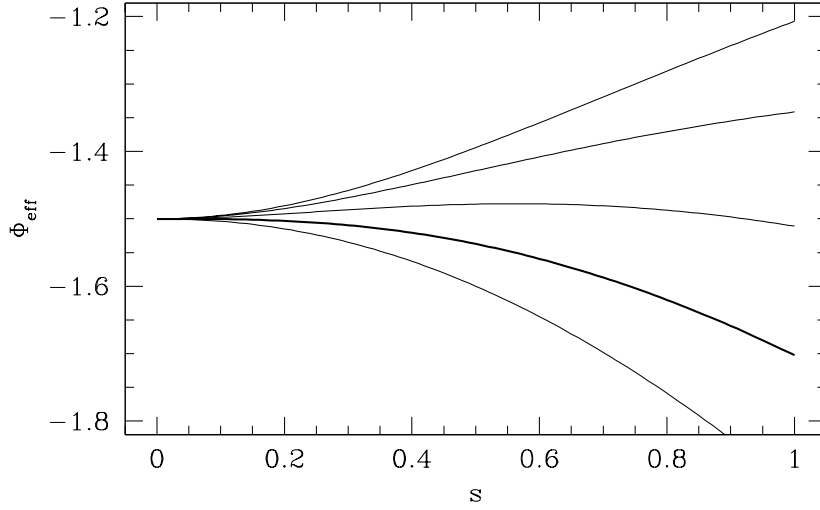


Fig. 15 The variation of the disk wind effective potential Φ_{eff} (in arbitrary units) with distance s along a field line. From top downwards, the curves show field lines inclined at 0° , 10° , 20° , 30° (in bold) and 40° from the normal to the disk surface. For angles of 30° and more from the vertical, there is no potential barrier to launching a cold MHD wind directly from the disk surface.

Evaluating this condition, we find,

$$\begin{aligned} 1 - 4 \sin^2 \theta_{\text{crit}} &= 0 \\ \Rightarrow \theta_{\text{crit}} &= 30^\circ, \end{aligned} \quad (110)$$

as the minimum inclination angle from the vertical needed for unimpeded wind launching in ideal MHD [69]. Since most of us are more familiar with mechanical rather than magnetic forces, this derivation in the rotating frame offers the easiest route to this result. But it can, of course, be derived just as well by working in the inertial frame of reference [386].

The rigid rotation of the field lines interior to the Alfvén surface means that gas being accelerated along them increases its specific angular momentum. The magnetic field, in turn, applies a torque to the disk that removes a corresponding amount of angular momentum. If a field line, anchored to the disk at radius r_0 , crosses the Alfvén surface at (cylindrical) radius r_A , it follows that the angular momentum flux is,

$$\dot{L}_w = \dot{M}_w \Omega_0 r_A^2, \quad (111)$$

where \dot{M}_w is the mass loss rate in the wind. Removing angular momentum at this rate from the disk results in a local accretion rate $\dot{M} = 2\dot{L}_w / \Omega_0 r_0^2$. The ratio of the disk accretion rate to the wind loss rate is,

$$\frac{\dot{M}}{\dot{M}_w} = 2 \left(\frac{r_A}{r_0} \right)^2. \quad (112)$$

If r_A substantially exceeds r_0 (by a factor of a few, which is reasonable for detailed disk wind solutions) a relatively weak wind can carry away enough angular momentum to support a much larger accretion rate.

The behavior of a disk that evolves under wind angular momentum loss depends on how the wind and the poloidal magnetic field respond to the induced accretion. It is not immediately obvious that a steady accretion flow is even possible. The form of the effective potential (Figure 15) suggests that the rate of mass and angular momentum loss in the wind ought to be a strong function of the inclination of the field lines — for $\theta < 30^\circ$ there is a potential barrier to wind launching, while for $\theta \geq 30^\circ$ there is no barrier at all. How θ responds to changes in the inflow rate through the disk is of critical importance [265, 80, 311], and there is no simple analog of the diffusive disk evolution equation. Despite this, viscous and wind-driven disks exhibit some qualitative difference that may enable observational tests. The classical test is the evolution of the outer disk radius, which expands in viscous models (*if* there is no mass loss, even in the form of a thermal wind) but contracts if an MHD wind dominates. Old and almost forgotten observations [384] of disk radius changes in dwarf novae (accreting white dwarfs in mass transfer binary systems) provided empirical support for viscous disk evolution *in those specific systems*. Disk winds also remove energy, and so another potential test is to look for evidence of the dissipation of accretion energy within the disk that is present in viscous models but absent for winds. At fixed accretion rate a wind-driven disk will have a lower effective temperature at small radii than its viscous counterpart, and this will alter the predicted spectral energy distribution (at large radii the temperature of both types of disk is set by irradiation, and no significant differences are expected).

4.5.1 Magnetic field transport

The strength and radial profile of the vertical magnetic field threading the disk are important quantities for disk winds, and for turbulence driven by MHD processes. Disks form from the collapse of magnetized molecular clouds, and it is inevitable that they will inherit non-zero flux at the time of formation. The poloidal component of that flux can subsequently be advected radially with the disk gas, diffuse relative to the gas, or (if the flux has varying sign across the disk) reconnect.

A theory for the radial transport of poloidal flux within geometrically thin accretion disks was developed by Lubow, Papaloizou & Pringle (1994) [264]. They considered a disk within which turbulence generates an effective viscosity ν and an effective magnetic diffusivity η . The disk is threaded by a vertical magnetic field $B_z(r, t)$, which is supported by a combination of currents within the disk and (potentially) a current external to the disk. Above the disk, as in Figure 13 the field is force-free. The field lines bend within the disk, such that the poloidal field has a radial component $B_{rs}(r, t)$ at the disk surface.

To proceed (following the notation in [165]), we first write the poloidal field in terms of a magnetic flux function ψ , such that $\mathbf{B} = \nabla\psi \times \mathbf{e}_\phi$, where \mathbf{e}_ϕ is a unit vector in the azimuthal directions. The components of the field are,

$$\begin{aligned} B_r &= -\frac{1}{r} \frac{\partial \psi}{\partial z}, \\ B_z &= \frac{1}{r} \frac{\partial \psi}{\partial r}. \end{aligned} \quad (113)$$

From the second of these relations we note that ψ is (up to a factor of 2π) just the vertical magnetic flux interior to radius r . We split ψ into two pieces, a piece ψ_{disk} due to currents within the disk, and a piece ψ_∞ due to external currents (“at infinity”),

$$\psi = \psi_{\text{disk}} + \psi_\infty. \quad (114)$$

The external current generates a magnetic field that is uniform across the disk.

With these definitions, the evolution of the poloidal field in the simplest analysis [264, 165] obeys,

$$\frac{\partial \psi}{\partial t} + r(v_{\text{adv}} B_z + v_{\text{diff}} B_{rs}) = 0, \quad (115)$$

where v_{adv} is the advective velocity of magnetic flux and v_{diff} its diffusive velocity due to the turbulent resistivity within the disk. The disk component of the flux function is related to the surface radial field via an integral over the disk. Schematically,

$$\psi_{\text{disk}}(r) = \int_{r_{\text{in}}}^{r_{\text{out}}} F(r, r') B_{rs}(r') dr', \quad (116)$$

where F is a rather complex function that can be found in Guilet & Ogilvie (2014) [165]. The appearance of this integral reflects the inherently global nature of the problem — a current at some radius within the disk affects the poloidal magnetic field everywhere, not just locally — and makes analytic or numerical solutions for flux evolution more difficult. Nonetheless, equation (116) can be inverted to find B_{rs} from ψ , after which the more familiar equation (115) can be solved for specified transport velocities to determine the flux evolution.

Equation (115) expresses a simple competition, the inflow of gas toward the star will tend to drag in poloidal magnetic field, but this will set up a radial gradient and be opposed by diffusion. The physical insight of Lubow et al. [264] was to note that although both of these are processes involving turbulence (and, very roughly, we might guess that $v \sim \eta$), the scales are quite distinct. From Figure 13, we note that because the field lines bend *within the disk*, a moderately inclined external field (with $B_{rs} \sim B_z$) above the disk only has to diffuse across a scale $\sim h$ to reconnect with its oppositely directed counterpart below the disk. Dragging in the field with the mean disk flow, however, requires angular momentum transport across a larger scale r . In terms of transport velocities, in a steady-state we have,

$$v_{\text{adv}} \sim \frac{v}{r},$$

$$v_{\text{diff}} \sim \frac{\eta B_{rs}}{h B_z}, \quad (117)$$

so that for $v \sim \eta$ and $B_{rs} \sim B_z$ diffusion beats advection by a factor $\sim (h/r)^{-1} \gg 1$. Defining the magnetic Prandtl number $P_m = v/\eta$ as the ratio of the turbulent viscosity to the turbulent resistivity, we would then expect that in steady-state [264],

$$\frac{B_{rs}}{B_z} \sim \frac{h}{r} P_m. \quad (118)$$

This argument is the origin of the claim that *thin disks do not drag in external magnetic fields*. It suggests that obtaining enough field line bending to launch a magneto-centrifugal wind ought to be hard, and that whatever primordial flux the disk is born with may be able to escape easily.

The physical arguments given above are robust, but a number of authors have emphasized that the calculation of the transport velocities that enter into equation (115) involves some subtleties [311, 261, 164, 165, 398]. The key point is that the viscosity and resistivity that enter into the equation for flux transport should not be computed as density-weighted vertical averages, but rather (in the case of the induction equation) as conductivity-weighted averages [164]. This makes a large difference for protoplanetary disks, where the conductivity is both generally low, and highest near the disk surface where the density is small. The derived transport velocities are, moreover, functions of the poloidal field strength, in the sense that diffusion becomes relatively less efficient as the field strength decreases. It should be noted that none of the flux transport calculations fully includes all of the MHD effects expected to be present in protoplanetary disks (see §5.4.3). It seems possible, though, that the variable efficiency of flux diffusion could simultaneously allow,

- For rapid flux loss from the relatively strongly magnetized disks formed from star formation [250], averting overly rapid wind angular momentum loss that would be inconsistent with observed disk lifetimes.
- For convergence toward a weak but non-zero net poloidal flux (possibly with a ratio of thermal to poloidal field magnetic pressure at the mid-plane $\beta \sim 10^4 - 10^7$) later in the disk lifetime [165].

As we will discuss in the next section, poloidal field strengths in roughly this range are of interest for their role in stimulating MHD instabilities within weakly ionized disks, so this is a speculative but interesting scenario.

- Isolated protoplanetary disks are expected to evolve under a combination of (i) internal redistribution of angular momentum, often referred to informally as viscosity, (ii) mass loss due to accretion and thermal winds, and (iii) mass and angular momentum loss in MHD winds. The relative importance of these processes for disk evolution is not clearly established.

- In the limit where local internal redistribution of angular momentum dominates, the disk surface density evolves according to a diffusion equation that matches the one derived for a viscous fluid. The viscosity in this equation must be interpreted as an effective viscosity resulting from a turbulent process.
- The use of the α prescription, and the extension of viscous models to complex non-axisymmetric geometries, are common and sometimes useful approximations. Neither, however, has a clear physical justification.
- The dissipation of accretion energy within the disk modifies its vertical temperature structure, and can lead to much higher mid-plane temperatures within a few AU of the star.
- Magnetic winds can be launched along sufficiently inclined field lines that thread the disk surface. The long-term evolution of such winds depends upon the efficiency of magnetic flux transport relative to gas accretion.

5 Turbulence

Turbulence within protoplanetary disks is important for two independent reasons. First, if it is strong enough and has the right properties, it could account for disk evolution by redistributing angular momentum much faster than molecular viscosity. Second, turbulence has its fingers in a plethora of planet formation processes, ranging from the collision velocities of small particles [315] to the formation of planetesimals [198] and the migration rate of low-mass planets [219]. For these reasons we would like to understand disk turbulence, even if (as is possible) it is not always responsible for disk evolution.

The first order of business when considering possibly turbulent fluid systems is usually to estimate the Reynolds number, which is a dimensionless measure of the relative importance of inertial and viscous forces. For a system with characteristic size L , velocity U , and (molecular) viscosity ν , the Reynolds number is defined as,

$$\text{Re} = \frac{UL}{\nu}. \quad (119)$$

There is no unique or “best” definition of U and L for protoplanetary disks, but whatever choice we make gives a very large number. For example, taking $L = h$ and $U = c_s$ then our estimate of the viscosity at 1 AU (equation 73) implies $\text{Re} \sim 10^{11}$. By terrestrial standards this is an enormous Reynolds number. Experiments on flow through pipes, for example — including those of Osborne Reynolds himself — show that turbulence is invariably present once $\text{Re} > 10^4$ [119]. If turbulence is present within protoplanetary disks there is no doubt that viscous forces will be negligible on large scales, and the turbulence will exhibit a broad inertial range.

Figure 16 lists some of the possible sources of turbulence within protoplanetary disks. It’s a long list! We can categorize the candidates according to various criteria,

- The physics involved in generating the turbulence. The simplest possibility (which appears unlikely) is that turbulence develops spontaneously in an isothermal, purely hydrodynamical shear flow. More complete physical models invoke entropy gradients, disk self-gravity or magnetic fields as necessary elements for the origin of turbulence.
- The origin of the free energy that sustains the turbulence, which could be the radial or vertical shear, heating from the star, or velocity differences between gas and solid particles.
- The character of the instabilities proposed to initiate turbulence from an initially non-turbulent flow. *Linear* instabilities grow exponentially from arbitrarily small perturbations, while *non-linear* instabilities require a finite amplitude disturbance. Demonstrating the existence of linear instabilities is relatively easy, whereas proving that a fluid system is non-linearly stable is very hard.
- The species involved. In this section we concentrate on instabilities present in purely gaseous disks; additional instabilities are present once we consider how gas interacts aerodynamically with its embedded solid component (§7.3).

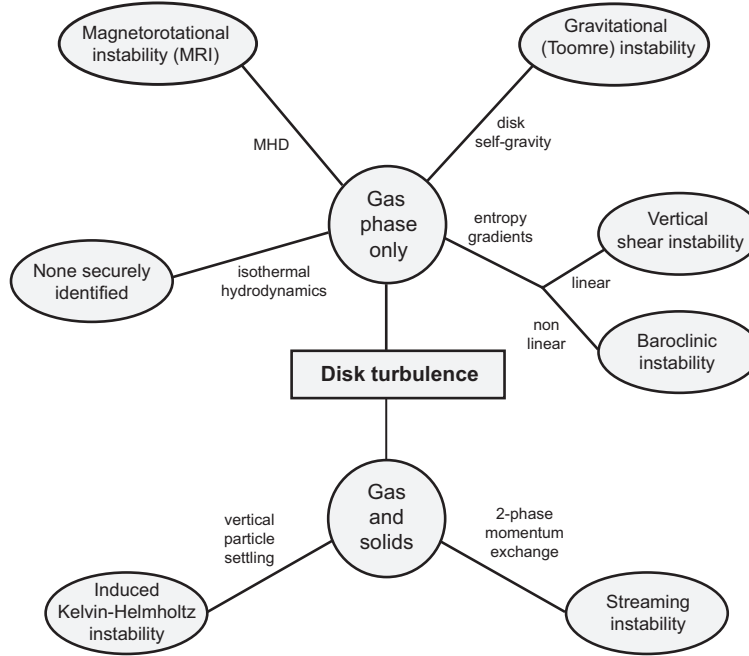


Fig. 16 A menu of the leading suspects for creating turbulence within protoplanetary disks.

Figure 17 illustrates the dominant fluid motions or forces involved in some of the most important disk instabilities.

For each candidate instability we would like to know the disk conditions under which it would be present, its growth rate, and the strength and nature of the turbulence that eventually develops. For disk evolution we are particularly interested in how efficiently the turbulence transports angular momentum (normally characterized by an effective α). In most cases the efficiency of transport can only be determined using numerical simulations, whose fluctuating velocity and magnetic fields can be analyzed to determine α via the relation [45],

$$\alpha = \left\langle \frac{\delta v_r \delta v_\phi}{c_s^2} - \frac{B_r B_\phi}{4\pi \rho c_s^2} \right\rangle_\rho, \quad (120)$$

where the angle brackets denote a density weighted average over space (and time, in some instances). The first term in this expression is the Reynolds stress from correlated fluctuations in the radial and perturbed azimuthal velocity, the second term is the Maxwell stress from MHD turbulence. We speak of the stress as being “turbulent” if the averages in the above relation are dominated by contributions from small spatial scales. It is also possible for a disk to sustain large scale stresses — for example at some radius we might have non-zero *mean* radial and azimuthal magnetic fields — which are normally described as being “laminar”. Note that it is

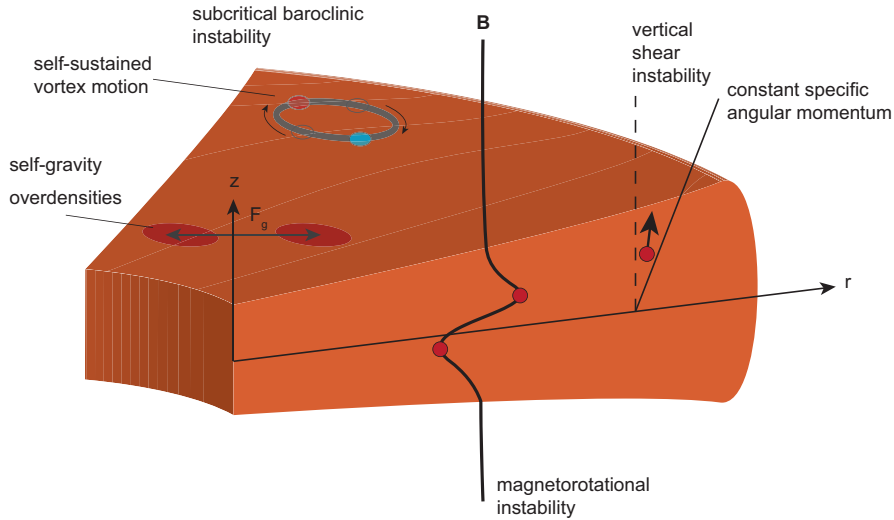


Fig. 17 A summary of the most important instabilities that can be present in protoplanetary disks. *Self-gravity* is important for sufficiently massive and cold disks. It leads to spiral arms and gravitational torques between regions of over-density. The *magnetorotational instability* occurs whenever a weak magnetic field is sufficiently coupled to differential rotation. The magnetic field acts to couple fluid elements at different radii, leading to an instability that can sustain MHD turbulence and angular momentum transport. The *vertical shear instability* feeds off the vertical shear that is set up in disks with realistic temperature profiles. It is a linear instability characterized by near-vertical growing modes. The *subcritical baroclinic instability* is a non-linear instability that operates in the presence of a sufficiently steep radial entropy gradient. It resembles radial convection, and leads to self-sustained vortices within the disk.

possible for the velocity field to exhibit turbulence on small scales even if the stress is dominated by large scale contributions.

5.1 Hydrodynamic turbulence

The dominant motion in protoplanetary disks is Keplerian orbital motion about a central point mass. Simplifying as much as possible, we first ask whether, in the absence of magnetic fields⁹, the radial shear present in a low-mass disk would be unstable to the development of turbulence. We first consider (rather unrealistically) a radially isothermal disk, where according to equation (28) there is no *vertical* shear. We then turn to the more general case where the temperature varies with

⁹ Ignoring magnetic fields in astrophysical accretion flows is generally a stupid thing to do, and indeed there is broad consensus that the magnetorotational instability (MRI) [45] is responsible for turbulence and angular momentum transport in most accretion disks. In protoplanetary disks, however, the low ionization fraction means that the dominance of MHD instabilities is much less obvious, and purely hydrodynamic effects could in principle be important.

radius, giving rise both to vertical shear and qualitatively distinct possibilities for instability.

5.1.1 Linear and non-linear stability

The linear stability of a shear flow with a smoothly varying $\Omega(r)$ against axisymmetric perturbations is given by Rayleigh’s criterion (this is derived in most fluids textbooks, see e.g. [343]). The flow is stable if the specific angular momentum increases with radius,

$$\frac{dl}{dr} = \frac{d}{dr} (r^2 \Omega) > 0 \rightarrow \text{stability}. \quad (121)$$

A Keplerian disk has $l \propto \sqrt{r}$ and is linearly stable.

There is no mathematical proof of the non-linear stability of Keplerian shear flow, but nor is there any known instability. The apparently analogous cases of pipe flow and Cartesian shear flows — which are linearly stable but undergo non-linear transitions to turbulence — are in fact sufficiently different problems as to offer no guidance [45]. There are analytic and numerical arguments against the existence of non-linear instabilities [46], which although not decisive [350] essentially rule out the hypothesis that a non-linear instability could result in *astrophysically interesting* levels of turbulence [242]. The same conclusion follows from laboratory experiments that have studied the stability of quasi-Keplerian rotation profiles in Taylor-Couette experiments [120]. One caveat is that laboratory experiments, and most theoretical work, consider the stability of unstratified cylindrical shear flows. Marcus and collaborators have identified a new instability (of a distinct character, related to the existence of locations in the flow known as critical layers, for a review of this physics see [286]) that can arise when the vertical stratification present in disks is included [278, 277]. The existence of this instability, which leads to self-replication of vortices, has been reproduced independently [246], and also shown to depend upon the radiative properties of the disk. Conditions in most regions of protoplanetary disks do not appear especially propitious for it to play a major role, but investigations remain in their infancy at the time of writing.

5.1.2 Entropy-driven instabilities

A separate class of purely hydrodynamic instabilities (no self-gravity, no magnetic fields) are what might loosely be called “entropy-driven” instabilities, in that they rely on the existence of a non-trivial temperature structure. The prototypical entropy-driven instability is of course convection, which could occur in the vertical direction if dissipation (associated with the physical process behind angular momentum transport) sets up an unstable entropy profile. This is evidently only conceivable in the region where viscous dissipation dominates, as irradiation prefers a nearly isothermal vertical structure. Even there, convective turbulence in disks is less efficient at transporting angular momentum than it is in transporting heat [243],

and this disparity creates a formidable barrier to creating consistent models in which convection is the primary source of disk turbulence. Convection may still be present in some regions of disks, perhaps especially at high accretion rates, but as a byproduct of independent angular momentum transport processes (for an example in dwarf novae, see [184]).

A disk that has a radial temperature gradient necessarily has vertical shear (equation 28). The free energy associated with the vertical shear can be accessed via the vertical shear instability (VSI) analyzed by Nelson, Gressel & Umurhan [303]. The VSI is a disk application of the Goldreich-Schubert-Fricke instability [156, 140] of rotating stars, and was proposed as a source of protoplanetary disk transport by Urpin & Brandenburg [419]¹⁰. The VSI is a linear instability with a maximum growth rate that is of the order of $h\Omega_K$ [253], but which is strongly dependent on the radiative properties of the disk. The reason is that to access the free energy in the vertical shear requires vertical fluid displacements, which are easy in the limit that the disk is strictly vertically isothermal but strongly suppressed if it is stably stratified. The local *cooling time* of the fluid is thus a critical parameter, and the VSI will only operate in regions of the disk where radiative cooling and heating processes result in a cooling time that is the same or shorter than the dynamical time Ω_K^{-1} . This, in practice, restricts the application of the VSI to specific radii that depend upon the disk structure (Lin & Youdin suggest 5-50 AU [253], Malygin et al. 15-180 AU [274]), and limits its effectiveness if the dust opacity is reduced (due to coagulation into large particles). Under the right conditions, however, numerical simulations suggest that the VSI can generate relatively small but possibly significant levels of transport, with both Nelson et al. [303] and Stoll & Kley [391] finding α of a few $\times 10^{-4}$.

The radial entropy gradient may itself be unstable. The simplest instability would be radial convection (a linear instability). For a disk with pressure profile $P(r)$, density profile $\rho(r)$, and adiabatic index γ , we define the Brunt-Väisälä frequency,

$$N_r^2 = -\frac{1}{\gamma\rho} \frac{dP}{dr} \frac{d}{dr} \ln\left(\frac{P}{\rho^\gamma}\right). \quad (122)$$

The Solberg-Høiland criterion indicates that a Keplerian disk is convectively unstable if,

$$N_r^2 + \Omega_K^2 < 0. \quad (123)$$

Protoplanetary disks never (or at least almost never) have a steep enough profile of entropy to meet this condition, so radial convection will not set in. A different instability (the subcritical baroclinic instability, SBI) is possible, however, if the weaker condition $N_r^2 < 0$ (which is just the Schwarzschild condition for non-rotating convection) is satisfied [331, 332, 245]. The SBI, which is likely related to observations of vortex formation in earlier numerical simulations [217], is a non-linear instability that can be excited by finite amplitude perturbations. (Confusingly, it is unrelated to the linear “baroclinic instability” studied in planetary atmospheres.) The SBI relies

¹⁰ As we shall see, a general rule is that all disk instabilities have long histories and pre-histories.

on radial buoyancy forces to sustain vortical motion via baroclinic driving. This type of effect is possible in disks in which surfaces of constant density are not parallel to surface of constant pressure. Mathematically, for a fluid with vorticity $\boldsymbol{\omega} = \nabla \times \mathbf{v}$, we can take the curl of the momentum equation to get an equation for the vortensity $\boldsymbol{\omega}/\rho$,

$$\frac{D}{Dt} \left(\frac{\boldsymbol{\omega}}{\rho} \right) = \left(\frac{\boldsymbol{\omega}}{\rho} \right) \cdot \nabla \mathbf{v} - \frac{1}{\rho} \nabla \left(\frac{1}{\rho} \right) \times \nabla P. \quad (124)$$

The baroclinic term, which for the SBI is responsible for generating and maintaining vorticity in the presence of dissipation, is the second term on the right hand side. The SBI, as with the VSI, is sensitive to the cooling time [245, 346], in this case because the baroclinic driving depends on the disk neither cooling too fast (which would eliminate the buoyancy effect) nor too slow (which would lead to constant temperature around the vortex). In compressible simulations, Lesur & Papaloizou [245] found that under favorable disk conditions the SBI could lead to outward transport of angular momentum with $\alpha \sim 10^{-3}$.

5.2 Self-gravity

A disk is described as *self-gravitating* if it is unstable to the growth of surface density perturbations when the gravitational force between different fluid elements in the disk is included along with the force from the central star. For a disk with sound speed c_s , surface density Σ and angular velocity Ω (assumed to be *close* to Keplerian) a linear analysis (for textbook treatments, see e.g. [17, 343]) shows that a disk becomes self-gravitating when the Toomre Q [407],

$$Q \equiv \frac{c_s \Omega}{\pi G \Sigma} < Q_{\text{crit}}, \quad (125)$$

where $Q_{\text{crit}} \sim 1$. We can deduce this result informally using an extension of the time scale argument that gives the thermal Jeans mass. We first note that pressure will prevent the gravitational collapse of a clump of gas, on scale Δr , if the sound-crossing time $\Delta r/c_s$ is shorter than the free-fall time $\sqrt{\Delta r^3/G\Delta r^2\Sigma}$. (We're ignoring factors of 2, π and so on.) Equating these time scales gives the minimum scale that might be vulnerable to collapse as $\Delta r \sim c_s^2/G\Sigma$. On larger scales, collapse can be averted if the free-fall time is longer than the time scale on which radial shear will separate initially neighboring fluid elements. For a Keplerian disk this time scale is $\sim \Omega^{-1}$. If the disk is just on the edge of instability the minimum collapse scale set by pressure support must equal the maximum collapse scale set by shear. Imposing this condition for marginal stability we obtain $c_s \Omega/G\Sigma \sim 1$, in accord with the formal result quoted above.

To glean some qualitative insight into where a disk might be self-gravitating, consider a steady-state disk that is described by an α model in which the transport arises from some process *other* than self-gravity. Collecting some previous results,

the steady-state condition implies $v\Sigma = \dot{M}/3\pi$, the α prescription is $v = \alpha c_s h$, and hydrostatic equilibrium gives $h = c_s/\Omega$. Substituting into equation (125) we find,

$$Q = \frac{3\alpha c_s^3}{GM}. \quad (126)$$

Protoplanetary disks generically get colder (and hence have lower c_s) at larger distances from the star, and this is where self-gravity is most likely to be important.

The disk mass required for self-gravity to become important can be estimated. Ignoring radial gradients of all quantities, we write the disk mass $M_{\text{disk}} \sim \pi r^2 \Sigma$, and again use the hydrostatic equilibrium result $h = c_s/\Omega$. Equation (125) then gives,

$$\frac{M_{\text{disk}}}{M_*} > \left(\frac{h}{r}\right), \quad (127)$$

as the condition for instability. This manipulation of a local stability criterion into some sort of global condition is ugly, and begs the question of *where* in the disk M_{disk} and h/r should be evaluated. We can safely conclude, nonetheless, that for a typical protoplanetary disk with $(h/r) \simeq 0.05$ a disk mass of $10^{-2} M_*$ will not be self-gravitating, whereas one with $0.1 M_*$ may well be.

There are two possible outcomes of self-gravity in a disk,

- The disk may establish a (quasi) stable state, characterized globally by trailing spiral overdensities. Gravitational torques between different annuli in the disk *transport angular momentum* outward, leading to accretion.
- The pressure and tidal forces, which by definition are unable to prevent the onset of gravitational collapse, may never be able to stop it once it starts. In this case the disk *fragments* into bound objects, which interact with (and possibly accrete) the remaining gas.

Both possibilities are of interest. Angular momentum transport due to self-gravity may be dominant, at least on large scales, at early times while the disk is still massive. Fragmentation, which was once considered a plausible mechanism for forming the Solar System's giant planets [230], remains of interest as a way to form sub-stellar objects and (perhaps) very massive planets. Kratter & Lodato [226] review the physics of disk self-gravity in both the angular momentum transporting and fragmenting regimes. Here we summarize some mostly elementary arguments.

Gravity is a long-range force, and it is not at all obvious that we can deploy the machinery developed for viscous disks to study angular momentum transport in a self-gravitating disk. The transport could be largely non-local, driven for example by large-scale structures in the density field (such as bars) or by waves that transport energy and angular momentum a significant distance before dissipating [47]. There is no precise criterion for when self-gravitating transport can be described using a local theory, but numerical simulations indicate that this is a reasonable approximation for low-mass disks with $M_{\text{disk}}/M_* \approx 0.1$ [256, 103, 136, 387]. Transport in more massive disks, such as might be present during the Class 0 and Class I phases of star formation, cannot be described locally (for multiple reasons, e.g. [257, 412]).

In cases where a local description of the transport is valid, we can use a thermal balance argument to relate the efficiency of angular momentum transport to the cooling time. Adopting a one-zone model for the vertical structure, we define the thermal energy of the disk, per unit surface area, as,

$$U = \frac{c_s^2 \Sigma}{\gamma(\gamma - 1)}, \quad (128)$$

where c_s is the mid-plane sound speed and γ is the adiabatic index. The cooling time (analogous to the Kelvin-Helmholtz time for a star) is then,

$$t_{\text{cool}} = \frac{U}{2\sigma T_{\text{disk}}^4}, \quad (129)$$

where T_{disk} is the effective temperature. Equating the cooling rate, $Q_- = 2\sigma T_{\text{disk}}^4$, to the local viscous heating rate, $Q_+ = (9/4)\nu\Sigma\Omega^2$ (equation 91), and adopting the α -prescription (equation 76), we find,

$$\alpha = \frac{4}{9\gamma(\gamma - 1)} \frac{1}{\Omega t_{\text{cool}}}. \quad (130)$$

This relation, which is a general property of α disks quite independent of self-gravity, just says that a rapidly cooling disk needs efficient angular momentum transport if it to generate heat fast enough to remain in thermal equilibrium.

For most sources of angular momentum transport we are no more able to determine t_{cool} from first principles than we are α , so the above relation does not move us forward. Self-gravitating disks, however, have the unusual property that their Toomre Q , measured in the *saturated* (non-linear) state, is roughly constant and similar to the critical value Q_{crit} determined from *linear* theory. This property arises, roughly speaking, because the direct dependence of the linear stability criterion on temperature (via c_s) invites a stabilizing feedback loop — a disk that cools so that $Q < Q_{\text{crit}}$ is more strongly self-gravitating, and produces more heating, while one that heats so that $Q > Q_{\text{crit}}$ shuts off the instability. It is therefore reasonable to assume that a self-gravitating disk that does not fragment maintains itself close to marginal stability, as conjectured by Paczynski [323].

If we assume that $Q = Q_0$ exactly (where Q_0 is some constant presumably close to Q_{crit}) then we have enough constraints to explicitly determine the functional form of α for a self-gravitating disk. Since Q depends on the mid-plane sound speed, $c_s = \sqrt{k_B T_c / \mu m_H}$, the condition of marginal stability directly gives us $T_c(\Sigma, \Omega)$,

$$T_c = \pi^2 Q_0^2 G^2 \left(\frac{\mu m_H}{k_B} \right) \frac{\Sigma^2}{\Omega^2}. \quad (131)$$

We can use this to determine t_{cool} , and from that α , with the aid of the vertical structure relations developed in §4.3. To keep things simple, we adopt an opacity,

$$\kappa_R = \kappa_0 T_c^2 \quad (132)$$

that is appropriate for ice grains, and assume the disk is optically thick. The opacity law, together with the relations for the optical depth, $\tau = (1/2)\Sigma\kappa_R$, and the mid-plane temperature, $T_c^4/T_{\text{disk}}^4 \simeq (3/4)\tau$, then leads to,

$$\alpha = \frac{64\pi^2 Q_0^2 G^2 \sigma}{27\kappa_0} \left(\frac{\mu m_H}{k_B} \right)^2 \Omega^{-3}, \quad (133)$$

which coincidentally (for this opacity law) is only a function of Ω . It may look cumbersome — and the numerical factors are *certainly* not to be trusted — but what we have shown is that for a locally self-gravitating disk α is simply a constant times a determined function of Σ and Ω . This result allows for the evolution of low-mass self-gravitating disks to be modeled as a pseudo-viscous process [247, 93, 347].

Self-gravity is typically important in protoplanetary disks at large radii, where irradiation is usually the dominant factor determining the disk's thermal state (except at high accretion rates). The generalization of the self-regulation argument given above is obvious; if irradiation is not so strong as to stabilize the disk on its own then viscous heating from the self-gravitating “turbulence” has to make up the difference. The partially irradiated regime of self-gravitating disks has been studied using local numerical simulations [354], and the analytic generalization for the effective α that results can be found in Rafikov [348].

Ignoring irradiation again (and trusting the numerical factors that we just said were not to be trusted) we can examine the implications of equation (133) for protoplanetary disks. Taking $Q_0 = 1.5$ and $\kappa_0 = 2 \times 10^{-4} \text{ cm}^2 \text{ g}^{-1} \text{ K}^{-2}$ [59] we find, across the region of the disk where ice grains would be the dominant opacity source, that,

$$\alpha \sim 0.3 \left(\frac{r}{50 \text{ AU}} \right)^{9/2}. \quad (134)$$

The steep radial dependence of the estimated self-gravitating α means that, unless all other sources of transport are *extremely* small, it will play no role in the inner disk. In the outer disk, on the other hand, we predict vigorous transport. The physical origin of the transport is density inhomogeneities that are caused by self-gravity, which become increasing large as α grows (explicitly, it is found [103] that the average fractional surface density perturbation $\delta\Sigma/\Sigma \propto \alpha^{1/2}$). Since even the linear threshold for gravitational instability implies that pressure forces can barely resist collapse, we expect that beyond some critical strength of turbulence a self-gravitating disk will be unable to maintain a steady-state. Rather, it will fragment into bound objects that are not (at least not immediately) subsequently sheared out or otherwise disrupted.

Our discussion up to this point might lead one to conjecture that the threshold for fragmentation could be written in terms of a critical dimensionless cooling time,

$$\beta_{\text{crit}} \equiv \Omega t_{\text{cool,crit}}, \quad (135)$$

or via a maximum α_{crit} that a self-gravitating disk can sustain without fragmenting (these are almost equivalent, but defining the threshold in terms of α incorporates

the varying compressibility as expressed through γ). Gammie [150], using local two dimensional numerical simulations, obtained $\beta_{\text{crit}} \simeq 3$ for a two-dimensional adiabatic index $\gamma = 2$. Early global simulations by Rice et al. [353], which were broadly consistent with Gammie’s estimate, implied a maximum effective transport efficiency $\alpha_{\text{crit}} \simeq 0.1$ [356].

The idea that the fragmentation threshold is uniquely determined by a single number is too simplistic. Several additional physical effects matter. First, fragmentation requires that collapsing clumps can radiate the heat generated by adiabatic compression. There is therefore a dependence not just on the magnitude of the opacity, but also on how it scales with density and temperature [205, 102]. Second, if we view fragmentation as requiring a critical over-density in a random turbulent field there should be a time scale dependence, with statistically rarer fluctuations that lead to collapse becoming probable the longer we wait [320]. (This introduces an additional implicit dependence on γ , because the statistics of turbulent density fields depend upon how compressible the gas is [128].) Finally, disks can be prompted to fragment not only if they cool too quickly, but also if they accrete mass faster than self-gravity can transport it away. This regime is clearly relevant for Class 0 and Class I disks, where envelope accretion is ongoing. Accretion-induced fragmentation appears inevitable for very massive disks, where it would lead to binary formation [227].

In addition to these physical complexities, work by Meru & Bate [290] initiated a debate as to whether the critical cooling time scale derived from early simulations was robust. A number of simulations — run with both Smooth Particle Hydrodynamics (SPH) and grid-based methods — showed an increase in β_{crit} at higher numerical resolution, with little or no evidence for convergence. Recent work has revisited the problem using a Godunov-type mesh-free Lagrangian hydrodynamics scheme as implemented within the GIZMO code [188]. The use of a Riemann solver allows for significantly less numerical dissipation compared to SPH (which is also mesh-free and Lagrangian), which appears to be at the root of the convergence problem. Using GIZMO, Deng et al. [109] obtain a converged estimate $\beta_{\text{crit}} \approx 3$ from global simulations of isolated self-gravitating disks with a disk-to-star mass ratio of 0.1. Baehr et al. [30] obtain the same threshold value from local three-dimensional simulations at high resolution. The fact that the most recent work largely agrees with the earliest relatively crude simulations, but not with the assuredly better calculations carried out in the intervening years, appears to be coincidental.

We can combine numerical estimates of α_{crit} with the formula for $\alpha(r)$ (equation 134) to determine where isolated protoplanetary disks ought to be vulnerable to fragmentation. For a Solar mass star, fragmentation is expected beyond $r \sim 10^2$ AU [287, 93, 347], with an uncertainty in that estimate of perhaps a factor of two. In most (but perhaps not all) cases, it is expected that the disk conditions that allow fragmentation would lead to objects with masses in the brown dwarf regime, or above [228].

5.3 *Magnetohydrodynamic turbulence and transport*

The Rayleigh stability criterion (equation 121) applies to a fluid disk. It does not apply to a disk containing even an arbitrarily weak magnetic field, if that field is perfectly coupled to the gas (the regime of ideal MHD). In ideal MHD a weakly magnetized disk has entirely different stability properties from an unmagnetized one, and is unstable provided only that the angular velocity decreases outward. This is the magnetorotational instability (MRI) [44, 45], which is accepted as the dominant source of turbulence in well-ionized accretion disks (winds could still contribute to or dominate angular momentum loss). In protoplanetary disks the ideal MHD version of the MRI applies only in the thermally ionized region close to the star; across most of the disk we also need to consider both the dissipative (Ohmic diffusion, ambipolar diffusion) and the non-dissipative (the Hall effect) effects of non-ideal MHD. The Ohmic and ambipolar terms can be considered as modifying — albeit very dramatically — the ideal MHD MRI, while the Hall term introduces new effects (in part) via the Hall shear instability [231], which is a different beast unrelated to the ideal MHD MRI. The phenomenology of disk instabilities in non-ideal MHD is rich, and appears to give rise to both turbulent and laminar angular momentum transport as well as phenomena, such as MHD disk winds, that may be observable.

5.4 *The magnetorotational instability*

The MRI [44] is an instability of cylindrical shear flows that contain a weak (roughly, if the field is vertical, sub-thermal) magnetic field¹¹. In ideal MHD the condition for instability is simply that,

$$\frac{d\Omega^2}{dr} < 0. \quad (136)$$

The fact that this condition is always satisfied in disks (though not in star-disk boundary layers) accounts for the MRI's central role in modern accretion theory.

Figure 18 illustrates what is going on to destabilize a disk that contains a magnetic field. A basically vertical field is slightly perturbed radially, so that it links fluid elements in the disk at different radii. Because of the shear in the disk, the fluid closer to the star orbits faster than the fluid further out, creating a toroidal field component out of what was initially just vertical and radial field. The tension in the magnetic field linking the two elements (which can be thought of, even mathematically, as being analogous to a stretched spring) imparts azimuthal forces to both the inner fluid (in the direction *opposite* to its orbital motion) and the outer fluid (*along*

¹¹ The mathematics of the MRI was worked out by Velikhov [424] and Chandrasekhar [85] around 1960. Thirty years passed before Balbus & Hawley [44] recognized the importance of the instability for accretion flows.

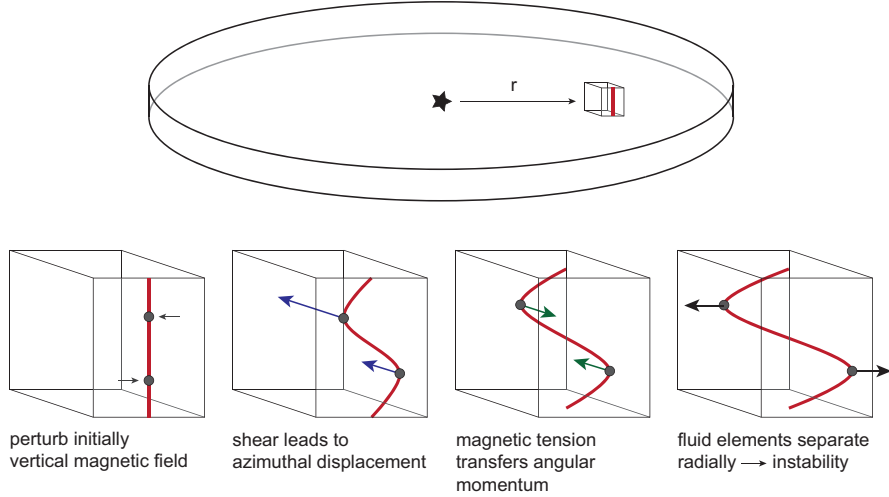


Fig. 18 Illustration showing why a weak vertical magnetic field destabilizes a Keplerian disk (the *magnetorotational instability* [45]). An initially uniform vertical field (weak enough that magnetic tension is not dominant) is perturbed radially. Due to the shear in the disk, an inner fluid element coupled to the field advances azimuthally faster than an outer one. Magnetic tension along the field line then acts to *remove* angular momentum from the inner element, and *add* angular momentum to the outer one. This causes further radial displacement, leading to an instability.

its orbital motion). The tension force thus reduces the angular momentum of the inner fluid element, and increases that of the outer element. The inner fluid then moves further inward (and the outer fluid further outward) and we have an instability.

We can derive the MRI instability condition in a very similar setup as Figure 18. Consider a disk with a power-law angular velocity profile, $\Omega \propto r^{-q}$, that is threaded by a uniform vertical magnetic field B_0 . We ignore any radial or vertical variation in density (and consistent with that, ignore the vertical component of gravity) and adopt an isothermal equation of state, $P = \rho c_s^2$, with c_s a constant. Our task is to determine whether infinitesimal perturbations to this equilibrium state are stable, or whether instead they grow exponentially with time, signaling a linear instability.

To proceed (largely following [141]) we define a locally Cartesian patch of disk that corotates at radius r_0 , where the angular frequency is Ω_0 . The Cartesian coordinates (x, y, z) are related to cylindrical co-ordinates (r, ϕ, z') via,

$$\begin{aligned} x &= r - r_0, \\ y &= r_0 \phi, \\ z &= z'. \end{aligned} \tag{137}$$

The local “shearing-sheet” (or in three dimensions, “shearing box”) model is useful for both analytic stability studies, and for numerical simulations [173, 239]. In this co-rotating frame, the equations of ideal MHD pick up terms representing the fictitious Coriolis and centrifugal forces,

$$\begin{aligned}
\frac{\partial \rho}{\partial t} + \nabla \cdot (\rho \mathbf{v}) &= 0, \\
\frac{\partial \mathbf{v}}{\partial t} + (\mathbf{v} \cdot \nabla) \mathbf{v} &= -\frac{1}{\rho} \nabla P + \frac{1}{4\pi\rho} (\nabla \times \mathbf{B}) \times \mathbf{B} - 2\Omega_0 \times \mathbf{v} + 2q\Omega_0^2 x \hat{\mathbf{x}}, \\
\frac{\partial \mathbf{B}}{\partial t} &= \nabla \times (\mathbf{v} \times \mathbf{B}).
\end{aligned} \tag{138}$$

Here $\hat{\mathbf{x}}$ is a unit vector in the x -direction. As noted above, the initial equilibrium has uniform density, $\rho = \rho_0$, and a magnetic field $\mathbf{B} = (0, 0, B_0)$. There are no pressure or magnetic forces, so the velocity field is determined by a balance between the Coriolis and centrifugal terms,

$$2\Omega_0 \times \mathbf{v} = 2q\Omega_0^2 x \hat{\mathbf{x}}. \tag{139}$$

The equilibrium velocity field that completes the definition of the initial state is,

$$\mathbf{v} = (0, -q\Omega_0 x, 0), \tag{140}$$

which has a linear shear (with $q = 3/2$ for a Keplerian disk) around the reference radius r_0 .

To assess the stability of the equilibrium, we write the density, velocity and magnetic field as the sum of their equilibrium values plus a perturbation. We can recover the MRI with a particularly simple perturbation which depends on z and t only¹². For the velocity components, for example, we write,

$$\begin{aligned}
v_x &= v'_x(z, t), \\
v_y &= -q\Omega_0 x + v'_y(z, t), \\
v_z &= v'_z(z, t),
\end{aligned} \tag{141}$$

and do likewise for the density and magnetic field. We substitute these expressions into the continuity, momentum and induction equations, and discard any terms that are quadratic in the primed variables, assuming them to be *small* perturbations. This would give us seven equations in total (one from the continuity equation, and three each from the other equations), but the x and y components of the momentum and induction equations are all we need to derive the MRI. The relevant linearized equations are,

$$\begin{aligned}
\frac{\partial v'_x}{\partial t} &= \frac{B_0}{4\pi\rho_0} \frac{\partial B'_x}{\partial z} + 2\Omega_0 v'_y, \\
\frac{\partial v'_y}{\partial t} - q\Omega_0 v'_x &= \frac{B_0}{4\pi\rho_0} \frac{\partial B'_y}{\partial z} - 2\Omega_0 v'_x,
\end{aligned}$$

¹² An analysis that retains the x -dependence can be found in the original Balbus & Hawley (1991) paper [44], and follows an essentially identical approach. Studying the stability of non-axisymmetric perturbations (in y), however, requires a different and more involved analysis [104, 312, 403, 330].

$$\begin{aligned}\frac{\partial B'_x}{\partial t} &= B_0 \frac{\partial v'_x}{\partial z}, \\ \frac{\partial B'_y}{\partial t} &= B_0 \frac{\partial v'_y}{\partial z} - q\Omega_0 B'_x.\end{aligned}\quad (142)$$

We convert these linearized differential equations into algebraic equations by taking the perturbations to have the form, e.g.,

$$B'_x = \bar{B}'_x e^{i(\omega t - kz)}, \quad (143)$$

where ω is the frequency of a perturbation with vertical wave-number k . The time derivatives then pull down a factor of $i\omega$, while the spatial derivatives become ik . Our four equations simplify to,

$$\begin{aligned}i\omega v'_x &= -ik \frac{B_0 B'_x}{4\pi\rho_0} + 2\Omega_0 v'_y, \\ i\omega v'_y &= -ik \frac{B_0 B'_y}{4\pi\rho_0} + (q-2)\Omega_0 v'_x, \\ i\omega B'_x &= -ik B_0 v'_x, \\ i\omega B'_y &= -ik B_0 v'_y - q\Omega_0 B'_x.\end{aligned}\quad (144)$$

(We've dropped the bars on the variables for clarity.) Eliminating the perturbation variables from these equations, we finally obtain the *MRI dispersion relation*,

$$\omega^4 - \omega^2 [2k^2 v_A^2 + 2(2-q)\Omega_0^2] + k^2 v_A^2 [k^2 v_A^2 - 2q\Omega_0^2] = 0, \quad (145)$$

where $v_A^2 = B_0^2/(4\pi\rho_0)$ is the Alfvén speed associated with the net field.

If $\omega^2 > 0$ then ω itself will be real and the perturbation $e^{i\omega t}$ will oscillate in time. Instability requires $\omega^2 < 0$, since in this case ω is imaginary and the perturbation will grow exponentially. Solving the dispersion relation we find the instability criterion is,

$$(kv_A)^2 - 2q\Omega_0^2 < 0. \quad (146)$$

Letting the field strength go to zero ($B_z \rightarrow 0$, $v_A \rightarrow 0$) we find that the condition for instability is simply that $q > 0$, i.e. that the angular velocity decrease outward. Even for an arbitrarily weak field, the result is completely different from Rayleigh's for a strictly hydrodynamic disk.

The growth rate of the instability and what it means for the magnetic field to be “weak” can also be derived from equation (145). Specializing to a Keplerian rotation law with $q = 3/2$ the dispersion relation takes the form shown in Figure 19. For a fixed magnetic field strength (and hence a fixed Alfvén speed v_A) the flow is unstable for wavenumbers $k < k_{\text{crit}}$ (i.e. on large enough spatial scales), where,

$$k_{\text{crit}} v_A = \sqrt{3}\Omega_0. \quad (147)$$

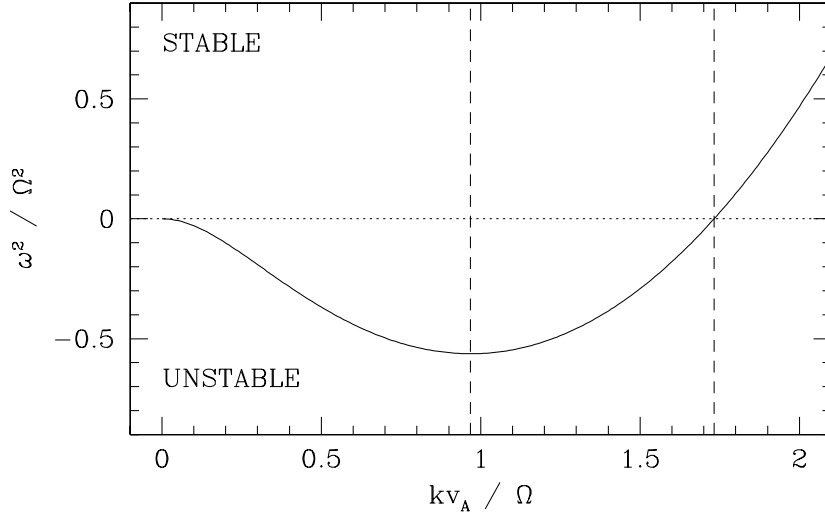


Fig. 19 The unstable branch of the MRI dispersion relation is plotted for a Keplerian rotation law. The flow is unstable ($\omega^2 < 0$) for all spatial scales smaller than $kv_A < \sqrt{3}\Omega$ (rightmost dashed vertical line). The most unstable scale (shown as the dashed vertical line at the center of the plot) is close to $kv_A \simeq \Omega$.

As the magnetic field becomes stronger, the *smallest* scale $\lambda = 2\pi/k_{\text{crit}}$ which is unstable grows, until eventually it exceeds the disk's vertical extent $\approx 2h$. For stronger vertical fields no unstable MRI modes fit within the disk, and the instability is suppressed. Using $h = c_s/\Omega$, the condition that the vertical magnetic field is weak enough to admit the MRI (i.e. that $\lambda < 2h$) becomes

$$B_0^2 < \frac{12}{\pi} \rho c_s^2 \quad (148)$$

If we define the plasma β parameter as the ratio of gas to magnetic pressure,

$$\beta \equiv \frac{8\pi P}{B_0^2} \quad (149)$$

this condition can be expressed alternatively as,

$$\beta > \frac{2\pi^2}{3}. \quad (150)$$

A magnetic field whose *vertical* component approaches equipartition with the thermal pressure ($\beta \sim 1$) will be too strong to admit the existence of linear MRI modes, but a wide range of weaker fields are acceptable.

The maximum growth rate is determined by setting $d\omega^2/d(kv_A) = 0$ for the unstable branch of the dispersion relation plotted in Figure 19. The most unstable scale for a Keplerian disk is,

$$(kv_A)_{\max} = \frac{\sqrt{15}}{4}\Omega_0, \quad (151)$$

where the growth rate is,

$$|\omega_{\max}| = \frac{3}{4}\Omega_0. \quad (152)$$

This result implies an *extremely* vigorous growth of the instability, with an exponential growth time scale that is a fraction of an orbital period. This means that if a disk is unstable to the MRI its growth rate will invariably be faster than that of hydrodynamic instabilities that may additionally be present. One cannot strictly be sure that, when several instabilities co-exist, the total angular momentum transport is dominated by the one with the fastest linear growth rate. Simulations, however, show that the MRI in the ideal MHD limit saturates to yield a turbulent state with a moderately high efficiency of angular momentum transport $\alpha \approx 0.02$ [107, 380]. It is likely to overwhelm plausible hydrodynamic sources of transport.

5.4.1 Non-ideal MHD

The MRI in its ideal MHD guise is relevant to protoplanetary disks only in the thermally ionized region close to the star (§3.3.1), where $T > 10^3$ K. The very weakly ionized gas further out is imperfectly coupled to the magnetic field, and this both modifies the properties of the MRI and leads to new MHD instabilities. We will begin by sketching the derivation of the non-ideal MHD equations (following Balbus [43], who justifies several of the approximations that we will make), and then estimate the magnitude of the extra terms that arise in protoplanetary disks.

The physics of how magnetic fields affect weakly-ionized fluids is easy to visualize. We consider a gas that is almost entirely neutral, with only a small admixture of ions and electrons (analogous considerations apply if the charge carriers are dust particles, but we will not go there). Magnetic fields exert Lorentz forces on the charged species, but not on the neutrals. Collisions between the neutrals and either the ions or the electrons lead to momentum exchange whenever the neutral fluid has a velocity differential with respect to the charged fluids.

We begin by considering the momentum equation. For the neutrals we have,

$$\rho \frac{\partial \mathbf{v}}{\partial t} + \rho(\mathbf{v} \cdot \nabla)\mathbf{v} = -\nabla P - \rho \nabla \Phi - p_{nl} - p_{ne}. \quad (153)$$

Here ρ , \mathbf{v} and P (without subscripts) refer to the neutral fluid, and p_{nl} and p_{ne} are the rate of momentum exchange due to collisions between the neutrals and the ions / electrons respectively. Identical equations apply to the charged species, but for the addition of Lorentz forces,

$$\begin{aligned}\rho_e \frac{\partial \mathbf{v}_e}{\partial t} + \rho_e (\mathbf{v}_e \cdot \nabla) \mathbf{v}_e &= -\nabla P_e - \rho_e \nabla \Phi - en_e \left(\mathbf{E} + \frac{\mathbf{v}_e \times \mathbf{B}}{c} \right) - p_{en}, \\ \rho_I \frac{\partial \mathbf{v}_I}{\partial t} + \rho_I (\mathbf{v}_I \cdot \nabla) \mathbf{v}_I &= -\nabla P_I - \rho_I \nabla \Phi + Zen_I \left(\mathbf{E} + \frac{\mathbf{v}_I \times \mathbf{B}}{c} \right) - p_{In}.\end{aligned}\quad (154)$$

In these equations \mathbf{E} and \mathbf{B} are the electric and magnetic fields, the ions have charge Ze , where $-e$ is the charge on an electron, and of course $p_{ne} = -p_{en}$ and $p_{nI} = -p_{In}$. Having three momentum equations looks complicated, but we can make a large simplification to the system by noting that the time scale for macroscopic evolution of the fluid is generally much longer than the time scale for collisional or magnetic forces to alter a charged particle's momentum. We can then ignore *everything* in the charged species' momentum equations, except for the Lorentz and collisional terms. For the ions we have,

$$Zen_I \left(\mathbf{E} + \frac{\mathbf{v}_I \times \mathbf{B}}{c} \right) - p_{In} = 0, \quad (155)$$

with a similar equation for the electrons. Imposing charge neutrality, $n_e = Zn_I$, we eliminate the electric field between the ion and electron equations to find an expression for the sum of the momentum transfer terms,

$$p_{In} + p_{en} = \frac{en_e}{c} (\mathbf{v}_I - \mathbf{v}_e) \times \mathbf{B}. \quad (156)$$

The current density $\mathbf{J} = en_e(\mathbf{v}_I - \mathbf{v}_e)$, so we can write this as,

$$p_{In} + p_{en} = \frac{\mathbf{J} \times \mathbf{B}}{c}. \quad (157)$$

Finally, we go to Maxwell's equations, and note that the current can be written as,

$$\frac{4\pi}{c} \mathbf{J} = \nabla \times \mathbf{B} + \frac{1}{c} \frac{\partial \mathbf{E}}{\partial t}. \quad (158)$$

The second term in Maxwell's equation is the displacement current, which is $\mathcal{O}(v^2/c^2)$ and consistently ignorable in non-relativistic MHD. Doing so, we substitute equation (157) in the neutral equation of motion to obtain,

$$\rho \frac{\partial \mathbf{v}}{\partial t} + \rho (\mathbf{v} \cdot \nabla) \mathbf{v} = -\nabla P - \rho \nabla \Phi + \frac{1}{4\pi} (\nabla \times \mathbf{B}) \times \mathbf{B}. \quad (159)$$

This is identical to the *ideal* MHD momentum equation (stated without derivation as equation 138) and pleasingly simple; we have reduced the three momentum equations to an equation for a single (neutral) fluid with a magnetic force term whose dependence on \mathbf{B} is independent of the make-up of the gas. As one might guess, the consistent simplification of non-ideal MHD to a momentum equation for a single fluid is not always possible. Roughly speaking it works provided that the plasma's inertia is negligible compared to that of the neutral fluid, the coupling between

charged and neutral species is strong, and the recombination time is short. Zweibel [451] gives an accessible account of the conditions necessary for a valid single-fluid description. Although some of the early analytic and numerical work on the MRI in weakly-ionized disks utilized a two-fluid approach [68, 174], in many protoplanetary disk situations a single fluid model is both justified [31] and substantially simpler. In the single fluid limit all of the complexities of non-ideal MHD enter only via the induction equation.

Deducing the non-ideal induction equation requires us to specify the form of the momentum coupling terms. Writing these in standard notation (which is different for the two terms, somewhat obscuring the symmetry),

$$\begin{aligned} p_{ne} &= n_e v_{ne} m_e (\mathbf{v} - \mathbf{v}_e), \\ p_{nI} &= \rho \rho_I \gamma (\mathbf{v} - \mathbf{v}_I), \end{aligned} \quad (160)$$

where v_{ne} is the collision frequency of an electron with the neutrals, and γ is called the drag-coefficient. The ion-neutral coupling involves longer-range interactions than the electron-neutral coupling, and is accordingly stronger [43].

We now go back to the force balance deduced from the electron momentum equation,

$$-en_e \left(\mathbf{E} + \frac{\mathbf{v}_e \times \mathbf{B}}{c} \right) - p_{en} = 0, \quad (161)$$

and attempt to write the terms involving \mathbf{v}_e and p_{en} entirely in terms of the current. We start with the exactly equivalent expression,

$$\mathbf{E} + \frac{1}{c} [\mathbf{v} + (\mathbf{v}_e - \mathbf{v}_I) + (\mathbf{v}_I - \mathbf{v})] \times \mathbf{B} + \frac{v_{ne} m_e}{e} [(\mathbf{v}_e - \mathbf{v}_I) + (\mathbf{v}_I - \mathbf{v})] = 0, \quad (162)$$

and deal with the terms in turn. We have two terms that involve $(\mathbf{v}_e - \mathbf{v}_I)$, which can be replaced immediately with the current,

$$(\mathbf{v}_e - \mathbf{v}_I) = -\frac{\mathbf{J}}{en_e}. \quad (163)$$

The first term with $(\mathbf{v}_I - \mathbf{v})$ is exactly equal to $p_{In}/(\rho \rho_I \gamma)$. If, however, $|p_{In}| \gg |p_{en}|$, then equation (157) implies that, approximately,

$$(\mathbf{v}_I - \mathbf{v}) \simeq \frac{\mathbf{J} \times \mathbf{B}}{c \rho \rho_I \gamma}. \quad (164)$$

Finally it can be shown (see Balbus [43] for details) that the final term with $(\mathbf{v}_I - \mathbf{v})$ can be consistently dropped. The version of Ohm's Law that we end up with is,

$$\mathbf{E} + \frac{\mathbf{v} \times \mathbf{B}}{c} - \frac{\mathbf{J} \times \mathbf{B}}{en_e c} + \frac{(\mathbf{J} \times \mathbf{B}) \times \mathbf{B}}{c^2 \rho \rho_I \gamma} - \frac{v_{ne} m_e}{e^2 n_e} \mathbf{J} = 0. \quad (165)$$

The non-ideal induction equation is then obtained by applying Faraday's law,

$$\nabla \times \mathbf{E} = -\frac{1}{c} \frac{\partial \mathbf{B}}{\partial t}, \quad (166)$$

to eliminate any explicit reference to the electric field. In its usual form,

$$\frac{\partial \mathbf{B}}{\partial t} = \nabla \times \left[\mathbf{v} \times \mathbf{B} - \eta \nabla \times \mathbf{B} - \frac{\mathbf{J} \times \mathbf{B}}{en_e} + \frac{(\mathbf{J} \times \mathbf{B}) \times \mathbf{B}}{c\gamma\rho_I} \right]. \quad (167)$$

We have defined the magnetic resistivity,

$$\eta = \frac{c^2}{4\pi\sigma} \quad (168)$$

where σ is (here) the electrical conductivity,

$$\sigma = \frac{e^2 n_e}{m_e \nu_{en}}. \quad (169)$$

As before we can replace the current with the magnetic field via,

$$\mathbf{J} = \frac{c}{4\pi} \nabla \times \mathbf{B}, \quad (170)$$

so that the induction equation is solely a function of \mathbf{B} . The terms on the right-hand-side are referred to as the inductive, Ohmic, Hall and ambipolar terms respectively.

The non-ideal terms in the induction equation depend upon the ionization state of the gas (through n_e and ρ_I) and upon the collision rates between the neutral and charged species (via η and γ). Standard values for these quantities are [68, 115]¹³,

$$\begin{aligned} \eta &= 234 \left(\frac{n}{n_e} \right) T^{1/2} \text{ cm}^2 \text{ s}^{-1}, \\ \gamma &= 3 \times 10^{13} \text{ cm}^3 \text{ s}^{-1} \text{ g}^{-1}. \end{aligned} \quad (171)$$

We are now ready to estimate the importance of the non-ideal terms in the environment of protoplanetary disks, and to ask what effect they have both on the MRI, and on the more general question of whether there is MHD turbulence or transport in disks.

¹³ Several assumptions are hardwired into these numbers. For the resistivity, it is assumed that currents are carried by the electrons, and that the conductivity is limited by electron-neutral collisions. For the drag coefficient we assume that the neutral gas is predominantly molecular hydrogen, and that the ions are moderately massive $m_i \simeq 30 - 40 m_H$. It would be prudent to consult Blaes & Balbus (1994) [68], and references therein, should one encounter situations where these assumptions might fail.

5.4.2 Ohmic, ambipolar and Hall physics in protoplanetary disks

The non-ideal terms in equation (167) all depend inversely on the electron or ion density, so the strength of all non-ideal MHD effects relative to the inductive term increases with smaller ionization fraction. The three terms also have different dependencies on density, magnetic field strength and temperature, so the *relative* ordering of the non-ideal MHD effects varies with these parameters.

The Ohmic, Hall and ambipolar terms have different dependencies on the magnetic field geometry, and in a disk setting they influence the MRI in distinct ways (most importantly, the Hall effect differs from the others in being non-dissipative). There is therefore no model-independent way to precisely demarcate when each term will affect disk evolution. As a first guess, however, we can treat the magnetic field as a scalar and simply take the ratio of the Hall to the Ohmic term and the ambipolar to the Hall term,

$$\begin{aligned}\frac{\text{H}}{\text{O}} &= \frac{cB}{4\pi e\eta n_e}, \\ \frac{\text{A}}{\text{H}} &= \frac{en_e B}{c\gamma\rho_I}.\end{aligned}\tag{172}$$

Since $\eta \propto (n/n_e)$ and $n_e \propto \rho_I$ both of these ratios depend on (B/n) . Substituting for η and γ , and taking the ion mass that enters into the ambipolar term as $30m_H$, we can estimate the magnetic field strength for which the Ohmic and Hall terms have equal magnitude, and similarly for the Hall and ambipolar terms,

$$\begin{aligned}B_{\text{O=H}} &\approx 0.5 \left(\frac{n}{10^{15} \text{ cm}^{-3}} \right) \left(\frac{T}{100 \text{ K}} \right)^{1/2} \text{ G}, \\ B_{\text{H=A}} &\approx 4 \times 10^{-3} \left(\frac{n}{10^{10} \text{ cm}^{-3}} \right) \text{ G}.\end{aligned}\tag{173}$$

Figure 20 shows these dividing lines in the (n, B) plane. Ohmic diffusion is dominant at high densities / low magnetic field strengths. Ambipolar diffusion dominates for low densities / high field strengths. The Hall effect is strongest for a fairly broad range of intermediate densities.

Estimating where protoplanetary disks fall in the (n, B) plane can be done in various ways. For a Solar System-motivated estimate we can start with the disk field inferred from laboratory measurements of chondrules in the Semarkona meteorite [144], which suggest that near the snow line ($r \simeq 3$ AU) the disk field was $B \simeq 0.5$ G. (There are caveats and a large systematic uncertainty associated with this measurement, all of which we ignore for now.) Let us assume that the surface density and temperature profiles are $\Sigma \propto r^{-3/2}$ and $T \propto r^{-1/2}$ respectively, and that the magnetic field pressure is the same fraction of the thermal pressure at all radii in the disk. Taking $\Sigma \simeq 300 \text{ g cm}^{-2}$ and $T = 150 \text{ K}$ at 3 AU, the inferred scalings of mid-plane density and magnetic field strength are then,

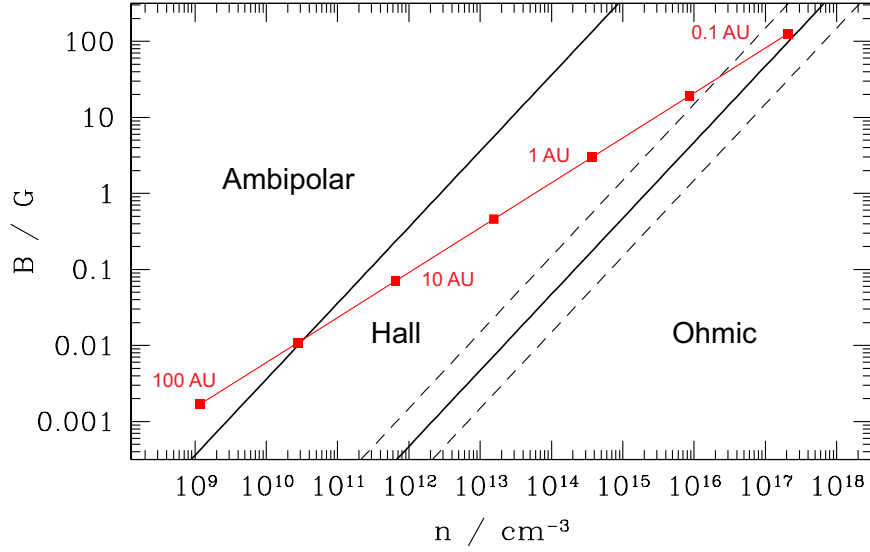


Fig. 20 Regions of the (n, B) parameter space in which different non-ideal terms are dominant. The boundary between the Ohmic and Hall regimes is plotted for $T = 100$ K (solid line) and also for temperatures of 10^3 K (upper dashed line) and 10 K (lower dashed line). The red line shows a very rough estimate of how the magnetic field in the disk might vary with density between the inner disk at 0.1 AU and the outer disk at 100 AU.

$$\begin{aligned}
 n &\approx 2 \times 10^{13} \left(\frac{r}{3 \text{ AU}} \right)^{-11/4} \text{ cm}^{-3}, \\
 B &\approx 0.5 \left(\frac{r}{3 \text{ AU}} \right)^{-13/8} \text{ G}.
 \end{aligned}
 \tag{174}$$

The track defined by these relations is plotted in Figure 20 for radii between 0.1 AU and 100 AU.

As we have emphasized, neither our approach to ranking the strength of the non-ideal terms, nor our estimate of the radial scaling of disk conditions, are anything more than crude guesses. Other approximations are equally valid (for example, one can order the terms in the (n, T) plane instead [48, 232, 19]). Nevertheless, because n and B vary by so many orders of magnitude across Figure 20 the critical inferences we can draw are quite robust. We predict that the Hall effect is the dominant non-ideal MHD process at the disk mid-plane between (conservatively) 1 AU and 10 AU. Ohmic diffusion can become important as we approach the thermally ionized region interior to 1 AU. Ambipolar diffusion dominates at sufficiently large radii, of the order of 100 AU, and in the lower density gas away from the mid-plane.

5.4.3 The dead zone

The linear stability of Keplerian disk flow in non-ideal MHD has been extensively investigated (see, e.g. [68, 197, 428, 48, 232, 110]), and the reader interested in the non-ideal analogs to the MRI dispersion relation derived as equation (145) should start there. Proceeding less formally, we follow Gammie [148] to estimate the conditions under which Ohmic dissipation (ignoring for now the Hall term) would damp the MRI. The basic idea is to compare the time scale on which the ideal MRI would generate tangled magnetic fields to that on which Ohmic diffusion would smooth them out. We first note that diffusion erases small-scale structure in the field more efficiently than large scale features, so that the appropriate comparison is between growth and damping of the largest scale MRI models. Starting from the MRI dispersion relation (equation 145), for a Keplerian disk we consider the weak-field / long wavelength limit ($kv_A/\Omega \ll 1$). The growth rate of the MRI is,

$$|\omega| \simeq \sqrt{3}kv_A. \quad (175)$$

Writing this as a function of the spatial scale $\lambda = 2\pi/k$, we have,

$$|\omega| \simeq 2\pi\sqrt{3}\frac{v_A}{\lambda}. \quad (176)$$

Up to numerical factors the MRI on a given scale then grows on the Alfvén crossing time. Equating this growth rate to the Ohmic damping rate,

$$|\omega_\eta| \sim \frac{\eta}{\lambda^2} \quad (177)$$

we conclude that Ohmic dissipation will suppress the MRI on the largest available scale $\lambda \approx h$ provided that,

$$\eta > 2\pi\sqrt{3}v_A h. \quad (178)$$

We can express this result in a different form. Analogous to the fluid Reynolds number (equation 119) the magnetic Reynolds number Re_M is defined as,

$$\text{Re}_M \equiv \frac{UL}{\eta} \quad (179)$$

where U is a characteristic velocity and L a characteristic scale. Taking $U = v_A$ and $L = h$ for a disk, the condition for Ohmic dissipation to suppress the MRI becomes

$$\text{Re}_M < 1 \quad (180)$$

where order unity numerical factors have been omitted.

We now convert the condition for the suppression of the MRI into a limit on the ionization fraction $x \equiv n_e/n$. We make use of the formula for the magnetic resistivity (equation 171) and assume that Maxwell stresses transport angular momentum, so that $\alpha \sim v_A^2/c_s^2$ (this follows approximately from equation 120). The magnetic

Reynolds number can then be estimated to be,

$$\text{Re}_M = \frac{v_A h}{\eta} = \frac{\alpha^{1/2} c_s^2}{\eta \Omega}. \quad (181)$$

Substituting for η and c_s^2 , the magnetic Reynolds number in a protoplanetary disk scales as,

$$\text{Re}_M \approx 1.4 \times 10^{12} x \left(\frac{\alpha}{10^{-2}} \right)^{1/2} \left(\frac{r}{1 \text{ AU}} \right)^{3/2} \left(\frac{T}{300 \text{ K}} \right)^{1/2} \left(\frac{M_*}{M_\odot} \right)^{-1/2}. \quad (182)$$

For the given parameters, the critical ionization fraction below which Ohmic diffusion will quench the MRI is

$$x_{\text{crit}} \sim 10^{-12}. \quad (183)$$

Clearly a very small ionization fraction suffices to couple the magnetic field to the gas and allows the MRI to operate, but there are large regions of the disk where even these ionization levels are not obtained and non-ideal effects are important.

Based on this analysis Gammie [148] noted, first, that the criterion for the MRI to operate under near-ideal MHD conditions in the inner disk coincides with the requirement that the alkali metals are thermally ionized (Figure 7). The development of magnetized turbulence in the disk at radii where $T > 10^3$ K can therefore be modeled in ideal MHD. Second, he proposed that Ohmic diffusion would damp MHD turbulence in the low ionization environment near the disk mid-plane on scales of the order of 1 AU, creating a *dead zone* of sharply reduced turbulence and transport. Gammie's original model is incomplete, as it did not include either ambipolar diffusion or the Hall effect, but the basic idea motivates much of the current work on MHD instabilities in disks.

5.4.4 Turbulence and transport in non-ideal MHD

Once we consider the full set of non-ideal terms, the first question is to assess the level of turbulence and transport that is expected as a function of their strengths. This is a well-defined but already difficult theoretical question, given that interesting values of the Ohmic, ambipolar and Hall terms span a broad range (depending physically on the temperature, density, ionization fraction and magnetic field strength). To define the problem in its most idealized form, we rewrite the non-ideal induction equation (167) as,

$$\frac{\partial \mathbf{B}}{\partial t} = \nabla \times \left[\mathbf{v} \times \mathbf{B} - \eta_O \nabla \times \mathbf{B} - \eta_H \frac{\mathbf{J} \times \mathbf{B}}{B} - \eta_A \frac{(\mathbf{J} \times \mathbf{B}) \times \mathbf{B}}{B^2} \right], \quad (184)$$

where *dimensionally* η_O , η_H and η_A are all diffusivities. There are different ways to construct dimensionless numbers from the diffusivities, but one useful set is,

$$\begin{aligned}
\Lambda_O &\equiv \frac{v_A^2}{\Omega \eta_O} \text{ (Ohmic Elsasser number),} \\
\text{Ha} &\equiv \frac{v_A^2}{\Omega \eta_H} \text{ (Hall Elsasser number),} \\
\text{Am} &\equiv \frac{v_A^2}{\Omega \eta_A} \text{ (ambipolar Elsasser number).} \tag{185}
\end{aligned}$$

(Note that the ambipolar Elsasser number can also be written as $\text{Am} \equiv \gamma \rho_I / \Omega$, which is the number of ion-neutral collisions per dynamical time Ω^{-1} .) We further specify the net vertical magnetic field (if any) via the ratio of the mid-plane gas and magnetic field pressures (equation 149),

$$\beta_z = \frac{8\pi P}{B_z^2}. \tag{186}$$

Our question can then be rephrased; what is the level of angular momentum transport and turbulence in an MHD disk at radii where the non-ideal terms are characterized by the dimensionless parameters (Λ_O , Ha, Am, β_z).

Ohmic diffusion acts as a strictly dissipative process that stabilizes disks to magnetic field instabilities on scales below some critical value. Ambipolar diffusion is in principle more complex, because it does not dissipate currents that are parallel to the magnetic field. This distinction substantially impacts the linear stability of ambipolar-dominated disks [232], but appears to matter less for the non-linear evolution, whose properties are analogous to Ohmic diffusion. For both dissipative processes, simulations show that MRI-driven turbulence is strongly damped when the relevant dimensionless parameter (either Λ_0 or Am) drops below a critical value that depends upon the initial field geometry but is $\sim 1 - 10^2$ [368, 416, 381, 38, 379]. Consistent with the dead zone idea [148], we therefore expect substantial modification of the properties of MHD turbulence both in the mid-plane around 1 AU (where Ohmic diffusion is the dominant dissipative process) and in the disk atmosphere and at large radii $\sim 10^2$ AU (where ambipolar diffusion dominates).

The MRI dispersion relation is also modified by the Hall effect [428, 48], which differs from the other non-ideal terms in that it modifies the field structure without any attendant dissipation. In this respect the Hall term most closely resembles the inductive term $\nabla \times (\mathbf{v} \times \mathbf{B})$, and its strength can usefully be characterized by the ratio of the Hall to the inductive term. Non-linear simulations of the Hall effect in disks, which were pioneered by Sano & Stone [369, 370], have only recently been able to access the strongly Hall-dominated regime relevant to protoplanetary disks [233, 241, 32, 33, 383]¹⁴. In vertically stratified disks with a net vertical field, Lesur et al. [241] find that the Hall effect has a controlling influence on disk dynamics

¹⁴ The numerical implementation of the Hall effect in simulation codes remains challenging, and the presence of large-scale fields in the saturated state suggests that local simulations may not be adequate to describe the outcome. Observationally important issues such as the level of fluid turbulence that accompanies the predominantly large-scale transport by Maxwell stresses remain to be fully understood.

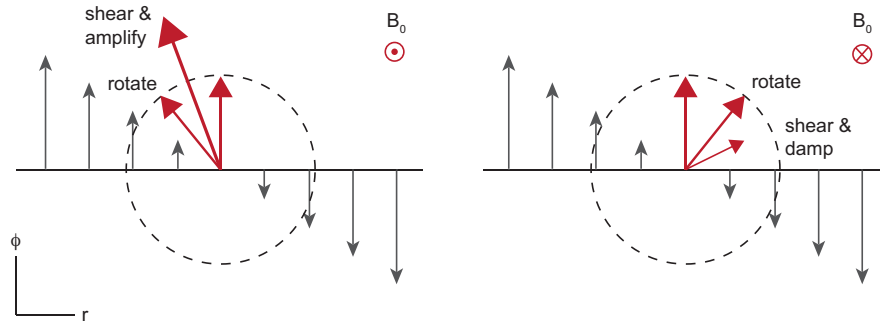


Fig. 21 An illustration (adapted from Kunz [231]) of the Hall shear instability. In the presence of a vertical field threading the disk, the Hall effect acts to rotate an initially toroidal field component either clockwise or anti-clockwise, depending upon the *sign* of the vertical field. The rotated field vector is then either amplified or damped by the shear. This instability differs from the MRI both technically (in that there is no reference to orbital motion, any shear flow suffices) and physically (via the dependence on the direction of the vertical magnetic field as well as its strength).

on scales between 1 AU and 10 AU. For $\beta_z = 10^5$ a strong but *laminar* Maxwell stress (i.e. one dominated by large-scale radial and toroidal fields in equation 120) results when the net field is aligned with the rotation axis of the disk, whereas anti-alignment leads to extremely weak turbulence and transport.

The results from Hall-MHD simulations of protoplanetary disks are best interpreted not as a modification of the MRI, but rather as the signature of a distinct *Hall shear instability* [231]. In the presence of a net vertical magnetic field the Hall effect acts to *rotate* magnetic field vectors lying in the orbital plane (Figure 21), with the sense of the rotation determined by whether the new field is aligned or anti-aligned to the rotation axis. In the aligned field case, the Hall-induced rotation allows the magnetic field to be amplified by the shear, while damping occurs in the anti-aligned limit. Unlike the MRI, the Hall shear instability does not depend on the Coriolis force, and is indifferent to the sign of the angular velocity gradient. By generating a radial field directly from an azimuthal one, the Hall effect (given a net field) supports a mean-field disk dynamo cycle [409, 241] that is qualitatively different from anything that is possible in ideal MHD.

Going beyond the idealized question of the effect of the non-ideal terms on turbulence and transport, our goal is to use the results described above to predict the structure and evolution of protoplanetary disks. This introduces new layers of uncertainty. To predict disk properties from first principles, we need at a minimum to know the strength of the different sources of ionization (§3.3.2), the rates of gas-phase and dust-induced recombination, and the global evolution of any net magnetic field (§4.5.1). We also need to model (or have good reasons to ignore) various non-MHD effects, including the hydrodynamic angular momentum transport processes already discussed and mass loss by photoevaporation [4] (§9). Given these uncertainties, the best that we can currently do is to highlight a number of qualitative predictions that receive support from numerical simulations:

- Net vertical magnetic fields are important for disk evolution. A vertical magnetic field enhances angular momentum transport by the MRI even in ideal MHD (roughly as $\alpha \propto \beta_z^{-1/2}$ [173]). In non-ideal MHD, local simulations by Simon et al. [379, 378] suggest that ambipolar damping of the MRI in the outer disk prevents resupply of the inner disk with gas *unless* a net field is present¹⁵. A net field with $\beta_z \simeq 10^4 - 10^5$ suffices, comparable to the fields expected in global models of flux evolution [165] but much weaker than the likely initial field left over from star formation. Accretion on scales of 30-100 AU occurs predominantly through a thin surface layer that is ionized by FUV photons [329, 379, 378], and is largely independent of the Hall effect [33].
- MHD winds and viscous transport can co-exist in disks. Local numerical simulations in ideal MHD by Suzuki & Inutsuka [394] showed that in the presence of net vertical field, the MRI was accompanied by mass and angular momentum loss in a disk wind. Winds are likewise seen in Bai & Stone’s net field protoplanetary disk simulations at 1 AU that include Ohmic and ambipolar diffusion [39], in simulations at 30-100 AU where ambipolar diffusion dominates [378], and in simulations that include all non-ideal terms [241]. Caution is required before interpreting these local simulation results as quantitative predictions, because although the effective potential for wind launching is correctly represented (equation 108) there is a known and unphysical dependence of the mass loss rate on the vertical size of the simulation domain [142]. Outflows are also seen in recent *global* net field simulations [162, 64, 34], however, supporting the view that outflows driven by a combination of MHD and thermal processes could be a generic feature of protoplanetary disk accretion.
- Turbulence and angular momentum transport are not synonymous. In classical disk theory, the value of α determines not only the rate at which the disk evolves, but also the strength of turbulence and its effect on small solid particles. This link is doubly broken in more complete disk models. First, as already noted, angular momentum loss via winds (which need not be accompanied by turbulence) may be stronger than viscous transport at some radii. Second, even the internal component of transport may be primarily a large-scale “laminar” Maxwell stress, rather than small-scale turbulence [378, 241].
- The sign of the net field could lead to bimodality in disk properties. The Hall effect is the strongest non-ideal term interior to about 10 AU, and simulations [241, 32, 33] confirm the expectation from linear theory [428, 48, 231] that a disk with a weak field that is aligned to the rotation axis behaves quite differently from one with an anti-aligned field. Although there are possible confounding factors — for example the long-term evolution of the net field may itself differ with the sign of the field — it appears likely that the striking asymmetry seen in simulations introduces *some* observable bimodality in disk structure [383].

¹⁵ It is not obvious that the inner disk *is* resupplied by gas, or, to put it more formally, that the disk attains a steady-state. Out to ~ 10 AU the viscous time scale is short enough that the disk will plausibly adjust to a steady state (provided only that a steady state is possible, see §6), but no such argument works out to 100 AU. Ultimately the question of whether gas at 100 AU ever reaches the star will need to be settled by observations as well as by theory.

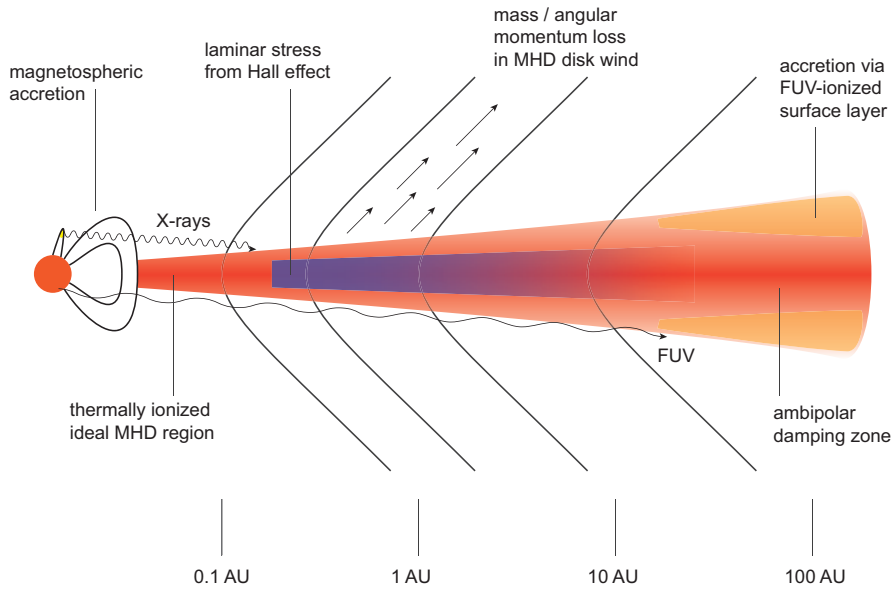


Fig. 22 A suggested structure for protoplanetary disks *if* MHD processes dominate over other sources of transport. The different regions are defined by the strength of non-ideal MHD terms (Ohmic diffusion, ambipolar diffusion and the Hall effect), and by mass and angular momentum loss in MHD disk winds. The Hall effect is predicted to behave differently if the net field threading the disk is anti-aligned to the rotation axis (here, alignment is assumed). Ionization by stellar X-rays and by FUV photons couples the stellar properties to those of the disk.

Hall MHD can also affect the properties of disks at an earlier time, during the collapse of molecular clouds and the formation of protostellar disks [225, 411], influencing for example their initial sizes.

Figure 22 illustrates a possible disk structure implied by the above results. The figure should be regarded as a work in progress; there is plenty of work remaining before we fully understand either the physics of potential angular momentum transport and loss processes, or how to tie that knowledge together into a consistent scenario for disk structure and evolution.

5.5 Transport in the boundary layer

The nature of transport in the boundary layer deserves a brief discussion. As discussed in §4.2.1 boundary layers are expected when the accretion rate is high enough to overwhelm the disruptive influence of the stellar magnetosphere (see equation 86 for a semi-quantitative statement of this condition). For most stars this requires high accretion rates, so the boundary layer and adjacent disk are hot enough to put us into the regime of thermal ionization and ideal MHD. In the disk we then expect angular momentum transport via the MRI. In the boundary layer, however, we face a problem. By definition, $d\Omega/dr > 0$ in the boundary layer (see Figure 10), and this angular velocity profile is *stable* against the MRI (equation 136). Something else much be responsible for transport in this region.

The angular velocity profile in the boundary layer is stable against the generation of turbulence by either the Rayleigh criterion or the MRI. It turns out to be *unstable*, however, to the generation of waves via a mechanism analogous to the hydrodynamic Papaloizou-Pringle instability of narrow tori [326]. Belyaev et al. [60, 61], using both analytic and numerical arguments, have shown that waves generated from the supersonic shear provide weak non-local transport of angular momentum (and energy) across the boundary layer. Magnetic fields are amplified by the shear [16] but do not play an essential role in boundary layer transport [61]. In protostellar systems boundary layers are present during eruptive accretion phases (see §6) when strong radiation fields are present [218]. Future work will need to combine the recent appreciation of the importance of wave angular momentum transport with radiation hydrodynamics for a full description of the boundary layer.

- Purely gas-phase turbulence in protoplanetary disks can be driven by MHD instabilities of Keplerian shear flow (the MRI and Hall-shear instability), by hydrodynamic instabilities that occur for specific vertical and / or radial entropy profiles, and by self-gravity.
- The magnetorotational instability probably dominates whenever the disk is thermally ionized, at temperatures exceeding about 10^3 K. Elsewhere, non-ideal MHD effects are important. Ohmic diffusion damps turbulence in high density regions, while ambipolar diffusion fulfills a similar role at large radii and in the disk atmosphere where the density is low. The Hall effect can enhance or inhibit angular momentum transport on $\sim 1 - 10$ AU scales, depending upon the sign of any net magnetic field relative to the disk angular momentum vector. The long-term evolution of the disk is thus coupled to the strength and evolution of net magnetic fields inherited from the star formation process.
- Self-gravity driven by ongoing envelope infall contributes to transport in young, massive disks. Fragmentation is expected to occur on sufficiently large scales (of the order of 10^2 AU), probably giving rise to objects with masses above the planetary mass regime.

- Entropy driven hydrodynamic instabilities could yield a significant level of transport in regions where MHD transport is suppressed. The operation of these instabilities is closely tied to the thermal structure and radiative properties of the disk.

6 Episodic accretion

Young stellar objects (YSOs) are observed to be variable. The short time scale (lasting hours to weeks) component of that variability is complex [99], but can probably be attributed to a combination of turbulent inhomogeneities in the inner disk, stellar rotation [74], and the complex dynamics of magnetospheric accretion [3]. There is also longer time scale variability — lasting from years to (at least) many decades, that in some cases takes the form of well-defined outbursts in which the YSO brightens dramatically. The traditional classification of outbursting sources divides them into FU Orionis events [178, 172], characterized by a brightening of typically 5 magnitudes followed by a decay over decades, and EXors [179], which display repeated brightenings of several magnitudes over shorter time scales. The statistics on these uncommon long-duration outbursts (especially FU Orionis events [183]) are limited, and it is not even clear — either observationally or theoretically — whether FUOrs and EXors are variations on a theme or genuinely different phenomena [26]. Nonetheless, it is established that episodic accretion is common enough to matter for both stellar accretion and for planet formation processes occurring in the inner disk [26]. Our focus here is on the origin of these accretion outbursts.

Observations show that FU Orionis outbursts involve a large increase in the mass accretion rate through the inner disk on to the star [172]. During the outburst the inner disk will be relatively thick ($h/r \approx 0.1$), and hot enough to be thermally ionized. We therefore expect efficient angular momentum transport from the MRI, with $\alpha \approx 0.02$. Writing the viscous time scale (equation 69) in terms of these parameters,

$$t_v = \frac{1}{\alpha\Omega} \left(\frac{h}{r}\right)^{-2}, \quad (187)$$

we can estimate the disk radius associated with a (viscously driven) outburst of duration t_{burst} ,

$$r \simeq (GM_*)^{1/3} \alpha^{2/3} \left(\frac{h}{r}\right)^{4/3} t_{\text{burst}}^{2/3}. \quad (188)$$

For a Solar mass star we find,

$$r \simeq 0.25 \left(\frac{\alpha}{0.02}\right)^{2/3} \left(\frac{h/r}{0.1}\right)^{4/3} \left(\frac{t_{\text{burst}}}{100 \text{ yr}}\right)^{2/3} \text{ AU}. \quad (189)$$

Disk-driven outbursts of broadly the right duration are thus likely to involve events on sub-AU scales, and could be associated physically with the magnetosphere, with the thermally ionized inner disk, or with the inner edge of the dead zone.

The physical origin of episodic accretion in YSOs has not been securely identified. Mooted ideas, illustrated in Figure 23, fall into two categories. The first category invokes secular instabilities of protoplanetary disk structure that may occur on AU and sub-AU scales. The idea is that the inner disk may be intrinsically unable to accrete at a steady rate, and instead alternates between periods of high accretion rate when gas is draining on to the star and periods of low accretion rate when gas

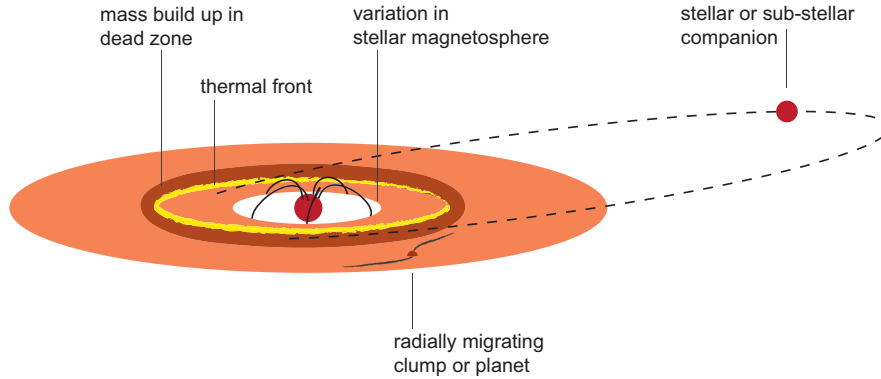


Fig. 23 An illustration of some of the processes suggested as the origin of episodic YSO accretion.

is accumulating in the inner disk. The instability could be a classical thermal instability [59], of the type accepted as causing dwarf nova outbursts [238], or a related instability of dead zone structure [149, 23]. The second category appeal to triggers independent of the inner disk to initiate the outburst. Ideas in this class are various and include perturbations from binary companions [72], the tidal disruption of radially migrating gas clumps / giant planets [425, 302], and disk variability linked to a stellar magnetic cycle [14, 106, 21]. Neither category of ideas is fully compelling (in the sense of being both fully worked out and consistent with currently accepted disk physics), so our discussion here will focus on a few key concepts that are useful for understanding current and future models of episodic accretion.

6.1 Secular disk instabilities

The classical instabilities that may afflict thin accretion disks are the thermal and viscous instabilities [340]. These are quite distinct from the basic fluid dynamical instabilities (the MRI, the VSI etc) that we discussed in §5, in that they address the stability of derived disk models rather than the fluid per se. Thus the thermal instability is an instability of the equilibrium vertical structure of the disk, while viscous instability is an instability of an (assumed) smooth radial structure under viscous evolution.

Before discussing how thermal or viscous instability might arise, we first define what these terms mean. Consider an annulus of the disk that is initially in hydrostatic and thermal equilibrium, such that the heating rate Q_+ matches the cooling rate Q_- . The heating rate per unit area depends upon the central temperature (equation 91), and can be written assuming the α -prescription as,

$$Q_+ = \frac{9}{4} v \Sigma \Omega^2 = \frac{9}{4} \alpha \frac{k_B T_c}{\mu m_H} \Sigma \Omega. \quad (190)$$

The cooling rate directly depends upon the effective temperature, T_{disk} , but this can always be rewritten in terms of T_c using a calculation of the vertical thermal structure (§4.3). In the simple case when the disk is optically thick, for example, we have from equation (98) that $T_c^4/T_{\text{disk}}^4 \simeq (3\tau/4)$, and hence,

$$Q_- = \frac{8\sigma}{3\tau} T_c^4. \quad (191)$$

Both α and τ may be functions of T_c . Now consider perturbing the central temperature on a time scale that is long compared to the dynamical time scale (so that hydrostatic equilibrium holds) but short compared to the viscous time scale (so that Σ remains fixed)¹⁶. The disk will be unstable to runaway heating if an upward perturbation to the temperature increases the heating rate more than it increases the cooling rate, i.e. if,

$$\frac{d \log Q_+}{d \log T_c} > \frac{d \log Q_-}{d \log T_c}. \quad (192)$$

The same criterion predicts runaway cooling in the event of a downward perturbation. A disk that is unstable in this sense is described as *thermally unstable*. It would heat up (or cool down) until it finds a new structure in which heating and cooling again balance.

To determine the condition for viscous stability, we start by considering a steady-state solution $\Sigma(r)$ to the diffusive disk evolution equation (63). Following Pringle [340] we write $\mu \equiv v\Sigma$ and consider perturbations $\mu \rightarrow \mu + \delta\mu$ on a time scale long enough that *both* hydrostatic and thermal equilibrium hold (in this limit T_c is uniquely determined and $v = v(\Sigma)$). Substituting in equation (63) the perturbation $\delta\mu$ obeys,

$$\frac{\partial}{\partial t} (\delta\mu) = \frac{\partial \mu}{\partial \Sigma} \frac{3}{r} \frac{\partial}{\partial r} \left[r^{1/2} \frac{\partial}{\partial r} (r^{1/2} \delta\mu) \right]. \quad (193)$$

The perturbation $\delta\mu$ will grow if the diffusion coefficient, which is proportional to $\partial\mu/\partial\Sigma$, is negative. This is *viscous instability*, and it occurs if,

$$\frac{\partial}{\partial \Sigma} (v\Sigma) < 0. \quad (194)$$

A disk that is viscously unstable would tend to break up into rings, whose amplitude would presumably be limited by the onset of fluid instabilities that could be thought of as modifying the $v(\Sigma)$ relation.

6.1.1 The S-curve: a toy model

The instabilities of interest for YSO episodic accretion can broadly be considered to be thermal-type instabilities. Noting that $Q_+ \propto \alpha T_c$, and $Q_- \propto T_c^4/\tau \propto T_c^4/\kappa$ (where

¹⁶ This may seem to require fine tuning, but in fact the ordering of time scales in a geometrically thin disk always allows for such a choice [340].

κ is the opacity at temperature T_c), we see that instability may occur according to equation (192) if,

- $d \log Q_+ / d \log T_c$ is large, i.e. if α is strongly increasing with temperature.
- $d \log Q_- / d \log T_c$ is small, i.e. if κ is strongly increasing with temperature.

We expect α to increase rapidly with T_c at temperatures around 10^3 K, as we transition between damped non-ideal MHD turbulence at low temperature and the more vigorous ideal MHD MRI at higher temperature. We expect κ to increase most strongly at temperatures around 10^4 K, as hydrogen is becoming ionized and there is a strong contribution to the opacity from H^- scattering (in this regime κ can vary as something like T^{10} [59]). Either of these changes can result in instability.

Before detailing the specifics of possible thermal and dead zone instabilities in protoplanetary disks, it is useful to analyze a toy model that displays their essential features. We consider an optically thick disk described by the usual classical equations [139] whose angular momentum transport efficiency α and opacity κ are both piece-wise constant functions of central temperature T_c . Specifically,

$$\begin{aligned} T_c < T_{\text{crit}} : \alpha &= \alpha_{\text{low}}, \kappa = \kappa_{\text{low}}, \\ T_c > T_{\text{crit}} : \alpha &= \alpha_{\text{high}}, \kappa = \kappa_{\text{high}}, \end{aligned} \quad (195)$$

with $\alpha_{\text{low}} \leq \alpha_{\text{high}}$ and $\kappa_{\text{low}} \leq \kappa_{\text{high}}$. Our goal is to calculate the explicit form of the $\dot{M}(\Sigma)$ relation in the “low” and “high” states below and above the critical temperature T_{crit} . For a steady-state disk, at $r \gg R_*$, heated entirely by viscous dissipation, the equations we need (mostly from §4) read,

$$\begin{aligned} T_{\text{disk}}^4 &= \frac{3\Omega^2}{8\pi\sigma} \dot{M}, \\ \frac{T_c^4}{T_{\text{disk}}^4} &= \frac{3}{4} \tau, \\ \tau &= \frac{1}{2} \kappa \Sigma, \\ v \Sigma &= \frac{\dot{M}}{3\pi}, \\ v &= \alpha \frac{c_s^2}{\Omega} = \frac{\alpha}{\Omega} \frac{k_B T_c}{\mu m_H}. \end{aligned} \quad (196)$$

Note that the stellar mass M_* and radius in the disk r enter these formulae only via their combination in the Keplerian angular velocity Ω . Eliminating T_c , T_{disk} , τ and v between these equations, we obtain a solution for $\dot{M}(\Sigma)$,

$$\dot{M} = \frac{9\pi}{4} \left(\frac{k_B^4}{\mu^4 m_H^4 \sigma} \right)^{1/3} \kappa^{1/3} \alpha^{4/3} \Omega^{-2/3} \Sigma^{5/3}, \quad (197)$$

valid on either the low or the high branch when the appropriate values for α and κ are inserted. A solution on the low branch is possible provided that $\Sigma \leq \Sigma_{\text{max}}$, where

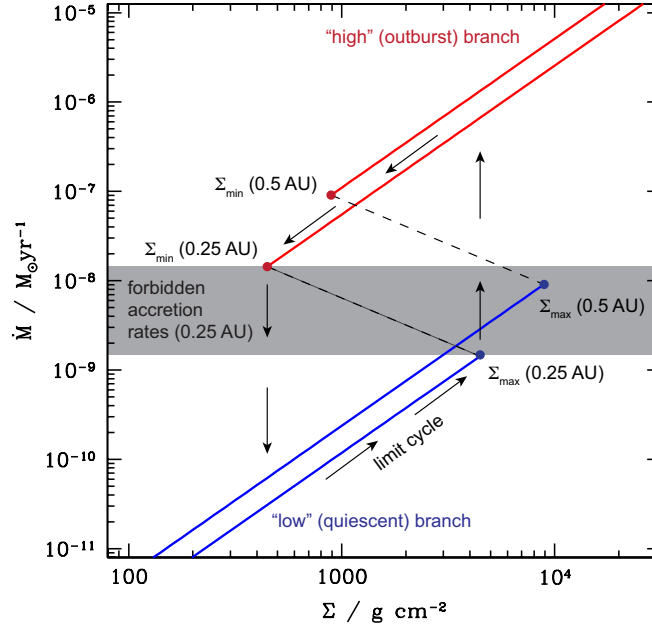


Fig. 24 Example S-curves in the accretion rate–surface density plane from the toy model described in the text. For these curves we take $\kappa_{\text{low}} = \kappa_{\text{high}} = 1 \text{ cm}^2 \text{ g}^{-1}$, $\alpha_{\text{low}} = 10^{-4}$, $\alpha_{\text{high}} = 10^{-2}$, and $T_{\text{crit}} = 10^3 \text{ K}$. The lower of the two curves is for $\Omega = 1.6 \times 10^{-6} \text{ s}^{-1}$ (0.25 AU for a Solar-mass star), the upper for $\Omega = 5.6 \times 10^{-7} \text{ s}^{-1}$ (0.5 AU).

Σ_{max} is defined by the condition that $T_c = T_{\text{crit}}$. Similarly, a high branch solution requires $\Sigma \geq \Sigma_{\text{min}}$ with $T_c = T_{\text{crit}}$ at Σ_{min} . The limiting surface densities are given by,

$$\begin{aligned} \Sigma_{\text{max}} &= \frac{8}{3^{3/2}} \left(\frac{\mu m_H \sigma}{k_B} \right)^{1/2} \Omega^{-1/2} T_{\text{crit}}^{3/2} \kappa_{\text{low}}^{-1/2} \alpha_{\text{low}}^{-1/2}, \\ \Sigma_{\text{min}} &= \frac{8}{3^{3/2}} \left(\frac{\mu m_H \sigma}{k_B} \right)^{1/2} \Omega^{-1/2} T_{\text{crit}}^{3/2} \kappa_{\text{high}}^{-1/2} \alpha_{\text{high}}^{-1/2}. \end{aligned} \quad (198)$$

If $\kappa_{\text{high}} > \kappa_{\text{low}}$ and / or $\alpha_{\text{high}} > \alpha_{\text{low}}$, then $\Sigma_{\text{max}} > \Sigma_{\text{min}}$ and there will be a range of surface densities where accretion rates corresponding to either the low or the high branch are possible.

Figure 24 shows, for a fairly arbitrary choice of the model parameters, the thermal equilibrium solutions that correspond to the low and high states of the disk annulus. One should not take the results of such a toy model very seriously, but it captures several features of more realistic models,

- The solution has stable thermal equilibrium solutions on two branches, a low state branch where \dot{M} for a given surface density is small, and a high state branch where it is substantially larger. In the toy model these branches are entirely separate, but in more complete models they are linked by an *unstable* middle branch (giving the plot the appearance of an “S”-curve).
- There is a range of surface densities for which either solution is possible.
- There is a band of accretion rates for which no stable equilibrium solutions exist.
- The position of the S-curve in the $\Sigma - \dot{M}$ plane is a function of radius, with the band of forbidden accretion rates moving to higher \dot{M} further from the star.

The S-curve is derived from a local analysis, and the existence of annuli whose thermal equilibrium solutions have this morphology is a necessary but not sufficient condition for a global disk outburst. That time dependent behavior of some sort is inevitable can be seen by supposing that the annulus at 0.25 AU in Figure 24 is fed with gas from outside at a rate that falls into the forbidden band. No stable thermal equilibrium solution with this accretion rate is possible. If the disk is initially on the lower branch, the rate of gas supply exceeds the transport rate through the annulus, and the surface density increases. This continues until Σ reaches and exceeds Σ_{\max} , at which point the only available solution lies on the high branch at much higher accretion rate. The annulus transitions to the high branch, where the transport rate is now larger than the supply rate, and the surface density starts to drop. The cycle is completed when Σ falls below Σ_{\min} , triggering a transition back to the low state.

The evolution of a disk that is potentially unstable (i.e. one that has some annuli with S-curve thermal equilibria) is critically dependent upon the *radial* flow of mass and heat, which are the key extra ingredients needed if an unstable disk is to “organize” itself and produce a long-lived outburst. To see this, imagine a disk where annuli outside r_f are already on the high branch of the S-curve, while those inside remain on the low branch. The strong radial gradient of T_c implies a similarly rapid change in v , which leads to a large mass flux from the annuli that are already in outburst toward those that remain quiescent (equation 64). The resulting increase in surface density, along with the heat that goes with it, can push the neighboring annulus on to the high branch, initiating a propagating “thermal front” that triggers a large scale transition of the disk into an outburst state.

The quantitative modeling of global disk evolution including these thermal processes is well-developed within the classical α disk formalism [238]. For a minimal model, all that is needed is to supplement the disk evolution equation (63) with a model for the vertical structure (conceptually as described for the toy model above) and an equation for the evolution of the central temperature. This takes the form [79, 238],

$$\frac{\partial T_c}{\partial t} = \frac{Q_+ - Q_-}{c_p \Sigma} - \frac{\mathcal{R} T_c}{\mu c_p} \frac{1}{r} \frac{\partial}{\partial r} (r v_r) - v_r \frac{\partial T_c}{\partial r} + \dots \quad (199)$$

Here c_p is the specific heat capacity at constant pressure, and \mathcal{R} is the gas constant. The first term on the right hand side describes the direct heating and cooling due to viscosity and radiative losses, while the second and third terms describe PdV work and the advective transport of heat associated with radial mass flows. In general

there should be additional terms to represent the radial flow of heat due to radiative and / or turbulent diffusion (these effects are small in most thin disk situations, but become large when there is an abrupt change in T_c at a thermal front). The treatment of these additional terms is somewhat inconsistent in published models, though they can significantly impact the character of derived disk outbursts [316].

6.1.2 Classical thermal instability

In physical rather than toy models for episodic accretion α and κ are smooth rather than discontinuous functions of the temperature. A local instability, with a resulting S-curve, occurs if one or both of these functions changes sufficiently rapidly with T_c (so that equation 192 is satisfied). No simple condition specifies when a disk that has some locally unstable annuli will generate well-defined global outbursts, but loosely speaking outbursts occur provided that the branches of the S-curve (and the values of Σ_{\max} and Σ_{\min}) are well separated.

The classical cause of disk thermal instability is the rapid increase in opacity associated with the ionization of hydrogen, at $T \simeq 10^4$ K. Around this temperature κ can rise as steeply as T^{10} , and the disk will invariably satisfy at least the condition for local thermal instability. The evolution of disks subject to a hydrogen ionization thermal instability was first investigated as a model for dwarf novae (eruptive disk systems in which a white dwarf accretes from a low-mass companion star) [168, 291], and subsequently applied to low-mass X-ray binaries. Thermal instability models provide a generally good match to observations of outbursts in these systems (which are of shorter duration than YSO outbursts, and correspondingly better characterized empirically), and are accepted as the probable physical cause. Good fits to data require models to include not only the large change in κ that is the cause of classical thermal instability, but also changes in α between the low and high branches of the S-curve. Typically $\alpha_{\text{low}} \leq 10^{-2}$, whereas $\alpha_{\text{high}} \sim 0.1$ [216]. MHD simulations that include radiation transport have shown that the S-curve derived from α disk models can be approximately recovered as a consequence of the MRI, and that the difference in stress between the quiescent and outburst states may be attributable in part to the development of vertical convection within the hot disk [184, 100].

By eye, the light curves of FU Orionis events look quite similar to scaled versions of dwarf novae outbursts, so the success of thermal instability models in the latter sphere makes them a strong candidate for YSO accretion outbursts. The central temperature of some outbursting FUOr disks, moreover, almost certainly does exceed the 10^4 K needed to ionize hydrogen, making it inevitable that thermal instability physics will play some role in the phenomenon. Detailed thermal instability models of FU Orionis events were constructed by Bell & Lin [59], who combined a one-dimensional (in r) treatment of the global evolution with detailed α model vertical structure calculations. They were able to find periodic solutions that describe “self-regulated” disk outbursts (i.e., requiring no external perturbation or trigger), with the disk alternating between quiescent periods (with $\dot{M} = 10^{-8} - 10^{-7} M_{\odot} \text{ yr}^{-1}$)

and outburst states (with $\dot{M} \geq 10^{-5} M_{\odot} \text{ yr}^{-1}$). These properties, and the inferred outburst duration of $\sim 10^2$ yr, are in as good an agreement with observations as could reasonably be expected given the simplicity of the model.

The weakness of classical thermal instability models as an explanation for YSO accretion outbursts is that they require unnatural choices of the viscosity parameter α [15]. Thermal instability is immutably tied to the hydrogen ionization temperature, which exceeds even the mid-plane temperatures customarily attained in protoplanetary disks. The required temperatures can be reached (if at all) only extremely close to the star, and the radial region affected by instability extends to no more than 0.1-0.2 AU. The viscous time scale on these scales is short, so matching the century-long outbursts seen in FUOrs requires a very weak viscosity — Bell & Lin [59] adopt $\alpha_{\text{high}} = 10^{-3}$. This is at least an order of magnitude lower than the expected efficiency of MRI transport under ideal MHD conditions [107, 380]. Moreover, in the specific case of FU Orionis itself, radiative transfer models suggest that the region of high accretion rate during the outburst extends out to 0.5-1 AU [443], substantially larger than would be expected in the thermal instability scenario.

6.1.3 Instabilities of dead zones

A dead zone in which the MRI is suppressed by Ohmic resistivity (§5.4.3) supports a related type of instability whose high and low states are distinguished primarily by different values of α , rather than by the thermal instability’s different values of κ . The origin of instability is clear within Gammie’s original conception [148] of the dead zone, which has a simple two-layer structure. The surface of the disk, ionized by X-rays¹⁷, is MRI-active and supports accretion with a local $\alpha \sim 10^{-2}$. Below a critical column density Ohmic resistivity completely damps MRI-induced turbulence (according to equation 181), and the disk is dead with $\alpha = 0$. This structure can be bistable if the surface density exceeds that of the ionized surface layer. The low accretion rate state corresponds to a cool, externally heated disk with a dead zone; the high accretion rate state to a hot thermally ionized disk at the same Σ .

Martin & Lubow [283, 285] have shown that the local physics of Ohmic dead zone instability can be analyzed in a manner closely analogous to thermal instability. The sole difference lies in the reason why the lower state ceases to exist above a critical surface density (Σ_{max} in Figure 24). For thermal instability Σ_{max} is set by the onset of ionization at the disk mid-plane, and the attendant rise in opacity. A simple dead zone, however, *does not get hotter with increasing Σ* , because the heating (either from irradiation, or viscous dissipation in the ionized surface layer) occurs at low optical depth at a rate that is independent of the surface density. It is then not obvious how even a very thick dead zone can be heated above 10^3 K, “ignited”, and induced to transition to the high state of the S-curve.

One way to trigger a jump to the high state is to postulate that some source of turbulence other than the MRI is present to heat the disk. Gammie [149] suggested

¹⁷ Cosmic rays in the original model, though this is an unimportant distinction.

that inefficient transport through the ionized surface layer would lead to the build of mass in the dead zone [148] until $Q \approx 1$ and self-gravity sets in (see §5.2). We can readily estimate the properties we might expect for an instability triggered in this manner by the onset of self-gravity at small radii. Suppose that at 1 AU the temperature in the quiescent (externally irradiated) disk state is 150 K. Then to reach $Q = 1$ requires gas to build up until $\Sigma \simeq 7 \times 10^4 \text{ g cm}^{-2}$, at which point the mass interior is $M \sim \pi r^2 \Sigma \sim 0.025 M_\odot$. This is comparable to the amount of mass accreted per major FU Orionis-like outburst. In the outburst state the disk will be moderately thick (say $h/r = 0.3$ [58]), and the viscous time scale $(1/\alpha\Omega)(h/r)^{-2}$ works out to be about 200 yr for $\alpha = 0.01$, again similar to inferred FUOr time scales. At this crude level of estimate, it therefore seems possible that a self-gravity triggered dead zone instability could be consistent both with the inferred size of the outbursting region [443] and with theoretical best guesses as to the strength of angular momentum transport in ideal MHD conditions.

Time-dependent models for outbursts arising from a dead zone instability were computed by Armitage et al. [23], and subsequently by several groups in both one-dimensional [446, 444, 283, 316] and two-dimensional models [445, 29]. The more recent studies show that a self-gravity triggered instability of an Ohmic dead zone can give rise to outbursts whose properties are broadly consistent with those of observed FUOrs. Instability persists even if there is a small residual viscosity within the dead zone [28, 285], which could arise hydrodynamically in response to the “stirring” from the overlying turbulent surface layer [131]. How well such models work when either or both of the Hall effect and MHD winds contribute to the dynamics close to the star remains unclear. In principle these effects could also lead to entirely different types of eruptive behavior.

6.2 Triggered accretion outbursts

Accretion variability, including (perhaps) the large scale outbursts of FUOrs, can also be triggered by processes largely independent of the inner disk itself. Stellar activity cycles, binaries with small periastron distances, and tidal disruption of gaseous clumps or planets may all contribute.

6.2.1 Stellar activity cycles

As discussed in §4.2.2 the inner disk is expected [220] and observed [73] to be disrupted by the stellar magnetosphere. The complex dynamics of the interaction between the field — which may be misaligned to the stellar spin axis and have non-dipolar components [207] — and the disk [234] is likely the dominant cause of T Tauri variability on time scales comparable to the stellar rotation period (i.e. days to weeks). If the strength of the field also varies systematically due to the presence of activity cycles analogous to the Solar cycle, these could trigger longer time scale

(years to decades) accretion variability. The simplest mechanism is modulation of the magnetospheric radius across corotation [94]. When the field is strong and $r_m > r_{\text{co}}$ the linkage between the stellar field lines and the disks adds angular momentum to the disk, impeding accretion in the same way as gravitational torques from a binary (§4.2.3)¹⁸. Gas then accumulates just outside the magnetospheric radius, and can subsequently be accreted in a burst when the field weakens.

The viability of such magnetically “gated” accretion as an origin for large scale variability is limited by the short viscous time scale of the disk at $r \approx r_m$, which makes it hard to accumulate large masses of gas if the stellar fields are, as expected, of no more than kG strength. Models [14] suggest that significant decade-long variability could be associated with protostellar activity cycles, but there is no clear path to generating FU Orionis outbursts. Activity cycles are more promising as an explanation for lower amplitude, periodic EXor outbursts [105, 106]. The interaction between the time-variable stellar magnetic field and the non-ideal physics of the inner disk, just outside the thermally ionized region, could be significant [21].

6.2.2 Binaries

An eccentric binary with an AU-scale periastron distance could funnel gas into the inner disk, increasing the accretion rate and leading to an outburst if the increased surface density is high enough to trigger thermal or dead zone instability. This mechanism was proposed by Bonnell & Bastien [72], and has subsequently been studied with higher resolution simulations [333, 135]. Although there are some differences between the predicted outbursts and those observed (this is almost inevitable, as the limited sample of FUOrs is already quite diverse), it is clear that close encounters from binary or cluster companions induce episodes of substantially enhanced accretion. The obvious prediction — that FUOrs ought to be found with observable binary companions or preferentially associated with higher-density star forming regions — is neither confirmed nor ruled out given the small sample of known objects.

6.2.3 Clump tidal disruption

A final possibility is that accretion outbursts could be triggered by the tidal disruption of a bound object (a planet or gas cloud) that migrates too close to the star. The necessary condition for this to occur is given by the usual argument for the Roche limit. If we consider a planet with radius R_p and mass M_p , orbiting a star of mass M_* at radius r , the differential (tidal) gravitational force between the center of the planet and its surface is,

$$F_{\text{tidal}} = \frac{GM_*}{r^2} - \frac{GM_*}{(r+R_p)^2} \simeq \frac{2GM_*}{r^3} R_p. \quad (200)$$

¹⁸ In compact object accretion, this is described as the “propeller” regime of accretion [190].

Equating the tidal force to the planet's own self-gravity, $F_{\text{self}} = GM_p/R_p^2$, we find that tidal forces will disrupt the planet at a radius r_{tidal} given approximately by,

$$r_{\text{tidal}} = \left(\frac{M_*}{M_p} \right)^{1/3} R_p. \quad (201)$$

An equivalent condition is that tidal disruption occurs when the mean density of the planet $\bar{\rho} < M_*/r^3$.

It is difficult to tidally disrupt a mature giant planet. A Jupiter mass planet has a radius of $R_p \simeq 1.5 R_J$ at an age of 1 Myr [279], and will not be disrupted outside the photospheric radius of a typical young star. (Though such planets, if present in the inner disk, could alter the course of thermal or dead zone instability [97, 254].) If tidal disruption is to be relevant to episodic accretion we require, first, that the outer disk is commonly gravitationally unstable to fragmentation, and, second, that the clumps that form migrate rapidly inward (in the Type 1 regime discussed by Kley in this volume) without contracting too rapidly. Numerical evidence supports the idea that clump migration can be rapid [425, 54, 84, 292], though it is at best unclear whether contraction can be deferred sufficiently to deliver clumps that would be tidally disrupted on sub-AU scales [147]. Assuming that these pre-conditions are satisfied, however, Nayakshin & Lodato [302] studied the tidal mass loss from the close-in planets and its impact on the disk. They found that the tidal disruption of $\sim 20 R_J$ clumps, interior to 0.1 AU, led to accretion outbursts consistent with the basic properties of FUOrs.

The primary theoretical doubts about tidal disruption as a source of outbursts concern the relative rates of inward migration and clump contraction, which are both hard to calculate at substantially better than order of magnitude level. Observationally, this process would produce outbursts in systems whose disks were young, massive, and probably still being fed by envelope infall.

- Episodic accretion on to Young Stellar Objects occurs in several different flavors, including high-amplitude outbursts such as FU Orionis events that would certainly have an important influence on disk chemistry and planet formation close to the star.
- A possible explanation for episodic accretion is an instability in the equilibrium disk structure on AU or sub-AU scales, related to the classical thermal instability that explains outbursts in dwarf nova systems. A potential instability of dead zone structure has been demonstrated in one- and two-dimensional models, but may need to be modified to take account of additional non-ideal MHD physics and disk winds.
- Outbursts could also be *internally* triggered, for example by changes in the stellar magnetic field, or *externally* triggered, if dense clumps of gas migrate quickly into the inner disk and are tidally disrupted.

7 Single and collective particle evolution

The evolution of solid particles within disks differs from that of gas because solid bodies are unaffected by pressure gradients but do experience aerodynamic forces. We discuss here how these differences affect the motion of single particles orbiting within the gas disk, and how we can describe the evolution of a “fluid” made up of small solid particles interacting aerodynamically with the gas. Issues such as the rate and outcome of particle collisions, that are central to early stage planet formation, are treated in the accompanying part by Kley, and elsewhere [18].

The key parameter describing the aerodynamic coupling between solid particles and gas is the *stopping time*. For a particle of mass m that is moving with velocity Δv relative to the local gas, the stopping time is defined as,

$$t_s \equiv \frac{m\Delta v}{|F_{\text{drag}}|}, \quad (202)$$

where F_{drag} is the magnitude of the aerodynamic drag force that acts in the opposite direction to Δv . Very frequently, what matters most is how the stopping time compares to the orbital time at the location of the particle. We therefore define a dimensionless stopping time by multiplying t_s by the orbital frequency Ω_K ,

$$\tau_s \equiv t_s \Omega_K. \quad (203)$$

The dimensionless stopping time is also called the *Stokes number*.

For our immediate purposes it largely suffices to describe aerodynamic effects in terms of the stopping time, but eventually you will want to translate the results into concrete predictions for how particles of various sizes and material properties behave. This requires specifying F_{drag} , whose form depends on the size of the particle relative to the mean free path of gas molecules, and (in the fluid regime) on the Reynolds number of the flow around the particle [433]. If the particle radius s is small compared to the mean free path λ ($s < 9\lambda/4$) the particle experiences *Epstein drag*, with a drag force,

$$\mathbf{F}_{\text{drag}} = -\frac{4\pi}{3} \rho s^2 v_{\text{th}} \Delta \mathbf{v}. \quad (204)$$

Here ρ is the density of the surrounding gas, and the thermal speed of the molecules,

$$v_{\text{th}} = \sqrt{\frac{8k_B T}{\pi \mu m_H}}, \quad (205)$$

is roughly the same as the sound speed. Because Epstein drag is proportional to the velocity difference Δv (rather than the more familiar square of the velocity difference), the stopping time is a function of the particle properties that is independent of the velocity difference. For a spherical particle of material density ρ_m ,

$$t_s = \frac{\rho_m}{\rho} \frac{s}{v_{\text{th}}}. \quad (206)$$

The mean free path in protoplanetary disks is of the order of cm (larger in the outer disk), so the Epstein regime is relevant for particles that range from dust to those of small macroscopic dimensions. Drag laws appropriate for larger bodies, which fall into the Stokes regime of drag, are given by Whipple [433].

7.1 Radial drift

The most important consequence of aerodynamic forces is the phenomenon of *radial drift*. In §3.1.2 we showed that radial pressure gradients result in a gas orbital velocity that differs from the Keplerian value by 50-100 m s⁻¹ (using typical disk parameters at 1 AU). Most commonly, the gas is partially supported against gravity by the pressure gradient, and so rotates more slowly than the Keplerian value. We will consider how this velocity differential affects the evolution of solids in various limits. We will start by ignoring both turbulence and the feedback of aerodynamic forces *on the gas*, before revisiting the problem with these processes included.

7.1.1 Particle drift without feedback

Large bodies ($\tau_s \gg 1$) orbit at close to the Keplerian speed, and the effect of gas on their evolution can be considered as a simple “headwind” if the disk is sub-Keplerian. Suppose that the gas orbits at a speed $v_K - \Delta v$, with $\Delta v \ll v_K$. The drag force $|F_{\text{drag}}| = m\Delta v\Omega_K/\tau_s$ does work at a rate,

$$\dot{E} \simeq -|F_{\text{drag}}|v_K, \quad (207)$$

that leads to a change in the orbital energy $E = -GM_*m/2a$, where a is the radius of the orbit. Noting that,

$$\dot{E} = \frac{GM_*m}{2a^2} \frac{da}{dt}, \quad (208)$$

and equating the two expressions for \dot{E} , we find that the orbit decays at a speed $v_r = da/dt$ that is given by,

$$v_r = -\frac{2}{\tau_s} \Delta v. \quad (209)$$

The radial drift of large bodies is inversely proportional to their Stokes number.

The simple headwind argument fails for small particles with $\tau_s \ll 1$, which instead are forced to orbit *at the gas speed* by the strong aerodynamic coupling. The particles do not feel the pressure gradient, so their non-Keplerian orbital motion results in a net radial force,

$$\frac{F_r}{m} = \frac{(v_K - \Delta v)^2}{a} - \frac{GM_*}{a^2} \simeq -\frac{2v_K\Delta v}{a}. \quad (210)$$

Equating this to the drag force for *radial* motion at speed v_r , $|F_{\text{drag}}|/m = v_r \Omega_K / \tau_s$, we find that radial drift for small particles occurs at the terminal drift speed,

$$v_r = -2\tau_s \Delta v. \quad (211)$$

This is the speed relative to the gas, so for a disk that is accreting there is an additional component given by the gas' radial velocity.

Intermediate-sized particles orbit at some speed between that of the gas and that given by the Keplerian velocity. To derive the general rate of radial drift [430, 397], we consider a gas disk whose orbital velocity is,

$$v_{\phi, \text{gas}} = v_K (1 - \eta)^{1/2}. \quad (212)$$

The parameter $\eta \propto (h/r)^2$. For example, if the disk has $\Sigma \propto r^{-1}$ and central temperature $T_c \propto r^{-1/2}$, we showed in §3.1.2 that $\eta = (11/4)(h/r)^2$. Defining the particle radial and azimuthal velocities to be v_r and v_ϕ respectively, the equations of motion are,

$$\frac{dv_r}{dt} = \frac{v_\phi^2}{r} - \Omega_K^2 r - \frac{1}{t_s} (v_r - v_{r, \text{gas}}) \quad (213)$$

$$\frac{d}{dt} (rv_\phi) = -\frac{r}{t_s} (v_\phi - v_{\phi, \text{gas}}). \quad (214)$$

The azimuthal equation can be simplified by noting that the specific angular momentum remains close to Keplerian,

$$\frac{d}{dt} (rv_\phi) \simeq v_r \frac{d}{dr} (rv_K) = \frac{1}{2} v_r v_K. \quad (215)$$

This yields,

$$v_\phi - v_{\phi, \text{gas}} \simeq -\frac{1}{2} \frac{t_s v_r v_K}{r}. \quad (216)$$

We now substitute for Ω_K in the radial equation using equation (212). Discarding higher order terms we obtain,

$$\frac{dv_r}{dt} = -\eta \frac{v_K^2}{r} + \frac{2v_K}{r} (v_\phi - v_{\phi, \text{gas}}) - \frac{1}{t_s} (v_r - v_{r, \text{gas}}). \quad (217)$$

The dv_r/dt term is negligible. Dropping that, we eliminate $(v_\phi - v_{\phi, \text{gas}})$ between equations (216) and (217) to obtain,

$$v_r = \frac{(r/v_K)t_s^{-1} v_{r, \text{gas}} - \eta v_K}{(v_K/r)t_s + (r/v_K)t_s^{-1}}. \quad (218)$$

In terms of the Stokes number the final result for the particle radial velocity is,

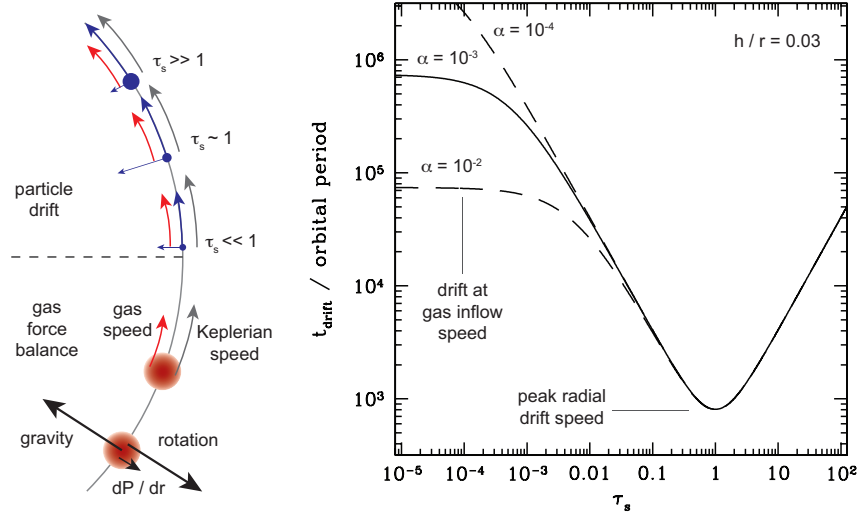


Fig. 25 Particles drift inwards in a disk wherever dP/dr , due to the combination of aerodynamic forces and sub-Keplerian gas rotation. The radial drift time scale $t_{\text{drift}} = r/|v_r|$, in units of the local orbital period, is plotted as a function of the dimensionless stopping time τ_s . The fastest radial drift occurs for $\tau_s = 1$. The specific numbers shown in the plot are appropriate for a disk with $h/r = 0.03$ and α values of 10^{-2} (lowest curve on the left-hand side of the figure), 10^{-3} and 10^{-4} .

$$v_r = \frac{\tau_s^{-1} v_{r,\text{gas}} - \eta v_K}{\tau_s + \tau_s^{-1}}. \quad (219)$$

The previously derived results for very small and very large particles are recovered by taking the appropriate limits.

The speed of the radial drift implied by equation (219) is shown in Figure 25. Very rapid drift is predicted for particles with $\tau_s \sim 1$. For our fiducial disk model with $\Sigma \propto r^{-1}$, $T_c \propto r^{-1/2}$ and $h/r = 0.03$, the radial drift time scale $t_{\text{drift}} = r/|v_r|$ is just 10^3 orbital periods — one thousand years at 1 AU! Particles with this stopping time are very roughly meter-sized, and their rapid drift is the origin of the “meter-sized barrier” that severely constrains models of planetesimal formation [89, 198].

7.1.2 Drift with diffusion

If the disk is turbulent, small dust particles that are aerodynamically well-coupled to the gas will diffuse radially and vertically. (The same physics will apply to trace gas species, such as water or CO molecules.) Diffusion will tend to equalize the *concentration* of the dust or trace gas species relative to the dominant gaseous component in the disk. To derive an equation for the evolution of the trace species [96], we initially ignore any radial drift due to aerodynamic effects and write the concentration

of the trace gas or dust (generically the “contaminant”) as,

$$f = \frac{\Sigma_d}{\Sigma}, \quad (220)$$

where Σ_d is the surface density of the contaminant. If the contaminant is neither created nor destroyed within the region of the disk under consideration, continuity demands that,

$$\frac{\partial \Sigma_d}{\partial t} + \nabla \cdot \mathbf{F}_d = 0, \quad (221)$$

where \mathbf{F}_d , the flux, can be decomposed into two parts: an advective piece describing transport of the dust or gas with the mean disk flow, and a diffusive piece describing the tendency of turbulence to equalize the concentration of the contaminant across the disk. For $f \ll 1$ we can assume that the diffusive properties of the disk depend only on the *gas* surface density, in which case the flux can be written as,

$$\mathbf{F}_d = \Sigma_d \mathbf{v} - D \Sigma \nabla \left(\frac{\Sigma_d}{\Sigma} \right). \quad (222)$$

Here \mathbf{v} is the mean velocity of gas in the disk and D is the turbulent diffusion coefficient. The diffusive term vanishes if f is constant. Combining this equation with the continuity equation for the gaseous component, we obtain an evolution equation for f in an axisymmetric disk. In cylindrical polar co-ordinates,

$$\frac{\partial f}{\partial t} = \frac{1}{r \Sigma} \frac{\partial}{\partial r} \left(D r \Sigma \frac{\partial f}{\partial r} \right) - v_r \frac{\partial f}{\partial r}. \quad (223)$$

This result has the form of an advection-diffusion equation, with the advective component being due to the radial flow of the disk gas. It is easy to generalize this equation to account for the radial drift of larger particles that are imperfectly coupled to the gas, by adding an additional flux representing the radial drift speed [5].

Determining what is the appropriate value for the turbulent diffusion coefficient D involves many of the same uncertainties that afflict the determination of the turbulent viscosity. For trace gas species and very small dust particles the zeroth-order expectation is that $D \approx \nu$ [298], though simulations of non-ideal MHD disk turbulence show both significant deviations from ν and anisotropy between the vertical and radial directions [449]. For larger bodies there is a well-determined analytic scaling with the Stokes number of the particles [440].

7.1.3 Particle pile-up

Solids that experience significant radial drift tend to become concentrated (“pile-up”) in the inner disk [441, 438]. The basic effect is present in the simplest case where diffusion and inward drag by the mean flow are small, and feedback of the particles on the gas can be neglected. The radial drift speed is then, approximately,

$$v_r \simeq -\tau_s \eta v_K, \quad (224)$$

with $\eta \propto (h/r)^2$. For particles that are in the Epstein regime of drag, the stopping time in the mid-plane is (from equations 206 and 16),

$$t_s = \frac{\rho_m s}{\rho_0 v_{th}} = \sqrt{2\pi} \frac{\rho_m h}{\Sigma} \frac{s}{v_{th}}. \quad (225)$$

Since $h = c_s/\Omega$, and c_s and v_{th} differ only by a numerical factor, we obtain,

$$\tau_s = \frac{\pi \rho_m}{2 \Sigma} s. \quad (226)$$

Suppose now (perhaps not very realistically) that the surface density profile of solids has attained a steady-state, such that the mass flux is constant with radius. Then,

$$\dot{M}_d = -2\pi r \Sigma_d v_r = \text{constant}, \quad (227)$$

and substituting for v_r we find,

$$\frac{\Sigma_d}{\Sigma} \propto \left(\frac{h}{r}\right)^{-2} r^{-1/2}. \quad (228)$$

For a disk with constant (h/r) the steady-state concentration of solids increases closer to the star as $r^{-1/2}$. In the more realistic case of a flaring disk with mid-plane temperature profile, say, $T_c \propto r^{-1/2}$, the effect is stronger. A constant α model of such a disk has a steady-state gas surface density profile $\Sigma \propto r^{-1}$, with the solids following $\Sigma_d \propto r^{-2}$.

7.1.4 The Nakagawa-Sekiya-Hayashi equilibrium

Up till now we have implicitly assumed that the evolution of the gas is unaffected by the evolution of the solids within it. Obviously this can never be strictly correct. If a population of solid particles are losing angular momentum to the gas through aerodynamic forces and spiraling inward, the gas must gain a corresponding amount of angular momentum. If the solid to gas ratio is only of the order of 1%, however, one might suppose that the effect of the angular momentum exchange on the gas would be small and, perhaps, ignorable. This is only partially true. First, a number of processes, including vertical particle settling [117], gas loss via photo-evaporation [404, 5] or MHD winds, and radial drift itself [438], can boost the solid to gas ratio, at least locally. Second, the equilibrium solution for radial drift in the presence of back reaction on to the gas can be unstable to the *streaming instability* [439], which can result in strong localized clumping of the solids.

The generalization of the radial drift formula (equation 219) to account for the back reaction of the drift on the gas is known as the Nakagawa-Sekiya-Hayashi (NSH) equilibrium [301]. The NSH solution is derived by considering the inter-

action between solids and gas in a simple disk model that ignores the effects of turbulence and vertical gravity. Both the gas, with density ρ_g , pressure P and velocity \mathbf{v}_g , and the solid particles, with density density ρ_p and velocity \mathbf{v}_p , are treated as fluids that interact with each other via aerodynamic drag. They obey continuity and momentum equations of the form [439],

$$\frac{\partial \rho_p}{\partial t} + \nabla \cdot (\rho_p \mathbf{v}_p) = 0, \quad (229)$$

$$\nabla \cdot \mathbf{v}_g = 0, \quad (230)$$

$$\frac{\partial \mathbf{v}_p}{\partial t} + \mathbf{v}_p \cdot \nabla \mathbf{v}_p = -\Omega_K^2 \mathbf{r} - \frac{1}{t_s} (\mathbf{v}_p - \mathbf{v}_g), \quad (231)$$

$$\frac{\partial \mathbf{v}_g}{\partial t} + \mathbf{v}_g \cdot \nabla \mathbf{v}_g = -\Omega_K^2 \mathbf{r} + \frac{1}{t_s} \frac{\rho_p}{\rho_g} (\mathbf{v}_p - \mathbf{v}_g) - \frac{\nabla P}{\rho_g}. \quad (232)$$

We have replaced the continuity equation for the gas with the condition for incompressibility, which is valid provided that velocities remain highly subsonic. The only other differences between the equations for the two species are the presence of a pressure gradient term in the gas momentum equation, and the pre-factor in the aerodynamic drag term expressing the differing inertia of the two fluids.

It is straightforward to derive the steady-state axisymmetric solution for the drift of solids and gas from the above equations [301, 439]. To illustrate the difference between the NSH and no-feedback solutions, we quote here just the result for the relative radial velocity of the solids and the gas. With our definition of η (equation 212) this takes the form,

$$v_{r,\text{rel}} = -\frac{\rho_g}{\rho} \frac{\eta \tau_s v_K}{1 + (\tau_s \rho_g / \rho)^2}, \quad (233)$$

where $\rho = \rho_g + \rho_p$. Equation (219) is recovered in the case where $\rho_p \ll \rho_g$ and feedback can be neglected (note that we have ignored any radial gas motions due to processes *other* than particle-gas coupling in this version of the NSH solution).

The predicted relative radial velocity between the solid and gas components is plotted in Figure 26 for various values of the solid to gas ratio. For $\rho_p / \rho_g = 10^{-2} - 10^{-1}$ the rate of drift at a given value of the stopping time is very similar to the no-feedback solution given by equation (219). For large values of ρ_p / ρ_g , however, the peak of the relative velocity curve (which in this limit is predominantly outward motion of the *gas*) shifts to somewhat higher values of τ_s .

7.2 Vertical settling

Aerodynamic drag also modifies the vertical distribution of solids relative to gas. We first consider the forces acting on a small particle of mass m at height z above the mid-plane of a laminar disk. The vertical component of stellar gravity exerts a

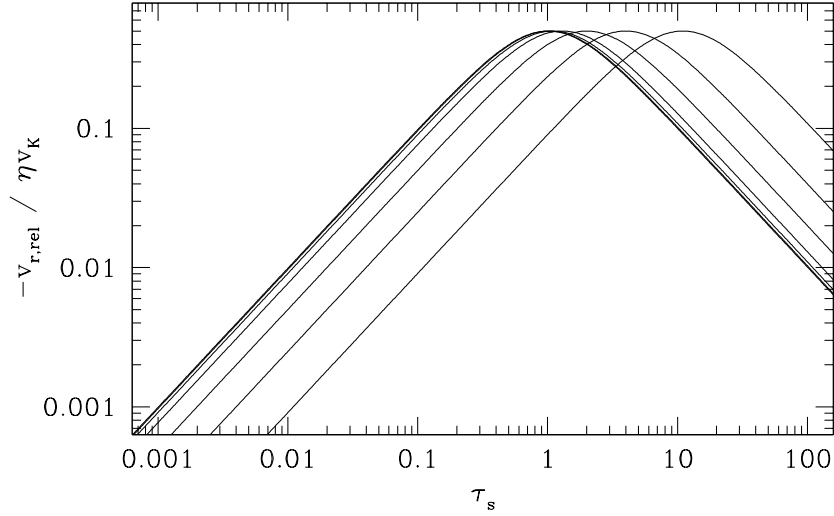


Fig. 26 The relative velocity of solids compared to gas (normalized by ηv_K , the parameter specifying departure of the gas disk from Keplerian rotation) is plotted as a function of the Stokes number τ_s . From left to right the curves show the NSH equilibrium solutions for $\rho_p/\rho_g = 10^{-2}$ (effectively identical to the no-feedback solution), 3×10^{-2} , 0.1, 0.3, 1, 3 and 10.

force,

$$|F_{\text{grav}}| = m \Omega_K^2 z. \quad (234)$$

The gas in the disk is supported against this force by the vertical pressure gradient, but solid particles are not. If started at rest a particle will accelerate until the gravitational force is balanced by drag. In the Epstein regime (given by equation 204) the resulting terminal velocity is,

$$v_{\text{settle}} = \frac{\rho_m}{\rho} \frac{s}{v_{\text{th}}} \Omega_K^2 z. \quad (235)$$

Using numerical values appropriate for a $1 \mu\text{m}$ particle at $z \sim h$ at 1 AU ($\rho = 6 \times 10^{-10} \text{ g cm}^{-3}$, $z = 3 \times 10^{11} \text{ cm}$, $v_{\text{th}} = 10^5 \text{ cm s}^{-1}$) gives a settling speed $v_{\text{settle}} \approx 0.06 \text{ cm s}^{-1}$. The settling time, defined as,

$$t_{\text{settle}} = \frac{z}{|v_{\text{settle}}|}, \quad (236)$$

is about $1.5 \times 10^5 \text{ yr}$. In the absence of turbulence micron-sized particles ought to settle out of the upper layers of the disk on a time scale that is shorter than the disk lifetime.

Turbulent diffusion acts to counteract the effects of settling. If the particle fluid with density ρ_p behaves as a trace species (i.e. $\rho_p/\rho \ll 1$) then it obeys an advection-

diffusion equation [117, 143],

$$\frac{\partial \rho_p}{\partial t} = D \frac{\partial}{\partial z} \left[\rho \frac{\partial}{\partial z} \left(\frac{\rho_p}{\rho} \right) \right] + \frac{\partial}{\partial z} (\Omega_K^2 t_s \rho_p z). \quad (237)$$

Steady-state solutions to this equation can be found in the limit where the particle layer is thin enough that the *gas* density is approximately constant across the particle scale height. The dimensionless friction time τ_s is then independent of z and we find,

$$\frac{\rho_p}{\rho} = \left(\frac{\rho_p}{\rho} \right)_{z=0} \exp \left[-\frac{z^2}{2h_p^2} \right], \quad (238)$$

where h_p , the scale height of the particle concentration ρ_p/ρ , is,

$$h_p = \sqrt{\frac{D}{\Omega_K^2 t_s}}. \quad (239)$$

If the turbulent diffusivity is comparable to the turbulent viscosity, i.e. $D \sim \nu$, the ratio of the concentration scale height to the gas scale height is just,

$$\frac{h_p}{h} \simeq \sqrt{\frac{\alpha}{\tau_s}}. \quad (240)$$

Solid particles become strongly concentrated toward the disk mid-plane whenever their dimensionless friction time substantially exceeds α . For reasonable values of α this requires substantial particle growth.

7.3 Streaming instability

Youdin & Goodman [439] demonstrated that the aerodynamically coupled system of gas and solids, described by the NSH equilibrium, is linearly unstable to the growth of perturbations. The instability, known as the *streaming instability* by (very rough) analogy with the two-stream instability of plasmas, taps the free energy present in the relative motion between the solid and gaseous fluids, which is ultimately sustained by the background gradient in the pressure. It provides a physically plausible route to forming planetesimals (km or larger bodies that are largely decoupled from the gas) rapidly from smaller solids with $\tau_s \sim 1$ or less.

The pre-requisites for the existence of the streaming instability are two-way aerodynamic coupling between gas and dust within a rotating system (with shear and Coriolis force). A minimal mathematical analysis can be performed in the “terminal velocity approximation”, in which the relative velocity between gas and dust is,

$$\Delta \mathbf{v} = -\frac{\nabla P}{\rho} t_s. \quad (241)$$

This approximation yields a third-order dispersion relation [439], while a more complete analysis (still neglecting vertical stratification) results in a sixth-order system. The linear growth rates, plotted in Youdin & Goodman [439], are functions of τ_s and the ratio of solid to gas density, ρ_d/ρ_g . Growth is typically substantially slower than dynamical, with the most unstable modes having scales $\ll h$. For $\tau_s \sim 10^{-2}$ and $\rho_p/\rho_g \sim 0.1$, for example, the linear growth time scale is a few hundred orbits.

A simple physical (as opposed to mathematical) explanation of the streaming instability is frustratingly elusive. (Analogies to “traffic jams”, or to the drag reducing properties of pelotons in bicycle races, are more relevant to the strong clustering that *results* from the streaming instability than to its existence as a linear instability.) The reader distressed by this state of affairs may seek solace in papers by Chiang & Youdin [89], and by Jacquet et al. [196], who discuss the origin of instabilities in simplified or related physical systems.

The relationship between the saturated state of the streaming instability (which is of greatest interest when the fluctuations in particle density are very strongly non-linear) and the linear growth phase is non-obvious, and requires numerical simulations. Starting with the work of Johansen & Youdin [202], several authors have quantified the outcome of the instability in protoplanetary disks (for recent examples, see e.g. [36, 199, 436]). Simplifying greatly, the streaming instability depends on the particle stopping time τ_s , the local solid to gas ratio (or metallicity, with super-Solar metallicities $Z > 10^{-2}$ being favored [204, 36]) and on the magnitude of the deviation from Keplerian velocity $\eta v_K/c_s$ (with *small* values of this parameter promoting clumping [37]). Using two-dimensional simulations Carrera et al. [81] and Yang et al. [437] find that strong clumping occurs for $Z > Z_{\text{crit}}(\tau_s)$, where the critical metallicity is fit by a piece-wise function,

$$\begin{aligned} \log Z_{\text{crit}} &= 0.10(\log \tau_s)^2 + 0.20 \log \tau_s - 1.76 \quad (\tau_s < 0.1), \\ \log Z_{\text{crit}} &= 0.30(\log \tau_s)^2 + 0.59 \log \tau_s - 1.57 \quad (\tau_s > 0.1). \end{aligned} \quad (242)$$

These results suggest that the sweet spot where the lowest metallicity is required for strong clustering occurs for $\tau_s \approx 0.1$ at $Z \approx 0.015$.

The existence of a strongly inhomogenous distribution of solid particles has important implications for particle growth and planetesimal formation, irrespective of whether the over-densities are strong or very strong. There is particular interest, however, in determining whether the streaming instability can yield over-densities that exceed the Roche density (§6.2.3), given approximately by,

$$\rho_p \sim \frac{M_*}{r^3}. \quad (243)$$

Particle clumps whose density exceeds the Roche density can collapse gravitationally into planetesimals, whose properties (such as size and binarity [304]) will depend upon the statistics of the particle density field generated by the streaming instability. Collapse is a likely outcome in regions of the disk where the streaming instability is strong [201, 199]. Current simulation results suggest that collapse forms a population of planetesimals with an initial mass function that can be fit with a

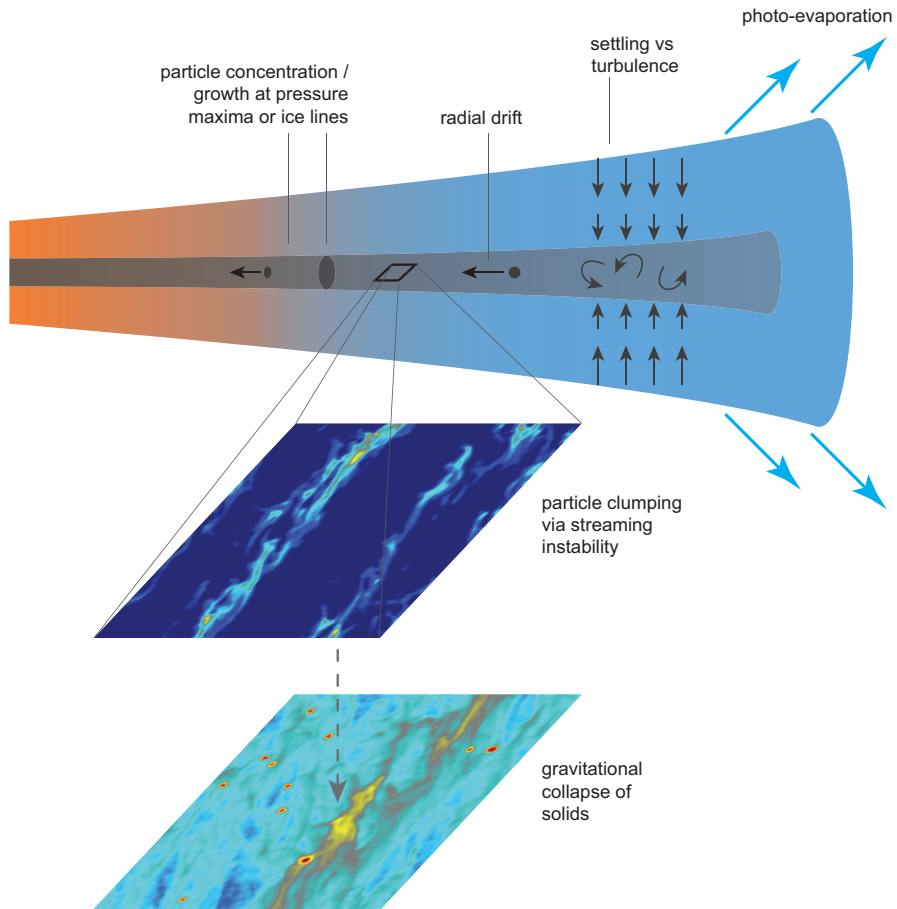


Fig. 27 Illustration of some of the processes that can lead to streaming instability in the aerodynamically coupled particle-gas system. (Simulations of the streaming instability and gravitational collapse by Jake Simon [376])

power-law [200, 376, 371],

$$\frac{dN}{dM_p} \propto M_p^{-1.6}, \quad (244)$$

whose exponent displays at most a weak dependence on the stopping time of the particles that participate in the instability [377]. This predicted mass function is top-heavy, in the sense that most of the mass resides in a handful of the largest objects (in contrast to the stellar IMF, which has the opposite property [55]). The role of intrinsic gas-phase disk turbulence (which is not included in most of the recent calculations) in modifying the predicted mass function has not, however, been fully established.

The circumstances that lead to the formation of streaming-unstable regions within protoplanetary disks, along with the outcome of the instability when it occurs, are by no means definitively established. Figure 27 illustrates the flavor of theoretical models now under investigation [198], which invoke the single particle processes discussed in this section as essential elements. Vertical settling and radial drift, operating on particles that have grown through collisions [70] to be imperfectly coupled to the gas, act to enhance the local metallicity toward the values where the streaming instability would operate. Settling and pile-up, however, may not always be sufficient, and the next section is devoted to processes that can generate structure and additional enhancement in the local metallicity within the disk.

- Particles with sizes from microns up to centimeters are coupled to the disk gas by aerodynamic forces, operating in the Epstein regime (where the particle size is smaller than the molecular mean-free-path, leading to a linear dependence of the drag on relative velocity).
- Aerodynamic forces acting on particles lead to radial drift, because the gas in the disk feels radial pressure forces that are not experienced by the particles. Drift is directed toward pressure maxima. In a disk with a monotonically declining pressure profile drift is inward, extremely rapid, and can lead to a transient pile-up of solids in the inner disk regions.
- Vertical settling also occurs on a time scale that is short compared to the disk lifetime. It can be inhibited by even modest levels of fluid turbulence, and is usually accompanied by coagulation and fragmentation processes.
- When the feedback of a radially drifting particle fluid on the gas is accounted for, the resulting coupled system of gas and particles is often linearly unstable to the streaming instability. Given appropriate conditions this can lead to very strong clustering of the particles, followed by gravitational collapse.

8 Structure formation in protoplanetary disks

Up until now we have largely assumed that the gas and dust in protoplanetary disks follow axisymmetric distributions, with smooth (but very probably different [12]) radial profiles. This is an approximation, which is known to fail spectacularly in some observed systems. As discussed in §2 disks show a variety of structures:

- Classification of a significant fraction of protoplanetary disks as *transitional disks* [124], based on evidence of inner cavities in (at least) the dust distribution.
- Radial structure in molecular emission linked to the presence of ice lines, for example of CO [344].
- Multiple rings of emission seen in high resolution mm / sub-mm observations of HL Tau [8] and other systems.
- Pronounced non-axisymmetric (“horseshoe”-shaped) sub-mm emission in systems including IRS 48 [422].
- Spiral arms and other non-axisymmetric structures seen in scattered light images of disks [161].

An open and important question is whether these structures are a consequence of — or a precursor to — planet formation. That question cannot yet be answered, but keeping it in mind we discuss here a number of processes that can lead to the formation of directly observable (and hence necessarily large-scale) structure in one or both of the gas and dust distributions within disks. Independent of the topical observational interest, any process that can generate inhomogeneity in the solid distribution is potentially important theoretically. In particular planetesimal formation could be made easier if there are processes that enhance the ratio of solids relative to the gas (in rings, vortices etc), creating conditions more favorable for both direct collisions and for the streaming instability.

8.1 Ice lines

The water snow line, together with the silicate sublimation front and various ice lines in the outer disk, are potentially critical locations for planet formation. Most often, this importance is quantified by noting that the equilibrium chemical composition of a Solar abundance gas has a substantially larger mass of condensible solids outside the snow line than inside (by about a factor of 4 in the classical Minimum Mass Solar Nebula [175], rather less than that using more modern calculations of the chemical equilibrium [258]). The likelihood that this leads to a jump in solid surface density at the snow line is then invoked as the reason why the Solar System has only terrestrial planets at smaller radii, and giants beyond.

These arguments are valid but incomplete. First, the equilibrium chemical composition is only linked directly to the solid surface density in the limit where the solid particles remain small and well-coupled to the gas. Particles that grow to be

large enough that radial drift becomes significant will instead develop a surface density profile that is both different from that of the gas (§7.1.3, [441]), and dependent on the size distribution. If icy particles are typically substantially larger than silicates (as is frequently suggested) their more rapid radial drift could lead to an instantaneously *lower* surface density of solids outside the snow line than inside. Second, although it is *possible* to construct models in which an assumed jump in planetesimal surface density at the snow line contributes to efficient core formation, the compositional effect is not the whole story. The greater area of planetary feeding zones at larger radii, along with more complex effects such as Type I migration and pebble accretion, affect the outcome of planet formation at different radii to a similar extent. The most important role of ice lines may instead be as a preferential site for planetesimal formation, or perhaps as a location where Type I migration stalls.

The pressure in the protoplanetary disk is substantially below that of the triple point of water, and hence the snow line marks a radial transition between ice and water vapor. Under mid-plane conditions, the corresponding temperature is typically $T = 150 - 180$ K. Where this isotherm lies in the disk is a function of the stellar luminosity and accretion rate — neither of which are constant over time — and of the disk opacity which may change due to coagulation. Theoretical models [240, 151, 293] suggest that when $\dot{M} \approx 10^{-7} M_{\odot} \text{ yr}^{-1}$ r_{snow} is at ≈ 3 AU, before moving inward to within 1 AU as the accretion drops to $\dot{M} \approx 10^{-9} M_{\odot} \text{ yr}^{-1}$. At still lower \dot{M} the inner disk becomes optically thin, and the resultant rise in temperature pushes the snow line back out to 2-3 AU.

The above estimates, calculated within the framework of relatively simple disk models that include viscous heating and irradiation, are significantly modified [282] if the true disk structure instead resembles Gammie's [148] layered model with a mid-plane dead zone. The calculation of snow line evolution may require further revision if winds, which potentially change both the surface density profile and the fraction of potential energy that goes into disk heating, are important on AU-scales.

Figure 28 illustrates some of the key physical processes occurring near ice lines. Where ice lines occur can be calculated by use of the Clausius-Clapeyron relation, which gives the saturated vapor pressure P_{eq} at temperature T in terms of the latent heat L of the phase transition,

$$P_{\text{eq}} = C_L e^{-L/\mathcal{R}T}. \quad (245)$$

Here \mathcal{R} is the gas constant, and C_L is a constant that depends upon the species involved. For water, $L/\mathcal{R} = 6062$ K and $C_L = 1.14 \times 10^{13} \text{ g cm}^{-1} \text{ s}^{-2}$ [91]. We can compare this pressure to the actual partial pressure of vapor in the disk. Using water (molecular weight $\mu_{\text{H}_2\text{O}} = 18$) as an example, if the surface density of vapor is Σ_v , the mid-plane pressure is,

$$P_v = \frac{1}{\sqrt{2\pi}} \frac{\Sigma_v}{h} \frac{k_B T}{\mu_{\text{H}_2\text{O}} m_H}. \quad (246)$$

If $P_v < P_{\text{eq}}$ water ice will sublimate, whereas if $P_v > P_{\text{eq}}$ vapor will condense into solid form. For small particles whose sizes are measured in mm or cm sublimation is

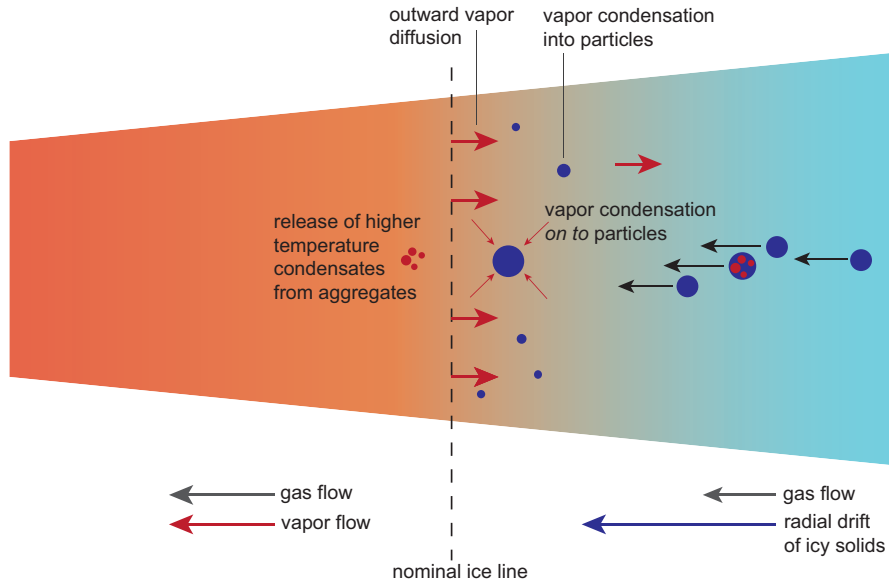


Fig. 28 Illustration of some of the physical processes occurring near ice lines in the protoplanetary disk. Icy materials drifting radially inward sublimate when they reach the ice line, releasing any higher temperature materials that were embedded into aggregates [91]. The resulting vapor flows toward the star at the same speed as the rest of the gas, but also diffuses outward down the steep gradient in concentration [390]. It may then recondense, either into new particles or on to pre-existing particles [363]. Some combination of these effects may feedback upon the gas physics via changes to either the opacity or, in models where MHD processes dominate angular momentum transport, the ionization state [229].

rapid [91], and hence to a reasonable approximation sublimation and condensation processes act to maintain the vapor pressure close to the equilibrium value.

The large value of L/\mathcal{R} implies that the snow line is a sharply defined transition within the disk. At 150 K, the characteristic temperature interval over which the equilibrium vapor pressure varies, $P_{\text{eq}}/(dP_{\text{eq}}/dT)$, is just a few Kelvin. If sublimation of icy particles that drift through the snow line is fast, this has the consequence of imposing a sharp radial gradient in water vapor concentration at the snow line which, in a turbulent disk, will in turn result in a diffusive outward flux of vapor (equation 222). Re-condensation of the vapor can then lead to an enhancement of the solid surface density immediately outside the snow line.

Stevenson & Lunine [390] proposed that a vapor diffusion / condensation cycle of this type could enhance the surface density of ice enough to promote the rapid formation of Jupiter's core. The strength of the effect depends upon the size of the icy solids drifting in toward the snow line, and upon what is assumed about processes including disk turbulence, condensation and coagulation / fragmentation. Figure 29 shows the results of a particularly simple calculation ([22] after [96, 91]), which assumes that vapor condenses (or, condenses and rapidly coagulates) into solid particles of a single size that *matches* the size of icy solids drifting in from

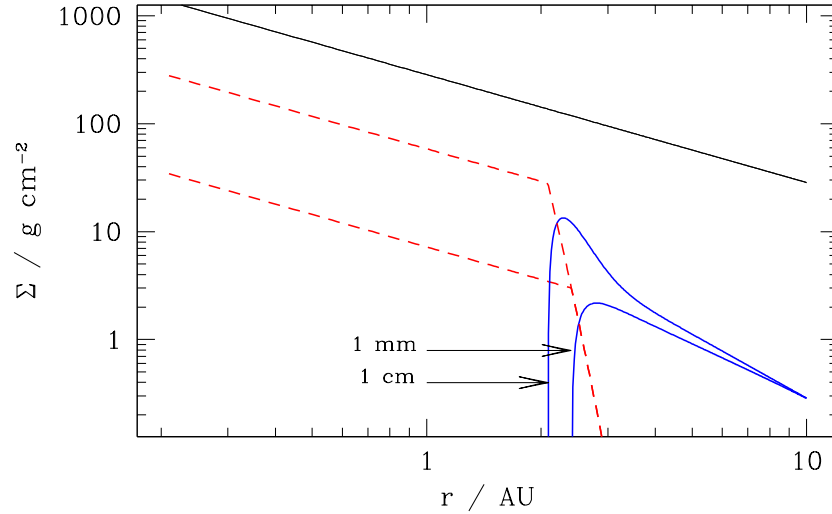


Fig. 29 Example steady-state profiles of gas (upper solid line), radially drifting icy particles (solid blue lines) and water vapor (red dashed lines) in a turbulent protoplanetary disk. The assumed disk model has an accretion rate of $10^{-8} M_{\odot} \text{ yr}^{-1}$, a temperature $T = 150(r/3 \text{ AU})^{-1/2}$, and an α parameter of 5×10^{-3} . The ratio of the turbulent diffusivity to the turbulent viscosity is taken to be unity, and the concentration of icy solids is set (arbitrarily) to be 10^{-2} at 10 AU. The rapid radial drift of cm-sized particles leads to a high concentration of water vapor in the inner disk. Outward diffusion and re-condensation of this vapor — assumed here to form particles of a single fixed size — leads to an enhancement of solids just outside the snow line [390]. Note also the more elementary conclusion that the vapor concentration in the inner disk is a direct probe of the mass flux of radially drifting solids encountering the snow line.

larger radii. For the adopted disk model, mm-sized icy solids have relatively low drift velocities, and these particles sublime into vapor without generating any local enhancement in the surface density of solids. Larger cm-sized particles, conversely, are enhanced by a factor of several outside the snow line as a consequence of the diffusive transport of vapor followed by condensation. Surface density enhancements of this magnitude could be important, particularly in models where planetesimal formation depends upon the disk locally exceeding a threshold value of metallicity (as is the case for the streaming instability, see §7.3, [204]).

Ros & Johansen [363] investigated a related possibility. Instead of assuming that vapor condenses into new particles (or, on to very small grains released when aggregates break up at the snow line), they modeled the growth of pre-existing solids as vapor condenses on to their surfaces. A simple collisional argument gives the growth rate due to vapor condensation / sublimation as,

$$\frac{dm}{dt} = 4\pi s^2 v_{\text{th}} \rho_v \left(1 - \frac{P_{\text{eq}}}{P_v} \right), \quad (247)$$

for a particle of mass m and radius s , surrounded by vapor of density ρ_v and thermal speed v_{th} . (As noted by Supulver & Lin [393], this is not an exact expression [176].) Using a Monte Carlo approach, Ros & Johansen [363] found that condensation on to particle surfaces could provide an efficient growth mechanism up to sizes of the order of 10 cm. This could aid planetesimal formation by boosting the stopping time of particles into the range preferred by the streaming instability [81]. Moreover, by removing mass from the directly observable mm-size regime, condensation-driven growth could suppress the mm and sub-mm flux from disks in the vicinity of ice lines [442].

The aforementioned physics affects only trace components of the disk — the icy solids and the resulting vapor. It is easy, however, to contemplate feedback processes that couple the evolution of solids at ice lines to the bulk of the gas disk. At a minimum the opacity will vary depending upon the radial distribution of solids. Beyond that, we have already noted that the efficiency of angular momentum transport (in MHD models) is expected to be a function of the local ionization state, and that the ionization balance is affected by the abundance of small grains. Kretke & Lin [229] suggested that the enhanced abundance of solids near the snow line would act to suppress the rate of angular momentum transport, and that this could lead to the formation of a local pressure maximum that would act to trap particles (producing, in principle, a positive feedback loop). This argument (which has been invoked in some models of collisional growth [76]) is highly plausible, though the breadth and complexity of the physics involved makes quantitative investigation challenging.

Although we have focused here on the snow line, analogous considerations carry over to other ice lines. The CO ice line corresponds to a temperature of $T = 17 - 19$ K [66], and is somewhat more complicated to model because the CO is typically mixed with N_2 and water ices. The silicate “ice line” (or sublimation front) could also be important, since it lies at radii where a high fraction of stars are observed to host short-period planetary systems.

8.2 Particle traps

In a disk with a monotonically declining pressure profile radial drift is always inward. More generally, however, aerodynamic drift is directed toward pressure maxima, and can be outward if there is a local pressure maximum within the disk. This possibility was recognized in a prescient paper by Whipple [433], who appealed to it as part of a model for the formation of comets¹⁹. The tendency for solids to be aerodynamically enhanced in the vicinity of pressure maxima is often described as particle “trapping”, though this term is somewhat misleading; in a turbulent disk small particles are at most temporarily detained by pressure maxima rather than being permanently trapped.

¹⁹ Quoting from his paper, “should it be possible for a toroid of higher density to occur in the Solar nebula, the growing planetesimals would be drawn toward it from the inside as well as from the outside...”.

The effect of local pressure maxima on the radial distribution of solids can be derived, in the limit where the solids remain a trace contaminant, following the methods described in §7.1.1 and §7.1.2. For an axisymmetric disk with an arbitrary mid-plane pressure profile, the radial velocity v_r of particles under the action of aerodynamic forces remains as given by equation (219), with the parameter η describing the deviation from Keplerian velocity becoming [397],

$$\eta = - \left(\frac{h}{r} \right)^2 \left[\frac{d \ln \Sigma}{d \ln r} + (q - 3) \right]. \quad (248)$$

In this formula q is defined as the local power-law index describing the flaring of the disk,

$$\frac{h}{r} \propto r^{q-1}, \quad (249)$$

such that a non-flaring disk has $q = 1$. In axisymmetry and steady-state, equations (221) and (222) can be immediately integrated to give,

$$r(F_{\text{diff}} + F_{\text{adv}}) = k, \quad (250)$$

where the diffusive and advective fluxes are,

$$\begin{aligned} F_{\text{diff}} &= -D\Sigma \frac{d}{dr} \left(\frac{\Sigma_d}{\Sigma} \right), \\ F_{\text{adv}} &= \Sigma_d v_r, \end{aligned} \quad (251)$$

and the constant k is just the radial flux of solid material. Written out explicitly, the concentration of particles $f \equiv \Sigma_d/\Sigma$ obeys a first-order differential equation,

$$\frac{df}{dr} - \frac{v_r}{D} f = \frac{k}{D\Sigma} \frac{1}{r}. \quad (252)$$

Analytic solutions to this equation are possible for simple choices of v_r , D and Σ . A straightforward quadrature gives the solution for the concentration profile given more realistic choices of these functions.

Figure 30 shows an illustrative numerical solution to equation (252). For this example, we have modeled a trap by assuming (arbitrarily) that the viscosity in the gas disk is reduced across a moderately narrow annulus. The lower viscosity leads to a higher surface density, producing a pressure maximum which in turn concentrates particles. The concentration effect is strongly size-dependent. Small particles (in this example those with radii of 0.1 mm and 1 mm) have a radial velocity that is similar to that of the gas, and are largely unaffected by the pressure maximum. Larger cm-sized particles, on the other hand, have a larger magnitude of radial drift, and can be strongly concentrated at the location of the pressure maximum. The enhancement in the local particle density can reach several orders of magnitude, depending both on the particle size and on the “strength” (radial width and amplitude) of the pressure maximum within the gas disk.

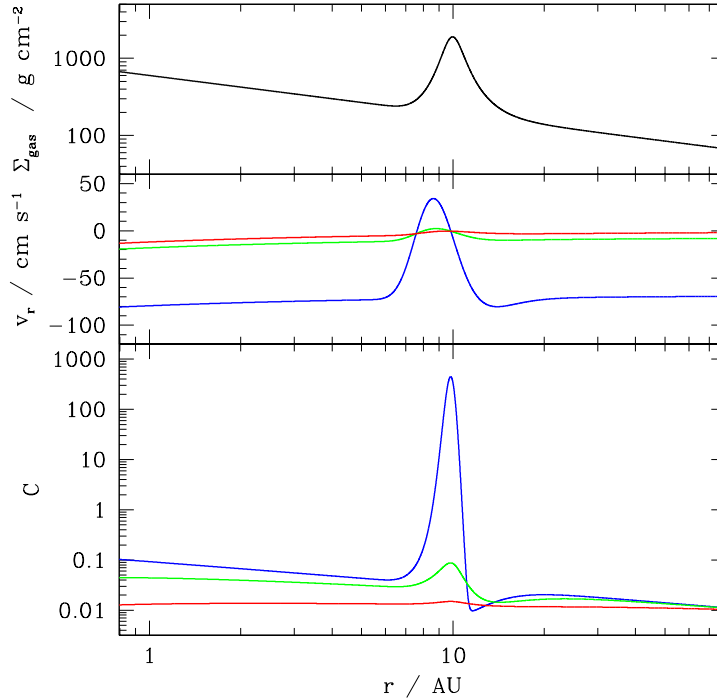


Fig. 30 The steady-state radial distribution of solids in a turbulent disk with an axisymmetric local pressure maximum (a particle “trap”). Upper panel: the surface density of the gas. Middle panel: the radial velocity of 0.1 mm (red), 1 mm (green) and 1 cm (blue) particles. The smallest particles have a radial velocity that is almost indistinguishable from that of the gas, while the larger particles experience rapid radial drift that can be outward near the location of the pressure maximum. Lower panel: the concentration $C = \Sigma_d / \Sigma_{\text{gas}}$, normalized to an arbitrary value of 10^{-2} at 100 AU. The assumed disk model for this calculation has $\dot{M} = 10^{-8} M_{\odot} \text{ yr}^{-1}$, $M_* = M_{\odot}$, $h/r = 0.5$, $\alpha = 10^{-3}$ and $D = v$ (c.f. equation 223). The trap is modeled as a gaussian-shaped reduction in α to a minimum of 10^{-4} , with a width of $4h$. The particles are assumed to be spherical, with a material density of 1 g cm^{-3} , and to follow the Epstein drag law.

It should be noted that in a turbulent disk (and ignoring particle feedback on the gas) it is *always* possible to find a steady-state solution for the radial particle concentration in which the particle mass flux is a constant at all radii. Physically, this is because particles accumulate near pressure maxima until the radial gradient in concentration becomes large enough for turbulent diffusion to allow them to leak out [427, 447]. Pressure maxima only act as a “filter” [355], *permanently* removing large particles from the inward radial drift flow, when additional physical effects are included [447]. If the local concentration of large particles becomes large enough, for example, planetesimal formation [169] could cause some fraction of the solid material to drop out of the radial flow.

A number of physical effects have been identified that could lead to the formation of local pressure maxima within protoplanetary disks. These include the exterior edges of planet-carved gaps [321, 355, 447], the outer edges of cavities created by photoevaporation (§9.1, [5]), and a photoelectric heating instability that may operate in gas-poor systems (primarily debris disks) [63, 271]. Spiral arms in self-gravitating disks [357, 153] and the inner edges of dead zones [270] can also concentrate solids via closely related physical processes, though these environments typically involve significant non-axisymmetry. With the exception of self-gravity, these possible locations for pressure maxima either form at specific places within the disk (e.g. at the inner dead zone edge, defined by a characteristic mid-plane temperature), or at a time after when we expect planets to have formed (during photoevaporative disk clearing, or in *response* to pre-existing massive planets). It is possible, however, for the turbulence within the gas disk to be generically unstable to the formation of pressure maxima within zonal flows. This would be interesting because it would imply the (possibly transient) existence of multiple particle traps within the disk, that could play a role in early-stage planet formation [334].

8.3 Zonal flows

It is evident from equation (23) that an equilibrium can be set up in which radial forces from a complex pressure profile (that may include local pressure maxima) are balanced by radial variations in azimuthal velocity. In a local description (equation 138, but here ignoring magnetic fields) the balance is between the pressure gradient term $\nabla P/\rho$ and that describing the Coriolis force $2\Omega_0 \times \mathbf{v}$. When these terms balance, such that

$$\frac{dP}{dx} = 2\Omega_0 \rho v_y, \quad (253)$$

the system is said to be in *geostrophic balance* (here x is the radial direction, and y the azimuthal). The pressure gradient is compensated by variations in the orbital velocity, creating *zonal flows* analogous to the banded structure of winds in giant planet atmospheres.

A disk zonal flow is an equilibrium solution to the fluid equations, but that equilibrium may not be stable. Too pronounced a deviation from Keplerian rotation results in a shear profile that is unstable to Rossby wave instability [260]. We will discuss this instability, which is similar to Kelvin-Helmholtz instability, in §8.5. Even if the rotation profile is stable, the diffusive nature of a classical viscosity (equation 62) would tend to erase any small-scale perturbations in the pressure that are sourced from surface density fluctuations. Persistent zonal flows are thus not expected in classical disk theory. They have been observed, however, in local numerical simulations of MHD turbulent disks [203]. The key to their formation appears to be the ability of MHD disk turbulence to generate large-scale structure in the magnetic field [380], which could be viewed as an inverse cascade of turbulent power. The details of how and when zonal flows form are not entirely clear, though Johansen

et al. [203] describe a simplified dynamical model in which large-scale variations in the Maxwell stress lead first to azimuthal velocity perturbations and thence to axisymmetric structure in the pressure and density.

The lifetime and radial scale of zonal flows in protoplanetary disks depend upon the same factors that determine the properties of MHD disk turbulence more generally (§5.4.4), namely the strength of non-ideal terms in the induction equation and the presence of net vertical magnetic field. In ideal MHD, lifetimes of tens of orbital periods and radial scales of the order of $10 h$ appear to be typical [203, 380], though these results require a double dose of caveats — first because the inferred scales are not much smaller than the size of the local simulation domains used, and second because they are large enough that curvature terms neglected in local models may be important. Nonetheless, the amplitude, scale and lifetime of zonal flows under ideal MHD conditions plausibly lead to strong local enhancements in the dust to gas ratio for particles with stopping times $\tau_s \sim 0.1 - 1$ [111]. The presence of net vertical fields substantially enhances the amplitude of zonal flows [40].

Zonal flows are also found in MHD disk simulations that include ambipolar diffusion, and can be comparable in amplitude to the ideal MHD case if the net field is sufficient to stimulate a significant $\alpha \sim 10^{-2}$ [375]. However, both inferences from local simulations [375], and explicit tracking of particles in global simulations [449], suggest that zonal flows in the outer regions of protoplanetary disks, where ambipolar diffusion dominates, have properties close to the boundary beyond which strong particle enhancement would be expected.

In summary, zonal flows are likely to be present in the inner disk, where ideal MHD is a good approximation, though these flows would only strongly influence the dynamics of relatively large solid particles. In the outer disk, where ambipolar diffusion is important and even mm-sized particles have significant stopping times, zonal flows could introduce observable large-scale axisymmetric structure and may contribute to particle concentration. In the Hall-dominated regime that prevails around 1 AU theoretical expectations are less clear. Extremely strong zonal structures were observed in local vertically unstratified Hall-MHD simulations [233], whereas comparable stratified runs instead led to large-scale Maxwell stress [241]. It is therefore unclear whether there are circumstances in which zonal flows on AU-scales could contribute to particle concentration and planetesimal formation.

8.4 Vortices

Few issues in planet formation are as long-debated as the possible role of vortices. Very general arguments suggest that large-scale vortices could be present in protoplanetary disks and play an important role in planetesimal formation. We note first that disks are (approximately) two dimensional fluid systems, and in contrast to three dimensional systems they therefore support an inverse cascade of turbulent energy toward large scales [224]. Second, for a barotropic disk (i.e. $P = P(\rho)$ only) the vorticity ω/ρ is conserved (equation 124). Taken together, these proper-

ties imply that vortices within disks have the potential to form persistent long-lived structures. Indeed, simulations of strictly two dimensional flows show that disks seeded with small-scale vorticity perturbations evolve to form a small number of large and persistent anticyclonic vortices [154, 206]. Anticyclonic vortices are high pressure regions that attract marginally coupled solids [51, 400], potentially catalyzing the subsequent formation of planetesimals. Even absent planetesimal formation, the natural tendency of vortices to form large-scale non-axisymmetric dust features makes it tempting to identify them with observed disk asymmetries [422].

The basic properties of disk vortices are well-established. What is much trickier is to determine (1) whether vortices form spontaneously in disks or only *after* planet formation (for the reasons already mentioned, spontaneous vortex formation generally requires non-barotropic processes), and (2) whether three dimensional instabilities and / or particle feedback are fatal impediments to their survival. Observations as well as theory are probably needed to resolve these issues.

8.4.1 The Kida solution

The magnitude of the vorticity in a strictly Keplerian disk is $\omega_K = -(3/2)\Omega_K$. A vortex can be modeled as a spatially localized elliptical perturbation, within which the vorticity $\omega = \omega_K + \omega_v$, with ω_v a constant. Other types of vortex are possible, but rather remarkably this type can be described by an exact non-linear solution [214] that is useful for both analytic and numerical studies.

The Kida solution [214] describes a vortex within a shearing-sheet approximation to disk flow. Following Lesur & Papaloizou [244] we define a cartesian co-ordinate system (x, y) that is centered at radius r_0 and which co-rotates with the background disk flow at angular velocity $\Omega_K = \Omega_K(r_0)$,

$$\begin{aligned} x &= r_0\phi, \\ y &= -(r - r_0). \end{aligned} \tag{254}$$

Kida considered time-dependent vortex solutions, but here we will worry only about vortices that are steady²⁰. Time-independent solutions are possible if the semi-major axis of the vortex is aligned with the azimuthal direction (x in the shearing sheet model), and the vorticity perturbation satisfies,

$$\frac{\omega_v}{\omega_K} = \frac{1}{\chi} \left(\frac{\chi + 1}{\chi - 1} \right). \tag{255}$$

Here $\chi = a/b$ is the aspect ratio of the vortex, which forms an elliptical patch with semi-major axis a and semi-minor axis b . The right-hand-side is evidently positive, which implies that the only steady Kida vortices in Keplerian disks are anticyclonic (with ω_v having the opposite sign to Ω_K).

²⁰ For a derivation of the steady Kida solution, see e.g. the appendix of Chavanis [88].

The complete Kida solution is written in terms of a streamfunction ψ in an elliptic co-ordinate systems (μ, ν) , where,

$$\begin{aligned} x &= f \cosh(\mu) \cos(\nu), \\ y &= f \sinh(\mu) \sin(\nu), \end{aligned} \quad (256)$$

and $f = a\sqrt{(\chi^2 - 1)/\chi^2}$. The solution can be split into a core and an exterior part,

$$\begin{aligned} \psi_{\text{core}} &= -\frac{3\Omega_K f^2}{4(\chi - 1)} [\chi^{-1} \cosh^2(\mu) \cos^2(\nu) + \chi \sinh^2(\mu) \sin^2(\nu)], \\ \psi_{\text{ext}} &= -\frac{3\Omega_K f^2}{8(\chi - 1)^2} [1 + 2(\mu - \mu_0) + 2(\chi - 1)^2 \sinh^2(\mu) \sin^2(\nu) \\ &\quad + \frac{\chi - 1}{\chi + 1} \exp[-2(\mu - \mu_0)] \cos(2\nu)], \end{aligned} \quad (257)$$

which match at $\mu = \mu_0 = \tanh^{-1}(\chi^{-1})$. The cartesian velocity field is then given by $v_x = -\partial\psi/\partial y$, $v_y = \partial\psi/\partial x$. In general the cartesian representation of the velocity has no simple form, but within the core it is,

$$\begin{aligned} v_{x,\text{core}} &= \frac{3\Omega_K \chi}{2(\chi - 1)} y, \\ v_{y,\text{core}} &= -\frac{3\Omega_K}{2\chi(\chi - 1)} x, \end{aligned} \quad (258)$$

describing simple elliptical motion. Figure 31 shows the contours (logarithmically spaced) of the full streamfunction for Kida vortices of varying aspect ratio.

Barge & Sommeria [51] studied the trajectories of aerodynamically coupled solids that encounter vortices (using a different and approximate vortex model). The high pressure within anticyclonic vortex cores acts as an attractor for solids. The cross-section for capture is maximized for particles with dimensionless stopping time $\tau_s = 1$ [88]. Since vortices can potentially grow to have radial extents $\Delta r \approx h$ (the supersonic velocity perturbations of larger vortices would radiate sound waves sapping their energy) a single large vortex can potentially trap a substantial mass of solids flowing radially toward it due to ordinary radial drift.

8.4.2 Stability of vortices

Although the geometry of protoplanetary disks is approximately two dimensional, the fact that disk vortices are limited in radial size to $\Delta r \approx h$ means that they are three dimensional objects that notice the vertical stratification. Barranco & Marcus [53] and Shen et al. [373], using three dimensional simulations, found that mid-plane vortices that would be highly stable in 2D are rapidly destroyed by three dimensional instabilities. The origin of these observed instabilities, at least in part, appears to be the *elliptical instability* [213], which occurs whenever there is a resonance between

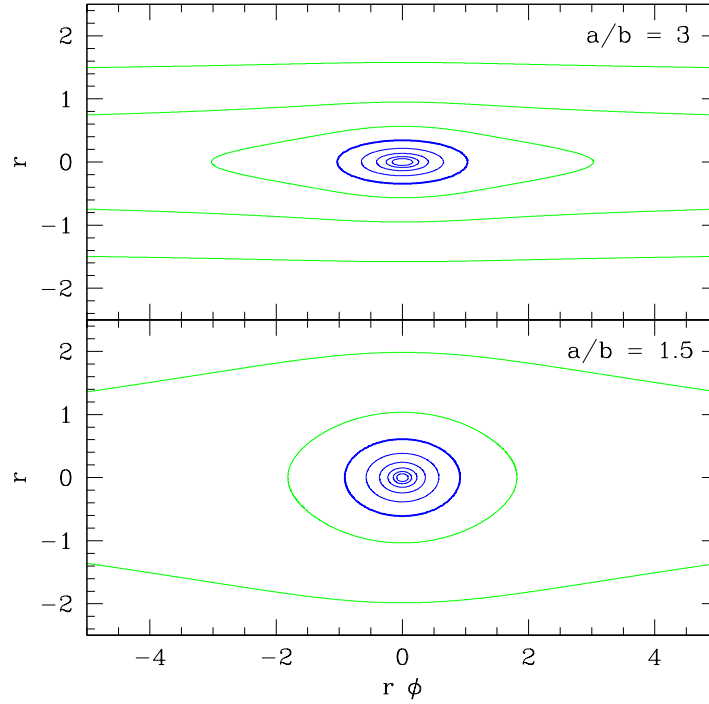


Fig. 31 Contours of the Kida vortex streamfunction $\psi(x, y)$ are shown for different values of the vortex aspect ratio $\chi \equiv a/b$. Within the vortex core, delineated by the bold contour, the streamlines defined by the solution are elliptical, with fixed aspect ratio. Outside the core, the vortex merges smoothly into the background shear flow of the disk.

the vortex rotation period and inertial waves within the disk. In a disk environment, Lesur & Papaloizou [244] find that purely gaseous vortices are unstable for almost all choices of the vortex aspect ratio and degree of vertical stratification, though these parameters strongly affect the linear growth time of the instability. The instability that afflicts 3D vortices, however, is typically slow-growing and of small radial scale. Numerically this makes studies of vortex survival particularly challenging. Physically it means that the questions of vortex formation and vortex survival are closely linked, except perhaps at very large radii (where “primordial vortices” might persist for interesting periods of time) the vortex population in a disk is expected to reflect an equilibrium between formation and destruction processes.

A significant loading of solids will also impact vortex longevity, generally for the worse. Raiton & Papaloizou [349] studied the stability of generalized Kida vortices, containing both gas and dust in the limit of strongly aerodynamically coupled particles. They found that these configurations were vulnerable to parametric instabilities in the same way as gas-only vortices. This is consistent with a wide range of other analytic and numerical work [86, 191, 145], which suggests that dust to

gas ratios in the range between 0.1 and 1 are sufficient to imperil the survival of disk vortices. This limitation may not, however, preclude vortices playing a role in planet formation. If we assume that there is a continual source of vorticity within the disk, then vortex particle concentration up to $\rho_p \sim \rho_g$ could be sufficient to initiate planetesimal formation via a variation of the streaming instability [345].

Observations have identified a number of systems (primarily transition disks) that show a non-axisymmetric distribution of sub-mm emission [83, 195, 422], consistent with that expected if aerodynamically coupled solids are accumulating in a vortex [448]. The putative vortices in these examples may all be *caused* by planets. It would be interesting to ask whether useful constraints on vortices could be derived from observations of the *most-axisymmetric* disks, where there is no independent suspicion that planets already exist.

8.5 Rossby wave instability

The Rossby wave instability (RWI) [260, 249, 248] is a well-characterized mechanism for producing vortices within protoplanetary disks. The RWI is a linear instability that grows whenever there is “sufficiently sharp” radial structure in the disk. Specifically, for a two dimensional disk model with angular velocity $\Omega(r)$, vertically integrated pressure $P(r)$, and adiabatic index γ , we define the entropy S and epicyclic frequency κ via,

$$\begin{aligned} S &= \frac{P}{\Sigma\gamma}, \\ \kappa^2 &= \frac{1}{r^3} \frac{\partial}{\partial r} (r^4 \Omega^2). \end{aligned} \quad (259)$$

In terms of these quantities, the stability of the disk to the RWI is determined by the radial profile of a generalized potential vorticity,

$$\mathcal{L}(r) = \frac{\kappa^2}{2\Omega\Sigma} \times S^{-2/\gamma}. \quad (260)$$

A necessary condition for RWI is that \mathcal{L} have an extremum. A precise sufficient condition is not known, but variations in the potential vorticity of the order of 10% over radial scales $\approx h$ appear to be enough to trigger instability, which leads to the formation of anticyclonic vortices on time scales that can be rapid — of the order of $10\Omega^{-1}$ [249]. The instability, which can be understood in terms of the local trapping of waves in the vicinity of the vortensity perturbation [155, 418], has similarities to the Papaloizou-Pringle [326] instability of accretion tori. The RWI is essentially a two dimensional instability [289, 252], though the vortices that it forms are as vulnerable to unrelated three dimensional instabilities as any others.

We have already remarked that the edges of dead zones (and ice lines [229]) are places where local pressure maxima may form. The RWI criterion (equation 260) is

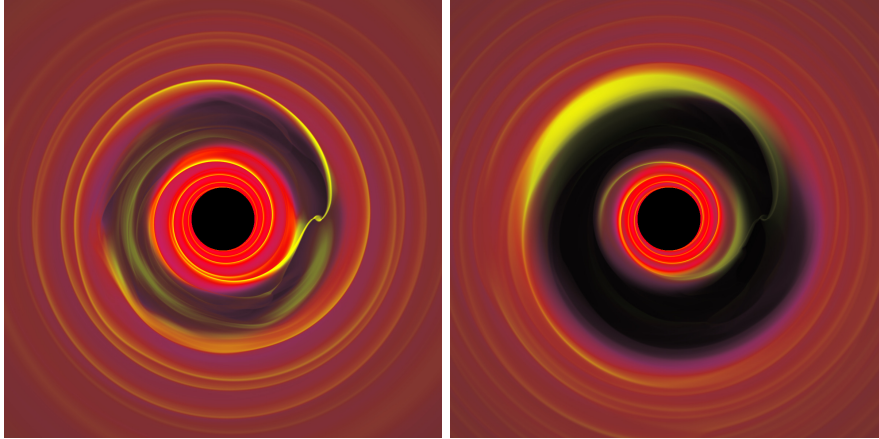


Fig. 32 Snapshots showing the hydrodynamic evolution of an almost inviscid disk containing a massive planet [20]. The planet rapidly clears an annular gap within the disk, whose edge is unstable to the generation of vortices. The system then evolves through a phase when the outer gap edge hosts a single large vortex, which can be an efficient trap for solid particles. The disk has $\alpha = 10^{-4}$ and $h/r = 0.05$ at the location of the planet, which has a mass ratio to the star of 5×10^{-3} .

not necessarily satisfied at every local pressure maximum, but it is nonetheless true that dead zone edges are plausible locations where the RWI may occur. Hydrodynamic models [423, 191, 269], and MHD simulations that include Ohmic diffusion as a simple model of dead zones [272, 126, 273, 132], support this expectation, and show that the radial disk structure introduced by dead zones is likely to be unstable to the RWI and subsequent formation of vortices. The vortices in turn act as sites of particle concentration [269]. Depending upon the radii involved, a single vortex generated by the RWI may have a lifetime that is very short as compared to the disk lifetime (this will be particularly true at the inner edge of the dead zone). However, in this scenario fresh generations of vortices may be expected to form as long as the non-ideal disk physics that sustains the RWI-unstable dead zone structure persists.

A second location where RWI may occur is at the edge of a gap created dynamically by a massive planet [221, 108]. Figure 32 shows the evolution of a disk in a two-dimensional simulation of this scenario. The formation of a massive planet creates an approximately axisymmetric gap within the disk, whose edges can be unstable to the RWI. The vortices that are generated fairly rapidly merge, creating a single large vortex at either edge of the gap then can subsequently trap particles. This process works best if the disk in the vicinity of the planet's orbit has a low viscosity (roughly $\alpha \sim 10^{-3}$ or lower), and is at least partially a transient effect — the vortices form during the phase when the planet accretes its gaseous envelope. For these reasons, observable structure from planet-initiated vortices is likely to be easiest to see in the outer disk, where ambipolar diffusion damps turbulence [379] and the absolute lifetime of a single generation of vortices against disruptive insta-

bilities is long. The particles trapped efficiently in the outer disk include those with $s \sim \text{mm}$ that can be seen in sub-mm observations of protoplanetary disks [450, 448].

- Condensation and sublimation processes are expected to modify the surface density and size distribution of particles in annuli that are adjacent to ice lines (of water, silicates, and possibly species such as CO with cooler condensation temperatures).
- Pressure maxima, whether caused by planets or by intrinsic disk processes such as zonal flows, lead to local axisymmetric enhancements in the particle surface density.
- Vortices can also trap particles. A population of vortices in a disk tend to merge to form a small number of large vortices, which unless replenished have a finite lifetime.
- Sharp features in the radial disk structure can trigger the Rossby Wave Instability, which generates vortices.

9 Disk dispersal

There is no leading order mystery as to where the gas in protoplanetary disks goes to. If we divide the mean disk mass estimated from sub-mm studies in Taurus ($M_d \sim 5 \times 10^{-3} M_\odot$ [9]) by the median accretion rate ($\dot{M} \sim 10^{-8} M_\odot \text{ yr}^{-1}$ [167]) estimated in the same region, we obtain a characteristic evolution timescale of 0.5 Myr. The lifetime of detectable disks might be expected to be a small multiple of this timescale — say a few Myr — which is indeed what is observed [182].

The above exercise establishes that, from a purely observational perspective, most or all of the gas in protoplanetary disks *could* be lost via accretion on to the star. Beyond that, it proves nothing. Disk mass estimates and measurements of stellar accretion rates are subject to uncertainties, which when combined probably allow us to shift the inferred characteristic lifetime by an order of magnitude in either direction. In particular, if disk masses are systematically *under-estimated* from sub-mm continuum observations (because of particle growth to sizes too large to contribute to the sub-mm opacity) the characteristic lifetime could approach or exceed the observed one.

The next order observational diagnostic probes the time-dependence of the decay of disk signatures. Here a puzzle does emerge. The classical disk evolution equation (63) admits a self-similar solution [268] that ought to approximate the evolution at sufficiently late times. For a disk with a viscosity that scales with radius as $\nu \propto r^\gamma$, the late-time evolution of the surface density close to the star is predicted to follow (e.g. [18]),

$$\Sigma \propto t^{-(5/2-\gamma)/(2-\gamma)}. \quad (261)$$

If $\gamma = 1$, for example, as would be the case for a disk with a steady-state surface density profile $\Sigma \propto r^{-1}$, then the predicted late-time decay goes as $t^{-3/2}$. This is relatively slow, and would probably lead to a population of stars with weak disk signatures (in gas and dust tracers) that are not observed (for a review of these observational arguments, see Alexander et al. [4]). One might argue, of course, that this is an illusory problem that we have created for ourselves by placing unwarranted faith in the validity of classical viscous disk theory. A resolution along these lines is possible. More commonly, however, the discrepancy between the simple theory and observations is taken to imply that some distinct process acts to rapidly disperse the disk and terminate accretion. Photoevaporation is almost certainly part of the story, on account both of robust theoretical estimates that suggest it should be important, and observations that are consistent with photoevaporation occurring in some relatively extreme situations.

9.1 Photoevaporation

Disk photoevaporation is a purely hydrodynamic process that occurs when molecular gas in the disk is dissociated or ionized by high energy (UV or X-ray) photons. If

the gas is heated sufficiently to become unbound, it accelerates away from the disk under the influence of pressure gradient forces to form a thermally driven wind. Early models for photoevaporative flows were developed in the 1980s by Bally & Scoville [50] in the context of massive stars surrounded by neutral disks, and in more quantitative detail by Begelman et al. [57] who studied X-ray heated disks around compact objects. The essential physics is thus very well-established. We will begin by considering how photoevaporation works if the disk is exposed to extreme ultraviolet (EUV) photons that have sufficient energy ($h\nu > 13.6$ eV) to ionize hydrogen. This is probably *not* the dominant driver of photoevaporation from protoplanetary disks around low mass stars, but it is amenable to an analytic treatment that exposes the main principles [187].

9.1.1 Thermal winds from disks

We consider a disk whose surfaces are illuminated by a source of high energy photons, that may come either from the central star or from other luminous stars within a cluster. The radiation heats a surface layer of the disk to a temperature T , with a sound speed c_s . A characteristic scale r_g (the “gravitational radius”) can be defined by asking where the sound speed equal the local Keplerian velocity,

$$r_g = \frac{GM_*}{c_s^2}. \quad (262)$$

Noting that the thermal energy per particle is $\sim k_B T$, the radius r_g is approximately equivalent to the smallest radius where the *total* energy of the gas in the heated surface layer (i.e. thermal plus gravitational) is zero. For radii $r > r_g$ the total energy is positive, and it is energetically possible for the surface gas to flow away in a thermal wind.

This is all quite rough, and we should really consider both the hydrodynamic structure of the wind (which is similar to the textbook example of a Parker wind [429]) and the role of rotation [251]. Doing so results in an improved estimate of the critical radius beyond which a thermal wind is launched, which scales with but is significantly smaller than r_g ,

$$r_c \approx 0.2 \frac{GM_*}{c_s^2} \approx 1.8 \left(\frac{M_*}{M_\odot} \right) \left(\frac{c_s}{10 \text{ km s}^{-1}} \right)^{-2} \text{ AU}. \quad (263)$$

We have picked 10 km s^{-1} as a fiducial sound speed because this is approximately the sound speed in EUV-ionized gas, which has a temperature near 10^4 K. X-rays or far ultraviolet (FUV) photons (those with $6 \text{ eV} < h\nu < 13.6 \text{ eV}$ that dissociate but do not ionize hydrogen) heat the surface to lower temperatures, $\sim 10^3$ K, resulting in correspondingly larger critical radii.

Interior to r_g the hot gas is bound, and unless some other process intervenes (such as a stellar wind or an MHD disk wind) it will form a static isothermal atmosphere with a scale height that varies with radius as $h \propto r^{3/2}$ (see §3.1.1). Outside r_g it

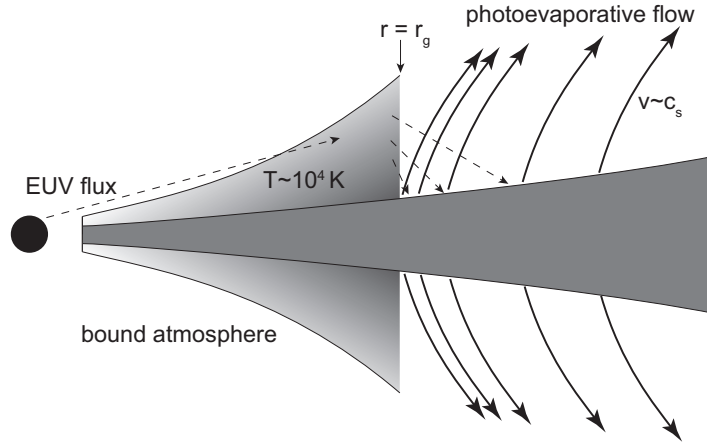


Fig. 33 Illustration of the simplest model of internal photoevaporation driven by extreme ultraviolet (EUV) radiation (based on the “weak stellar wind” case from Hollenbach et al. [187]). Stellar EUV radiation ionizes and heats the surface layers of the disk. Where the thermal energy of the surface layer remains small compared to the binding energy, the hot gas forms a bound atmosphere. At larger radii, where the gas is more weakly bound, the hot gas flows away in a thermally driven wind. Details of the radiative transfer and heating processes differ depending upon the nature of the high energy radiation, but a qualitatively similar scenario applies also to X-ray and FUV-driven photoevaporation.

will flow away, at a speed of the order of the sound speed. In the case of EUV illumination the hot and ionized surface layer is separated from the underlying cool gas by a sharp ionization front, which gives a clearly defined “base” to the wind. If the number density at the base is n_0 , we expect a mass loss rate per unit area of the disk that is given by,

$$\dot{\Sigma}_w \simeq 2\mu m_H n_0 c_s, \quad (264)$$

up to factors of order unity that depend again on the detailed hydrodynamic structure of the flow. In the EUV case the mass loss profile due to photoevaporation is then determined by the radial scaling of the base density $n_0(r)$. Noting that the integrated mass loss rate is just,

$$\dot{M}_w = \int_{r_c}^{r_{\text{out}}} 2\pi r \dot{\Sigma}_w dr, \quad (265)$$

we conclude that if $n_0(r)$ declines more steeply than r^{-2} the mass loss is predominantly from the inner disk (near r_c), whereas a shallower profile leads to most of the mass being lost from the outer disk.

Actually finding $n_0(r)$ for photoevaporation driven by EUV radiation from the central star requires the solution of a radiative transfer problem, whose geometry is illustrated in Figure 33. The base density is determined by equating the rate of ionization to that of recombination, which occurs at a rate per unit volume $\alpha n_e n_p$ with α , the recombination co-efficient, given by $\alpha \approx 3 \times 10^{-13}$. The main difficulty is determining the radial scaling of the ionization rate. This in principle has

two components, a “direct” flux from the star and a “diffuse” field that originates from the fraction (about one third) of recombinations within the bound atmosphere that go to the ground state and hence regenerate an ionizing photon. Hollenbach et al. [187] presented analytic and approximate numerical solutions to the radiative transfer problem that imply $n_0(r) \propto r^{-5/2}$, and this scaling has been widely adopted in subsequent work. Important features of the Hollenbach et al. solution have been verified in more detailed radiation hydrodynamic simulations (including the $\Phi^{1/2}$ of the mass loss with the ionizing photon flux [358]), though the slope of $n_0(r)$ at $r > r_g$ remains to be confirmed (indeed, a recent radiative transfer calculation is inconsistent with the canonical slope [399]).

9.1.2 Drivers of photoevaporation

Photoevaporation driven by a photon flux of EUV radiation from the central star Φ is estimated to result in a mass loss rate [134, 4],

$$\dot{M}_w \simeq 1.6 \times 10^{-10} \left(\frac{M_*}{M_\odot} \right)^{1/2} \left(\frac{\Phi}{10^{41} \text{ s}^{-1}} \right)^{1/2} M_\odot \text{ yr}^{-1}, \quad (266)$$

provided that the disk is present and optically thick at all radii. The dominant uncertainty in applying this estimate to specific systems comes from lack of knowledge of Φ , which can be constrained but which remains hard to pin down precisely [6, 327]. For low mass stars ($M \leq M_\odot$) reasonable estimates imply that EUV photoevaporation rates are negligible when compared to the median accretion rate of T Tauri stars [167], but large enough to matter for disk dispersal if no stronger mass loss processes are operative. (EUV photon fluxes are of course vastly larger for massive stars, for which the theory was originally developed.)

Low mass pre-main-sequence stars are strong emitters of FUV and X-ray radiation [137, 338, 163]. The FUV luminosity has a base level that is set by chromospheric activity, on top of which there is a potentially much larger component from accretion [192]. The X-ray luminosity scales linearly with the bolometric luminosity, $\log(L_X/L_{\text{bol}}) = -3.6$ [338], but with a large scatter. Qualitatively, these photons affect the disk in the same way as the EUV. The surfaces of the disk are heated, albeit to a somewhat lower temperature than the 10^4 K that is characteristic of HII regions, and where this heating results in unbound gas a wind ensues. Quantitatively, the main difference is that X-ray and FUV heated layers are not separated from the cool underlying disk by any analog of a sharp ionization front, and this makes modeling of FUV and X-ray photoevaporation more difficult. State of the art calculations [159, 318, 317], however, suggest that X-rays and FUV radiation drive mass loss rates that are substantially higher than the EUV prediction — with values of the order of $10^{-8} M_\odot \text{ yr}^{-1}$ being possible — with X-rays likely dominating in the inner region. The exact mass loss rates have a significant dependence on the adopted thermochemistry within the disk [426]

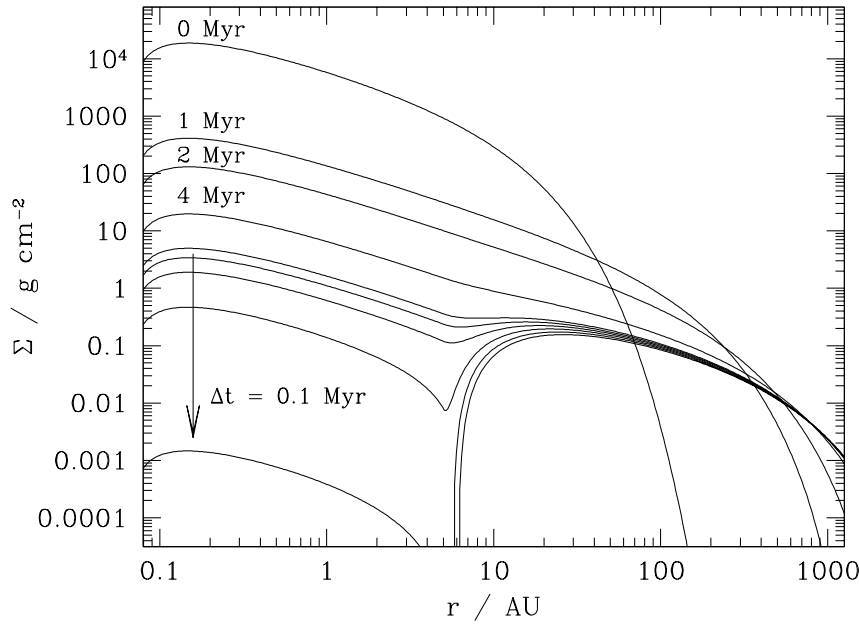


Fig. 34 An illustrative calculation of disk evolution including photoevaporative mass loss. The model plotted is based on a disk with $\nu \propto r$, and wind mass loss that scales as $\dot{\Sigma}_w \propto r^{-5/2}$ outside 5 AU. The disk displays the two time scale evolutionary behavior that is reasonably generic to internal photoevaporation models, with a long period of slow “viscous” evolution being followed by rapid inside-out dispersal.

9.1.3 Disk evolution including photoevaporation

Including photoevaporation in classical viscous models for disk evolution is particularly simple, because thermal winds exert no torque on the disk (equation 74). The rate and radial dependence of the mass loss, moreover, is primarily a function of the spectral energy distribution of the irradiation. This may depend upon the stellar accretion rate (if the FUV luminosity is an important driver of photoevaporation) but it is not coupled at leading order to details of the disk structure²¹. These properties mean that disks evolving under the joint action of viscosity and photoevaporation exhibit two distinct phases of evolution, an early phase in which viscosity dominates and a short subsequent phase in which the wind results in rapid disk dispersal [95].

Figure 34, based on the original calculations by Clarke et al. [95], shows how a disk evolves under the action of viscosity and EUV photoevaporation from the central star. In addition to the two time scale evolutionary behavior, the concentration

²¹ In more detail, however, the grain population within the disk will affect the absorption of high energy photons and hence the local mass loss rate [160].

of EUV mass loss toward the inner disk leads to a characteristic radial structure of disk dispersal. As the disk accretion rate drops, photoevaporation first dominates the evolution near to the innermost radius where mass loss is possible (in the illustrated example, this is taken to be 5 AU). A gap opens at this location, separating the inner disk (with a short viscous time scale) from the outer disk (where the viscous time scale is much longer). The inner disk then drains on to the star, stellar accretion ceases, and the disk is dispersed from the inside-out. The final dispersal is rapid, because the formation of a hole in the disk allows EUV [7] or X-ray [319] radiation to directly illuminate the inner edge of the disk, which typically accelerates mass loss. The dust to gas ratio in whatever is left of the disk increases during the dispersal phase [404, 5, 160]. Although the details depend on the radial profile of the photoevaporative wind, broadly similar evolution is predicted in most models [158]. The observed lifetimes of disks are broadly consistent with theoretically estimates that are based on “best-guess” values of photoevaporative mass loss rates [27].

There is no universal form describing how the action of photoevaporation cuts off accretion in the inner disk. For simple models of EUV photoevaporation, however, it can be shown that the inner accretion rate $\dot{M}(t)$ is related to the accretion rate \dot{M}_{SS} that would be predicted by a self-similar model [268] without mass loss via [365],

$$\dot{M} = \left[1 - \left(\frac{t}{t_0} \right)^{3/2} \right] \dot{M}_{\text{SS}}, \quad (267)$$

where t_0 is the time at which accretion ceases. This formula is derived for a specific viscosity law ($\nu \propto r$) and photoevaporation model, but provides a qualitative idea of how the inner disk drains under more general circumstances.

The inside-out character of photoevaporative dispersal applies only in the limit where radiation from the central star is dominant. In sufficiently rich stellar clusters, photoevaporation due to intense FUV radiation fields from other (massive) stars is more important. Unlike in the case of central star photoevaporation, for which the observational evidence is indirect [4], photoevaporative flows driven by external UV fields can sometimes be seen directly, most spectacularly in the core of the Orion Nebula [49]. Adams et al. [1] and Clarke [92] have modeled the evolution of viscous disks under external photoevaporation, and shown that it results in destruction of the disk from the outside-in. For the fraction of stars that form in such clusters, this process evidently limits the time over which gas-rich disks would be present on scales comparable to the Solar System’s Kuiper Belt.

9.2 MHD winds

The theoretical and observational arguments for photoevaporation being an important component of disk evolution are strong, but other processes may also contribute to disk dispersal. The obvious alternate candidate is MHD winds, which are likely to be present if mature disks retain a dynamically significant net magnetic field (see

the discussion in §5.4.4). MHD disk winds have obvious qualitative differences from their photoevaporative cousins,

- Their strength depends upon the disk's net flux, rather than on the stellar radiation field.
- They can be accelerated from arbitrarily small radii, where even EUV-ionized gas would be bound, with a velocity proportional to the Keplerian velocity at the magnetic field footpoint.
- The local mass loss rate is (roughly) expected to scale with the disk surface density, rather than being (approximately) a constant independent of the underlying column.
- Predominantly neutral or molecular gas can, at least in principle, be accelerated (though it might subsequently be dissociated or ionized by stellar radiation).

If MHD disk winds are sufficiently strong, they can affect disk dispersal via some combination of mass and angular momentum loss. The resultant evolution can be quite similar to the photoevaporative case. In particular, if mass rather than angular momentum loss is dominant, Suzuki et al. [395, 396] showed that MHD winds lead to the formation of a shallow surface density profile at small radii and, eventually, an expanding inner hole. In the opposite limit where angular momentum loss is strong (and mass loss negligible) Armitage et al. [24] suggested that dispersal could occur through the late onset of magnetic braking. Whether this is possible depends entirely on how the mass to flux ratio of the disk changes over time, and hence on the uncertain question of how net flux is transported and lost (§4.5.1). The most realistic scenario is one in which winds are driven by a combination of thermal (i.e. photoevaporative) and MHD processes, with the rate and radial profile of the mass and angular momentum loss depending jointly on the magnetic field structure and on the strength of impinging high energy photons [41].

- High-energy radiation in the form of FUV, EUV and X-ray photons heats the upper layers of protoplanetary disks, and drives a thermal wind from radii where the hot gas is unbound.
- Photoevaporative winds lead to distinct dispersal pathways for relatively isolated disks (where the high energy flux comes from the central star) and disks in rich clusters where FUV from massive stars dominates.
- Both thermal (photoevaporative) and MHD driving may contribute to disk evolution and dispersal, though the latter depends on the persistence of a significant net magnetic flux to late times.

Acknowledgements My work on protoplanetary disk physics and planet formation has been supported by the National Science Foundation, by NASA under the Origins of Solar Systems, Exoplanet Research and Astrophysics Theory programs, and by the Space Telescope Science Institute. I acknowledge the hospitality of the IIB at the University of Liverpool, where much of this chapter was written, and thank Kaitlin Kratter for an informal review of the manuscript.

References

1. Adams, F.C., Hollenbach, D., Laughlin, G., Gorti, U.: Photoevaporation of Circumstellar Disks Due to External Far-Ultraviolet Radiation in Stellar Aggregates. *ApJ*, **611**, 360–379 (2004). DOI 10.1086/421989
2. Adams, F.C., Lada, C.J., Shu, F.H.: Spectral evolution of young stellar objects. *ApJ*, **312**, 788–806 (1987). DOI 10.1086/164924
3. Alencar, S.H.P., Teixeira, P.S., Guimarães, M.M., McGinnis, P.T., Gameiro, J.F., Bouvier, J., Aigrain, S., Flaccomio, E., Favata, F.: Accretion dynamics and disk evolution in NGC 2264: a study based on CoRoT photometric observations. *A&A*, **519**, A88 (2010). DOI 10.1051/0004-6361/201014184
4. Alexander, R., Pascucci, I., Andrews, S., Armitage, P., Cieza, L.: The Dispersal of Protoplanetary Disks. *Protostars and Planets VI* pp. 475–496 (2014)
5. Alexander, R.D., Armitage, P.J.: Dust dynamics during protoplanetary disc clearing. *MNRAS*, **375**, 500–512 (2007). DOI 10.1111/j.1365-2966.2006.11341.x
6. Alexander, R.D., Clarke, C.J., Pringle, J.E.: Constraints on the ionizing flux emitted by T Tauri stars. *MNRAS*, **358**, 283–290 (2005). DOI 10.1111/j.1365-2966.2005.08786.x
7. Alexander, R.D., Clarke, C.J., Pringle, J.E.: Photoevaporation of protoplanetary discs - I. Hydrodynamic models. *MNRAS*, **369**, 216–228 (2006). DOI 10.1111/j.1365-2966.2006.10293.x
8. ALMA Partnership, Brogan, C.L., Pérez, L.M., Hunter, T.R., Dent, W.R.F., Hales, A.S., Hills, R.E., Corder, S., Fomalont, E.B., Vlahakis, C., Asaki, Y., Barkats, D., Hirota, A., Hodge, J.A., Impellizzeri, C.M.V., Kneissl, R., Liuzzo, E., Lucas, R., Marcelino, N., Matsushita, S., Nakanishi, K., Phillips, N., Richards, A.M.S., Toledo, I., Aladro, R., Broguiere, D., Cortes, J.R., Cortes, P.C., Espada, D., Galarza, F., Garcia-Appadoo, D., Guzman-Ramirez, L., Humphreys, E.M., Jung, T., Kamenno, S., Laing, R.A., Leon, S., Marconi, G., Mignano, A., Nikolic, B., Nyman, L.A., Radiszcz, M., Remijan, A., Rodón, J.A., Sawada, T., Takahashi, S., Tilanus, R.P.J., Vila Vilaro, B., Watson, L.C., Wiklind, T., Akiyama, E., Chapillon, E., de Gregorio-Monsalvo, I., Di Francesco, J., Gueth, F., Kawamura, A., Lee, C.F., Nguyen Luong, Q., Mangum, J., Pietu, V., Sanhueza, P., Saigo, K., Takakuwa, S., Ubach, C., van Kempen, T., Wootten, A., Castro-Carrizo, A., Francke, H., Gallardo, J., Garcia, J., Gonzalez, S., Hill, T., Kaminski, T., Kurono, Y., Liu, H.Y., Lopez, C., Morales, F., Plarre, K., Schieven, G., Testi, L., Videla, L., Villard, E., Andreani, P., Hibbard, J.E., Tatematsu, K.: The 2014 ALMA Long Baseline Campaign: First Results from High Angular Resolution Observations toward the HL Tau Region. *ApJL*, **808**, L3 (2015). DOI 10.1088/2041-8205/808/1/L3
9. Andrews, S.M., Williams, J.P.: Circumstellar Dust Disks in Taurus-Auriga: The Submillimeter Perspective. *ApJ*, **631**, 1134–1160 (2005). DOI 10.1086/432712
10. Andrews, S.M., Wilner, D.J., Espaillat, C., Hughes, A.M., Dullemond, C.P., McClure, M.K., Qi, C., Brown, J.M.: Resolved Images of Large Cavities in Protoplanetary Transition Disks. *ApJ*, **732**, 42 (2011). DOI 10.1088/0004-637X/732/1/42
11. Andrews, S.M., Wilner, D.J., Hughes, A.M., Qi, C., Dullemond, C.P.: Protoplanetary Disk Structures in Ophiuchus. *ApJ*, **700**, 1502–1523 (2009). DOI 10.1088/0004-637X/700/2/1502
12. Andrews, S.M., Wilner, D.J., Hughes, A.M., Qi, C., Rosenfeld, K.A., Öberg, K.I., Birnstiel, T., Espaillat, C., Cieza, L.A., Williams, J.P., Lin, S.Y., Ho, P.T.P.: The TW Hya Disk at 870 μm : Comparison of CO and Dust Radial Structures. *ApJ*, **744**, 162 (2012). DOI 10.1088/0004-637X/744/2/162
13. Andrews, S.M., Wilner, D.J., Zhu, Z., Birnstiel, T., Carpenter, J.M., Pérez, L.M., Bai, X.N., Öberg, K.I., Hughes, A.M., Isella, A., Ricci, L.: Ringed Substructure and a Gap at 1 au in the Nearest Protoplanetary Disk. *ApJL*, **820**, L40 (2016). DOI 10.3847/2041-8205/820/2/L40
14. Armitage, P.J.: Magnetic cycles and photometric variability of T Tauri stars. *MNRAS*, **274**, 1242–1248 (1995)
15. Armitage, P.J.: Turbulence and Angular Momentum Transport in a Global Accretion Disk Simulation. *ApJL*, **501**, L189–L192 (1998). DOI 10.1086/311463

16. Armitage, P.J.: Magnetic activity in accretion disc boundary layers. *MNRAS*, **330**, 895–900 (2002). DOI 10.1046/j.1365-8711.2002.05152.x
17. Armitage, P.J.: Lecture notes on the formation and early evolution of planetary systems. *ArXiv Astrophysics e-prints* (2007)
18. Armitage, P.J.: *Astrophysics of Planet Formation* (2010)
19. Armitage, P.J.: Dynamics of Protoplanetary Disks. *ARA&A*, **49**, 195–236 (2011). DOI 10.1146/annurev-astro-081710-102521
20. Armitage, P.J.: A Trap for Planet Formation. *Science* **340**, 1179–1180 (2013). DOI 10.1126/science.1239404
21. Armitage, P.J.: EXor Outbursts from Disk Amplification of Stellar Magnetic Cycles. *ApJL*, **833**, L15 (2016). DOI 10.3847/2041-8213/833/2/L15
22. Armitage, P.J., Eisner, J.A., Simon, J.B.: Prompt Planetesimal Formation beyond the Snow Line. *ApJL*, **828**, L2 (2016). DOI 10.3847/2041-8205/828/1/L2
23. Armitage, P.J., Livio, M., Pringle, J.E.: Episodic accretion in magnetically layered protoplanetary discs. *MNRAS*, **324**, 705–711 (2001). DOI 10.1046/j.1365-8711.2001.04356.x
24. Armitage, P.J., Simon, J.B., Martin, R.G.: Two Timescale Dispersal of Magnetized Protoplanetary Disks. *ApJL*, **778**, L14 (2013). DOI 10.1088/2041-8205/778/1/L14
25. Artymowicz, P., Lubow, S.H.: Mass Flow through Gaps in Circumbinary Disks. *ApJL*, **467**, L77 (1996). DOI 10.1086/310200
26. Audard, M., Ábrahám, P., Dunham, M.M., Green, J.D., Grosso, N., Hamaguchi, K., Kastner, J.H., Kóspál, Á., Lodato, G., Romanova, M.M., Skinner, S.L., Vorobyov, E.I., Zhu, Z.: Episodic Accretion in Young Stars. *Protostars and Planets VI* pp. 387–410 (2014)
27. Bae, J., Hartmann, L., Zhu, Z., Gammie, C.: The Long-term Evolution of Photoevaporating Protoplanetary Disks. *ApJ*, **774**, 57 (2013). DOI 10.1088/0004-637X/774/1/57
28. Bae, J., Hartmann, L., Zhu, Z., Gammie, C.: Variable Accretion Outbursts in Protostellar Evolution. *ApJ*, **764**, 141 (2013). DOI 10.1088/0004-637X/764/2/141
29. Bae, J., Hartmann, L., Zhu, Z., Nelson, R.P.: Accretion Outbursts in Self-gravitating Protoplanetary Disks. *ApJ*, **795**, 61 (2014). DOI 10.1088/0004-637X/795/1/61
30. Baehr, H., Klahr, H., Kratter, K.M.: The Fragmentation Criteria in Local Vertically Stratified Self-gravitating Disk Simulations. *ApJ*, **848**, 40 (2017). DOI 10.3847/1538-4357/aa8a66
31. Bai, X.N.: Magnetorotational-instability-driven Accretion in Protoplanetary Disks. *ApJ*, **739**, 50 (2011). DOI 10.1088/0004-637X/739/1/50
32. Bai, X.N.: Hall-effect-Controlled Gas Dynamics in Protoplanetary Disks. I. Wind Solutions at the Inner Disk. *ApJ*, **791**, 137 (2014). DOI 10.1088/0004-637X/791/2/137
33. Bai, X.N.: Hall Effect Controlled Gas Dynamics in Protoplanetary Disks. II. Full 3D Simulations toward the Outer Disk. *ApJ*, **798**, 84 (2015). DOI 10.1088/0004-637X/798/2/84
34. Bai, X.N.: Global Simulations of the Inner Regions of Protoplanetary Disks with Comprehensive Disk Microphysics. *ApJ*, **845**, 75 (2017). DOI 10.3847/1538-4357/aa7dda
35. Bai, X.N., Goodman, J.: Heat and Dust in Active Layers of Protostellar Disks. *ApJ*, **701**, 737–755 (2009). DOI 10.1088/0004-637X/701/1/737
36. Bai, X.N., Stone, J.M.: Dynamics of Solids in the Midplane of Protoplanetary Disks: Implications for Planetesimal Formation. *ApJ*, **722**, 1437–1459 (2010). DOI 10.1088/0004-637X/722/2/1437
37. Bai, X.N., Stone, J.M.: The Effect of the Radial Pressure Gradient in Protoplanetary Disks on Planetesimal Formation. *ApJL*, **722**, L220–L223 (2010). DOI 10.1088/2041-8205/722/2/L220
38. Bai, X.N., Stone, J.M.: Effect of Ambipolar Diffusion on the Nonlinear Evolution of Magnetorotational Instability in Weakly Ionized Disks. *ApJ*, **736**, 144 (2011). DOI 10.1088/0004-637X/736/2/144
39. Bai, X.N., Stone, J.M.: Wind-driven Accretion in Protoplanetary Disks. I. Suppression of the Magnetorotational Instability and Launching of the Magnetocentrifugal Wind. *ApJ*, **769**, 76 (2013). DOI 10.1088/0004-637X/769/1/76
40. Bai, X.N., Stone, J.M.: Magnetic Flux Concentration and Zonal Flows in Magnetorotational Instability Turbulence. *ApJ*, **796**, 31 (2014). DOI 10.1088/0004-637X/796/1/31

41. Bai, X.N., Ye, J., Goodman, J., Yuan, F.: Magneto-thermal Disk Winds from Protoplanetary Disks. *ApJ*, **818**, 152 (2016). DOI 10.3847/0004-637X/818/2/152
42. Bakes, E.L.O., Tielens, A.G.G.M.: The photoelectric heating mechanism for very small graphitic grains and polycyclic aromatic hydrocarbons. *ApJ*, **427**, 822–838 (1994). DOI 10.1086/174188
43. Balbus, S.A.: Magnetohydrodynamics of Protostellar Disks, pp. 237–282 (2011)
44. Balbus, S.A., Hawley, J.F.: A powerful local shear instability in weakly magnetized disks. I - Linear analysis. II - Nonlinear evolution. *ApJ*, **376**, 214–233 (1991). DOI 10.1086/170270
45. Balbus, S.A., Hawley, J.F.: Instability, turbulence, and enhanced transport in accretion disks. *Reviews of Modern Physics* **70**, 1–53 (1998). DOI 10.1103/RevModPhys.70.1
46. Balbus, S.A., Hawley, J.F., Stone, J.M.: Nonlinear Stability, Hydrodynamical Turbulence, and Transport in Disks. *ApJ*, **467**, 76 (1996). DOI 10.1086/177585
47. Balbus, S.A., Papaloizou, J.C.B.: On the Dynamical Foundations of α Disks. *ApJ*, **521**, 650–658 (1999). DOI 10.1086/307594
48. Balbus, S.A., Terquem, C.: Linear Analysis of the Hall Effect in Protostellar Disks. *ApJ*, **552**, 235–247 (2001). DOI 10.1086/320452
49. Bally, J., O’Dell, C.R., McCaughrean, M.J.: Disks, Microjets, Windblown Bubbles, and Outflows in the Orion Nebula. *AJ*, **119**, 2919–2959 (2000). DOI 10.1086/301385
50. Bally, J., Scoville, N.Z.: Structure and evolution of molecular clouds near H II regions. II - The disk constrained H II region, S106. *ApJ*, **255**, 497–509 (1982). DOI 10.1086/159850
51. Barge, P., Sommeria, J.: Did planet formation begin inside persistent gaseous vortices? *A&A*, **295**, L1–L4 (1995)
52. Barker, A.J., Ogilvie, G.I.: Hydrodynamic instability in eccentric astrophysical discs. *MNRAS*, **445**, 2637–2654 (2014). DOI 10.1093/mnras/stu1939
53. Barranco, J.A., Marcus, P.S.: Three-dimensional Vortices in Stratified Protoplanetary Disks. *ApJ*, **623**, 1157–1170 (2005). DOI 10.1086/428639
54. Baruteau, C., Meru, F., Paardekooper, S.J.: Rapid inward migration of planets formed by gravitational instability. *MNRAS*, **416**, 1971–1982 (2011). DOI 10.1111/j.1365-2966.2011.19172.x
55. Bastian, N., Covey, K.R., Meyer, M.R.: A Universal Stellar Initial Mass Function? A Critical Look at Variations. *ARA&A*, **48**, 339–389 (2010). DOI 10.1146/annurev-astro-082708-101642
56. Beckwith, S.V.W., Sargent, A.I.: Particle emissivity in circumstellar disks. *ApJ*, **381**, 250–258 (1991). DOI 10.1086/170646
57. Begelman, M.C., McKee, C.F., Shields, G.A.: Compton heated winds and coronae above accretion disks. I Dynamics. *ApJ*, **271**, 70–88 (1983). DOI 10.1086/161178
58. Bell, K.R., Cassen, P.M., Klahr, H.H., Henning, T.: The Structure and Appearance of Protoplanetary Accretion Disks: Limits on Disk Flaring. *ApJ*, **486**, 372–387 (1997)
59. Bell, K.R., Lin, D.N.C.: Using FU Orionis outbursts to constrain self-regulated protostellar disk models. *ApJ*, **427**, 987–1004 (1994). DOI 10.1086/174206
60. Belyaev, M.A., Rafikov, R.R., Stone, J.M.: Angular Momentum Transport by Acoustic Modes Generated in the Boundary Layer. I. Hydrodynamical Theory and Simulations. *ApJ*, **770**, 67 (2013). DOI 10.1088/0004-637X/770/1/67
61. Belyaev, M.A., Rafikov, R.R., Stone, J.M.: Angular Momentum Transport by Acoustic Modes Generated in the Boundary Layer. II. Magnetohydrodynamic Simulations. *ApJ*, **770**, 68 (2013). DOI 10.1088/0004-637X/770/1/68
62. Bergin, E.A., Cleeves, L.I., Gorti, U., Zhang, K., Blake, G.A., Green, J.D., Andrews, S.M., Evans II, N.J., Henning, T., Öberg, K., Pontoppidan, K., Qi, C., Salyk, C., van Dishoeck, E.F.: An old disk still capable of forming a planetary system. *Nature*, **493**, 644–646 (2013). DOI 10.1038/nature11805
63. Besla, G., Wu, Y.: Formation of Narrow Dust Rings in Circumstellar Debris Disks. *ApJ*, **655**, 528–540 (2007). DOI 10.1086/509495
64. Béthune, W., Lesur, G., Ferreira, J.: Global simulations of protoplanetary disks with net magnetic flux. I. Non-ideal MHD case. *A&A*, **600**, A75 (2017). DOI 10.1051/0004-6361/201630056

65. Birnstiel, T., Klahr, H., Ercolano, B.: A simple model for the evolution of the dust population in protoplanetary disks. *A&A*, **539**, A148 (2012). DOI 10.1051/0004-6361/201118136
66. Bisschop, S.E., Fraser, H.J., Öberg, K.I., van Dishoeck, E.F., Schlemmer, S.: Desorption rates and sticking coefficients for CO and N₂ interstellar ices. *A&A*, **449**, 1297–1309 (2006). DOI 10.1051/0004-6361:20054051
67. Bjorkman, J.E., Wood, K.: Radiative Equilibrium and Temperature Correction in Monte Carlo Radiation Transfer. *ApJ*, **554**, 615–623 (2001). DOI 10.1086/321336
68. Blaes, O.M., Balbus, S.A.: Local shear instabilities in weakly ionized, weakly magnetized disks. *ApJ*, **421**, 163–177 (1994). DOI 10.1086/173634
69. Blandford, R.D., Payne, D.G.: Hydromagnetic flows from accretion discs and the production of radio jets. *MNRAS*, **199**, 883–903 (1982)
70. Blum, J., Wurm, G.: The Growth Mechanisms of Macroscopic Bodies in Protoplanetary Disks. *ARA&A*, **46**, 21–56 (2008). DOI 10.1146/annurev.astro.46.060407.145152
71. Bollard, J., Connelly, J.N., Whitehouse, M.J., Pringle, E.A., Bonal, L., Jørgensen, J.K., Nordlund, Å., Moynier, F., Bizzarro, M.: Early formation of planetary building blocks inferred from Pb isotopic ages of chondrules. *Science Advances* **3**, e1700407 (2017). DOI 10.1126/sciadv.1700407
72. Bonnell, I., Bastien, P.: A binary origin for FU Orionis stars. *ApJL*, **401**, L31–L34 (1992). DOI 10.1086/186663
73. Bouvier, J., Alencar, S.H.P., Harries, T.J., Johns-Krull, C.M., Romanova, M.M.: Magnetospheric Accretion in Classical T Tauri Stars. *Protostars and Planets V* pp. 479–494 (2007)
74. Bouvier, J., Cabrit, S., Fernandez, M., Martin, E.L., Matthews, J.M.: Coyotes-I - the Photometric Variability and Rotational Evolution of T-Tauri Stars. *A&A*, **272**, 176 (1993)
75. Bouvier, J., Matt, S.P., Mohanty, S., Scholz, A., Stassun, K.G., Zanni, C.: Angular Momentum Evolution of Young Low-Mass Stars and Brown Dwarfs: Observations and Theory. *Protostars and Planets VI* pp. 433–450 (2014)
76. Brauer, F., Henning, T., Dullemond, C.P.: Planetesimal formation near the snow line in MRI-driven turbulent protoplanetary disks. *A&A*, **487**, L1–L4 (2008). DOI 10.1051/0004-6361:200809780
77. Burke, J.R., Hollenbach, D.J.: The gas-grain interaction in the interstellar medium - Thermal accommodation and trapping. *ApJ*, **265**, 223–234 (1983). DOI 10.1086/160667
78. Calvet, N., D’Alessio, P., Watson, D.M., Franco-Hernández, R., Furlan, E., Green, J., Sutter, P.M., Forrest, W.J., Hartmann, L., Uchida, K.I., Keller, L.D., Sargent, B., Najita, J., Herter, T.L., Barry, D.J., Hall, P.: Disks in Transition in the Taurus Population: Spitzer IRS Spectra of GM Aurigae and DM Tauri. *ApJL*, **630**, L185–L188 (2005). DOI 10.1086/491652
79. Cannizzo, J.K.: The Accretion Disk Limit Cycle Model: Toward an Understanding of the Long-Term Behavior of SS Cygni. *ApJ*, **419**, 318 (1993). DOI 10.1086/173486
80. Cao, X., Spruit, H.C.: Instability of an accretion disk with a magnetically driven wind. *A&A*, **385**, 289–300 (2002). DOI 10.1051/0004-6361:20011818
81. Carrera, D., Johansen, A., Davies, M.B.: How to form planetesimals from mm-sized chondrules and chondrule aggregates. *A&A*, **579**, A43 (2015). DOI 10.1051/0004-6361/201425120
82. Casassus, S., Marino, S., Pérez, S., Roman, P., Dunhill, A., Armitage, P.J., Cuadra, J., Wootten, A., van der Plas, G., Cieza, L., Moral, V., Christiaens, V., Montesinos, M.: Accretion Kinematics through the Warped Transition Disk in HD142527 from Resolved CO(6-5) Observations. *ApJ*, **811**, 92 (2015). DOI 10.1088/0004-637X/811/2/92
83. Casassus, S., van der Plas, G., M, S.P., Dent, W.R.F., Fomalont, E., Hagelberg, J., Hales, A., Jordán, A., Mawet, D., Ménard, F., Wootten, A., Wilner, D., Hughes, A.M., Schreiber, M.R., Girard, J.H., Ercolano, B., Canovas, H., Román, P.E., Salinas, V.: Flows of gas through a protoplanetary gap. *Nature*, **493**, 191–194 (2013). DOI 10.1038/nature11769
84. Cha, S.H., Nayakshin, S.: A numerical simulation of a ‘Super-Earth’ core delivery from 100 to 8 au. *MNRAS*, **415**, 3319–3334 (2011). DOI 10.1111/j.1365-2966.2011.18953.x
85. Chandrasekhar, S.: Hydrodynamic and hydromagnetic stability (1961)
86. Chang, P., Oishi, J.S.: On the Stability of Dust-laden Protoplanetary Vortices. *ApJ*, **721**, 1593–1602 (2010). DOI 10.1088/0004-637X/721/2/1593

87. Chauvin, G., Vigan, A., Bonnefoy, M., Desidera, S., Bonavita, M., Mesa, D., Boccaletti, A., Buenzli, E., Carson, J., Delorme, P., Hagelberg, J., Montagnier, G., Mordasini, C., Quanz, S.P., Segransan, D., Thalmann, C., Beuzit, J.L., Biller, B., Covino, E., Feldt, M., Girard, J., Gratton, R., Henning, T., Kasper, M., Lagrange, A.M., Messina, S., Meyer, M., Mouillet, D., Moutou, C., Reggiani, M., Schlieder, J.E., Zurlo, A.: The VLT/NaCo large program to probe the occurrence of exoplanets and brown dwarfs at wide orbits. II. Survey description, results, and performances. *A&A*, **573**, A127 (2015). DOI 10.1051/0004-6361/201423564
88. Chavanis, P.H.: Trapping of dust by coherent vortices in the solar nebula. *A&A*, **356**, 1089–1111 (2000)
89. Chiang, E., Youdin, A.N.: Forming Planetesimals in Solar and Extrasolar Nebulae. *Annual Review of Earth and Planetary Sciences* **38**, 493–522 (2010). DOI 10.1146/annurev-earth-040809-152513
90. Chiang, E.I., Goldreich, P.: Spectral Energy Distributions of T Tauri Stars with Passive Circumstellar Disks. *ApJ*, **490**, 368–376 (1997)
91. Ciesla, F.J., Cuzzi, J.N.: The evolution of the water distribution in a viscous protoplanetary disk. *Icarus*, **181**, 178–204 (2006). DOI 10.1016/j.icarus.2005.11.009
92. Clarke, C.J.: The photoevaporation of discs around young stars in massive clusters. *MNRAS*, **376**, 1350–1356 (2007). DOI 10.1111/j.1365-2966.2007.11547.x
93. Clarke, C.J.: Pseudo-viscous modelling of self-gravitating discs and the formation of low mass ratio binaries. *MNRAS*, **396**, 1066–1074 (2009). DOI 10.1111/j.1365-2966.2009.14774.x
94. Clarke, C.J., Armitage, P.J., Smith, K.W., Pringle, J.E.: Magnetically modulated accretion in T Tauri stars. *MNRAS*, **273**, 639–642 (1995)
95. Clarke, C.J., Gendrin, A., Sotomayor, M.: The dispersal of circumstellar discs: the role of the ultraviolet switch. *MNRAS*, **328**, 485–491 (2001). DOI 10.1046/j.1365-8711.2001.04891.x
96. Clarke, C.J., Pringle, J.E.: The diffusion of contaminant through an accretion disc. *MNRAS*, **235**, 365–373 (1988)
97. Clarke, C.J., Syer, D.: Low-mass companions to T Tauri stars: a mechanism for rapid-rise FU Orionis outbursts. *MNRAS*, **278**, L23–L27 (1996)
98. Cleeves, L.I., Bergin, E.A., Qi, C., Adams, F.C., Öberg, K.I.: Constraining the X-Ray and Cosmic-Ray Ionization Chemistry of the TW Hya Protoplanetary Disk: Evidence for a Sub-interstellar Cosmic-Ray Rate. *ApJ*, **799**, 204 (2015). DOI 10.1088/0004-637X/799/2/204
99. Cody, A.M., Stauffer, J., Baglin, A., Micela, G., Rebull, L.M., Flaccomio, E., Morales-Calderón, M., Aigrain, S., Bouvier, J., Hillenbrand, L.A., Gutermuth, R., Song, I., Turner, N., Alencar, S.H.P., Zwintz, K., Plavchan, P., Carpenter, J., Findeisen, K., Carey, S., Terebey, S., Hartmann, L., Calvet, N., Teixeira, P., Vrba, F.J., Wolk, S., Covey, K., Poppenhaeger, K., Günther, H.M., Forbrich, J., Whitney, B., Affer, L., Herbst, W., Hora, J., Barrado, D., Holtzman, J., Marchis, F., Wood, K., Medeiros Guimarães, M., Lillo Box, J., Gillen, E., McQuillan, A., Espaillat, C., Allen, L., D’Alessio, P., Favata, F.: CSI 2264: Simultaneous Optical and Infrared Light Curves of Young Disk-bearing Stars in NGC 2264 with CoRoT and Spitzer — Evidence for Multiple Origins of Variability. *AJ*, **147**, 82 (2014). DOI 10.1088/0004-6256/147/4/82
100. Coleman, M.S.B., Kotko, I., Blaes, O., Lasota, J.P., Hirose, S.: Dwarf nova outbursts with magnetorotational turbulence. *MNRAS*, **462**, 3710–3726 (2016). DOI 10.1093/mnras/stw1908
101. Connolly, H.C., Jones, R.H.: Chondrules: The canonical and noncanonical views. *Journal of Geophysical Research (Planets)* **121**, 1885–1899 (2016). DOI 10.1002/2016JE005113
102. Cossins, P., Lodato, G., Clarke, C.: The effects of opacity on gravitational stability in protoplanetary discs. *MNRAS*, **401**, 2587–2598 (2010). DOI 10.1111/j.1365-2966.2009.15835.x
103. Cossins, P., Lodato, G., Clarke, C.J.: Characterizing the gravitational instability in cooling accretion discs. *MNRAS*, **393**, 1157–1173 (2009). DOI 10.1111/j.1365-2966.2008.14275.x
104. Curry, C., Pudritz, R.E.: On the Global Stability of Magnetized Accretion Disks. II. Vertical and Azimuthal Magnetic Fields. *ApJ*, **453**, 697 (1995). DOI 10.1086/176431
105. D’Angelo, C.R., Spruit, H.C.: Episodic accretion on to strongly magnetic stars. *MNRAS*, **406**, 1208–1219 (2010). DOI 10.1111/j.1365-2966.2010.16749.x

106. D'Angelo, C.R., Spruit, H.C.: Accretion discs trapped near corotation. *MNRAS*, **420**, 416–429 (2012). DOI 10.1111/j.1365-2966.2011.20046.x
107. Davis, S.W., Stone, J.M., Pessah, M.E.: Sustained Magnetorotational Turbulence in Local Simulations of Stratified Disks with Zero Net Magnetic Flux. *ApJ*, **713**, 52–65 (2010). DOI 10.1088/0004-637X/713/1/52
108. de Val-Borro, M., Artymowicz, P., D'Angelo, G., Peplinski, A.: Vortex generation in protoplanetary disks with an embedded giant planet. *A&A*, **471**, 1043–1055 (2007). DOI 10.1051/0004-6361:20077169
109. Deng, H., Mayer, L., Meru, F.: Convergence of the Critical Cooling Rate for Protoplanetary Disk Fragmentation Achieved: The Key Role of Numerical Dissipation of Angular Momentum. *ApJ*, **847**, 43 (2017). DOI 10.3847/1538-4357/aa872b
110. Desch, S.J.: Linear Analysis of the Magnetorotational Instability, Including Ambipolar Diffusion, with Application to Protoplanetary Disks. *ApJ*, **608**, 509–525 (2004). DOI 10.1086/392527
111. Dittrich, K., Klahr, H., Johansen, A.: Gravoturbulent Planetesimal Formation: The Positive Effect of Long-lived Zonal Flows. *ApJ*, **763**, 117 (2013). DOI 10.1088/0004-637X/763/2/117
112. D'Orazio, D.J., Haiman, Z., MacFadyen, A.: Accretion into the central cavity of a circumbinary disc. *MNRAS*, **436**, 2997–3020 (2013). DOI 10.1093/mnras/stt1787
113. Draine, B.T.: Photoelectric heating of interstellar gas. *ApJS*, **36**, 595–619 (1978). DOI 10.1086/190513
114. Draine, B.T.: On the Submillimeter Opacity of Protoplanetary Disks. *ApJ*, **636**, 1114–1120 (2006). DOI 10.1086/498130
115. Draine, B.T., Roberge, W.G., Dalgarno, A.: Magnetohydrodynamic shock waves in molecular clouds. *ApJ*, **264**, 485–507 (1983). DOI 10.1086/160617
116. Draine, B.T., Sutin, B.: Collisional charging of interstellar grains. *ApJ*, **320**, 803–817 (1987). DOI 10.1086/165596
117. Dubrulle, B., Morfill, G., Sterzik, M.: The dust subdisk in the protoplanetary nebula. *Icarus*, **114**, 237–246 (1995). DOI 10.1006/icar.1995.1058
118. Dutrey, A., Semenov, D., Chapillon, E., Gorti, U., Guilloteau, S., Hersant, F., Hogerheijde, M., Hughes, M., Meeus, G., Nomura, H., Piétu, V., Qi, C., Wakelam, V.: Physical and Chemical Structure of Planet-Forming Disks Probed by Millimeter Observations and Modeling. *Protostars and Planets VI* pp. 317–338 (2014)
119. Eckhardt, B., Schneider, T.M., Hof, B., Westerweel, J.: Turbulence Transition in Pipe Flow. *Annual Review of Fluid Mechanics* **39**, 447–468 (2007). DOI 10.1146/annurev.fluid.39.050905.110308
120. Edlund, E.M., Ji, H.: Nonlinear stability of laboratory quasi-Keplerian flows. *Phys. Rev. E*, **89**(2), 021004 (2014). DOI 10.1103/PhysRevE.89.021004
121. Eisner, J.A., Hillenbrand, L.A., Carpenter, J.M., Wolf, S.: Constraining the Evolutionary Stage of Class I Protostars: Multiwavelength Observations and Modeling. *ApJ*, **635**, 396–421 (2005). DOI 10.1086/497161
122. Ercolano, B., Barlow, M.J., Storey, P.J.: The dusty MOCASSIN: fully self-consistent 3D photoionization and dust radiative transfer models. *MNRAS*, **362**, 1038–1046 (2005). DOI 10.1111/j.1365-2966.2005.09381.x
123. Ercolano, B., Glassgold, A.E.: X-ray ionization rates in protoplanetary discs. *MNRAS*, **436**, 3446–3450 (2013). DOI 10.1093/mnras/stt1826
124. Espaillat, C., Muzerolle, J., Najita, J., Andrews, S., Zhu, Z., Calvet, N., Kraus, S., Hashimoto, J., Kraus, A., D'Alessio, P.: An Observational Perspective of Transitional Disks. *Protostars and Planets VI* pp. 497–520 (2014)
125. Evans II, N.J., Dunham, M.M., Jørgensen, J.K., Enoch, M.L., Merín, B., van Dishoeck, E.F., Alcalá, J.M., Myers, P.C., Stapelfeldt, K.R., Huard, T.L., Allen, L.E., Harvey, P.M., van Kempen, T., Blake, G.A., Koerner, D.W., Mundy, L.G., Padgett, D.L., Sargent, A.I.: The Spitzer c2d Legacy Results: Star-Formation Rates and Efficiencies; Evolution and Lifetimes. *ApJS*, **181**, 321–350 (2009). DOI 10.1088/0067-0049/181/2/321

126. Faure, J., Fromang, S., Latter, H., Meheut, H.: Vortex cycles at the inner edges of dead zones in protoplanetary disks. *A&A*, **573**, A132 (2015). DOI 10.1051/0004-6361/201424162
127. Fedele, D., Carney, M., Hogerheijde, M.R., Walsh, C., Miotello, A., Klaassen, P., Bruderer, S., Henning, T., van Dishoeck, E.F.: ALMA unveils rings and gaps in the protoplanetary system μ ASTROBJ HD 169142/ μ ASTROBJ: signatures of two giant protoplanets. *A&A*, **600**, A72 (2017). DOI 10.1051/0004-6361/201629860
128. Federrath, C., Banerjee, S.: The density structure and star formation rate of non-isothermal polytropic turbulence. *MNRAS*, **448**, 3297–3313 (2015). DOI 10.1093/mnras/stv180
129. Flaherty, K.M., Hughes, A.M., Rose, S.C., Simon, J.B., Qi, C., Andrews, S.M., Kóspál, Á., Wilner, D.J., Chiang, E., Armitage, P.J., Bai, X.n.: A Three-dimensional View of Turbulence: Constraints on Turbulent Motions in the HD 163296 Protoplanetary Disk Using DCO⁺. *ApJ*, **843**, 150 (2017). DOI 10.3847/1538-4357/aa79f9
130. Flaherty, K.M., Hughes, A.M., Rosenfeld, K.A., Andrews, S.M., Chiang, E., Simon, J.B., Kerzner, S., Wilner, D.J.: Weak Turbulence in the HD 163296 Protoplanetary Disk Revealed by ALMA CO Observations. *ApJ*, **813**, 99 (2015). DOI 10.1088/0004-637X/813/2/99
131. Fleming, T., Stone, J.M.: Local Magnetohydrodynamic Models of Layered Accretion Disks. *ApJ*, **585**, 908–920 (2003). DOI 10.1086/345848
132. Flock, M., Ruge, J.P., Dzyurkevich, N., Henning, T., Klahr, H., Wolf, S.: Gaps, rings, and non-axisymmetric structures in protoplanetary disks. From simulations to ALMA observations. *A&A*, **574**, A68 (2015). DOI 10.1051/0004-6361/201424693
133. Follette, K.B., Rameau, J., Dong, R., Pueyo, L., Close, L.M., Duchêne, G., Fung, J., Leonard, C., Macintosh, B., Males, J.R., Marois, C., Millar-Blanchaer, M.A., Morzinski, K.M., Mullen, W., Perrin, M., Spiro, E., Wang, J., Ammons, S.M., Bailey, V.P., Barman, T., Bulger, J., Chilcote, J., Cotten, T., De Rosa, R.J., Doyon, R., Fitzgerald, M.P., Goodsell, S.J., Graham, J.R., Greenbaum, A.Z., Hibon, P., Hung, L.W., Ingraham, P., Kalas, P., Konopacky, Q., Larkin, J.E., Maire, J., Marchis, F., Metchev, S., Nielsen, E.L., Oppenheimer, R., Palmer, D., Patience, J., Poyneer, L., Rajan, A., Rantakyö, F.T., Savransky, D., Schneider, A.C., Sivaramkrishnan, A., Song, I., Soummer, R., Thomas, S., Vega, D., Wallace, J.K., Ward-Duong, K., Wiktorowicz, S., Wolff, S.: Complex Spiral Structure in the HD 100546 Transitional Disk as Revealed by GPI and MagAO. *AJ*, **153**, 264 (2017). DOI 10.3847/1538-3881/aa6d85
134. Font, A.S., McCarthy, I.G., Johnstone, D., Ballantyne, D.R.: Photoevaporation of Circumstellar Disks around Young Stars. *ApJ*, **607**, 890–903 (2004). DOI 10.1086/383518
135. Forgan, D., Rice, K.: Stellar encounters in the context of outburst phenomena. *MNRAS*, **402**, 1349–1356 (2010). DOI 10.1111/j.1365-2966.2009.15974.x
136. Forgan, D., Rice, K., Cossins, P., Lodato, G.: The nature of angular momentum transport in radiative self-gravitating protostellar discs. *MNRAS*, **410**, 994–1006 (2011). DOI 10.1111/j.1365-2966.2010.17500.x
137. France, K., Schindhelm, E., Bergin, E.A., Roueff, E., Abgrall, H.: High-resolution Ultraviolet Radiation Fields of Classical T Tauri Stars. *ApJ*, **784**, 127 (2014). DOI 10.1088/0004-637X/784/2/127
138. France, K., Schindhelm, E., Herczeg, G.J., Brown, A., Abgrall, H., Alexander, R.D., Bergin, E.A., Brown, J.M., Linsky, J.L., Roueff, E., Yang, H.: A Hubble Space Telescope Survey of H₂ Emission in the Circumstellar Environments of Young Stars. *ApJ*, **756**, 171 (2012). DOI 10.1088/0004-637X/756/2/171
139. Frank, J., King, A., Raine, D.J.: *Accretion Power in Astrophysics: Third Edition* (2002)
140. Fricke, K.: Instabilität stationärer Rotation in Sternen. *Zeitschrift für Astrophysik*, **68**, 317 (1968)
141. Fromang, S.: MRI-driven angular momentum transport in protoplanetary disks. In: P. Hennebelle, C. Charbonnel (eds.) *EAS Publications Series, EAS Publications Series*, vol. 62, pp. 95–142 (2013). DOI 10.1051/eas/1362004
142. Fromang, S., Latter, H., Lesur, G., Ogilvie, G.I.: Local outflows from turbulent accretion disks. *A&A*, **552**, A71 (2013). DOI 10.1051/0004-6361/201220016
143. Fromang, S., Papaloizou, J.: Dust settling in local simulations of turbulent protoplanetary disks. *A&A*, **452**, 751–762 (2006). DOI 10.1051/0004-6361:20054612

144. Fu, R.R., Weiss, B.P., Lima, E.A., Harrison, R.J., Bai, X.N., Desch, S.J., Ebel, D.S., Suavet, C., Wang, H., Glenn, D., Le Sage, D., Kasama, T., Walsworth, R.L., Kuan, A.T.: Solar nebula magnetic fields recorded in the semarkona meteorite. *Science* (2014). DOI 10.1126/science.1258022. URL <http://www.sciencemag.org/content/early/2014/11/12/science.1258022.abstract>
145. Fu, W., Li, H., Lubow, S., Li, S., Liang, E.: Effects of Dust Feedback on Vortices in Protoplanetary Disks. *ApJL*, **795**, L39 (2014). DOI 10.1088/2041-8205/795/2/L39
146. Galicher, R., Marois, C., Macintosh, B., Zuckerman, B., Barman, T., Konopacky, Q., Song, I., Patience, J., Lafrenière, D., Doyon, R., Nielsen, E.L.: The International Deep Planet Survey. II. The frequency of directly imaged giant exoplanets with stellar mass. *A&A*, **594**, A63 (2016). DOI 10.1051/0004-6361/201527828
147. Galvagni, M., Hayfield, T., Boley, A., Mayer, L., Roškar, R., Saha, P.: The collapse of protoplanetary clumps formed through disc instability: 3D simulations of the pre-dissociation phase. *MNRAS*, **427**, 1725–1740 (2012). DOI 10.1111/j.1365-2966.2012.22096.x
148. Gammie, C.F.: Layered Accretion in T Tauri Disks. *ApJ*, **457**, 355 (1996). DOI 10.1086/176735
149. Gammie, C.F.: Instabilities in Circumstellar Disks. In: J.A. Sellwood, J. Goodman (eds.) *Astrophysical Disks - an EC Summer School, Astronomical Society of the Pacific Conference Series*, vol. 160, p. 122 (1999)
150. Gammie, C.F.: Nonlinear Outcome of Gravitational Instability in Cooling, Gaseous Disks. *ApJ*, **553**, 174–183 (2001). DOI 10.1086/320631
151. Garaud, P., Lin, D.N.C.: The Effect of Internal Dissipation and Surface Irradiation on the Structure of Disks and the Location of the Snow Line around Sun-like Stars. *ApJ*, **654**, 606–624 (2007). DOI 10.1086/509041
152. Garufi, A., Quanz, S.P., Schmid, H.M., Mulders, G.D., Avenhaus, H., Boccaletti, A., Ginski, C., Langlois, M., Stolker, T., Augereau, J.C., Benisty, M., Lopez, B., Dominik, C., Gratton, R., Henning, T., Janson, M., Ménard, F., Meyer, M.R., Pinte, C., Sissa, E., Vigan, A., Zurlo, A., Bazzon, A., Buenzli, E., Bonnefoy, M., Brandner, W., Chauvin, G., Cheetham, A., Cudel, M., Desidera, S., Feldt, M., Galicher, R., Kasper, M., Lagrange, A.M., Lannier, J., Maire, A.L., Mesa, D., Mouillet, D., Peretti, S., Perrot, C., Salter, G., Wildi, F.: The SPHERE view of the planet-forming disk around HD 100546. *A&A*, **588**, A8 (2016). DOI 10.1051/0004-6361/201527940
153. Gibbons, P.G., Mamatsashvili, G.R., Rice, W.K.M.: Planetesimal formation in self-gravitating discs - the effects of particle self-gravity and back-reaction. *MNRAS*, **442**, 361–371 (2014). DOI 10.1093/mnras/stu809
154. Godon, P., Livio, M.: The Formation and Role of Vortices in Protoplanetary Disks. *ApJ*, **537**, 396–404 (2000). DOI 10.1086/309019
155. Goldreich, P., Goodman, J., Narayan, R.: The stability of accretion tori. I - Long-wavelength modes of slender tori. *MNRAS*, **221**, 339–364 (1986)
156. Goldreich, P., Schubert, G.: Differential Rotation in Stars. *ApJ*, **150**, 571 (1967). DOI 10.1086/149360
157. Goodman, A.A., Benson, P.J., Fuller, G.A., Myers, P.C.: Dense cores in dark clouds. VIII - Velocity gradients. *ApJ*, **406**, 528–547 (1993). DOI 10.1086/172465
158. Gorti, U., Dullemond, C.P., Hollenbach, D.: Time Evolution of Viscous Circumstellar Disks due to Photoevaporation by Far-Ultraviolet, Extreme-Ultraviolet, and X-ray Radiation from the Central Star. *ApJ*, **705**, 1237–1251 (2009). DOI 10.1088/0004-637X/705/2/1237
159. Gorti, U., Hollenbach, D.: Photoevaporation of Circumstellar Disks By Far-Ultraviolet, Extreme-Ultraviolet and X-Ray Radiation from the Central Star. *ApJ*, **690**, 1539–1552 (2009). DOI 10.1088/0004-637X/690/2/1539
160. Gorti, U., Hollenbach, D., Dullemond, C.P.: The Impact of Dust Evolution and Photoevaporation on Disk Dispersal. *ApJ*, **804**, 29 (2015). DOI 10.1088/0004-637X/804/1/29
161. Grady, C.A., Muto, T., Hashimoto, J., Fukagawa, M., Currie, T., Biller, B., Thalmann, C., Sitko, M.L., Russell, R., Wisniewski, J., Dong, R., Kwon, J., Sai, S., Hornbeck, J., Schneider, G., Hines, D., Moro Martín, A., Feldt, M., Henning, T., Pott, J.U., Bonnefoy, M., Bowman, J., Lacour, S., Mueller, A., Juhász, A., Crida, A., Chauvin, G., Andrews, S., Wilner, D.,

- Kraus, A., Dahm, S., Robitaille, T., Jang-Condell, H., Abe, L., Akiyama, E., Brandner, W., Brandt, T., Carson, J., Egner, S., Follette, K.B., Goto, M., Guyon, O., Hayano, Y., Hayashi, M., Hayashi, S., Hodapp, K., Ishii, M., Iye, M., Janson, M., Kandori, R., Knapp, G., Kudo, T., Kusakabe, N., Kuzuhara, M., Mayama, S., McElwain, M., Matsuo, T., Miyama, S., Morino, J.I., Nishimura, T., Pyo, T.S., Serabyn, G., Suto, H., Suzuki, R., Takami, M., Takato, N., Terada, H., Tomono, D., Turner, E., Watanabe, M., Yamada, T., Takami, H., Usuda, T., Tamura, M.: Spiral Arms in the Asymmetrically Illuminated Disk of MWC 758 and Constraints on Giant Planets. *ApJ*, **762**, 48 (2013). DOI 10.1088/0004-637X/762/1/48
162. Gressel, O., Turner, N.J., Nelson, R.P., McNally, C.P.: Global Simulations of Protoplanetary Disks With Ohmic Resistivity and Ambipolar Diffusion. *ApJ*, **801**, 84 (2015). DOI 10.1088/0004-637X/801/2/84
163. Güdel, M., Briggs, K.R., Arzner, K., Audard, M., Bouvier, J., Feigelson, E.D., Franciosini, E., Glauser, A., Grosso, N., Micela, G., Monin, J.L., Montmerle, T., Padgett, D.L., Palla, F., Pillitteri, I., Rebull, L., Scelsi, L., Silva, B., Skinner, S.L., Stelzer, B., Telleschi, A.: The XMM-Newton extended survey of the Taurus molecular cloud (XEST). *A&A*, **468**, 353–377 (2007). DOI 10.1051/0004-6361:20065724
164. Guilet, J., Ogilvie, G.I.: Transport of magnetic flux and the vertical structure of accretion discs - I. Uniform diffusion coefficients. *MNRAS*, **424**, 2097–2117 (2012). DOI 10.1111/j.1365-2966.2012.21361.x
165. Guilet, J., Ogilvie, G.I.: Global evolution of the magnetic field in a thin disc and its consequences for protoplanetary systems. *MNRAS*, **441**, 852–868 (2014). DOI 10.1093/mnras/stu532
166. Gullbring, E., Calvet, N., Muzerolle, J., Hartmann, L.: The Structure and Emission of the Accretion Shock in T Tauri Stars. II. The Ultraviolet-Continuum Emission. *ApJ*, **544**, 927–932 (2000). DOI 10.1086/317253
167. Gullbring, E., Hartmann, L., Briceño, C., Calvet, N.: Disk Accretion Rates for T Tauri Stars. *ApJ*, **492**, 323–341 (1998). DOI 10.1086/305032
168. Hōshi, R.: Accretion Model for Outbursts of Dwarf Nova. *Progress of Theoretical Physics* **61**, 1307–1319 (1979). DOI 10.1143/PTP.61.1307
169. Haghighipour, N., Boss, A.P.: On Pressure Gradients and Rapid Migration of Solids in a Nonuniform Solar Nebula. *ApJ*, **583**, 996–1003 (2003). DOI 10.1086/345472
170. Haisch Jr., K.E., Lada, E.A., Lada, C.J.: Disk Frequencies and Lifetimes in Young Clusters. *ApJL*, **553**, L153–L156 (2001). DOI 10.1086/320685
171. Hartmann, L., Calvet, N., Gullbring, E., D’Alessio, P.: Accretion and the Evolution of T Tauri Disks. *ApJ*, **495**, 385–400 (1998). DOI 10.1086/305277
172. Hartmann, L., Kenyon, S.J.: The FU Orionis Phenomenon. *ARA&A*, **34**, 207–240 (1996). DOI 10.1146/annurev.astro.34.1.207
173. Hawley, J.F., Gammie, C.F., Balbus, S.A.: Local Three-dimensional Magnetohydrodynamic Simulations of Accretion Disks. *ApJ*, **440**, 742 (1995). DOI 10.1086/175311
174. Hawley, J.F., Stone, J.M.: Nonlinear Evolution of the Magnetorotational Instability in Ion-Neutral Disks. *ApJ*, **501**, 758–771 (1998). DOI 10.1086/305849
175. Hayashi, C.: Structure of the Solar Nebula, Growth and Decay of Magnetic Fields and Effects of Magnetic and Turbulent Viscosities on the Nebula. *Progress of Theoretical Physics Supplement* **70**, 35–53 (1981). DOI 10.1143/PTPS.70.35
176. Haynes, D.R., Tro, N.J., George, S.M.: Condensation and evaporation of H₂O on ice surfaces. *Journal of Physical Chemistry* **96**, 8502–8509 (1992)
177. Henning, T., Semenov, D.: Chemistry in Protoplanetary Disks. *Chemical Reviews* **113**, 9016–9042 (2013). DOI 10.1021/cr400128p
178. Herbig, G.H.: Eruptive phenomena in early stellar evolution. *ApJ*, **217**, 693–715 (1977). DOI 10.1086/155615
179. Herbig, G.H.: History and Spectroscopy of EXor Candidates. *AJ*, **135**, 637–648 (2008). DOI 10.1088/0004-6256/135/2/637
180. Herczeg, G.J., Hillenbrand, L.A.: UV Excess Measures of Accretion onto Young Very Low Mass Stars and Brown Dwarfs. *ApJ*, **681**, 594–625 (2008). DOI 10.1086/586728

181. Hernández, J., Hartmann, L., Megeath, T., Gutermuth, R., Muzerolle, J., Calvet, N., Vivas, A.K., Briceño, C., Allen, L., Stauffer, J., Young, E., Fazio, G.: A Spitzer Space Telescope Study of Disks in the Young σ Orionis Cluster. *ApJ*, **662**, 1067–1081 (2007). DOI 10.1086/513735
182. Hernández, J., Hartmann, L., Megeath, T., Gutermuth, R., Muzerolle, J., Calvet, N., Vivas, A.K., Briceño, C., Allen, L., Stauffer, J., Young, E., Fazio, G.: A Spitzer Space Telescope Study of Disks in the Young σ Orionis Cluster. *ApJ*, **662**, 1067–1081 (2007). DOI 10.1086/513735
183. Hillenbrand, L.A., Findeisen, K.P.: A Simple Calculation in Service of Constraining the Rate of FU Orionis Outburst Events from Photometric Monitoring Surveys. *ApJ*, **808**, 68 (2015). DOI 10.1088/0004-637X/808/1/68
184. Hirose, S., Blaes, O., Krolik, J.H., Coleman, M.S.B., Sano, T.: Convection Causes Enhanced Magnetic Turbulence in Accretion Disks in Outburst. *ApJ*, **787**, 1 (2014). DOI 10.1088/0004-637X/787/1/1
185. Hirose, S., Turner, N.J.: Heating and Cooling Protostellar Disks. *ApJL*, **732**, L30 (2011). DOI 10.1088/2041-8205/732/2/L30
186. Hogerheijde, M.R., Bergin, E.A., Brinch, C., Cleves, L.I., Fogel, J.K.J., Blake, G.A., Dominik, C., Lis, D.C., Melnick, G., Neufeld, D., Panić, O., Pearson, J.C., Kristensen, L., Yıldız, U.A., van Dishoeck, E.F.: Detection of the Water Reservoir in a Forming Planetary System. *Science* **334**, 338 (2011). DOI 10.1126/science.1208931
187. Hollenbach, D., Johnstone, D., Lizano, S., Shu, F.: Photoevaporation of disks around massive stars and application to ultracompact H II regions. *ApJ*, **428**, 654–669 (1994). DOI 10.1086/174276
188. Hopkins, P.F.: A new class of accurate, mesh-free hydrodynamic simulation methods. *MNRAS*, **450**, 53–110 (2015). DOI 10.1093/mnras/stv195
189. Ilgner, M., Nelson, R.P.: On the ionisation fraction in protoplanetary disks. I. Comparing different reaction networks. *A&A*, **445**, 205–222 (2006). DOI 10.1051/0004-6361:20053678
190. Illarionov, A.F., Sunyaev, R.A.: Why the Number of Galactic X-ray Stars Is so Small? *A&A*, **39**, 185 (1975)
191. Inaba, S., Barge, P.: Dusty Vortices in Protoplanetary Disks. *ApJ*, **649**, 415–427 (2006). DOI 10.1086/506427
192. Ingleby, L., Calvet, N., Hernández, J., Briceño, C., Espaillat, C., Miller, J., Bergin, E., Hartmann, L.: Evolution of X-ray and Far-ultraviolet Disk-dispersing Radiation Fields. *AJ*, **141**, 127 (2011). DOI 10.1088/0004-6256/141/4/127
193. Inutsuka, S.i., Sano, T.: Self-sustained Ionization and Vanishing Dead Zones in Protoplanetary Disks. *ApJL*, **628**, L155–L158 (2005). DOI 10.1086/432796
194. Isella, A., Guidi, G., Testi, L., Liu, S., Li, H., Li, S., Weaver, E., Boehler, Y., Carperter, J.M., De Gregorio-Monsalvo, I., Manara, C.F., Natta, A., Pérez, L.M., Ricci, L., Sargent, A., Tazzari, M., Turner, N.: Ringed Structures of the HD 163296 Protoplanetary Disk Revealed by ALMA. *Physical Review Letters* **117**(25), 251101 (2016). DOI 10.1103/PhysRevLett.117.251101
195. Isella, A., Pérez, L.M., Carpenter, J.M., Ricci, L., Andrews, S., Rosenfeld, K.: An Azimuthal Asymmetry in the LkH α 330 Disk. *ApJ*, **775**, 30 (2013). DOI 10.1088/0004-637X/775/1/30
196. Jacquet, E., Balbus, S., Latter, H.: On linear dust-gas streaming instabilities in protoplanetary discs. *MNRAS*, **415**, 3591–3598 (2011). DOI 10.1111/j.1365-2966.2011.18971.x
197. Jin, L.: Damping of the Shear Instability in Magnetized Disks by Ohmic Diffusion. *ApJ*, **457**, 798 (1996). DOI 10.1086/176774
198. Johansen, A., Blum, J., Tanaka, H., Ormel, C., Bizzarro, M., Rickman, H.: The Multifaceted Planetesimal Formation Process. *Protostars and Planets VI* pp. 547–570 (2014)
199. Johansen, A., Klahr, H., Henning, T.: High-resolution simulations of planetesimal formation in turbulent protoplanetary discs. *A&A*, **529**, A62 (2011). DOI 10.1051/0004-6361/201015979
200. Johansen, A., Mac Low, M.M., Lacerda, P., Bizzarro, M.: Growth of asteroids, planetary embryos, and Kuiper belt objects by chondrule accretion. *Science Advances* **1**, 1500109 (2015). DOI 10.1126/sciadv.1500109

201. Johansen, A., Oishi, J.S., Mac Low, M.M., Klahr, H., Henning, T., Youdin, A.: Rapid planetesimal formation in turbulent circumstellar disks. *Nature*, **448**, 1022–1025 (2007). DOI 10.1038/nature06086
202. Johansen, A., Youdin, A.: Protoplanetary Disk Turbulence Driven by the Streaming Instability: Nonlinear Saturation and Particle Concentration. *ApJ*, **662**, 627–641 (2007). DOI 10.1086/516730
203. Johansen, A., Youdin, A., Klahr, H.: Zonal Flows and Long-lived Axisymmetric Pressure Bumps in Magnetorotational Turbulence. *ApJ*, **697**, 1269–1289 (2009). DOI 10.1088/0004-637X/697/2/1269
204. Johansen, A., Youdin, A., Mac Low, M.M.: Particle Clumping and Planetesimal Formation Depend Strongly on Metallicity. *ApJL*, **704**, L75–L79 (2009). DOI 10.1088/0004-637X/704/2/L75
205. Johnson, B.M., Gammie, C.F.: Nonlinear Outcome of Gravitational Instability in Disks with Realistic Cooling. *ApJ*, **597**, 131–141 (2003). DOI 10.1086/378392
206. Johnson, B.M., Gammie, C.F.: Vortices in Thin, Compressible, Unmagnetized Disks. *ApJ*, **635**, 149–156 (2005). DOI 10.1086/497358
207. Johnstone, C.P., Jardine, M., Gregory, S.G., Donati, J.F., Hussain, G.: Classical T Tauri stars: magnetic fields, coronae and star-disc interactions. *MNRAS*, **437**, 3202–3220 (2014). DOI 10.1093/mnras/stt2107
208. Joy, A.H.: T Tauri Variable Stars. *ApJ*, **102**, 168 (1945). DOI 10.1086/144749
209. Kama, M., Bruderer, S., van Dishoeck, E.F., Hogerheijde, M., Folsom, C.P., Miotello, A., Fedele, D., Belloche, A., Güsten, R., Wyrowski, F.: Volatile-carbon locking and release in protoplanetary disks. A study of TW Hya and HD 100546. *A&A*, **592**, A83 (2016). DOI 10.1051/0004-6361/201526991
210. Kamp, I., Dullemond, C.P.: The Gas Temperature in the Surface Layers of Protoplanetary Disks. *ApJ*, **615**, 991–999 (2004). DOI 10.1086/424703
211. Kamp, I., van Zadelhoff, G.J.: On the gas temperature in circumstellar disks around A stars. *A&A*, **373**, 641–656 (2001). DOI 10.1051/0004-6361:20010629
212. Kenyon, S.J., Hartmann, L.: Spectral energy distributions of T Tauri stars - Disk flaring and limits on accretion. *ApJ*, **323**, 714–733 (1987). DOI 10.1086/165866
213. Kerswell, R.R.: Elliptical instability. *Annual Review of Fluid Mechanics* **34**, 83–113 (2002). DOI 10.1146/annurev.fluid.34.081701.171829
214. Kida, S.: Motion of an elliptic vortex in a uniform shear flow. *Journal of the Physical Society of Japan* **50**, 3517–3520 (1981). DOI 10.1143/JPSJ.50.3517
215. Kim, K.H., Watson, D.M., Manoj, P., Forrest, W.J., Furlan, E., Najita, J., Sargent, B., Hernández, J., Calvet, N., Adame, L., Espaillat, C., Megeath, S.T., Muzerolle, J., McClure, M.K.: The Spitzer Infrared Spectrograph Survey of Protoplanetary Disks in Orion A. I. Disk Properties. *ApJS*, **226**, 8 (2016). DOI 10.3847/0067-0049/226/1/8
216. King, A.R., Pringle, J.E., Livio, M.: Accretion disc viscosity: how big is alpha? *MNRAS*, **376**, 1740–1746 (2007). DOI 10.1111/j.1365-2966.2007.11556.x
217. Klahr, H.H., Bodenheimer, P.: Turbulence in Accretion Disks: Vorticity Generation and Angular Momentum Transport via the Global Baroclinic Instability. *ApJ*, **582**, 869–892 (2003). DOI 10.1086/344743
218. Kley, W., Lin, D.N.C.: The Structure of the Boundary Layer in Protostellar Disks. *ApJ*, **461**, 933 (1996). DOI 10.1086/177115
219. Kley, W., Nelson, R.P.: Planet-Disk Interaction and Orbital Evolution. *ARA&A*, **50**, 211–249 (2012). DOI 10.1146/annurev-astro-081811-125523
220. Koenigl, A.: Disk accretion onto magnetic T Tauri stars. *ApJL*, **370**, L39–L43 (1991). DOI 10.1086/185972
221. Koller, J., Li, H., Lin, D.N.C.: Vortices in the Co-orbital Region of an Embedded Protoplanet. *ApJL*, **596**, L91–L94 (2003). DOI 10.1086/379032
222. Königl, A., Salmeron, R.: The Effects of Large-Scale Magnetic Fields on Disk Formation and Evolution, pp. 283–352 (2011)

223. Kounkel, M., Hartmann, L., Loinard, L., Ortiz-León, G.N., Mioduszewski, A.J., Rodríguez, L.F., Dzib, S.A., Torres, R.M., Pech, G., Galli, P.A.B., Rivera, J.L., Boden, A.F., Evans II, N.J., Briceño, C., Tobin, J.J.: The Goulds Belt Distances Survey (GOBELINS) II. Distances and Structure toward the Orion Molecular Clouds. *ApJ*, **834**, 142 (2017). DOI 10.3847/1538-4357/834/2/142
224. Kraichnan, R.H.: Inertial Ranges in Two-Dimensional Turbulence. *Physics of Fluids* **10**, 1417–1423 (1967). DOI 10.1063/1.1762301
225. Krasnopolsky, R., Li, Z.Y., Shang, H.: Disk Formation in Magnetized Clouds Enabled by the Hall Effect. *ApJ*, **733**, 54 (2011). DOI 10.1088/0004-637X/733/1/54
226. Kratter, K., Lodato, G.: Gravitational Instabilities in Circumstellar Disks. *ARA&A*, **54**, 271–311 (2016). DOI 10.1146/annurev-astro-081915-023307
227. Kratter, K.M., Matzner, C.D., Krumholz, M.R., Klein, R.I.: On the Role of Disks in the Formation of Stellar Systems: A Numerical Parameter Study of Rapid Accretion. *ApJ*, **708**, 1585–1597 (2010). DOI 10.1088/0004-637X/708/2/1585
228. Kratter, K.M., Murray-Clay, R.A., Youdin, A.N.: The Runts of the Litter: Why Planets Formed Through Gravitational Instability Can Only Be Failed Binary Stars. *ApJ*, **710**, 1375–1386 (2010). DOI 10.1088/0004-637X/710/2/1375
229. Kretke, K.A., Lin, D.N.C.: Grain Retention and Formation of Planetesimals near the Snow Line in MRI-driven Turbulent Protoplanetary Disks. *ApJL*, **664**, L55–L58 (2007). DOI 10.1086/520718
230. Kuiper, G.P.: On the Origin of the Solar System. *Proceedings of the National Academy of Science* **37**, 1–14 (1951). DOI 10.1073/pnas.37.1.1
231. Kunz, M.W.: On the linear stability of weakly ionized, magnetized planar shear flows. *MNRAS*, **385**, 1494–1510 (2008). DOI 10.1111/j.1365-2966.2008.12928.x
232. Kunz, M.W., Balbus, S.A.: Ambipolar diffusion in the magnetorotational instability. *MNRAS*, **348**, 355–360 (2004). DOI 10.1111/j.1365-2966.2004.07383.x
233. Kunz, M.W., Lesur, G.: Magnetic self-organization in Hall-dominated magnetorotational turbulence. *MNRAS*, **434**, 2295–2312 (2013). DOI 10.1093/mnras/stt1171
234. Kurosawa, R., Romanova, M.M.: Spectral variability of classical T Tauri stars accreting in an unstable regime. *MNRAS*, **431**, 2673–2689 (2013). DOI 10.1093/mnras/stt365
235. Lada, C.J., Wilking, B.A.: The nature of the embedded population in the Rho Ophiuchi dark cloud - Mid-infrared observations. *ApJ*, **287**, 610–621 (1984). DOI 10.1086/162719
236. Lai, D.: Magnetically Driven Warping, Precession, and Resonances in Accretion Disks. *ApJ*, **524**, 1030–1047 (1999). DOI 10.1086/307850
237. Larwood, J.D., Nelson, R.P., Papaloizou, J.C.B., Terquem, C.: The tidally induced warping, precession and truncation of accretion discs in binary systems: three-dimensional simulations. *MNRAS*, **282**, 597–613 (1996)
238. Lasota, J.P.: The disc instability model of dwarf novae and low-mass X-ray binary transients. *New Astronomy Reviews*, **45**, 449–508 (2001). DOI 10.1016/S1387-6473(01)00112-9
239. Latter, H.N., Papaloizou, J.: Local models of astrophysical discs. *MNRAS*, **472**, 1432–1446 (2017). DOI 10.1093/mnras/stx2038
240. Lecar, M., Podolak, M., Sasselov, D., Chiang, E.: On the Location of the Snow Line in a Protoplanetary Disk. *ApJ*, **640**, 1115–1118 (2006). DOI 10.1086/500287
241. Lesur, G., Kunz, M.W., Fromang, S.: Thanatology in protoplanetary discs. The combined influence of Ohmic, Hall, and ambipolar diffusion on dead zones. *A&A*, **566**, A56 (2014). DOI 10.1051/0004-6361/201423660
242. Lesur, G., Longaretti, P.Y.: On the relevance of subcritical hydrodynamic turbulence to accretion disk transport. *A&A*, **444**, 25–44 (2005). DOI 10.1051/0004-6361:20053683
243. Lesur, G., Ogilvie, G.I.: On the angular momentum transport due to vertical convection in accretion discs. *MNRAS*, **404**, L64–L68 (2010). DOI 10.1111/j.1745-3933.2010.00836.x
244. Lesur, G., Papaloizou, J.C.B.: On the stability of elliptical vortices in accretion discs. *A&A*, **498**, 1–12 (2009). DOI 10.1051/0004-6361/200811577
245. Lesur, G., Papaloizou, J.C.B.: The subcritical baroclinic instability in local accretion disc models. *A&A*, **513**, A60 (2010). DOI 10.1051/0004-6361/200913594

246. Lesur, G.R.J., Latter, H.: On the survival of zombie vortices in protoplanetary discs. *MNRAS*, **462**, 4549–4554 (2016). DOI 10.1093/mnras/stw2172
247. Levin, Y.: Starbursts near supermassive black holes: young stars in the Galactic Centre, and gravitational waves in LISA band. *MNRAS*, **374**, 515–524 (2007). DOI 10.1111/j.1365-2966.2006.11155.x
248. Li, H., Colgate, S.A., Wendroff, B., Liska, R.: Rossby Wave Instability of Thin Accretion Disks. III. Nonlinear Simulations. *ApJ*, **551**, 874–896 (2001). DOI 10.1086/320241
249. Li, H., Finn, J.M., Lovelace, R.V.E., Colgate, S.A.: Rossby Wave Instability of Thin Accretion Disks. II. Detailed Linear Theory. *ApJ*, **533**, 1023–1034 (2000). DOI 10.1086/308693
250. Li, Z.Y., Banerjee, R., Pudritz, R.E., Jørgensen, J.K., Shang, H., Krasnopolsky, R., Maury, A.: The Earliest Stages of Star and Planet Formation: Core Collapse, and the Formation of Disks and Outflows. *Protostars and Planets VI* pp. 173–194 (2014)
251. Liffman, K.: The Gravitational Radius of an Irradiated Disk. *Publications of the Astronomical Society of Australia*, **20**, 337–339 (2003). DOI 10.1071/AS03019
252. Lin, M.K.: Non-barotropic Linear Rossby Wave Instability in Three-dimensional Disks. *ApJ*, **765**, 84 (2013). DOI 10.1088/0004-637X/765/2/84
253. Lin, M.K., Youdin, A.N.: Cooling Requirements for the Vertical Shear Instability in Protoplanetary Disks. *ApJ*, **811**, 17 (2015). DOI 10.1088/0004-637X/811/1/17
254. Lodato, G., Clarke, C.J.: Massive planets in FU Orionis discs: implications for thermal instability models. *MNRAS*, **353**, 841–852 (2004). DOI 10.1111/j.1365-2966.2004.08112.x
255. Lodato, G., Pringle, J.E.: Warp diffusion in accretion discs: a numerical investigation. *MNRAS*, **381**, 1287–1300 (2007). DOI 10.1111/j.1365-2966.2007.12332.x
256. Lodato, G., Rice, W.K.M.: Testing the locality of transport in self-gravitating accretion discs. *MNRAS*, **351**, 630–642 (2004). DOI 10.1111/j.1365-2966.2004.07811.x
257. Lodato, G., Rice, W.K.M.: Testing the locality of transport in self-gravitating accretion discs - II. The massive disc case. *MNRAS*, **358**, 1489–1500 (2005). DOI 10.1111/j.1365-2966.2005.08875.x
258. Lodders, K.: Solar System Abundances and Condensation Temperatures of the Elements. *ApJ*, **591**, 1220–1247 (2003). DOI 10.1086/375492
259. Loomis, R.A., Öberg, K.I., Andrews, S.M., MacGregor, M.A.: A Multi-ringed, Modestly Inclined Protoplanetary Disk around AA Tau. *ApJ*, **840**, 23 (2017). DOI 10.3847/1538-4357/aa6c63
260. Lovelace, R.V.E., Li, H., Colgate, S.A., Nelson, A.F.: Rossby Wave Instability of Keplerian Accretion Disks. *ApJ*, **513**, 805–810 (1999). DOI 10.1086/306900
261. Lovelace, R.V.E., Rothstein, D.M., Bisnovaty-Kogan, G.S.: Advection/Diffusion of Large-Scale B Field in Accretion Disks. *ApJ*, **701**, 885–890 (2009). DOI 10.1088/0004-637X/701/2/885
262. Lubow, S.H., Martin, R.G., Nixon, C.: Tidal Torques on Misaligned Disks in Binary Systems. *ApJ*, **800**, 96 (2015). DOI 10.1088/0004-637X/800/2/96
263. Lubow, S.H., Ogilvie, G.I.: On the Tilting of Protostellar Disks by Resonant Tidal Effects. *ApJ*, **538**, 326–340 (2000). DOI 10.1086/309101
264. Lubow, S.H., Papaloizou, J.C.B., Pringle, J.E.: Magnetic field dragging in accretion discs. *MNRAS*, **267**, 235–240 (1994)
265. Lubow, S.H., Papaloizou, J.C.B., Pringle, J.E.: On the Stability of Magnetic Wind-Driven Accretion Disks. *MNRAS*, **268**, 1010 (1994)
266. Luhman, K.L., Allen, P.R., Espaillat, C., Hartmann, L., Calvet, N.: The Disk Population of the Taurus Star-Forming Region. *ApJS*, **186**, 111–174 (2010). DOI 10.1088/0067-0049/186/1/111
267. Lynden-Bell, D.: On why discs generate magnetic towers and collimate jets. *MNRAS*, **341**, 1360–1372 (2003). DOI 10.1046/j.1365-8711.2003.06506.x
268. Lynden-Bell, D., Pringle, J.E.: The evolution of viscous discs and the origin of the nebular variables. *MNRAS*, **168**, 603–637 (1974)
269. Lyra, W., Johansen, A., Klahr, H., Piskunov, N.: Embryos grown in the dead zone. Assembling the first protoplanetary cores in low mass self-gravitating circumstellar disks of gas and solids. *A&A*, **491**, L41–L44 (2008). DOI 10.1051/0004-6361:200810626

270. Lyra, W., Johansen, A., Zsom, A., Klahr, H., Piskunov, N.: Planet formation bursts at the borders of the dead zone in 2D numerical simulations of circumstellar disks. *A&A*, **497**, 869–888 (2009). DOI 10.1051/0004-6361/200811265
271. Lyra, W., Kuchner, M.: Formation of sharp eccentric rings in debris disks with gas but without planets. *Nature*, **499**, 184–187 (2013). DOI 10.1038/nature12281
272. Lyra, W., Mac Low, M.M.: Rossby Wave Instability at Dead Zone Boundaries in Three-dimensional Resistive Magnetohydrodynamical Global Models of Protoplanetary Disks. *ApJ*, **756**, 62 (2012). DOI 10.1088/0004-637X/756/1/62
273. Lyra, W., Turner, N.J., McNally, C.P.: Rossby wave instability does not require sharp resistivity gradients. *A&A*, **574**, A10 (2015). DOI 10.1051/0004-6361/201424919
274. Malygin, M.G., Klahr, H., Semenov, D., Henning, T., Dullemond, C.P.: Efficiency of thermal relaxation by radiative processes in protoplanetary discs: constraints on hydrodynamic turbulence. *A&A*, **605**, A30 (2017). DOI 10.1051/0004-6361/201629933
275. Manara, C.F., Fedele, D., Herczeg, G.J., Teixeira, P.S.: X-Shooter study of accretion in Chamaeleon I. *A&A*, **585**, A136 (2016). DOI 10.1051/0004-6361/201527224
276. Manara, C.F., Testi, L., Natta, A., Rosotti, G., Benisty, M., Ercolano, B., Ricci, L.: Gas content of transitional disks: a VLT/X-Shooter study of accretion and winds. *A&A*, **568**, A18 (2014). DOI 10.1051/0004-6361/201323318
277. Marcus, P.S., Pei, S., Jiang, C.H., Barranco, J.A., Hassanzadeh, P., Lecoanet, D.: Zombie Vortex Instability. I. A Purely Hydrodynamic Instability to Resurrect the Dead Zones of Protoplanetary Disks. *ApJ*, **808**, 87 (2015). DOI 10.1088/0004-637X/808/1/87
278. Marcus, P.S., Pei, S., Jiang, C.H., Hassanzadeh, P.: Three-Dimensional Vortices Generated by Self-Replication in Stably Stratified Rotating Shear Flows. *Physical Review Letters* **111**(8), 084501 (2013). DOI 10.1103/PhysRevLett.111.084501
279. Marley, M.S., Fortney, J.J., Hubickyj, O., Bodenheimer, P., Lissauer, J.J.: On the Luminosity of Young Jupiters. *ApJ*, **655**, 541–549 (2007). DOI 10.1086/509759
280. Marois, C., Macintosh, B., Barman, T., Zuckerman, B., Song, I., Patience, J., Lafrenière, D., Doyon, R.: Direct Imaging of Multiple Planets Orbiting the Star HR 8799. *Science* **322**, 1348 (2008). DOI 10.1126/science.1166585
281. Marois, C., Zuckerman, B., Konopacky, Q.M., Macintosh, B., Barman, T.: Images of a fourth planet orbiting HR 8799. *Nature*, **468**, 1080–1083 (2010). DOI 10.1038/nature09684
282. Martin, R.G., Livio, M.: On the evolution of the snow line in protoplanetary discs. *MNRAS*, **425**, L6–L9 (2012). DOI 10.1111/j.1745-3933.2012.01290.x
283. Martin, R.G., Lubow, S.H.: The Gravo-magneto Limit Cycle in Accretion Disks. *ApJL*, **740**, L6 (2011). DOI 10.1088/2041-8205/740/1/L6
284. Martin, R.G., Lubow, S.H.: Tidal truncation of circumplanetary discs. *MNRAS*, **413**, 1447–1461 (2011). DOI 10.1111/j.1365-2966.2011.18228.x
285. Martin, R.G., Lubow, S.H.: The gravo-magneto disc instability with a viscous dead zone. *MNRAS*, **437**, 682–689 (2014). DOI 10.1093/mnras/stt1917
286. Maslowe, S.A.: Critical layers in shear flows. *Annual Review of Fluid Mechanics* **18**, 405–432 (1986). DOI 10.1146/annurev.fl.18.010186.002201
287. Matzner, C.D., Levin, Y.: Protostellar Disks: Formation, Fragmentation, and the Brown Dwarf Desert. *ApJ*, **628**, 817–831 (2005). DOI 10.1086/430813
288. McClure, M.K., Bergin, E.A., Cleaves, L.I., van Dishoeck, E.F., Blake, G.A., Evans II, N.J., Green, J.D., Henning, T., Öberg, K.I., Pontoppidan, K.M., Salyk, C.: Mass Measurements in Protoplanetary Disks from Hydrogen Deuteride. *ApJ*, **831**, 167 (2016). DOI 10.3847/0004-637X/831/2/167
289. Meheut, H., Casse, F., Varniere, P., Tagger, M.: Rossby wave instability and three-dimensional vortices in accretion disks. *A&A*, **516**, A31 (2010). DOI 10.1051/0004-6361/201014000
290. Meru, F., Bate, M.R.: Non-convergence of the critical cooling time-scale for fragmentation of self-gravitating discs. *MNRAS*, **411**, L1–L5 (2011). DOI 10.1111/j.1745-3933.2010.00978.x
291. Meyer, F., Meyer-Hofmeister, E.: On the Elusive Cause of Cataclysmic Variable Outbursts. *A&A*, **104**, L10 (1981)

292. Michael, S., Durisen, R.H., Boley, A.C.: Migration of Gas Giant Planets in Gravitationally Unstable Disks. *ApJL*, **737**, L42 (2011). DOI 10.1088/2041-8205/737/2/L42
293. Min, M., Dullemond, C.P., Kama, M., Dominik, C.: The thermal structure and the location of the snow line in the protosolar nebula: Axisymmetric models with full 3-D radiative transfer. *Icarus*, **212**, 416–426 (2011). DOI 10.1016/j.icarus.2010.12.002
294. Miranda, R., Lai, D.: Tidal truncation of inclined circumstellar and circumbinary discs in young stellar binaries. *MNRAS*, **452**, 2396–2409 (2015). DOI 10.1093/mnras/stv1450
295. Molyarova, T., Akimkin, V., Semenov, D., Henning, T., Vasyunin, A., Wiebe, D.: Gas mass tracers in protoplanetary disks: CO is still the best. *ArXiv e-prints* (2017)
296. Momose, M., Morita, A., Fukagawa, M., Muto, T., Takeuchi, T., Hashimoto, J., Honda, M., Kudo, T., Okamoto, Y.K., Kanagawa, K.D., Tanaka, H., Grady, C.A., Sitko, M.L., Akiyama, E., Currie, T., Follette, K.B., Mayama, S., Kusakabe, N., Abe, L., Brandner, W., Brandt, T.D., Carson, J.C., Egner, S., Feldt, M., Goto, M., Guyon, O., Hayano, Y., Hayashi, M., Hayashi, S.S., Henning, T., Hodapp, K.W., Ishii, M., Iye, M., Janson, M., Kandori, R., Knapp, G.R., Kuzuhara, M., Kwon, J., Matsuo, T., McElwain, M.W., Miyama, S., Morino, J.I., Moro-Martín, A., Nishimura, T., Pyo, T.S., Serabyn, E., Suenaga, T., Suto, H., Suzuki, R., Takahashi, Y.H., Takami, M., Takato, N., Terada, H., Thalmann, C., Tomono, D., Turner, E.L., Watanabe, M., Wisniewski, J., Yamada, T., Takami, H., Usuda, T., Tamura, M.: Detailed structure of the outer disk around HD 169142 with polarized light in H-band. *PASJ* **67**, 83 (2015). DOI 10.1093/pasj/psv051
297. Morbidelli, A., Chambers, J., Lunine, J.I., Petit, J.M., Robert, F., Valsecchi, G.B., Cyr, K.E.: Source regions and time scales for the delivery of water to Earth. *Meteoritics and Planetary Science* **35**, 1309–1320 (2000). DOI 10.1111/j.1945-5100.2000.tb01518.x
298. Morfill, G.E.: Some cosmochemical consequences of a turbulent protoplanetary cloud. *Icarus*, **53**, 41–54 (1983). DOI 10.1016/0019-1035(83)90019-2
299. Muranushi, T., Okuzumi, S., Inutsuka, S.i.: Interdependence of Electric Discharge and Magnetorotational Instability in Protoplanetary Disks. *ApJ*, **760**, 56 (2012). DOI 10.1088/0004-637X/760/1/56
300. Muzerolle, J., Hillenbrand, L., Calvet, N., Briceño, C., Hartmann, L.: Accretion in Young Stellar/Substellar Objects. *ApJ*, **592**, 266–281 (2003). DOI 10.1086/375704
301. Nakagawa, Y., Sekiya, M., Hayashi, C.: Settling and growth of dust particles in a laminar phase of a low-mass solar nebula. *Icarus*, **67**, 375–390 (1986). DOI 10.1016/0019-1035(86)90121-1
302. Nayakshin, S., Lodato, G.: Fu Ori outbursts and the planet-disc mass exchange. *MNRAS*, **426**, 70–90 (2012). DOI 10.1111/j.1365-2966.2012.21612.x
303. Nelson, R.P., Gressel, O., Umurhan, O.M.: Linear and non-linear evolution of the vertical shear instability in accretion discs. *MNRAS*, **435**, 2610–2632 (2013). DOI 10.1093/mnras/stt1475
304. Nesvorný, D., Youdin, A.N., Richardson, D.C.: Formation of Kuiper Belt Binaries by Gravitational Collapse. *AJ*, **140**, 785–793 (2010). DOI 10.1088/0004-6256/140/3/785
305. Nixon, C., King, A.: Warp Propagation in Astrophysical Discs. In: F. Haardt, V. Gorini, U. Moschella, A. Treves, M. Colpi (eds.) *Lecture Notes in Physics*, Berlin Springer Verlag, *Lecture Notes in Physics, Berlin Springer Verlag*, vol. 905, p. 45 (2016). DOI 10.1007/978-3-319-19416-5_2
306. Nixon, C.J., Pringle, J.E.: The observable effects of tidally induced warps in protostellar discs. *MNRAS*, **403**, 1887–1893 (2010). DOI 10.1111/j.1365-2966.2010.16331.x
307. O’dell, C.R., Wen, Z., Hu, X.: Discovery of new objects in the Orion nebula on HST images - Shocks, compact sources, and protoplanetary disks. *ApJ*, **410**, 696–700 (1993). DOI 10.1086/172786
308. Ogilvie, G.I.: The non-linear fluid dynamics of a warped accretion disc. *MNRAS*, **304**, 557–578 (1999). DOI 10.1046/j.1365-8711.1999.02340.x
309. Ogilvie, G.I.: Non-linear fluid dynamics of eccentric discs. *MNRAS*, **325**, 231–248 (2001). DOI 10.1046/j.1365-8711.2001.04416.x
310. Ogilvie, G.I., Latter, H.N.: Local and global dynamics of warped astrophysical discs. *MNRAS*, **433**, 2403–2419 (2013). DOI 10.1093/mnras/stt916

311. Ogilvie, G.I., Livio, M.: Launching of Jets and the Vertical Structure of Accretion Disks. *ApJ*, **553**, 158–173 (2001). DOI 10.1086/320637
312. Ogilvie, G.I., Pringle, J.E.: The non-axisymmetric instability of a cylindrical shear flow containing an azimuthal magnetic field. *MNRAS*, **279**, 152–164 (1996)
313. Olofsson, J., Augereau, J.C., van Dishoeck, E.F., Merín, B., Grosso, N., Ménard, F., Blake, G.A., Monin, J.L.: C2D Spitzer-IRS spectra of disks around T Tauri stars. V. Spectral decomposition. *A&A*, **520**, A39 (2010). DOI 10.1051/0004-6361/200913909
314. Oppenheimer, M., Dalgarno, A.: The Fractional Ionization in Dense Interstellar Clouds. *ApJ*, **192**, 29–32 (1974). DOI 10.1086/153030
315. Ormel, C.W., Cuzzi, J.N.: Closed-form expressions for particle relative velocities induced by turbulence. *A&A*, **466**, 413–420 (2007). DOI 10.1051/0004-6361:20066899
316. Owen, J.E., Armitage, P.J.: Importance of thermal diffusion in the gravomagnetic limit cycle. *MNRAS*, **445**, 2800–2809 (2014). DOI 10.1093/mnras/stu1928
317. Owen, J.E., Clarke, C.J., Ercolano, B.: On the theory of disc photoevaporation. *MNRAS*, **422**, 1880–1901 (2012). DOI 10.1111/j.1365-2966.2011.20337.x
318. Owen, J.E., Ercolano, B., Clarke, C.J., Alexander, R.D.: Radiation-hydrodynamic models of X-ray and EUV photoevaporating protoplanetary discs. *MNRAS*, **401**, 1415–1428 (2010). DOI 10.1111/j.1365-2966.2009.15771.x
319. Owen, J.E., Hudoba de Badyn, M., Clarke, C.J., Robins, L.: Characterizing thermal sweeping: a rapid disc dispersal mechanism. *MNRAS*, **436**, 1430–1438 (2013). DOI 10.1093/mnras/stt1663
320. Paardekooper, S.J.: Numerical convergence in self-gravitating shearing sheet simulations and the stochastic nature of disc fragmentation. *MNRAS*, **421**, 3286–3299 (2012). DOI 10.1111/j.1365-2966.2012.20553.x
321. Paardekooper, S.J., Mellema, G.: Planets opening dust gaps in gas disks. *A&A*, **425**, L9–L12 (2004). DOI 10.1051/0004-6361:200400053
322. Paczynski, B.: A model of accretion disks in close binaries. *ApJ*, **216**, 822–826 (1977). DOI 10.1086/155526
323. Paczynski, B.: A model of selfgravitating accretion disk. *Acta Astronomica*, **28**, 91–109 (1978)
324. Papaloizou, J., Pringle, J.E.: Tidal torques on accretion discs in close binary systems. *MNRAS*, **181**, 441–454 (1977)
325. Papaloizou, J.C.B., Pringle, J.E.: The time-dependence of non-planar accretion discs. *MNRAS*, **202**, 1181–1194 (1983)
326. Papaloizou, J.C.B., Pringle, J.E.: The dynamical stability of differentially rotating discs with constant specific angular momentum. *MNRAS*, **208**, 721–750 (1984)
327. Pascucci, I., Ricci, L., Gorti, U., Hollenbach, D., Hendler, N.P., Brooks, K.J., Contreras, Y.: Low Extreme-ultraviolet Luminosities Impinging on Protoplanetary Disks. *ApJ*, **795**, 1 (2014). DOI 10.1088/0004-637X/795/1/1
328. Pérez, L.M., Carpenter, J.M., Andrews, S.M., Ricci, L., Isella, A., Linz, H., Sargent, A.I., Wilner, D.J., Henning, T., Deller, A.T., Chandler, C.J., Dullemond, C.P., Lazio, J., Menten, K.M., Corder, S.A., Storm, S., Testi, L., Tazzari, M., Kwon, W., Calvet, N., Greaves, J.S., Harris, R.J., Mundy, L.G.: Spiral density waves in a young protoplanetary disk. *Science* **353**, 1519–1521 (2016). DOI 10.1126/science.aaf8296
329. Perez-Becker, D., Chiang, E.: Surface Layer Accretion in Conventional and Transitional Disks Driven by Far-ultraviolet Ionization. *ApJ*, **735**, 8 (2011). DOI 10.1088/0004-637X/735/1/8
330. Pessah, M.E., Psaltis, D.: The Stability of Magnetized Rotating Plasmas with Superthermal Fields. *ApJ*, **628**, 879–901 (2005). DOI 10.1086/430940
331. Petersen, M.R., Julien, K., Stewart, G.R.: Baroclinic Vorticity Production in Protoplanetary Disks. I. Vortex Formation. *ApJ*, **658**, 1236–1251 (2007). DOI 10.1086/511513
332. Petersen, M.R., Stewart, G.R., Julien, K.: Baroclinic Vorticity Production in Protoplanetary Disks. II. Vortex Growth and Longevity. *ApJ*, **658**, 1252–1263 (2007). DOI 10.1086/511523
333. Pfalzner, S.: Encounter-driven accretion in young stellar clusters - A connection to FUOrs? *A&A*, **492**, 735–741 (2008). DOI 10.1051/0004-6361:200810879

334. Pinilla, P., Birnstiel, T., Ricci, L., Dullemond, C.P., Uribe, A.L., Testi, L., Natta, A.: Trapping dust particles in the outer regions of protoplanetary disks. *A&A*, **538**, A114 (2012). DOI 10.1051/0004-6361/201118204
335. Podio, L., Kamp, I., Codella, C., Cabrit, S., Nisini, B., Dougados, C., Sandell, G., Williams, J.P., Testi, L., Thi, W.F., Woitke, P., Meijerink, R., Spaans, M., Aresu, G., Ménard, F., Pinte, C.: Water Vapor in the Protoplanetary Disk of DG Tau. *ApJL*, **766**, L5 (2013). DOI 10.1088/2041-8205/766/1/L5
336. Popham, R., Narayan, R., Hartmann, L., Kenyon, S.: Boundary Layers in Pre-Main-Sequence Accretion Disks. *ApJL*, **415**, L127 (1993). DOI 10.1086/187049
337. Preibisch, T., Kim, Y.C., Favata, F., Feigelson, E.D., Flaccomio, E., Getman, K., Micela, G., Sciortino, S., Stassun, K., Stelzer, B., Zinnecker, H.: The Origin of T Tauri X-Ray Emission: New Insights from the Chandra Orion Ultradeep Project. *ApJS*, **160**, 401–422 (2005). DOI 10.1086/432891
338. Preibisch, T., Kim, Y.C., Favata, F., Feigelson, E.D., Flaccomio, E., Getman, K., Micela, G., Sciortino, S., Stassun, K., Stelzer, B., Zinnecker, H.: The Origin of T Tauri X-Ray Emission: New Insights from the Chandra Orion Ultradeep Project. *ApJS*, **160**, 401–422 (2005). DOI 10.1086/432891
339. Pringle, J.E.: Soft X-ray emission from dwarf novae. *MNRAS*, **178**, 195–202 (1977)
340. Pringle, J.E.: Accretion discs in astrophysics. *ARA&A*, **19**, 137–162 (1981). DOI 10.1146/annurev.aa.19.090181.001033
341. Pringle, J.E.: The properties of external accretion discs. *MNRAS*, **248**, 754–759 (1991)
342. Pringle, J.E.: A simple approach to the evolution of twisted accretion discs. *MNRAS*, **258**, 811–818 (1992)
343. Pringle, J.E., King, A.: *Astrophysical Flows* (2007)
344. Qi, C., Öberg, K.I., Wilner, D.J., D’Alessio, P., Bergin, E., Andrews, S.M., Blake, G.A., Hogerheijde, M.R., van Dishoeck, E.F.: Imaging of the CO Snow Line in a Solar Nebula Analog. *Science* **341**, 630–632 (2013). DOI 10.1126/science.1239560
345. Raettig, N., Klahr, H., Lyra, W.: Particle Trapping and Streaming Instability in Vortices in Protoplanetary Disks. *ApJ*, **804**, 35 (2015). DOI 10.1088/0004-637X/804/1/35
346. Raettig, N., Lyra, W., Klahr, H.: A Parameter Study for Baroclinic Vortex Amplification. *ApJ*, **765**, 115 (2013). DOI 10.1088/0004-637X/765/2/115
347. Rafikov, R.R.: Properties of Gravitoturbulent Accretion Disks. *ApJ*, **704**, 281–291 (2009). DOI 10.1088/0004-637X/704/1/281
348. Rafikov, R.R.: Viscosity Prescription for Gravitationally Unstable Accretion Disks. *ApJ*, **804**, 62 (2015). DOI 10.1088/0004-637X/804/1/62
349. Railton, A.D., Papaloizou, J.C.B.: On the local stability of vortices in differentially rotating discs. *MNRAS*, **445**, 4409–4426 (2014). DOI 10.1093/mnras/stu2060
350. Rebusco, P., Umurhan, O.M., Kluźniak, W., Regev, O.: Global transient dynamics of three-dimensional hydrodynamical disturbances in a thin viscous accretion disk. *Physics of Fluids* **21**(7), 076,601 (2009). DOI 10.1063/1.3167411
351. Reipurth, B., Clarke, C.J., Boss, A.P., Goodwin, S.P., Rodríguez, L.F., Stassun, K.G., Tokovinin, A., Zinnecker, H.: Multiplicity in Early Stellar Evolution. *Protostars and Planets VI* pp. 267–290 (2014)
352. Ricci, L., Testi, L., Natta, A., Neri, R., Cabrit, S., Herczeg, G.J.: Dust properties of protoplanetary disks in the Taurus-Auriga star forming region from millimeter wavelengths. *A&A*, **512**, A15 (2010). DOI 10.1051/0004-6361/200913403
353. Rice, W.K.M., Armitage, P.J., Bate, M.R., Bonnell, I.A.: The effect of cooling on the global stability of self-gravitating protoplanetary discs. *MNRAS*, **339**, 1025–1030 (2003). DOI 10.1046/j.1365-8711.2003.06253.x
354. Rice, W.K.M., Armitage, P.J., Mamatsashvili, G.R., Lodato, G., Clarke, C.J.: Stability of self-gravitating discs under irradiation. *MNRAS*, **418**, 1356–1362 (2011). DOI 10.1111/j.1365-2966.2011.19586.x
355. Rice, W.K.M., Armitage, P.J., Wood, K., Lodato, G.: Dust filtration at gap edges: implications for the spectral energy distributions of discs with embedded planets. *MNRAS*, **373**, 1619–1626 (2006). DOI 10.1111/j.1365-2966.2006.11113.x

356. Rice, W.K.M., Lodato, G., Armitage, P.J.: Investigating fragmentation conditions in self-gravitating accretion discs. *MNRAS*, **364**, L56–L60 (2005). DOI 10.1111/j.1745-3933.2005.00105.x
357. Rice, W.K.M., Lodato, G., Pringle, J.E., Armitage, P.J., Bonnell, I.A.: Accelerated planetesimal growth in self-gravitating protoplanetary discs. *MNRAS*, **355**, 543–552 (2004). DOI 10.1111/j.1365-2966.2004.08339.x
358. Richling, S., Yorke, H.W.: Photoevaporation of protostellar disks. II. The importance of UV dust properties and ionizing flux. *A&A*, **327**, 317–324 (1997)
359. Rigliaco, E., Natta, A., Testi, L., Randich, S., Alcalà, J.M., Covino, E., Stelzer, B.: X-shooter spectroscopy of young stellar objects. I. Mass accretion rates of low-mass T Tauri stars in σ Orionis. *A&A*, **548**, A56 (2012). DOI 10.1051/0004-6361/201219832
360. Robitaille, T.P.: HYPERION: an open-source parallelized three-dimensional dust continuum radiative transfer code. *A&A*, **536**, A79 (2011). DOI 10.1051/0004-6361/201117150
361. Rodmann, J., Henning, T., Chandler, C.J., Mundy, L.G., Wilner, D.J.: Large dust particles in disks around T Tauri stars. *A&A*, **446**, 211–221 (2006). DOI 10.1051/0004-6361:20054038
362. Romanova, M.M., Ustyugova, G.V., Koldoba, A.V., Lovelace, R.V.E.: MRI-driven accretion on to magnetized stars: global 3D MHD simulations of magnetospheric and boundary layer regimes. *MNRAS*, **421**, 63–77 (2012). DOI 10.1111/j.1365-2966.2011.20055.x
363. Ros, K., Johansen, A.: Ice condensation as a planet formation mechanism. *A&A*, **552**, A137 (2013). DOI 10.1051/0004-6361/201220536
364. Rosenfeld, K.A., Andrews, S.M., Hughes, A.M., Wilner, D.J., Qi, C.: A Spatially Resolved Vertical Temperature Gradient in the HD 163296 Disk. *ApJ*, **774**, 16 (2013). DOI 10.1088/0004-637X/774/1/16
365. Ruden, S.P.: Evolution of Photoevaporating Protoplanetary Disks. *ApJ*, **605**, 880–891 (2004). DOI 10.1086/382524
366. Rybicki, G.B., Lightman, A.P.: Radiative processes in astrophysics (1979)
367. Salinas, V.N., Hogerheijde, M.R., Bergin, E.A., Cleeves, L.I., Brinch, C., Blake, G.A., Lis, D.C., Melnick, G.J., Panić, O., Pearson, J.C., Kristensen, L., Yıldız, U.A., van Dishoeck, E.F.: First detection of gas-phase ammonia in a planet-forming disk. NH_3 , N_2H^+ , and H_2O in the disk around TW Hydrae. *A&A*, **591**, A122 (2016). DOI 10.1051/0004-6361/201628172
368. Sano, T., Inutsuka, S.i.: Saturation and Thermalization of the Magnetorotational Instability: Recurrent Channel Flows and Reconnections. *ApJL*, **561**, L179–L182 (2001). DOI 10.1086/324763
369. Sano, T., Stone, J.M.: The Effect of the Hall Term on the Nonlinear Evolution of the Magnetorotational Instability. I. Local Axisymmetric Simulations. *ApJ*, **570**, 314–328 (2002). DOI 10.1086/339504
370. Sano, T., Stone, J.M.: The Effect of the Hall Term on the Nonlinear Evolution of the Magnetorotational Instability. II. Saturation Level and Critical Magnetic Reynolds Number. *ApJ*, **577**, 534–553 (2002). DOI 10.1086/342172
371. Schäfer, U., Yang, C.C., Johansen, A.: Initial mass function of planetesimals formed by the streaming instability. *A&A*, **597**, A69 (2017). DOI 10.1051/0004-6361/201629561
372. Shakura, N.I., Sunyaev, R.A.: Black holes in binary systems. Observational appearance. *A&A*, **24**, 337–355 (1973)
373. Shen, Y., Stone, J.M., Gardiner, T.A.: Three-dimensional Compressible Hydrodynamic Simulations of Vortices in Disks. *ApJ*, **653**, 513–524 (2006). DOI 10.1086/508980
374. Shu, F., Najita, J., Ostriker, E., Wilkin, F., Ruden, S., Lizano, S.: Magnetocentrifugally driven flows from young stars and disks. I: A generalized model. *ApJ*, **429**, 781–796 (1994). DOI 10.1086/174363
375. Simon, J.B., Armitage, P.J.: Efficiency of Particle Trapping in the Outer Regions of Protoplanetary Disks. *ApJ*, **784**, 15 (2014). DOI 10.1088/0004-637X/784/1/15
376. Simon, J.B., Armitage, P.J., Li, R., Youdin, A.N.: The Mass and Size Distribution of Planetesimals Formed by the Streaming Instability. I. The Role of Self-gravity. *ApJ*, **822**, 55 (2016). DOI 10.3847/0004-637X/822/1/55
377. Simon, J.B., Armitage, P.J., Youdin, A.N., Li, R.: Evidence for Universality in the Initial Planetesimal Mass Function. *ApJL*, **847**, L12 (2017). DOI 10.3847/2041-8213/aa8c79

378. Simon, J.B., Bai, X.N., Armitage, P.J., Stone, J.M., Beckwith, K.: Turbulence in the Outer Regions of Protoplanetary Disks. II. Strong Accretion Driven by a Vertical Magnetic Field. *ApJ*, **775**, 73 (2013). DOI 10.1088/0004-637X/775/1/73
379. Simon, J.B., Bai, X.N., Stone, J.M., Armitage, P.J., Beckwith, K.: Turbulence in the Outer Regions of Protoplanetary Disks. I. Weak Accretion with No Vertical Magnetic Flux. *ApJ*, **764**, 66 (2013). DOI 10.1088/0004-637X/764/1/66
380. Simon, J.B., Beckwith, K., Armitage, P.J.: Emergent mesoscale phenomena in magnetized accretion disc turbulence. *MNRAS*, **422**, 2685–2700 (2012). DOI 10.1111/j.1365-2966.2012.20835.x
381. Simon, J.B., Hawley, J.F.: Viscous and Resistive Effects on the Magnetorotational Instability with a Net Toroidal Field. *ApJ*, **707**, 833–843 (2009). DOI 10.1088/0004-637X/707/1/833
382. Simon, J.B., Hughes, A.M., Flaherty, K.M., Bai, X.N., Armitage, P.J.: Signatures of MRI-driven Turbulence in Protoplanetary Disks: Predictions for ALMA Observations. *ApJ*, **808**, 180 (2015). DOI 10.1088/0004-637X/808/2/180
383. Simon, J.B., Lesur, G., Kunz, M.W., Armitage, P.J.: Magnetically driven accretion in protoplanetary discs. *MNRAS*, **454**, 1117–1131 (2015). DOI 10.1093/mnras/stv2070
384. Smak, J.: Eruptive binaries. XI - Disk-radius variations in U GEM. *Acta Astronomica*, **34**, 93–96 (1984)
385. Soderblom, D.R., Hillenbrand, L.A., Jeffries, R.D., Mamajek, E.E., Naylor, T.: Ages of Young Stars. *Protostars and Planets VI* pp. 219–241 (2014)
386. Spruit, H.C.: Magnetohydrodynamic jets and winds from accretion disks. In: R.A.M.J. Wijers, M.B. Davies, C.A. Tout (eds.) *NATO Advanced Science Institutes (ASI) Series C, NATO Advanced Science Institutes (ASI) Series C*, vol. 477, pp. 249–286 (1996)
387. Steiman-Cameron, T.Y., Durisen, R.H., Boley, A.C., Michael, S., McConnell, C.R.: Convergence Studies of Mass Transport in Disks with Gravitational Instabilities. II. The Radiative Cooling Case. *ApJ*, **768**, 192 (2013). DOI 10.1088/0004-637X/768/2/192
388. Steinacker, J., Baes, M., Gordon, K.D.: Three-Dimensional Dust Radiative Transfer*. *ARA&A*, **51**, 63–104 (2013). DOI 10.1146/annurev-astro-082812-141042
389. Stepinski, T.F.: Generation of dynamo magnetic fields in the primordial solar nebula. *Icarus*, **97**, 130–141 (1992). DOI 10.1016/0019-1035(92)90062-C
390. Stevenson, D.J., Lunine, J.I.: Rapid formation of Jupiter by diffuse redistribution of water vapor in the solar nebula. *Icarus*, **75**, 146–155 (1988). DOI 10.1016/0019-1035(88)90133-9
391. Stoll, M.H.R., Kley, W.: Vertical shear instability in accretion disc models with radiation transport. *A&A*, **572**, A77 (2014). DOI 10.1051/0004-6361/201424114
392. Strom, K.M., Strom, S.E., Edwards, S., Cabrit, S., Skrutskie, M.F.: Circumstellar material associated with solar-type pre-main-sequence stars - A possible constraint on the timescale for planet building. *AJ*, **97**, 1451–1470 (1989). DOI 10.1086/115085
393. Supulver, K.D., Lin, D.N.C.: Formation of Icy Planetesimals in a Turbulent Solar Nebula. *Icarus*, **146**, 525–540 (2000). DOI 10.1006/icar.2000.6418
394. Suzuki, T.K., Inutsuka, S.i.: Disk Winds Driven by Magnetorotational Instability and Dispersal of Protoplanetary Disks. *ApJL*, **691**, L49–L54 (2009). DOI 10.1088/0004-637X/691/1/L49
395. Suzuki, T.K., Muto, T., Inutsuka, S.i.: Protoplanetary Disk Winds via Magnetorotational Instability: Formation of an Inner Hole and a Crucial Assist for Planet Formation. *ApJ*, **718**, 1289–1304 (2010). DOI 10.1088/0004-637X/718/2/1289
396. Suzuki, T.K., Ogihara, M., Morbidelli, A., Crida, A., Guillot, T.: Evolution of protoplanetary discs with magnetically driven disc winds. *A&A*, **596**, A74 (2016). DOI 10.1051/0004-6361/201628955
397. Takeuchi, T., Lin, D.N.C.: Radial Flow of Dust Particles in Accretion Disks. *ApJ*, **581**, 1344–1355 (2002). DOI 10.1086/344437
398. Takeuchi, T., Okuzumi, S.: Radial Transport of Large-scale Magnetic Fields in Accretion Disks. II. Relaxation to Steady States. *ApJ*, **797**, 132 (2014). DOI 10.1088/0004-637X/797/2/132
399. Tanaka, K.E.I., Nakamoto, T., Omukai, K.: Photoevaporation of Circumstellar Disks Revisited: The Dust-free Case. *ApJ*, **773**, 155 (2013). DOI 10.1088/0004-637X/773/2/155

400. Tanga, P., Babiano, A., Dubrulle, B., Provenzale, A.: Forming Planetesimals in Vortices. *Icarus*, **121**, 158–170 (1996). DOI 10.1006/icar.1996.0076
401. Tazzari, M., Testi, L., Ercolano, B., Natta, A., Isella, A., Chandler, C.J., Pérez, L.M., Andrews, S., Wilner, D.J., Ricci, L., Henning, T., Linz, H., Kwon, W., Corder, S.A., Dullemond, C.P., Carpenter, J.M., Sargent, A.I., Mundy, L., Storm, S., Calvet, N., Greaves, J.A., Lazio, J., Deller, A.T.: Multiwavelength analysis for interferometric (sub-)mm observations of protoplanetary disks. Radial constraints on the dust properties and the disk structure. *A&A*, **588**, A53 (2016). DOI 10.1051/0004-6361/201527423
402. Teague, R., Guilloteau, S., Semenov, D., Henning, T., Dutrey, A., Piétu, V., Birnstiel, T., Chapillon, E., Hollenbach, D., Gorti, U.: Measuring turbulence in TW Hydrae with ALMA: methods and limitations. *A&A*, **592**, A49 (2016). DOI 10.1051/0004-6361/201628550
403. Terquem, C., Papaloizou, J.C.B.: On the stability of an accretion disc containing a toroidal magnetic field. *MNRAS*, **279**, 767–784 (1996)
404. Throop, H.B., Bally, J.: Can Photoevaporation Trigger Planetesimal Formation? *ApJL*, **623**, L149–L152 (2005). DOI 10.1086/430272
405. Throop, H.B., Bally, J.: Tail-End Bondi-Hoyle Accretion in Young Star Clusters: Implications for Disks, Planets, and Stars. *AJ*, **135**, 2380–2397 (2008). DOI 10.1088/0004-6256/135/6/2380
406. Tobin, J.J., Kratter, K.M., Persson, M.V., Looney, L.W., Dunham, M.M., Segura-Cox, D., Li, Z.Y., Chandler, C.J., Sadavoy, S.I., Harris, R.J., Melis, C., Pérez, L.M.: A triple protostar system formed via fragmentation of a gravitationally unstable disk. *Nature*, **538**, 483–486 (2016). DOI 10.1038/nature20094
407. Toomre, A.: On the gravitational stability of a disk of stars. *ApJ*, **139**, 1217–1238 (1964). DOI 10.1086/147861
408. Torres, R.M., Loinard, L., Mioduszewski, A.J., Boden, A.F., Franco-Hernández, R., Vlemmings, W.H.T., Rodríguez, L.F.: VLBA Determination of the Distance to nearby Star-forming Regions. V. Dynamical Mass, Distance, and Radio Structure of V773 Tau A. *ApJ*, **747**, 18 (2012). DOI 10.1088/0004-637X/747/1/18
409. Tout, C.A., Pringle, J.E.: Accretion disc viscosity - A simple model for a magnetic dynamo. *MNRAS*, **259**, 604–612 (1992)
410. Trapman, L., Miotello, A., Kama, M., van Dishoeck, E.F., Bruderer, S.: Far-infrared HD emission as a measure of protoplanetary disk mass. *A&A*, **605**, A69 (2017). DOI 10.1051/0004-6361/201630308
411. Tsukamoto, Y., Iwasaki, K., Okuzumi, S., Machida, M.N., Inutsuka, S.: Bimodality of circumstellar disk evolution induced by Hall current. *ArXiv e-prints* (2015)
412. Tsukamoto, Y., Takahashi, S.Z., Machida, M.N., Inutsuka, S.: Effects of radiative transfer on the structure of self-gravitating discs, their fragmentation and the evolution of the fragments. *MNRAS*, **446**, 1175–1190 (2015). DOI 10.1093/mnras/stu2160
413. Turner, N.J., Benisty, M., Dullemond, C.P., Hirose, S.: Herbig Stars’ Near-infrared Excess: An Origin in the Protostellar Disk’s Magnetically Supported Atmosphere. *ApJ*, **780**, 42 (2014). DOI 10.1088/0004-637X/780/1/42
414. Turner, N.J., Drake, J.F.: Energetic Protons, Radionuclides, and Magnetic Activity in Protostellar Disks. *ApJ*, **703**, 2152–2159 (2009). DOI 10.1088/0004-637X/703/2/2152
415. Turner, N.J., Sano, T.: Dead Zone Accretion Flows in Protostellar Disks. *ApJL*, **679**, L131–L134 (2008). DOI 10.1086/589540
416. Turner, N.J., Sano, T., Dziourkevitch, N.: Turbulent Mixing and the Dead Zone in Protostellar Disks. *ApJ*, **659**, 729–737 (2007). DOI 10.1086/512007
417. Umebayashi, T., Nakano, T.: Effects of Radionuclides on the Ionization State of Protoplanetary Disks and Dense Cloud Cores. *ApJ*, **690**, 69–81 (2009). DOI 10.1088/0004-637X/690/1/69
418. Umurhan, O.M.: Potential vorticity dynamics in the framework of disk shallow-water theory. I. The Rossby wave instability. *A&A*, **521**, A25 (2010). DOI 10.1051/0004-6361/201015210
419. Urpin, V., Brandenburg, A.: Magnetic and vertical shear instabilities in accretion discs. *MNRAS*, **294**, 399 (1998). DOI 10.1046/j.1365-8711.1998.01118.x

420. Uyama, T., Hashimoto, J., Kuzuhara, M., Mayama, S., Akiyama, E., Currie, T., Livingston, J., Kudo, T., Kusakabe, N., Abe, L., Brandner, W., Brandt, T.D., Carson, J.C., Egner, S., Feldt, M., Goto, M., Grady, C.A., Guyon, O., Hayano, Y., Hayashi, M., Hayashi, S.S., Henning, T., Hodapp, K.W., Ishii, M., Iye, M., Janson, M., Kandori, R., Knapp, G.R., Kwon, J., Matsuo, T., Mcelwain, M.W., Miyama, S., Morino, J.I., Moro-Martin, A., Nishimura, T., Pyo, T.S., Serabyn, E., Suenaga, T., Suto, H., Suzuki, R., Takahashi, Y.H., Takami, M., Takato, N., Terada, H., Thalmann, C., Turner, E.L., Watanabe, M., Wisniewski, J., Yamada, T., Takami, H., Usuda, T., Tamura, M.: The SEEDS High-Contrast Imaging Survey of Exoplanets Around Young Stellar Objects. *AJ*, **153**, 106 (2017). DOI 10.3847/1538-3881/153/3/106
421. van Boekel, R., Henning, T., Menu, J., de Boer, J., Langlois, M., Müller, A., Avenhaus, H., Boccaletti, A., Schmid, H.M., Thalmann, C., Benisty, M., Dominik, C., Ginski, C., Girard, J.H., Gisler, D., Lobo Gomes, A., Menard, F., Min, M., Pavlov, A., Pohl, A., Quanz, S.P., Rabou, P., Roelfsema, R., Sauvage, J.F., Teague, R., Wildi, F., Zurlo, A.: Three Radial Gaps in the Disk of TW Hydrae Imaged with SPHERE. *ApJ*, **837**, 132 (2017). DOI 10.3847/1538-4357/aa5d68
422. van der Marel, N., van Dishoeck, E.F., Bruderer, S., Birnstiel, T., Pinilla, P., Dullemond, C.P., van Kempen, T.A., Schmalzl, M., Brown, J.M., Herczeg, G.J., Mathews, G.S., Geers, V.: A Major Asymmetric Dust Trap in a Transition Disk. *Science* **340**, 1199–1202 (2013). DOI 10.1126/science.1236770
423. Varnière, P., Tagger, M.: Reviving Dead Zones in accretion disks by Rossby vortices at their boundaries. *A&A*, **446**, L13–L16 (2006). DOI 10.1051/0004-6361:200500226
424. Velikhov, E.: Stability of an ideally conducting liquid flowing between rotating cylinders in a magnetic field. *Zhur. Eksptl'. i Teoret. Fiz.* **Vol: 36** (1959)
425. Vorobyov, E.I., Basu, S.: The Origin of Episodic Accretion Bursts in the Early Stages of Star Formation. *ApJL*, **633**, L137–L140 (2005). DOI 10.1086/498303
426. Wang, L., Goodman, J.: Hydrodynamic Photoevaporation of Protoplanetary Disks with Consistent Thermochemistry. *ApJ*, **847**, 11 (2017). DOI 10.3847/1538-4357/aa8726
427. Ward, W.R.: Particle Filtering by a Planetary Gap. In: Lunar and Planetary Science Conference, *Lunar and Planetary Inst. Technical Report*, vol. 40, p. 1477 (2009)
428. Wardle, M.: The Balbus-Hawley instability in weakly ionized discs. *MNRAS*, **307**, 849–856 (1999). DOI 10.1046/j.1365-8711.1999.02670.x
429. Waters, T.R., Proga, D.: Parker winds revisited: an extension to disc winds. *MNRAS*, **426**, 2239–2265 (2012). DOI 10.1111/j.1365-2966.2012.21823.x
430. Weidenschilling, S.J.: Aerodynamics of solid bodies in the solar nebula. *MNRAS*, **180**, 57–70 (1977)
431. Weidenschilling, S.J.: The distribution of mass in the planetary system and solar nebula. *Astrophysics and Space Science*, **51**, 153–158 (1977). DOI 10.1007/BF00642464
432. Weingartner, J.C., Draine, B.T.: Photoelectric Emission from Interstellar Dust: Grain Charging and Gas Heating. *ApJS*, **134**, 263–281 (2001). DOI 10.1086/320852
433. Whipple, F.L.: On certain aerodynamic processes for asteroids and comets. In: A. Elvius (ed.) *From Plasma to Planet*, p. 211 (1972)
434. Williams, J.P., Best, W.M.J.: A Parametric Modeling Approach to Measuring the Gas Masses of Circumstellar Disks. *ApJ*, **788**, 59 (2014). DOI 10.1088/0004-637X/788/1/59
435. Williams, J.P., Cieza, L.A.: Protoplanetary Disks and Their Evolution. *ARA&A*, **49**, 67–117 (2011). DOI 10.1146/annurev-astro-081710-102548
436. Yang, C.C., Johansen, A.: On the Feeding Zone of Planetesimal Formation by the Streaming Instability. *ApJ*, **792**, 86 (2014). DOI 10.1088/0004-637X/792/2/86
437. Yang, C.C., Johansen, A., Carrera, D.: Concentrating small particles in protoplanetary disks through the streaming instability. *A&A*, **606**, A80 (2017). DOI 10.1051/0004-6361/201630106
438. Youdin, A.N., Chiang, E.I.: Particle Pileups and Planetesimal Formation. *ApJ*, **601**, 1109–1119 (2004). DOI 10.1086/379368
439. Youdin, A.N., Goodman, J.: Streaming Instabilities in Protoplanetary Disks. *ApJ*, **620**, 459–469 (2005). DOI 10.1086/426895

440. Youdin, A.N., Lithwick, Y.: Particle stirring in turbulent gas disks: Including orbital oscillations. *Icarus*, **192**, 588–604 (2007). DOI 10.1016/j.icarus.2007.07.012
441. Youdin, A.N., Shu, F.H.: Planetesimal Formation by Gravitational Instability. *ApJ*, **580**, 494–505 (2002). DOI 10.1086/343109
442. Zhang, K., Blake, G.A., Bergin, E.A.: Evidence of Fast Pebble Growth Near Condensation Fronts in the HL Tau Protoplanetary Disk. *ApJL*, **806**, L7 (2015). DOI 10.1088/2041-8205/806/1/L7
443. Zhu, Z., Hartmann, L., Calvet, N., Hernandez, J., Muzerolle, J., Tannirkulam, A.K.: The Hot Inner Disk of FU Orionis. *ApJ*, **669**, 483–492 (2007). DOI 10.1086/521345
444. Zhu, Z., Hartmann, L., Gammie, C.: Long-term Evolution of Protostellar and Protoplanetary Disks. II. Layered Accretion with Infall. *ApJ*, **713**, 1143–1158 (2010). DOI 10.1088/0004-637X/713/2/1143
445. Zhu, Z., Hartmann, L., Gammie, C., McKinney, J.C.: Two-dimensional Simulations of FU Orionis Disk Outbursts. *ApJ*, **701**, 620–634 (2009). DOI 10.1088/0004-637X/701/1/620
446. Zhu, Z., Hartmann, L., Gammie, C.F., Book, L.G., Simon, J.B., Engelhard, E.: Long-term Evolution of Protostellar and Protoplanetary Disks. I. Outbursts. *ApJ*, **713**, 1134–1142 (2010). DOI 10.1088/0004-637X/713/2/1134
447. Zhu, Z., Nelson, R.P., Dong, R., Espaillat, C., Hartmann, L.: Dust Filtration by Planet-induced Gap Edges: Implications for Transitional Disks. *ApJ*, **755**, 6 (2012). DOI 10.1088/0004-637X/755/1/6
448. Zhu, Z., Stone, J.M.: Dust Trapping by Vortices in Transitional Disks: Evidence for Non-ideal Magnetohydrodynamic Effects in Protoplanetary Disks. *ApJ*, **795**, 53 (2014). DOI 10.1088/0004-637X/795/1/53
449. Zhu, Z., Stone, J.M., Bai, X.N.: Dust Transport in MRI Turbulent Disks: Ideal and Non-Ideal MHD With Ambipolar Diffusion. *ApJ*, **801**, 81 (2015). DOI 10.1088/0004-637X/801/2/81
450. Zhu, Z., Stone, J.M., Rafikov, R.R., Bai, X.N.: Particle Concentration at Planet-induced Gap Edges and Vortices. I. Inviscid Three-dimensional Hydro Disks. *ApJ*, **785**, 122 (2014). DOI 10.1088/0004-637X/785/2/122
451. Zweibel, E.G.: Ambipolar Diffusion, *Astrophysics and Space Science Library*, vol. 407, p. 285 (2015)